Design and Control of Versatile High-Speed and Large-Range Atomic Force Microscopes

by

Fangzhou Xia

S.M., Mechanical Engineering MIT (2017)
B.S., Mechanical Engineering University of Michigan (2015)
B.S., Electrical Engineering Shanghai Jiao Tong University (2015)

Submitted to the Department of Mechanical Engineering
in partial fulfillment of the requirements for the degree of

Doctor of Philosophy

at the

MASSACHUSETTS INSTITUTE OF TECHNOLOGY

September 2020

Author .....
Department of Mechanical Engineering
Aug 23, 2020

Certified by .....
Kamal Youcef-Toumi
Professor of Mechanical Engineering
Thesis Supervisor

Accepted by .....
Nicolas Hadjiconstantinou
Chairman, Department Committee on Graduate Students

Design and Control of Versatile High-Speed and Large-Range Atomic Force Microscopes

by

Fangzhou Xia

Submitted to the Department of Mechanical Engineering
on Aug 23, 2020, in partial fulfillment of the
requirements for the degree of
Doctor of Philosophy

Abstract

Microscopy instruments are important in nano-technology research for imaging of nanoscale phenomena. Among such tools is the atomic force microscope (AFM) for nanoscale imaging and surface characterization. An AFM scans a micro-cantilever over the sample surface to measure various quantities from the probe-sample interaction. With high-speed imaging, dynamic processes can be visualized to improve fundamental understanding of microscopic interactions. Scientists can use videos, in addition to images, to observe and compare experimental data with theoretical predictions, and verify models without speculating about intermediate dynamics. However, conventional AFMs have limited throughput that allow for static imaging only and require transparent working environments.

The contributions of this thesis remove such AFM restrictions and enable advanced visualization capabilities. Example applications include visualizing chemical reactions and biological responses in their native environments. To this end, the thesis addresses four main AFM limitations. These are (i) increase the low imaging throughput to be compatible for higher temporal resolution imaging, (ii) remove the transparency requirement, for AFMs that use optical beam deflection sensing, and enable imaging in harsh opaque liquids, (iii) establish automation algorithms to reduce operational overheads associated with experiment setup and controller tuning, and (iv) introduce custom design modifications resulting in affordable AFMs for engineering education.

These new capabilities are primarily enabled with the development of new subsystems. The key components include nano-positioners, cantilever probes, and control algorithms. New generation AFM nano-positioners are designed with high-speed, large-range or low-cost characteristics for different scanning needs. Coated active cantilever probes are developed for AFM imaging in specialized opaque environments. Multiple algorithms for scanner control, automatic tuning, and image formation are investigated to improve AFM imaging performance. Additional developments to support AFM imaging include high-bandwidth driver electronics, optical systems with vision-based automation, and software implementation for AFM big data processing.

Three AFM systems are integrated using these new subsystems for different applications. They include a versatile sample scan AFM for overview-and-zoom imaging in air and liquids, a multi-layer stacked scanner AFM for high-speed and large-range imaging in air, and a low-cost active probe AFM for engineering education. AFM images and videos at 20 frames per second are taken in various environments to verify the new capabilities. These developments have broader impacts in the fields of precision instrumentation, nano-fabrication, and nano-scale process video-rate visualization.

Thesis Supervisor: Kamal Youcef-Toumi
Title: Professor of Mechanical Engineering

Acknowledgments

First of all, I would like to express my gratitude for my advisor Professor Kamal Youcef-Toumi for his support and guidance during my years at MIT. His knowledge and insights both in the area of engineering and in life have played an important role in my professional development. The friendly environment and freedom to explore a the Mechatronics Research Laboratory (MRL) helped me a lot in facing the challenges. It has truly been an honor and a memorable experience to work with Professor Youcef-Toumi at MIT.

I want to show my appreciation for to Professor Ian Hunter and Prof. Alberto Rodriguez for being my thesis committee members. The comments and suggestions to my work are invaluable and provided great guidance to this thesis.

I also want to acknowledge Professor Harry Asada and Professor David Trumper for their advise and help. I have learned a lot from their insightful answers to my numerous questions.

I want to acknowledge my current and previous project team members Dr. Chen Yang, Dr. Yi Wang, Mr. Stephen Truncale and Dr. Iman Soltani Bozchalooi. I also feel grateful to my collaborators Prof. Ivo Rangelow, Dr. Mathias Holz, Mr. Christoph Reture and Mr. Xiaotong Zhang. It was a great pleasure working together push forward the frontier of technology.

During the years working on this thesis, I received help from a number of undergraduate research assistants. I would like to thank Ms. Janice C Moya, Ms. Emily Wang, Mr. Mingfei Duan, Mr. James Edwin Quigley, Mr.August Trollback, Ms. Ashisha Persad, Mr.Jose Martinez, Ms. Sarah Spector, Ms. Jesse Chang, Ms. Jennifer Yu, Druck Green, Ms. Khanh N. for their contributions to this work.

The good research environment in the lab is important for my work. I would like to thank my lab mates Dr. Kai Meng, Dr. Ali Hamoud Alshehri, Dr. Amith Somanath, Dr. You Wu, Ms. Bo Jiang, Mr. Yekuan Yang for creating such a friendly and pleasant environment at MRL. Their comments to my work during the lab meeting also provided me with valuable information to improve this thesis.

The smooth research activities are also indebted to the hardworking staff members. I would like to thank the staff members at the Mechanical Engineering Department of MIT, especially Ms. Leslie Regan, Ms. Catherine Anne Hogan, Mr.Brendan O'Brine, Ms. Dorothy S Hanna, Ms. Theresa L. Werth, and Ms. Nadiyah Shaheed for all their help to keep things going smoothly.

The success of nano-technology research relies greatly on the available funding. I want to acknowledge Synfuels Americas and Synfuels China for their financial support.

Last but definitely not least, I have my deep gratitude to my family for support and love. I would like to thank the love of my life, my wife Ms. Yao Tong, for bringing unlimited happiness and hope to my life. I also want to express my gratitude to my grandmother Fangnong Yan, my grandmother-in-law Yuqing Zhan, my mother Ms. Yi Wang, my mother-in-law Ms. Baomin Chen, my father Mr. Hai Xia, and my father-in-law Mr. Zhaohui Tong.

Contents

List of Figures

List of Tables

Chapter 1

Background

1.1 Introduction

Scanning probe microscopy (SPM) includes a family of microscopy techniques using physical probes. During operation the probe is scanned over the sample surface for image generation or manipulation. The family of SPM systems include many sub-fields under active research with applications in the fields of physics, chemistry, material science, microbiology, etc. [1, 2, 3, 4]. Among different types of SPM techniques, the Atomic Force Microscope (AFM) and the Scanning Tunneling Microscope (STM) are the most widely used tools for obtaining topography and local electron density of states information. A variety of modes have been developed centered around the fundamental principles of AFM and STM for specialized applications. Examples include Kelvin Probe Force Microscopy (KPFM), scattering type scanning near-field optical microscopy (s-SNOM), electro-chemical scanning tunneling microscope, etc. In this work, we focus on the development of AFM systems with new or improved imaging capabilities for various application scenarios.

Atomic force microscope (AFM) is a versatile nano-scale imaging tool [5]. In its basic form, AFMs create topography images with sub-nanometer resolution, which allows observation and manipulation of atomic lattice or molecular structure [6]. This capability significantly exceeds the optical microscopy resolution due to the diffraction limit from Rayleigh criterion. Compared to other types of high resolution microscopy

techniques such as the Scanning Electron Microscope (SEM), versatility is another important characteristic of AFMs. AFM systems can visualize samples in air, liquid or vacuum environments. There is also no sample conductivity requirement as compared to electron based microscopy techniques such as SEM or STM. These features make AFM an attractive candidate for the study of chemical and biological samples especially in liquid environment. With specially designed cantilever probes, AFM can also be used for nano-scale manipulation [7] and fabrication (e.g. scanning probe lithography) [8, 9]. With its comparative advantages in a number of applications scenarios, AFM has earned its place in both industry and academia such as semiconductor inspection, nano-technology research sample characterization, etc.

1.2 AFM System Overview

An AFM system has three main hardware components. These include a cantilever probe transducer, a positioning system, and driving electronics. Additional accessories and software are also needed to ensure good performance of the system. The design illustration of a conventional AFM with sample scan configuration is shown in Fig. 1-1.

The AFM imaging resolution and range capabilities are on the nanometer to micrometer scale. A typical AFM system has a scan range between tens of microns to over a hundred microns in both two in-plane directions. The out-of-plane travel range is between several microns to tens of microns. An in-plane resolution over several nanometers and an out-of-plane resolution on the sub-nanometer level are typical for commercially available systems. Atomic resolution AFM systems are also possible but generally require specialized design to reduce the noise floor. In the sample scan configuration, the positioner moves a relatively small sample (typical diameter below half an inch or 12.7 mm). Larger sample size can be accommodated by using a probe scan configuration. A brief overview of each subsystem is provided below for a conventional AFM.

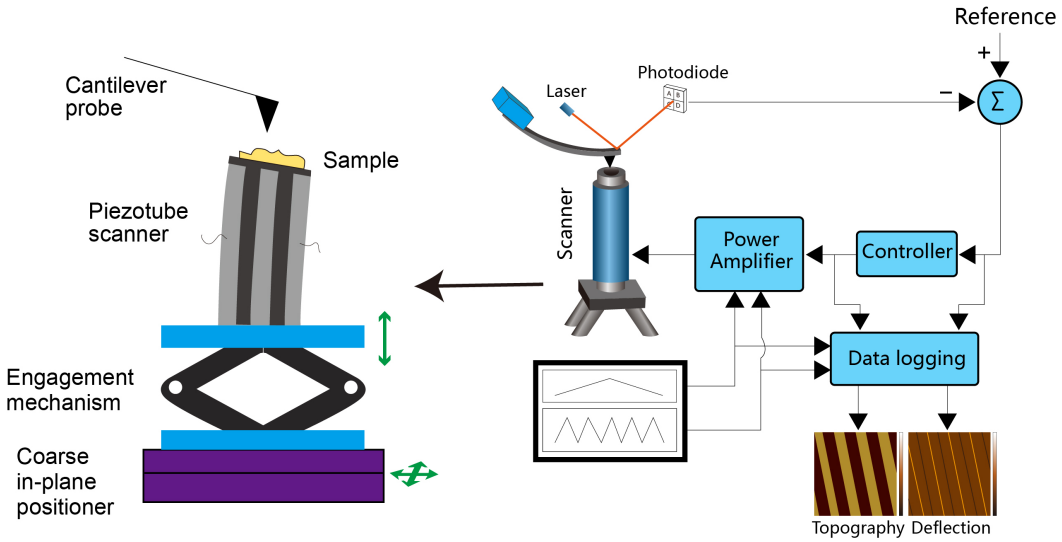

Figure 1-1: Overview of a conventional AFM system architecture including a scanner, a cantilever probe, an optical beam deflection system and a controller. An expanded view of the positioning system is shown on the left with a quadrature piezo tube scanner.

1.2.1 Cantilever Probe Transducer

At the heart of the AFM system is the cantilever probe. As shown in Fig. 1-2, a typical AFM probe is composed of a sharp tip, a cantilever beam and a base support chip for manual handling and mounting onto holders.

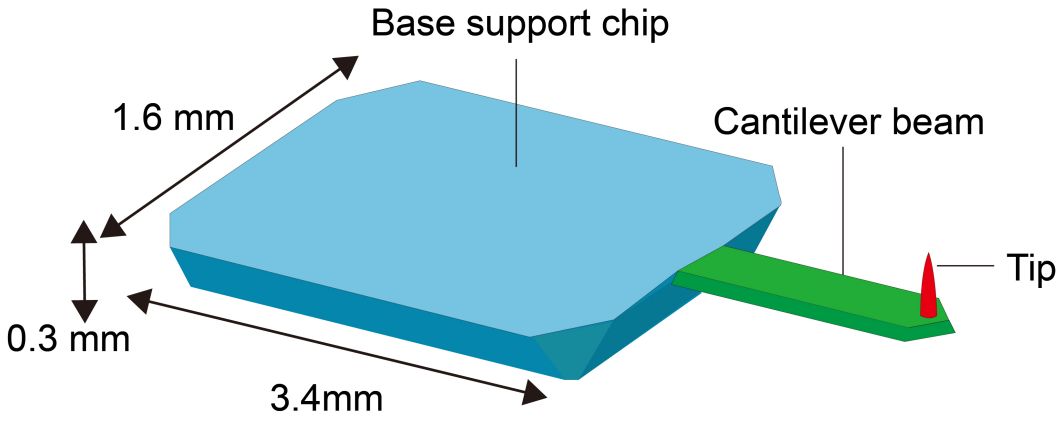

Figure 1-2: Geometric illustration of a standard passive AFM probe including the base support chip, the cantilever beam and the tip

Most AFM probe geometry are standardized. The industrial standard base chip has 3.4 mm length, 1.6 mm width, and 0.3 mm thickness for mounting into a standard

slot of the probe holder. The cantilever probe is usually micro-fabricated from bulk silicon or silicon nitride wafers. The cantilever can have various geometric shape depending on the application. The most common shape is a straight beam with rectangular cross sectional area. Other geometric shapes such as a solid or a hollow triangular shape with two crossing cantilever beams are also available. With modern nano-fabrication techniques, the probe tip with a tetrahedral pyramid or cone shape can have a nominal apex radius down to a single nanometer.

Cantilever deflection measurement and control is important during AFM imaging. For cantilever deflection measurement, conventional AFM designs use the optical beam deflection (OBD) system as shown in Fig. 1-1. A laser source is focused on the back of the micro-cantilever. The reflected light path amplifies the small angle change of the cantilever, which is then converted to electrical signal using a four-quadrant photodiode. For cantilever actuation, a piezoactuator is embedded into the probe holder to acoustically excite the cantilever resonance. There are many other sensing and actuation methods available that will be discussed in Chapter 3. Depending on whether the actuation and sensing systems are embedded into the cantilever itself or not, the cantilever probe transducer can in general be classified into passive and active.

1.2.2 Positioning System

The AFM positioning system has three main functionalities. First, a coarse positioner is used to bring the probe and sample into contact during the engagement process. Second, a fine positioner regulates the probe deflection or oscillation by controlling the relative distance between the probe tip and the sample in the out-of-plane direction. Third, a in-plane scanner realize the scanning trajectory to generate images. The positioning system plays an important role that determines the AFM imaging capability for throughput, resolution, range, etc. Fig. 1-1 shows a commonly used piezotube scanner for high resolution nano-positioning. Many different scanner designs have been proposed and implemented based on the application needs with more detailed discussion in Chapter 2. The positioning system works together with

the control algorithm to generate AFM images, which is the focus of discussion in Chapter 4.

1.2.3 Driving Electronics

Electrical circuits are needed to drive AFM subsystems. The driving electronics primarily include analog conditioning circuits, drivers and data acquisition systems. They handle the tasks of signal processing, probe deflection regulation, AFM image data collection, etc. Controller implementation on Field Programmable Gate Arrays (FPGAs) is typically used for high bandwidth signal processing. Both commercially available DAQ systems or custom systems can be used for AFM system design with more details in Chapter 5.

1.2.4 Additional Components

Additional accessories can be added to improve the AFM capabilities in various aspects. As an example, these could include additional in-plane positioner for ease of experiment setup, optical microscope for sample overview and computer vision algorithms for automated laser-probe alignment as will be discussed in Chapter 5. For operation in non-ambient environment, vacuum pumps or fluid circulation systems are needed for operation in vacuum or liquid environments. Additional imaging modalities can also been enabled by adding corresponding components such as laser optics for tip-enhanced spectroscopy.

1.3 AFM Imaging Principles

A conventional AFM operates by scanning a flexible micro-cantilever probe over the sample surface. The deflection signal of the probe tip is affected by the interaction force between the probe and the sample, which can be measured and regulated for interaction force control and image generation. In this section, we introduce the AFM imaging principles.

1.3.1 AFM Image Modes

A number of modes have been developed for AFM imaging. The imaging modes for obtaining mechanical related information can in general be classified into three categories by considering the motion state of the cantilever. The three main categories include the contact modes, the dynamic modes and the jumping modes with a visual illustration shown in Fig. 1-3.

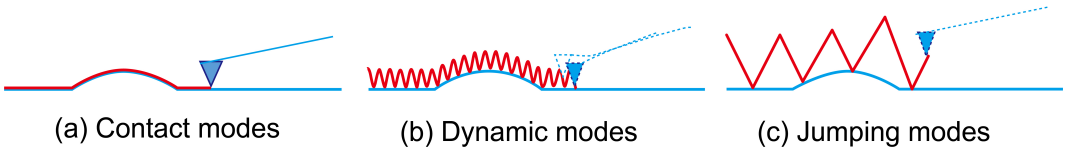

Figure 1-3: AFM mechanical modes of operation classification based on the motion state of the cantilever: (a) contact modes where the probe and the sample are in contact for all time, (b) dynamic modes where cantilever resonance is excited, (c) jumping modes where intermittent contacts are made without cantilever resonance excitation

Contact Modes

In contact modes, the cantilever probe tip and the sample surface remains in contact during imaging. There are primarily two modes of imaging in this category including the constant height mode and the constant force mode.

The constant height mode is used in the early years of AFM system with relatively simple design. The AFM probe is pressed against the sample in the vertical direction and the scanner produce a raster scanning motion in a plane (labeled as the x and y axis direction). The probe deflection signal varies as the sample height changes in the out-of-plane direction. The measured deflection signal is directly used for topography image generation in this case. The main disadvantage of this simplified design is its lack of capability for motion control in the out-of-plane z-axis direction. With typical cantilever deflection ranging up to hundreds of nanometer, samples with larger out-of-plane topography variation can be difficult to image. Moreover, the cantilever deflection variation induces in a changing probe-sample interaction force that cannot be regulated, which can result in sample or probe damage as well as inaccurate measurement due to sample deformation under varying applied force.

In constant force mode, a controller is used to regulate the cantilever deflection through the out-of-plane axis positioner. This allows the probe and sample to remain in contact and maintain a constant interaction force. This mode resolves the issues in the constant height mode but the control loop bandwidth can limit the imaging throughput in high-speed system. This mode is widely used for modern commercial AFM systems for contact mode imaging. When talking about contact mode, people usually refer to the constant force scanning mode.

Dynamic Modes

In dynamic modes, the resonance of the cantilever probe is excited. The oscillation characteristic can be used for both regulation and contrast mapping. For resonance excitation at a single frequency, the amplitude and the phase are commonly used for out-of-plane motion control and contrast mapping. The slight frequency shift due to interaction between the probe tip and the sample can also be used for imaging in frequency modulated AFM. Multiple resonance frequencies can be simultaneously excited for AFM imaging. Depending on which region of the Lennard-Jones potential are the tip-sample interaction lies, the dynamic modes can be further divided into non-contact mode for attractive region and tapping mode for the repulsive region. The dynamic modes are preferred for imaging of delicate samples that require small interaction forces.

Jumping Modes

For jumping modes, the probe tip and the sample also make intermittent contact. However, the resonance frequency of the cantilever is not excited during imaging as in the dynamic modes. A large sample area can be covered in a short time since the relative position between the probe tip and the sample does not need to be regulated during scanning when the probe moves from one point to another. One example is the force volume mode for getting deflection curve at each pixels for measurement of mechanical properties. Another good example would be the peak force tapping mode developed by Bruker company [10, 11], which is in principle similar to the force volume mode with additional control techniques for background noise cancellation through calibration.

Additional Modes The previously introduced imaging modes are just a subset of basic modes. Some operation modes can be considered as a mixture of the aforementioned modes. For example, the contact resonance mode is a combination of contact modes and dynamic modes. In this case, small magnitude modulation signal is added to the cantilever deflection reference signal while the probe tip remains in contact with sample. As another example, the induced vibration jumping mode [12] previously developed in our lab is essentially a combination of dynamic modes with jumping modes. A number of specialized mechanical imaging modes have been developed in research applications such as load force modulation mode [13], pulsed-force mode [14], lateral force mode [15], etc. The classification of AFM imaging modes can be accomplished differently depending on the criteria. The scope of consideration can also be expanded to include thermal, piezo-related, optical and electrical modalities.

1.3.2 Probe-Sample Interaction

The physical interaction between the probe and the sample is important for image formation. Models such as the Lennard-Jones potential and Van der Waals forces are used for approximation of microscopic interaction forces. The Van der Waals forces summarize the contribution of three Coulombic force including London dispersion force, Keesom polarization forces, and Debye dipole-induced dipole interaction forces [16]. For tip-sample interaction contact mechanics, geometry, intermolecular forces and elastic deformation need to be considered. For example, the Derjaguin-Müller-Toporov (DMT) model, Johnson-Kendall-Roberts (JKR) model and Maugis-Dugdale elastic contact model have all been proposed for modeling of AFM probe-sample interaction.

The AFM image formation process depends greatly on the cantilever deflection measurement and regulation of the probe sample interaction forces by controlling the motion of the scanner. Therefore, we have devoted significant effort in this work to extend the capabilities of the cantilever probe, the nano-positioner design and the control algorithms to be discussed in Chapter 2, 3 and 4.

1.4 Operation and Applications

For regular AFM users, it is important to understand the operation and suitable applications of the instrument. In this overview chapter, we provide a brief introduction of the typical AFM experiment procedure and applications.

1.4.1 Experiment Procedure

For AFM operation, five general steps are important to ensure high quality images are captured. These include the sample preparation, equipment calibration, experiment setup, controller parameter tuning, and post processing of the collected data. The key experiment steps to consider are visualized in Fig. 1-4.

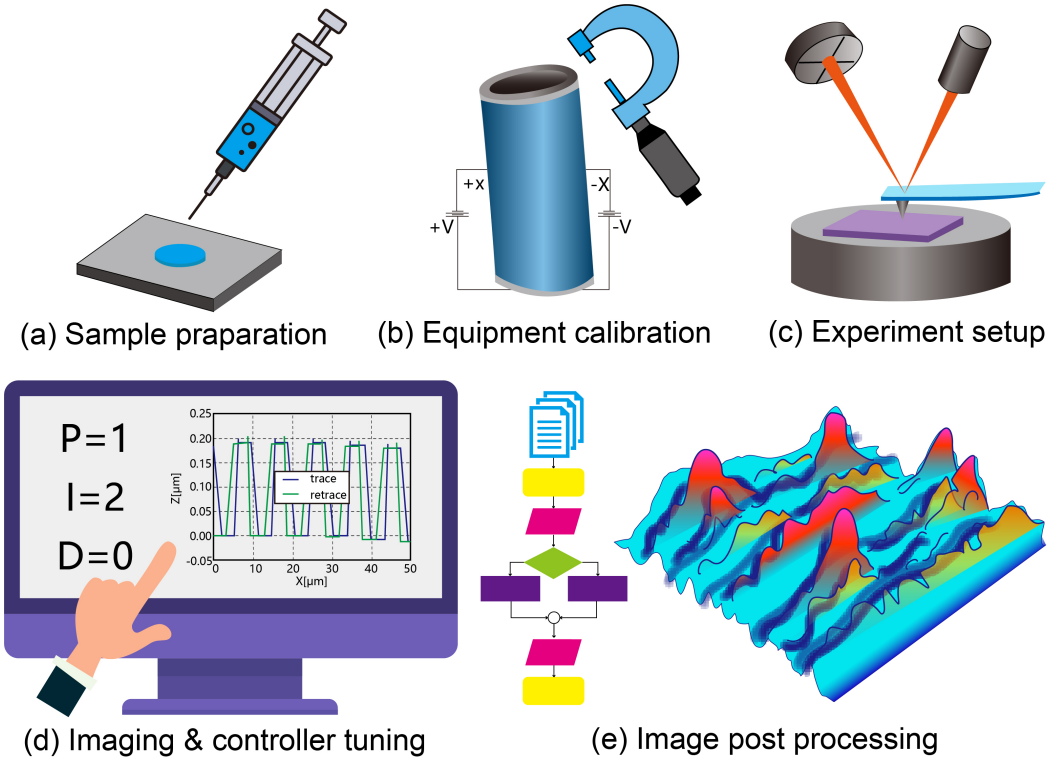

Figure 1-4: Common steps required in an AFM imaging experiment: (a) sample preparation, (b) equipment calibration, (c) experiment setup, (d) imaging and controller tuning, (e) image post processing

Sample preparation is a large filed of research with techniques depending on specific applications. A number of books are available for discussion on techniques to

prepare certain samples for AFM imaging such as biological specimens [17].

The equipment calibration step is important to ensure good AFM performance. It can be accomplished either on the subsystem level or for the entire AFM system using calibration gratings. This step is usually completed by the vendor. In certain situations, the users might also need to perform system level calibration usually with guided instructions from the vendor.

The AFM equipment setup process depends heavily on the specific experiment. Here, we discuss the fundamental steps for setting up a conventional AFM system with optical beam deflection system for contact mode topography imaging in an ambient environment. The steps illustrated below assumes the sample is properly prepared and the AFM system is properly calibrated. More complex steps are needed depending on the experiment requirement such as probe resonance identification for tapping mode imaging.

1. Attach the prepared sample on a sample puck to the AFM nano-positioning stage with sticky tape or with magnet.
2. Select and install the cantilever in the probe holder.
3. Mount the probe holder and align the laser spot with the cantilever probe tip.
4. Adjust the optics until the reflected laser spot is detected at the center of the four quadrant photodiode.
5. Identify the area of interest for imaging using optical microscope and adjust using manual in-plane positioner.
6. Set the engagement signal threshold in software and engage the probe with the sample.
7. Adjust the controller parameter and start imaging.

The Proportional-Integral-Derivative (PID) controller needs to be adjusted during imaging. The tuning process is typically accomplished manually by matching the trace and retrace tracking lines during imaging. An attempt to automate this process have been made in this work with more discussions in Chapter 4.

The post processing steps can be accomplished with both propriety software packages and custom code. The software is usually provided by the AFM vendor such as the Bruker NanoScope Analysis. Open source SPM data processing software such as Gwyddion can also be used. A number of built-in functions designed by considering SPM image formation are available to speed up the post-processing step. An AFM imaging batch processing tool has been developed in this work that will be discussed in Chapter 5. The Matlab software can also be used for better flexibility in visualization but requires extra implementation of SPM specific algorithms.

1.4.2 AFM Applications

In its basic form, AFM system can be used to measure surface topography. Without significant hardware modification, the capability for mechanical property imaging can be enabled. This native capability extension has application seemingly unrelated fields. For example, by using force spectroscopy techniques on cells, the antigen and antibody interaction and mechanical signaling between biological systems can be investigated that results in the development of the Mechanoimmunology field [18].

The AFM system can also be augmented to enable many new imaging modalities. A long list of AFM modalities have been developed to create images for mapping of material properties by electrical, optical, magnetic, and thermal methods. As an example, by combining spectroscopy methods with AFMs, tip-enhanced scanning near field optical Microscopy (SNOM) can be enabled. If the infrared spectrum laser is used and monitored [19], a mode named Nano-scale Fourier Transformation Infrared (nano-FTIR) spectroscopy is enabled to capture the infrared absorption pattern of the sample to provide material chemical property contrast [20, 21]. This combination adds a new modality to AFM imaging. On the other hand, the AFM also helps to improve the performance of these techniques such as going beyond the diffraction limit for optical based techniques. There are many other derivations of the basic AFM system for extended range of applications with new imaging modalities.

The development of active cantilever probes in recent years has enabled a number of new capabilities. Selected examples for AFM capability extension include paral-

lel active probe array imaging [22], active probe AFM in SEM system [23], multi-eigenmode tapping imaging [24], scanning thermal probe [25], etc. A new capability for imaging in chemically harsh opaque liquid imaging [26] has been developed in this work to be discussed in Chapter 3 and Chapter 6. Moreover, functionalized cantilevers can also be used as chemical gas sensors to detect chemical or biological particles [27, 28], liquid viscosity [29] and calorimetry [30]. As the development of active cantilevers benefits from techniques in nano-fabrication, they can be used as new tools in producing nanoscale structures. Selected SPM related techniques include scanning probe lithography [9], single dopant implantation [31], cluster-jet nano-particle printing [32], etc. A summary of these applications can be found in the review article [33].

1.5 Limitations and Research Motivations

In this work, we identified four main aspects of the AFM system for further improvement. First, the imaging throughput of AFM systems is primarily limited to several lines per second. However, there is a significant demand for high-speed imaging for visualization of process with high temporal resolution. Second, the requirement of optically transparent path for conventional AFM limits its application to opaque environments. However, the observation of many interesting phenomenons in their native environments would involve non-transparent liquid. Third, the experiment setup and controller tuning overhead can be time consuming even for experienced users and very difficult for novice users. It would be beneficial to automate the process to reduce experiment overhead. Fourth, after addressing the aforementioned limitations in this work, we also noticed the lack of instrumentation training for modification of AFM systems to enable new capabilities. A modular low-cost AFM platform is designed to address this issue. These developments can be helpful to extend the AFM system capabilities for a variety of applications. The motivations to address these four limitations through AFM capability extension and corresponding potential applications are discussed in this section.

1.5.1 Imaging Throughput Limitation

Most AFM systems have a limited imaging throughput. A single topography image created by a conventional AFM usually takes up several minutes for the probe to scan over the sample surface due to controller and scanner bandwidth limitation. The imaging throughput limits AFM applications primarily to the study of static samples. Conventional AFMs cannot be operated at high speeds majorly due to several reasons:

1. excitation of structural vibrations
2. limited positioning bandwidth
3. limited control/instrumentation bandwidth
4. limited probe dynamics
5. detrimental effect of increased probe-sample interaction forces
6. limited data processing/handling capability.

The definition of high imaging throughput depends on the specific application. The linear in-plane scanning speed of the cantilever probe tip is usually used for characterization of imaging throughput. Compared to the unit of frames per second, using the in-plane scanning speed can be more helpful to avoid confusion due to range, resolution and other difference between images. However, even with the same scanning speed, the throughput requirements can be very different depending on the applications and often yield contradictory restrictions. For example, the semiconductor industry uses the AFM to cover a large area over several hundreds of microns squared for inspection of fabricated semiconductor wafers. For this application, the sample is static and the large area being covered needs to be scanned only once. On the other hand, biology researchers are more interested in repetitively scanning of a small area up to several microns of range. In this situation, the frame rate is a more important parameter than range as biological sample of interest are usually sized within a micron and observing the dynamic change of living cells is crucial for understanding of reaction mechanism.

The fundamental tradeoff between bandwidth and operation range makes scanner design challenging. Previous approaches to increase AFM imaging speed primarily cover a small range at high frame rates for biological sample imaging [34, 35, 36, 37, 38, 39, 40]. However, the development is primarily limited to high-speed scanning at a relatively small area and we intend to extend this capability in this work.

1.5.2 Demand for High-speed Imaging

A high-speed AFM allows the study of dynamic nano-scale processes. Such a high-speed instrument can be used for real-time study of various chemical, electro-chemical and material processes such as dissolution[41], deposition[42], polymer melting [43], nucleation [44], crystalization [45], molecular self-assembly [46], phase transition [47] and etc. It can also be used to study biological processes such as cellular events [48], or biomolecule dynamics [49], etc. High-speed atomic force microscopy is also useful in high throughput nano-fabrication/manipulation [50], and for wide bandwidth nano-mechanical characterization [51]. Hence, improving the overall imaging speed of AFM system and potentially allow switching of operation modes would be helpful to extends the application region of AFM.

1.5.3 AFM Operation Versatility Limitation

Although being versatile compared to many other instruments, AFM still has some limitations on samples and environments. First, tip-sample interaction force for AFM operation at high speed needs to be considered for soft delicate samples to avoid the excessive alteration of the sample due to the probe scanning. Specialized control algorithm is therefore necessary to maintain a deflection set point to avoid large interaction force. Second, conventional AFM system utilize optical lever with laser source to amplify and measure the probe tip deflection. This limits its application to transparent liquid environment only as opaque liquid would block the laser. The first limitation has been addressed primarily in my master thesis [52] and we will focus on the second limitation in this work.

1.5.4 Demand for Versatile Imaging Environments

AFM imaging in opaque liquids can be very helpful in a number of applications. Opaque liquid environments have practical importance in many areas of research. As an example, in the refinery industry, crude oil is produced from a porous network of minerals including mica, silica, etc. It is important to understand the residual formation of crude oil components on these materials as the oil flow transport in the reservoir are affected by these residuals. Since most crude oils have a dark non-transparent color due to the presence of non-hydrocarbon, the study of the phenomenon were previously conducted with imaging in transparent liquid such as water or decane as substitute to the original crude oil with simlar properties [53, 54, 55]. However, it would be beneficial to conduct AFM imaging in the native crude oil environment to better understand the underlining physical phenomenon.

Another good application example lies in the field of biological research. The measurement of blood cells in the native whole blood environment can be beneficial for the understanding of their biological response. For conventional imaging, red blood cells are usually isolated and treated with glutaraldehyde to render them rigid and attached to glass slide with coating (e.g. fibrinogen) [56]. However, blood cells imaged in this way are not only not in their native environment but also biologically inactive as they are no longer alive. There are many other potential applications of opaque liquid AFM imaging in chemistry and material science that involve non-transparent liquid reaction on solid surfaces.

1.5.5 Experiment Overhead Limitation

AFM users dedicate significant time and effort working with the instrument to obtain good results. A number of tasks during the experiments are repetitive and require significant operator experience. First, the laser spot and the cantilever needs to be aligned for the OBD system each time the probe is changed. This is a repetitive task to complete that can take several minutes or even tens of minutes for new users. Due to the small size of the probe and laser spot, this process can be very time

consuming, and require skills and carefulness. Ideally the alignment should be done automatically to reduce the effort of the operator so that the researchers can focus on the experiment itself. Second, the operator needs to adjust the gain values of the PID controller to achieve good tracking of the surface topography. The adjustment process also requires operator experience and ideally knowledge of control theories, which the operator might not have previously been familiar with. The lack of automation for the current AFM system for experiment preparation and parameter tuning provides a large space for improvement. Third, post processing of multiple AFM images is again a repetitive but necessary task. This can become very time consuming for high-speed AFM systems.

1.5.6 Demand for Reduced Operation Overhead

Reducing the experiment overhead can have multiple benefits. First, it saves the time of researchers so that they can focus more on making new findings instead of getting caught in the instrument operation. Second, a reduced operation complexity increases the safety and allows relatively novice user to use the instrument. Third, an automated experiment setup opens up the potential for processing of multiple samples without human intervention [57]. This can be helpful for applications such as analyzing samples collected in outer space directly using an AFM without human operator. Third, automated image processing algorithms can be helpful to generate videos taken by high-speed AFM and pave the way for big data analysis of SPM images in general.

1.5.7 Limitations of AFM Platforms for Education

The AFM systems commercially available currently are mostly too expensive for precision instrumentation education. One important barrier for hands-on education of complex precision instrumentation is the lack of a suitable affordable platform. Moreover, the lack of modularity makes it difficult for the integration of custom designed subsystems. The lack of modularity also makes experiments with AFM

subsystems very difficult, which is important to illustrate engineering principles. Last but not least, the high-voltage piezo actuator drivers and tiny cantilever probes in most AFM designs can be dangerous and difficult for the students to handle.

1.5.8 Demand for an Educational AFM Platform

The development of microscopy instruments is important to push forward fundamental nanotechnology research. For AFM systems, many new capabilities can be realized with modified commercial systems or custom designs such as nano-FTIR [58, 59], correlative imaging with AFM in SEM system [23, 60], etc. The design and improvement of AFM systems rely heavily on the knowledge of precision instrumentation and mechatronics commonly beyond the training of nanotechnology researchers. Therefore, a low-cost modular and easy to operate AFM system is needed for engineering education on precision instrumentation. More detailed discussion on design principles and analysis of existing benchmark educational AFMs and discussion are provided in Chapter 6.

1.5.9 Research Objectives

The primary goals for the research work presented in this thesis are listed below.

1. Enable nano-scale dynamic phenomenon visualization capabilities by AFM design with high performance, large scan range and video-rate imaging.
2. Improve AFM versatility to handle samples in specialized conditions with hardware modification and control algorithm improvement.
3. Reduce experiment operation overhead with system automation and fundamental principle changes.
4. Design a modular, low-cost and easy-to-operate AFM platform for precision instrumentation education curriculum.

The four aspects of improvement in this work are visualized in Fig. 1-5. The top level includes the four aspects of improvement with development in this work

to enable new capabilities. The main limitations of imaging throughput, difficulty for opaque liquid environment operation, excess experiment overhead and lack of educational AFM platform are addressed in this thesis. The middle level includes selected applications of the new capabilities. The color coded blocks illustrate the key subsystem development involved to enable the new capabilities. These subsystems together form the main contributions of this work.

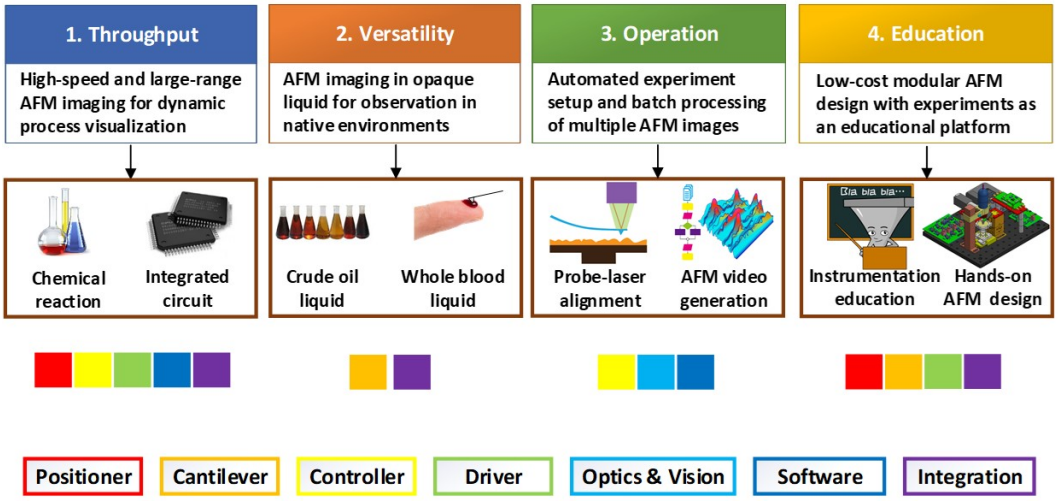

Figure 1-5: Research objective summary visualization including 4 aspects of improvement with new capability development in this work, selected potential applications and color coded subsystems from main contributions

1.6 Main Aspects of Contributions

In this section, we discuss main aspects of contributions of this work to achieve the overall research objectives. The key subsystem development are listed below.

1. AFM nano-positioners with high-speed, large-range or low-cost characteristics
2. Coated active cantilever probes for harsh opaque liquid operation
3. Algorithms for scanner control, automatic tuning and AFM imaging
4. High-bandwidth diver and signal conditioning electronics
5. Optical system for small probes with vision-based automation

6. Software development for high-speed big data processing

7. AFM system integration for visualization

Three AFM systems are developed to address the limitations and demands discussed in the previous section. We now explain the scope of each contribution.

1.6.1 AFM Nano-positioners with High-speed, Large-range or Low-cost Characteristics

The nano-positioner plays a crucial role in the high-speed capability of the instrument. Flexure constrained piezo actuated scanner are primarily used for AFM scanner design with a bandwidth and range tradeoff as discussed previously. To maintain large-range positioning and achieve high-speed performance, multi-actuation schemes have been used where two or more nano-positioners with different range and bandwidth characteristics are combined [61, 62, 63, 64]. In this research, various iterations of scanner design have been proposed and evaluated including a shear piezo block with constrained piezo cap scanner, a multi-axis flexure based scanner, a single axis dual actuated scanner and a modular stack structure multi-actuated scanner. A piezo buzzer actuated scanner is developed which has a very low cost and a low voltage for safety considerations. With their respective benefits and limitations in bandwidth, scanning range, ease of fabrication and assembly, the library of multiple scanners can be selected depending on the imaging needs. Three of the scanners are used in the final custom AFM designs in this work.

1.6.2 Coated Active Cantilever Probes for Harsh Opaque Liquid Operation

The cantilever probe deflection is the key variable to regulate during AFM operation. Sensors and actuators are used to measure and control the cantilever deflection. By applying nano-fabrication techniques, the sensors and actuators can be embedded into the cantilever to form active AFM probes. We worked with our collaborators to

develop active cantilever probes with embedded piezoresistive sensors and thermomechanical actuators [65, 66]. This design is beneficial for ease of experiment setup as it removes the need for any optical components and can potentially increase out-of-plane positioning bandwidth. Moreover, the embedded components opens up potentials for a variety of applications as discussed earlier in this chapter. In this work, we focus on extending the AFM imaging capabilities into specialized environments such as harsh opaque liquids. This is impossible with conventional AFM designs based on optical beam deflection. By applying proper coating onto active probes, the functional elements on the cantilever can be protected without significantly increasing the probe tip diameter. The functionality is demonstrated by imaging using the coated active probe with a custom AFM design.

1.6.3 Algorithms for Scanner Control, Automatic Tuning and AFM Imaging

The AFM controller commands both the lateral and out-of-plane positioning of the scanner [67, 68]. The control algorithms compensate for positioning inaccuracies from both the nonlinearities and dynamics of the AFM nano-positioner to ensure positioning accuracy. For high-speed in-plane scanning control, the nano-positioner properties and reference command characteristic can be utilized. For AFM imaging, the in-plane directions of X and Y axis usually follow periodic scanning patterns. Considering the formation of a topography image with typical in-plane resolution of several hundred pixels, the X axis line scan direction operates at several kilohertz at traditional video frame rate of 25 frames per second. With position sensor feedback, a new control algorithm using repetitive controller with bandwidth based gain allocation technique is developed. This algorithm utilizes the periodic scanning signal and the specialized frequency response of the multi-layer stacked scanner designed in this work. The Y axis has a lower bandwidth requirement at tens of hertz even for video rate imaging while precise positioning feedback is needed to align the frames.

The out-of-plane Z axis direction requires the highest operation bandwidth. To

regulate the probe-sample interaction forces for good tracking, both in-plane scanning speed and sample topography variation need to be considered. With significant difference between individual sample, a conventional PID controller is usually utilized for its simplicity and effectiveness. However, the controller parameter adjustment requires manual tuning based on experience. As the process of controller tuning depends not only on the sample characteristic but also on the operator experience and knowledge in the control field, we designed an algorithm to automate this process. A full dynamic model of AFM system is created to study the automatic PID tuning procedure.

By taking advantage of the AFM image formation principles, image level improvement algorithms can be developed. Using the full dynamic model of AFM created in this work, several algorithms are evaluated including equal space sampling, topography feedforward, error corrected image generation, adaptive scanning speed and a single neuron PID controller that can adapt to the varying sample characteristic. These algorithms are helpful to improve the imaging performance especially in high bandwidth operation.

1.6.4 High-bandwidth Diver and Signal Processing Electronics

High bandwidth driving of piezo actuators requires a large current supply. Conventional commercial drivers cannot supply sufficient current for our application. Therefore, high-bandwidth circuit are designed for using the new generation scanner. Moreover, we developed analog charge controllers implemented on hardware electronics for piezo actuator hysteresis compensation. AFM nano-positioners can benefit from this design especially when feedback sensors are not easily installed. The charge control work is the focus of other researchers in the group and the controller is integrated into the AFM to improve its overall performance. In addition, various signal processing circuits are developed for signal generation, waveform demodulation and sensor interfacing such as the quadrature photodiode.

1.6.5 Optical System for Small Probes with Vision-based Automation

To enable high-speed atomic force microscopy, the AFM optics is designed to work with small cantilever probes. A smaller AFM cantilever can have a higher first resonance frequency with a relatively small stiffness [69]. In this work, a custom optical system with focused laser and optical view is developed. The alignment of focused laser spot to the small cantilever probes can be more challenging compared to conventional probes due to the reduced size. To reduce the experimental overhead, an automatic alignment system is developed in this work. The system utilizes an optical microscope video input, a micro-positioning system and computer vision algorithm.

1.6.6 Software Development for High-speed Big Data Processing

High performance software implementation is important for AFM imaging and automation. For pre-experiment setup, Python and OpenCV library is used to implement probe-laser alignment computer vision algorithm. During the experiment, LabVIEW software is used extensively together with the data acquisition hardware from National Instruments. The low level scanner control and probe demodulation algorithms are implemented on Field Programmable Gate Arrays (FPGA). An event driven state machine is used to handle user interface and visualization on the real time system. For post processing of AFM images in batches, Python interface to Gwyddion and custom code in Matlab software are also developed in this work.

1.6.7 AFM System Integration for Visualization

By integrating selected subsystems, a total of three AFM systems have been developed in this work. First, a versatile sample scan AFM that can work with both passive and active cantilevers is developed. Second, a multi-layer stacked scanner AFM system is developed to enable the simultaneous high-speed and large-range imaging capa-

bility. Third, a modular low-cost and easy-to-operate AFM system is developed for engineering education. The imaging capabilities of these systems are verified through experiments. The system integration also verifies the functionality of the subsystems developed in this work.

1.7 Thesis Organization

In this thesis, we take a bottom up approach by introducing the key subsystem designs first. The organization of the thesis aligns with the discussion of main contributions in the last section. To enable the target capabilities, the positioning system design, cantilever transducer design and imaging control algorithms are the key components. Their design and implementation are discussed in detail in Chapter 2, 3, and 4, respectively. The development of various other subsystems including high-bandwidth electronics, optical systems for passive cantilever interface and software implementation are discussed in Chapter 5.

The integration of the three AFM systems are discussed in 6. References to detailed implementation of each subsystem are provided to the corresponding chapter and previous publications. Imaging experiments are also presented to demonstrate the AFM capabilities are also presented.

We conclude the thesis by summarizing the overall work and their broader impact to the related research fields. In the end, recommendations for future directions of continuing work to further extend AFM system capabilities are presented in Chapter 7.

Chapter 2

Positioning System Design and Modeling

2.1 Introduction

The design and modeling of positioning systems are important for AFM instrumentation. The resolution of the positioning system determines the precision of AFM for resolving features during imaging. The range of the positioning system limits the feature size that can be analyzed. The bandwidth of the positioning system affects the scanning speed and throughput. Depending on application needs, the positioning systems are designed with the required specifications. In this chapter, AFM positioning requirements and design principles are analyzed first. The modeling and characterization methods for the scanner performance are discussed next. Finally, the new AFM scanner designs developed in this work are presented as examples.

2.2 AFM Positioning System Design

Basic positioning systems usually have mechanical transmissions and actuators. For high-precision nano-positioning applications, additional components are added for improved performance such as high-resolution sensors and built-in electronics for feedback controllers. Depending on the application scenario, the positioning system

may have multiple axes that work together to produce the desired motion.

An AFM positioning system is typically composed of a coarse positioner and a high-precision scanner. The coarse positioner typically has micrometer-level repeatability. The high-precision scanner usually has sub-nanometer resolution for image formation. In most designs, both of the positioning systems have three Degrees Of Freedom (DOF) for linear motion along the axis directions of a Cartesian coordinate system. With the AFM sample being a relatively flat surface, the in-plane directions are aligned with the X and Y axes while the out-of-plane direction is aligned with the Z axis.

2.2.1 Coarse Positioner Design

The coarse positioner in an AFM system serves two main purposes. First, the probe-sample engagement and detachment are realized automatically by motion in the out-of-plane direction. Second, the coarse in-plane relative motion between the probe and the sample allows the user to identify the area of interest. These two tasks can be accomplished relatively easily by using a 3 DOF dovetail stage and a stepper motor. The stepper motor is used to drive the out-of-plane Z axis direction of the positioner for fine control of each increment during engagement. The in-plane movement can be realized using lead screws with knobs for manual adjustment. An optical microscope view can be used as visual guidance to find the area of interest.

As an example, a DS40-XYZ positioner from Newport is used as a coarse positioner in this work. The positioner has 80 Turns Per Inch (TPI) transmission ratio from rotational motion input to linear motion output, which corresponds to $0.3715 mm/rev$. A maximum travel range of 14 mm can be achieved with the positioner. Due to the backlash phenomenon, the specified position repeatability is around 1 μm. This would in principle be too large compared to the typical cantilever deflection (several hundred nanometers). However, as the engagement of probe and sample is a unidirectional process, the backlash phenomenon does not affect the engagement process significantly. A number mechanical design and control methods area available to reduce or compensate for the backlash issue if needed [70, 71].

For automatic probe-sample engagement, an actuator is needed. The out-of-plane direction of the DS40-XYZ positioner can be driven by a stepper motor with harmonic gear drive (PK523HPA-H50S, Oriental Motor) with 0.72° base step angle and 50 : 1 gear reduction. This stepper motor has a harmonic drive system that reduces the backlash in the overall assembly [72]. When driving the stage with the base step angle after gear reduction at 0.0144° per step, a 12.7 nm per step linear resolution can be realized. Photos of the positioner and the stepper motor used in this example design are shown in Fig. 2-1. The positioning resolution is sufficient for most AFM applications as a cantilever deflection below 100 nm usually does not damage the probe or the sample. If finer positioning resolution is needed, taking partial steps for the stepper motor. Alternatively, the fine resolution scanner can be used to sweep across the distance of each discrete step to produce the finest engagement for delicate samples.

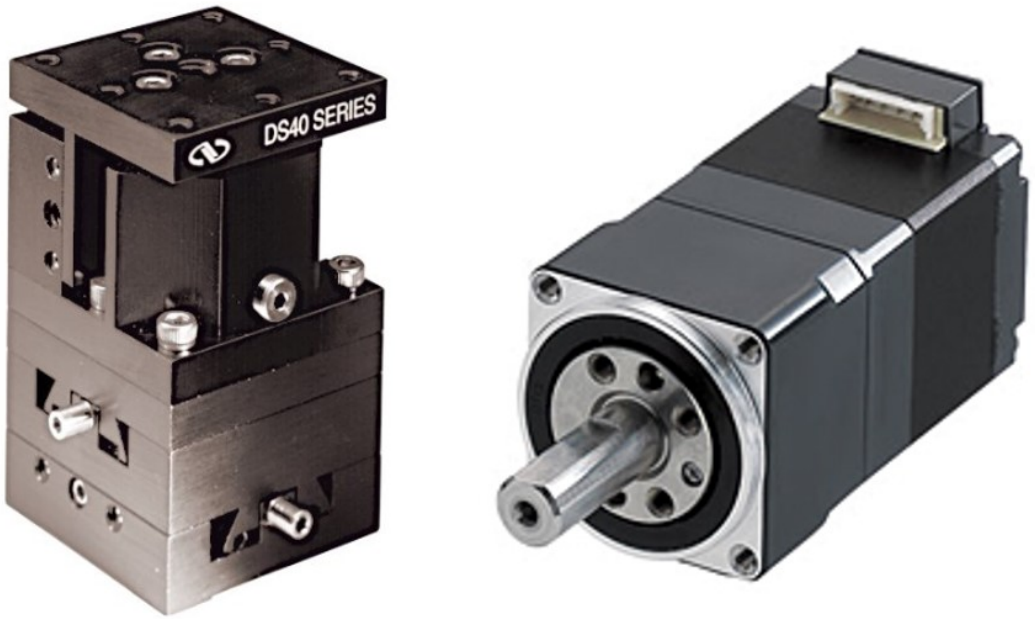

Figure 2-1: 3-axis DS40-XYZ positioner from Newport (left) and a PK523HPA-H50S stepper motor from Oriental Motor (right) for use in AFM coarse engagement system

The in-plane motion directions of the coarse positioner are typically adjusted manually. The motion can be guided by an optical microscope view to find target

locations.

2.2.2 Scanner Positioning Requirements

The high-precision AFM scanner performs both the in-plane scanning motion and the out-of-plane probe deflection regulation. For scanner design, the scanned object, application needs, imaging parameters, scanning trajectory.

Scanned Object

Both the sample and the cantilever probe can be scanned during AFM imaging. Most conventional AFMs use an optical beam deflection system for cantilever deflection measurement with more detailed discussion in Chapter 3. With this sensing principle, it is easier to keep the probe stationary and scan the sample. In sample scan configuration, the dimension of the sample is usually limited especially in high bandwidth scanning.

A probe scan configuration is preferred for large samples. Probe scan can be challenging to realize for OBD systems. This is due to the large dimension of the optical components and the high stability requirement for the relative position between the cantilever and the laser spot. With the development of active cantilever probes to be discussed in detail in chapter 3, it is relatively easier to realize the probe scan configuration. This is because the sensing and actuation components have smaller dimension and are embedded into the probe. For applications with multiple scanning modalities such as correlative imaging between SEM and AFM, both the sample and the probe are moved to separate the actuators for improved performance.

Application Needs

The design of AFM positioning systems depends largely on the application requirements. For generic imaging applications, scanners with in-plane scanning range up to 100 μm square, out-of-plane range of 20 μm with nanometer resolution are used for AFM system positioning. Conventional scanners scans at several lines per second to capture the AFM image. Specialized scanners with extended range and bandwidth are needed for different applications. For example, in semiconductor inspection, the nano-fabricated structures on the silicon wafers are static. However,

the overall size of the wafer can be fairly large (e.g. 4, 6, or 12 inches). In this case, it is desirable to have a scanner with large scanning range while the bandwidth is less than important as the sample is not changing. As another example in biology and chemical applications, the capability of high-bandwidth scanning is needed for observing sample dynamics during reaction processes. For specialized applications such as characterization of razor blade sharpness with [73], dedicated AFM scanners are needed to meet the high aspect ratio of the blade edge.

Imaging Parameters

AFM systems typically create images by scanning a cantilever probe across the sample. The topography data are captured pixel by pixel at a grid of sample locations. A number of imaging parameters are involved including the pixel resolution, the imaging ranges, the sample sharpness, the imaging speed, and the scanning trajectory. These parameters jointly determine the requirement for the scanner and data acquisition system as discussed below.

The pixel resolution is the number of pixels along each direction of the image. For analysis purpose, we denote the resolution along each in-plane axis as R_x and R_y. If a line-by-line raster scanning pattern is used for AFM imaging, the data are sampled R_x times within each line scan and a total of R_y lines are used to form a single image frame. Notice that interaction between the probe tip and the sample is continuous and the control loop works at its specified rate, which usually samples a lot more points each line than the pixel numbers for probe deflection regulation. The pixel resolution is in the image space and can be related to the physical spatial resolution with known imaging ranges.

The imaging ranges can be denoted as L_x and L_y. They are the physical dimension of the rectangular shape scanned in the in-plane directions. Larger imaging ranges increase the field of view but puts higher requirements on the scanner. First, the scanning range affects the mechanical design of the scanner. Most of the AFM scanners use piezoelectric actuators with a strain ratio roughly around 1 to 1000. Larger actuators or amplification mechanisms are needed to achieve larger scan ranges. Larger actuators often corresponds to a reduced scanning bandwidth due to the increased

mass. The range of feedback sensors should also be increased. Second, the bit resolution for the digital to analog (DAC) of the data acquisition system to control the scanner needs to be increased. A larger scanning range demands the increase of DAC resolution to maintain positioning accuracy. Third, to maintain the same spatial resolution between pixels, the pixel resolution often needs to increase with the imaging ranges, which results in a larger data size for each image.

The sample sharpness determines the smallest topography features that can be captured in the AFM image. A common method to quantify the sharpness in imaging processing is to use the spatial wavelength/frequency. Assuming the overall sample geometry is a periodical repetition of the captured image pixels, the 2D Fourier transformation can be applied in both the X and the Y directions to decompose the image into the spatial frequency domain. For AFM images, the spatial wavelength λ_x and λ_y are used to quantify the size of the topography features that can be resolved in a certain image. The image sharpness can be limited by the probe tip geometry, aspect ratio of the sample (e.g. deep trenches) or the ratio between the out-of-plane Z axis tracking bandwidth and the in-plane scanning speed. The sample sharpness usually cannot be controlled but rather specified as the minimum feature that can be resolved.

The imaging speed can be quantified in a number of ways for AFM systems. As conventional AFM images are often taken with raster scan patterns, the most commonly used specification is lines per second. For high-speed imaging, the throughput rate FR in terms of frames per second can be used, which characterizes the temporal resolution of the sample changes to be observed. With pixel by pixel capturing during scanning, the pixels are not taken at the same time as a time difference approximately equal to $1/FR$ exist between the first pixel and the last pixel. This time difference is unimportant if it is a lot smaller than the time scale of the process being observed. As an alternative, the relative in-plane scanning speed v_{ts} between the probe tip and the sample is a more accurate description of the imaging speed of the AFM. If both the pixel resolution and imaging ranges are provided, the frame rate FR and in-plane scanning speed v_{ts} can be directly related. To increase the imaging speed, both the

dynamic bandwidths of the scanner and the data acquisition system for controller implementation need to be improved. This will be the focus of discussion for scanner design as one of the main contributions of this work.

The out-of-plane tracking bandwidth is usually the bottle neck among various limiting factors. The aforementioned imaging parameters can be used together to solve for the out-of-plane controller bandwidth BW needed to achieve the prescribed imaging parameters. With linear raster scanning as an example, the controller bandwidth BW can be expressed with the aforementioned parameters as shown in Eq.(2.1).

$$BW \geq \frac{1}{k} \frac{FR \cdot R_y \cdot L_x}{\lambda_{min}} \tag{2.1}$$

The parameters involved in this expression are the frame rate FR, the pixel resolution R_y in the y direction, the imaging range L_x in the x direction, the sample spatial wavelength λ_{min} for the minimum features to capture, and a dimensionless proportionality constant k depending on the imaging condition. For example in tapping mode, k can be chosen as $k = \frac{\pi}{2\theta_m}$ with θ_m being the maximum phase lag allowed for the sample (e.g. $\pi/9$ for most protein AFM imaging) [74].

Scanning Trajectory

The scanning trajectory is another important factor to consider. It affects the requirement for in-plane scanning bandwidth, sampling frequency and out-of-plane tracking controller bandwidth. As illustrated in Fig. 2-2, there are primarily four scanning patterns used for AFM imaging including linear raster scan, sinusoidal raster scan, spiral scan, and Lissajous scan.

In linear raster scan, a triangle or a sawtooth waveform is applied along the X direction for fast scanning. A linear or stepwise linear waveform for each pixel line is applied in the Y direction. A sinusoidal raster scan replaces the signal in the X direction with a sine wave. By scanning back and forth along the X direction, the trace and retrace lines are formed during the scanning where either one can be selected to form the AFM image.

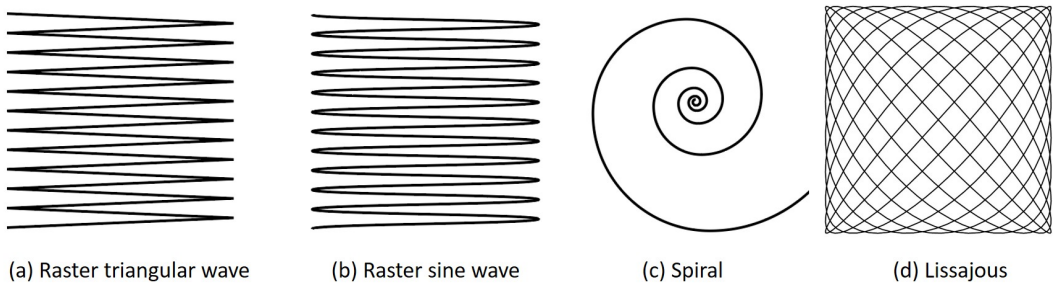

Figure 2-2: Illustration of common scan patterns for AFM imaging: (a) raster triangular wave, (b) raster sine wave, (c) spiral, (d) Lissajous. Sawtooth wave form can also be used in raster line by line scanning

The Lissajous scan pattern uses sine waves in both X and Y directions. The shapes of the scanning trajectories are determined by the amplitude $A_x,\ A_y$, frequency $\omega_x,\ \omega_y$ and phase $\phi_x,\ \phi_y$. The scanning waveforms can be defined by a combination of these parameters as in Eq.(2.2). The spiral scan waveforms can be generated by using a zero phase shift and identical values for frequency and amplitude in the formula of the Lissajous scan.

$$\begin{cases} x(t) = A_x \cos(\omega_x t + \phi_x) \\ y(t) = A_y \sin(\omega_y t + \phi_y) \end{cases} \tag{2.2}$$

The linear raster scan is the most widely used method for AFM imaging. This scanning pattern ensures a constant relative speed between the probe-tip and the sample during scanning. This is helpful to form a consistent topography measurement as the properties of the sample surface may depend on the scanning speed. On the other hand, due to the sharp turning angle of the triangular or sawtooth waveforms used in the scanning command, higher harmonics of the scanner can be excited during in-plane scanning. Fourier series expansion can be used to analyze the periodic triangular scanning signal as in Eq.(2.3).

$$y_{triangle}(t) = \frac{8A_y}{\pi^2} \sum_{k=0}^{\infty} (-1)^n \frac{\sin(2\pi f_y (2n+1)t)}{(2n+1)^2} \tag{2.3}$$

A similar series expansion can be performed for the sawtooth wave as shown in

Eq.(2.4).

$$y_{sawtooth}(t) = \frac{A_y}{2} - \frac{A_y}{\pi}\sum_{n=1}^{\infty}(-1)^n \frac{\sin(2\pi n f_y t)}{n} \tag{2.4}$$

Taking more than the first 5 terms of the Fourier series expansion is usually sufficient. It can maintain a good scanning linearity and reduce the effect of the unwanted high frequency harmonics beyond the bandwidth of the scanner. However, this would still limit the frequency of the triangular or sawtooth waveforms to be at least one order of magnitude smaller than the scanner bandwidth. To increase the imaging throughput, other scanning trajectories are considered.

A detailed analysis of the scanning pattern is available in the literature [75]. Based on the analysis, The spiral scan pattern requires the lowest scanning frequency for the scanner. The Lissajous scan pattern allows different frequencies to be used in the x and y directions for the scanner. However, twisting dynamics of the cantilever may be excited with both spiral and Lissajous scan patterns.

The sinusoidal raster scan is the most common choice for high-speed imaging for its several benefits. First, only one fast axis is needed, which makes AFM scanner design less challenging. Second, the cantilever twisting dynamics is not excited since the fast scan axis tip-sample interaction force does not create a torque around the longest axis of the cantilever. Third, the fast axis can operate near or even above the resonance frequency. Fourth, the reference command is periodic and suitable for internal model based repetitive control techniques. Last but not least, a square image can be created, which is difficult with spiral scan.

2.2.3 Actuators and Sensors for AFM Scanners

The actuator and sensor capabilities are important for the design of AFM scanners. On the microscopic scale, a number of physical principles that are not suitable for macroscopic applications can be used as actuators or sensors. In this section, we take a closer look at the actuators and sensors that are available for nano-positioning applications.

Nanoscale Actuators For AFM positioning systems, the actuator converts electromagnetic energies into mechanical forces and motion. Piezoelectric, magnetostrictive, electrostatic, electrothermal and electromagnetic effects have been used to design high-precision actuators [76]. We will primarily focus on the piezoelectric actuators as they are widely used in nano-positioner design. Selected stacked piezoelectric actuators used in this work are shown in Fig. 2-3. Piezo actuators are usually constrained in flexures for improved dynamics or motion amplification [77].

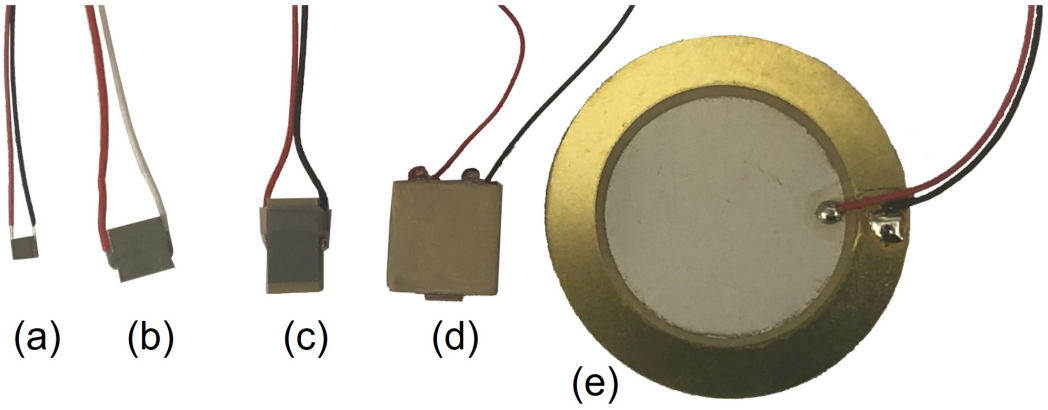

Figure 2-3: Selected piezoelectric actuators used in this work: (a) PI PL022.31 stacked piezo ($2 \times 2 \times 2$ mm), (b) Noliac NAC2013 stacked piezo ($5 \times 5 \times 2$ mm) (c) PI P-885.11 stacked piezo ($5 \times 5 \times 9$ mm), (d) PI P-141.10 shear piezo ($10 \times 10 \times 12$ mm), (e) piezo buzzer typically used in speakers

Piezoelectric effect is the charge generation across unit area described by the electrical displacement D when mechanical stress τ is applied. The converse effect is the generation of mechanical strain ε with externally applied electric field intensity E. The coefficients associated with the four quantities result in a total of $C_4^2 = 6$ constitutive relations between each pair. Variables within the mechanical domain and the electrical domain are related by the the mechanical stiffness modulus k, and the electrical permittivity α. Four more coefficients are defined for the cross-domain constitutive relations as shown in Eq.(2.5). The subscripts i and j corresponds to the direction of 3 linear and 3 rotational degrees of freedom. The superscript E and D

indicates the relation is defined when the other relations are held constant.

$$\begin{cases} d_{ij} := \left(\frac{\partial D_i}{\partial \sigma_j}\right)^E \\ e_{ij} := \left(\frac{\partial D_i}{\partial \varepsilon_j}\right)^E \\ g_{ij} := \left(\frac{\partial E_i}{\partial \sigma_j}\right)^D \\ h_{ij} := \left(\frac{\partial E_i}{\partial \varepsilon_j}\right)^D \end{cases} \tag{2.5}$$

The piezoelectric effect can be used for both sensing and actuation. The piezoelectric charge constant d_{ij} or the piezoelectric voltage constant g_{ij} are commonly used to determine the sensitivity or gain. With the ideal assumption that the energy is conserved within the electrical and mechanical domains, along each directional pair, the relation $E \times D = \sigma \times \varepsilon$ can be used for easy computation of the variables.

A piezoelectric actuator (abbreviated as "piezo actuator") uses the converse piezoelectric effect. It produces mechanical forces and motions from applied electrical voltage and current. Typical piezo actuators are formed by stacking multiple layers of piezoelectric ceramic materials where 1 mm thickness can generate approximately 1 μm motion range corresponding to a 1 : 1000 strain ratio. Typical stacked piezo actuators operate with an externally applied voltage between 100 V to 300 V. The large voltage and the small motion range is ideal for realization of high-precision positioning. For example, if an actuator has 100 V corresponding to 10 μm motion range, a 10 mV voltage increment would result in a 1 nm motion change. In addition to its precision, a large force on the order of hundreds of Newtons can be generated with piezo actuators with a cross section as small as 25 mm^2, which makes them ideal to achieve high bandwidth. Piezo actuators are very suitable for position and hold applications as the force can be maintained by the applied voltage without power dissipation in principle as no current is flowing. Both normal motion and shear motion can be realized depending on the orientation of the piezoelectric effect. Detailed modeling of piezo actuators as dynamic systems are discussed later in this chapter.

The magnetostrictive effect is the expansion or contraction of ferromagnetic materials with externally applied magnetic fields. The magnetoristrictive actuators can achieve high-precision positioning with a high force density on the same order as

piezoelectric actuators. However, the confinement of magnetic fields to avoid affecting external components are more difficult than the piezoelectric actuators and therefore used less often in nano-positioning applications.

The force generated by the electrostatic effect is usually too small for macroscopic AFM positioners. However, it can be used to actuate objects on the microscopic scale such as the AFM cantilever. The electrostatic actuator can be micro-fabricated to drive the positioner embedded in an active probe as will be discussed in Chapter 4.

The electrothermal actuation principle utilizes the thermal expansion of heated elements to generate force and motion. It can also be used for driving microscopic cantilevers and actuators.

By using the Lorentz force, electromagnetic actuators are capable of high precision positioning over a large range. A simple realization of electromagnetic actuation is the voice coil actuator using a permanent magnet and a coil for one degree of freedom motion. Magnetic levitation stages with six degrees of freedom are widely used in the semiconductor industry for handling of silicon wafers. In most cases, feedback control with high-precision sensors are needed for electromagnetic actuators to hold the position. Using mechanical elastic elements to maintain the position without sensors is possible but used less often due to two reasons. First, designing elastic elements for large motion range can be difficult. Second, the power dissipation during position and hold application are not reduced as the current flow is required to produce the Lorentz force.

In summary, several physical principles can be used for actuators to produce microscopic motions. The piezoelectric actuators are most widely used in AFM high-precision scanner design with its suitable characteristics with a few exceptions for specialized applications.

Nanoscale Positioning Sensors

Nanoscale positioning sensors are not necessary for AFM scanners. However, they can be helpful to provide feedback signals to the controllers for improved positioning accuracy. Resistive strain gauges, capacitive sensors and laser interferometers are most widely used in nano-poistioning systems for motion measurement. Three types

of the sensors used in this work for nano-positioner design are shown in Fig. 2-4.

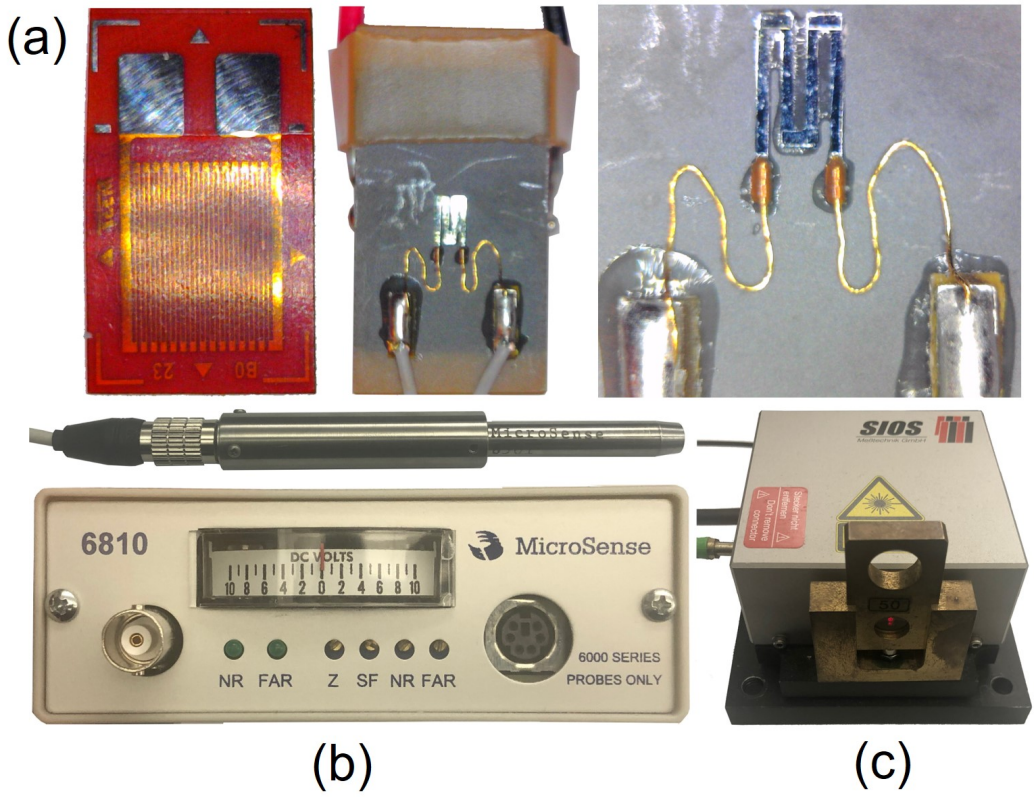

Figure 2-4: Selected nano-positioner sensors used in this work: (a) a resistive foil strain gauge (left), a strain gauge attached on P-885.11 piezo actuator (middle) and zoomed in view (right), (b) MicroSense 6501 active capacitive probe and 6810 active gauging module, (c) SIOS SP-120 laser interferometer sensor head

A resistive strain gauge is a transducer that converts the strain change due to externally applied forces to a change in the relative resistance. The resistance R of a resistor is related to the length L, the cross sectional area A and the resistivity ρ. The relative resistance change $\Delta R/R$ is affected by both the geometric change and the piezoresistive effect for resistivity change due to mechanical stress. The sensitivity of a resistive strain gauge is characterized by the gauge factor G as shown in Eq.(2.6). The formula is derived by taking the partial derivative of each element in the resistance

formula.

$$R = \rho\frac{L}{A} \Rightarrow G = \frac{\Delta R/R}{\varepsilon_{long}} = \frac{\Delta R/R}{\Delta L/L} = (1 + 2\nu) + \frac{d\rho/\rho}{\varepsilon_{long}} \tag{2.6}$$

In addition to the variables defined before, ε_{long} is the longitudinal strain and ν is the Poisson's ratio of the material. For most strain gauges made of metals, the geometric change determines the gauge factor and the resistivity change can be neglected. Since the Poisson's ratio is a constant typically ranging between 0.3 to 0.5, the gauge factor would usually be between 1.6 to 2. As the strain change and therefore the resistance change is usually small (less than 1 percent), a Wheatstone bridge circuit is used to measure the resistance change with more discussion in Chapter 3. The change of resistivity with mechanical stress or strain is the piezoresistive effect that can be observed in certain materials such as doped semiconductor. The piezoresistive coefficients can be much higher than the Poisson's ratio and therefore used in active cantilever probe design with more details in Chapter 3.

For AFM positioner design, the strain gauge can be attached to the side of a piezo actuator to measure its motion after calibration. Strain gauges have good resolution, linearity and repeatability. They are also cost efficient and easy to use. However, the measurement bandwidth and sensitivity to thermal expansion are the main limitations. Due to the mechanical structure of the stain gauge, measurement bandwidth beyond 5 kHz can be difficult to realize. As the measurement of strain is local and indirect, it is also difficult to distinguish the actuator motion from temperature change induced strain. Moreover, the location to place the strain gauge needs to be designed based on analysis results from mechanics.

Capacitive sensors are based on the principle of a parallel plate capacitor with governing equation shown in Eq.(2.7).

$$C = \frac{\epsilon A}{d} \tag{2.7}$$

where C is the capacitance, A is the area of the plate, d is the distance between the parallel plates, and ϵ is the electrical permittivity of the material between the plates.

For implementation, capacitive sensors require a conductive path. The path forms a loop between the sensing target and the housing of the sensor used as ground in the circuit loop. While the housing of the sensor is usually mounted to the fixed frame of the positioner, the center active area of the sensing probe is placed in close proximity to a clean conductive surface of the measurement target. The capacitance of the parallel plate capacitor formed between the sensor active area and the target surface of the scanner can then be measured electrically to derive the relative distance.

Capacitive sensors have better measurement capabilities than strain gauges. The capacitive sensors can achieve measurement ranges over hundreds of microns at sub-nanometer resolution with over 100 kHz bandwidth. These capabilities make the capacitive sensor an ideal choice for high-end positioning system design. However, due to the conductive loop and flat surface requirement, it is more difficult to use than the strain gauges. The capacitive sensor (several thousand dollars) is also more expensive than the strain gauge (several dollars).

Laser interferometer is another powerful versatile instrument for position measurement on the nanoscale. The interference pattern formed on the photodiode can be used to precisely measure the relative motion across using the laser wavelength as a reference ruler. The instrument is capable of measurement over macroscopic range at sub-nanometer resolution with over 1 MHz sampling rate. As long as a flat reflective surface is accessible by the beam of laser, the motion of the scanner can be measured on the nanoscale. The size of the beam spot is typically over hundreds of microns while focusing lens can be used to further reduce the diameter down to several microns for measurement of MEMS devices.

The flexibility of the laser interferometer makes it an ideal tool for testing and calibration of nano-positioning systems. Using the laser wavelength as reference, it also does not need calibration of length as required by the strain gauge and capacitive sensor. However, due to its high cost (tens of thousands of dollars) and relatively bulky size, it is usually not included in an AFM positioning system as feedback sensors for regular use.

In summary, both strain gauges and capacitive sensors can be used for AFM

positioning system design. Laser interferometers are used more widely for AFM positioning system calibration. A number of other techniques can be used for nanometer resolution displacement measurement such as the electrostatic sensor, the linear variable differential transformer, the giant magnetoresistance sensor, etc. These sensors are not discussed here as they are not commonly used as feedback sensors in the AFM scanner design.

2.2.4 AFM Scanner Design Considerations

A simple AFM scanner design primarily includes two aspects. They are the selection of actuators and the geometric design of the constrain structure. Sensors may also be added for feedback controllers depending on the application. As the motion principles of piezo actuators have been discussed before, we focus our attention on the constrain. The design of AFM scanners needs to comprehensively consider the target application, the required imaging parameters and the scanning pattern.

Flexure structures are usually used to constrain piezo actuators. They can be used to both reduce or amplify motion from. When designed correctly, flexure structures are compliant in the target directions as bearings without friction and rigid in other directions as constraints. For flexure design, the kinematics, range of motion, stiffness, loading capacity, structure bandwidths and ease of fabrication need to be considered. For simple flexure structures, analytical formulas can be used to analyze the design. Finite element analysis methods are needed for designs with more complex geometry. A systematic analysis of various flexure designs are summarized in the Freedom, Actuation, and Constraint Topologies (FACT) library can be used as references [78, 79]. To fabricate flexure structures, the electrical discharge machining (EDM) method is preferred as it does not apply mechanical force on the flexure like conventional milling and yields no heat affected zone like laser cutting. EDM also allows tight tolerance control to accurately realize the desired dimension of the flexures.

AFM systems typically have three linear axis of motion. Both serial and parallel kinematic structures can be used as shown in Fig. 2-5. The serial kinematic design stacks multiple simple axis scanner stages for easy design and fabrication. The reso-

nance frequency of each axis can be different as the bottom axis carries the mass of the top scanners in the stacked structure. The axis alignment needs to be accomplished carefully to ensure orthogonality. In a parallel kinematic design, multiple actuators drive the same platform to offer reduced mass and therefore increased resonance frequency in all axis. The parallel design is more difficult to fabricate and used more often in high-end applications.

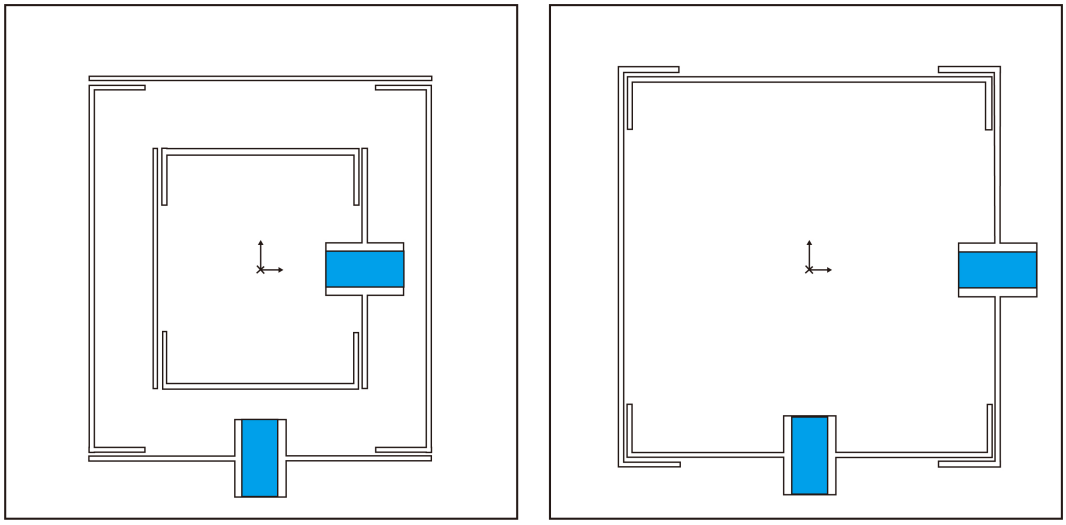

Figure 2-5: Serial kinematic (left) versus parallel kinematic (right) positioners

There are several related subsystems to support the AFM scanner. For high-speed AFM scanner design, the dynamics and linearity of both the actuator and the structure need to be considered in controller design. In addition, capabilities of the scanner support systems such as the driving electronics and data acquisition system also need to be extended to ensure the functionality of the scanner.

2.3 AFM Scanner Modeling and Characterization

The design of high-performance AFM scanners benefits significantly from good dynamic system models. In this section, the modeling and system identification methods commonly used and developed in this work for AFM scanner design are discussed. More details on the modeling of cantilever probe dynamics and AFM imaging are

discussed in Chpater 3.

2.3.1 Linear Dynamic Model

Being continuous structures, AFM scanner flexures have an infinite number of resonance modes. For practical considerations, AFM scanners operate below the first resonance frequency so that a second order mass-spring-damper system model is sufficient to capture the main linear dynamics. As a generic model, the displacement x can be described by the differential equation in Eq.(2.8). The key parameters include the mass m, the linear damping b, the spring stiffness k and the actuator force F.

$$m\frac{d^2x(t)}{dt^2} + b\frac{dx(t)}{dt} + kx(t) = F(t) \tag{2.8}$$

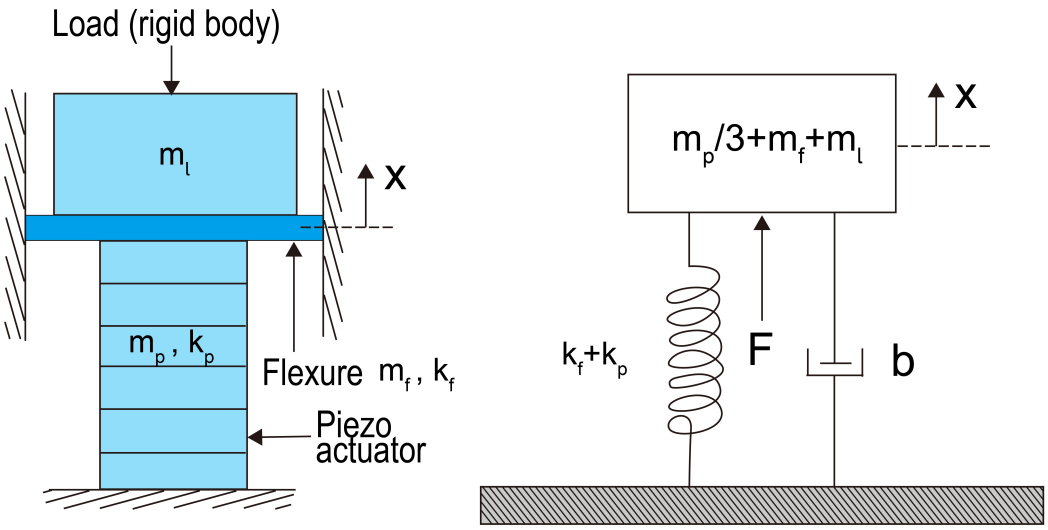

Figure 2-6: Variable definition (left) and lumped parameter mass-spring-damper model (right) for a flexure constrained piezo actuator with mass load

This is a linear constant coefficient time invariant system. The parameters of the system are assumed to remain unchanged over time. The transfer function of the system can be derived by taking the unilateral Laplace transformation in Eq.(2.9).

$$\frac{X(s)}{F(s)} = \frac{1}{ms^2 + bs + k} \tag{2.9}$$

For nano-positioner design, the mass m is replaced with the effective mass m_{eff} that includes the piezo m_p, flexure structure m_f and load being carried m_l. For most one-axis scanner design, a stacked piezo actuator is grounded on one end and constrained on the other end with a flexure to move a load. The effective mass of the system can then be written as in Eq.(2.10). The one-third factor of piezo mass arises as the fixed end is not moving while the the constrained end is moving together with the flexure and the mass load. Therefore, the velocity of the scanner linearly increase along its motion axis.

$$m_{eff} = \frac{m_p}{3} + m_f + m_l \tag{2.10}$$

The damping term in the equation is usually small and can originate from various sources. Direct measurement of damping coefficient is difficult and therefore usually obtained by fitting the model parameters to the frequency response obtained using system identification methods.

The spring constant term depends on both the piezo actuator stiffness k_p and the flexure stiffness k_f. The piezo actuator stiffness k_p can be obtained by dividing the maximum blocking force F_{block} by the maximum displacement without load ΔL_{max} as in Eq.(2.11).

$$k_p = F_{block}/\Delta L_{max} \tag{2.11}$$

The stiffness of the flexure k_f is usually easy to obtain. It can be computed from theoretical analysis of beam bending mechanics, applying FEA methods to the CAD design or direct measurement of deformation with known force.

The force input to the system is generated by the piezo actuator and applied to the flexure to move the load. It is in general proportional to the applied actuator voltage with some nonlinearities as discussed in the next section.

2.3.2 Piezo Actuator nonlinearity Model

Piezoelectric materials exhibit nonlinearities that can become problematic [80]. The main nonlinearities important for motion control are the hysteresis and the creep. The non-linear capacitance of the piezo actuator can also be important for driver design considerations. In this section, selected models to capture the piezo actuator nonlinearities are discussed. These models can later be used in simulation study or controller design for nonlinearity compensation.

Hysteresis Model

The hysteresis effect is widely observed in piezoelectric and electromagnetic phenomenons. For a system with hysteresis nonlinearity, the output of the system not only depends on its current input command but also on its internal states and the input history. This memory-like phenomenon is commonly observed in many electromagnetic systems. For a piezoelectric actuator, the hysteresis effect exists between the input voltage and the output mechanical force, which distorts the ideal linear relationship from the constitutive relationship.

The hysteresis effect in piezo actuators arises on the microscopic level. Many piezoelectric materials have a domain switching phenomenon. When the externally applied electric field reaches a threshold, the polarization direction of the microscopic elements change. To reverse the polarization direction to its original state, a different threshold needs to be reached. Moreover, the microscopic elements have different activation and deactivation thresholds for polarization direction change. This phenomenon is difficult to model analytically and therefore a number of phenomenological models based on hystrons are created.

Hystrons are used as basic elements of the hysteresis effect. The microscopic view of elements having different thresholds for activation gives the intuition for hystron models. Hystrons are microscopic elements that work together to generate the macroscopic hysteresis effect. Based on this idea, a number of hystron operators have been created such as Preisach operator, Prandtl operator, modified Prandtl-Ishlinskii operator, Krasnoselskii-Pokrovskii operator, etc. Other hysteresis models can also be

used [81]. Examples include the Duhem Model model, the Coleman-Hodgdon model, the Jiles Anthernon model, the Maxwell resistive capacitance model, etc.

In this chapter, we focus our discussion on the Preisach operator model. It is conceptually simple and captures the hysteresis phenomenon effectively [82]. The equation of a single Preisach hystron is shown in Eq.(2.12). The key variables include the time dependent input voltage V and the output force $F_{\alpha,\beta}$ for a hystron with activation level α and deactivation level β.

$$F_{\alpha,\beta}[V](t) = \begin{cases} 1 & V(t) > \alpha \\ F(t-1) & \beta \leq V(t) \leq \alpha \\ -1 & V(t) < \beta \end{cases} \tag{2.12}$$

The hysteresis model of a piezo actuator is obtained by combining the contribution of all hystrons. Hystrons with different thresholds α and β ($\beta < \alpha$) can have different weights. The minimum and maximum values of the threshold can be set to the rated piezo actuator operation range. The visualization of a single generic Preisach hystron element and a hysteresis activation plane with α versus β is shown in Fig. 2-9.

Within the $\alpha - \beta$ plane, the increase of input voltage activates the hystrons along the α axis. The decrease of the input voltage deactivates the hystrons along the β axis. It is evident from the visualization in Fig. 2-9 that a number of hystrons are left activated with a loop sweep of the input voltage. These hystrons together contribute to the hysteresis nonlinearity. The overall actuator output force $F(t)$ is obtained by integrating all the activated hystrons with corresponding weights $w(\alpha, \beta)$ over the triangle in the α and β plane.

$$F(t) = \iint_{\alpha \geq \beta} w(\alpha, \beta) F_{\alpha,\beta} d\beta d\alpha \tag{2.13}$$

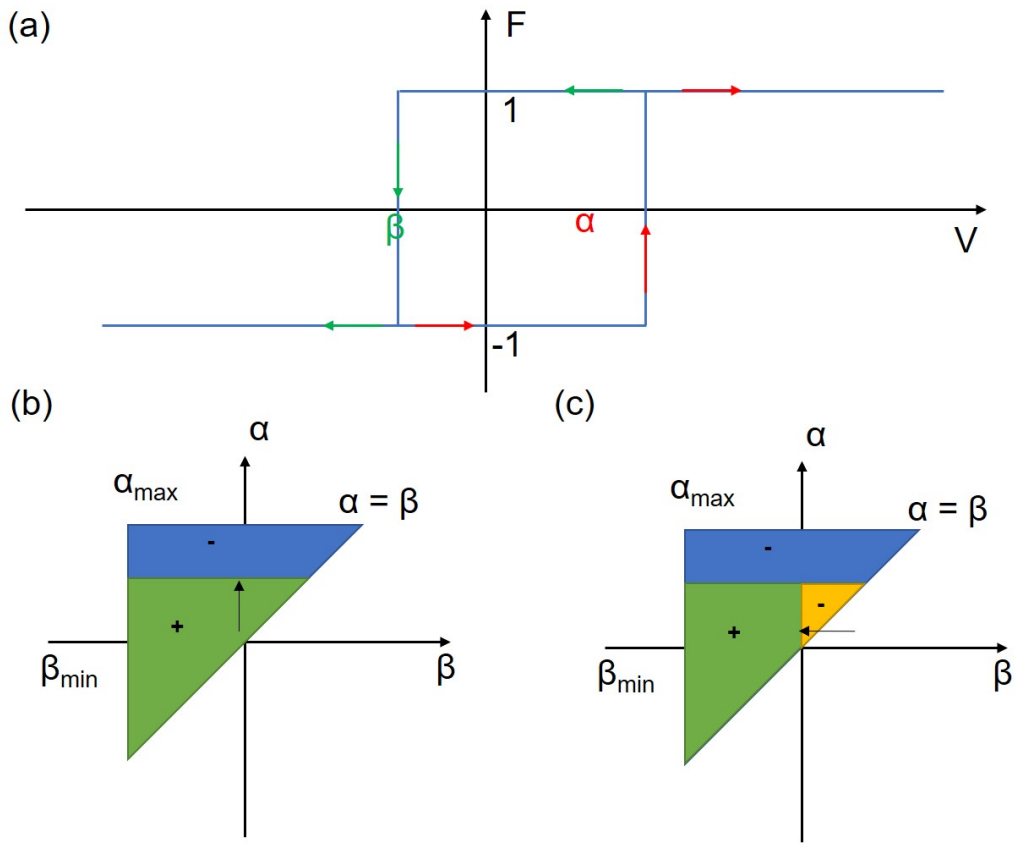

Figure 2-7: Preisach hysteresis model: (a) force versus voltage plot of a single hystron operator with activation level α and deactivation level β, (b) increasing voltage hystron elements activation map, (c) decreasing hystron elements deactivation map

To numerically implement the model, the α and β values are discretized into finite segments. Discretized summation can then be used to replace continuous integration. A model with 100 level discretization for both α and β is created based on the discretization for a P-885.11 piezo actuator from PI used in this work. The actuator is specified to have $0-100\ V$ input voltage and $0-300\ N$ output force. The simulation of a Preisach hysteresis model with assumed equal weights is shown in Fig. 2-8. The true weights for each hystron is assumed to be a constant and need to be identified with experiments, which will be discussed in the next section.

Hysteresis is an important nonlinearity to be considered especially for high-bandwidth applications. The Preisach model can be identified and inverted for feedforward control [83]. If sensors are available, feedback control techniques can be used to treat the

nonlinearity compensation as a disturbance rejection problem. Since the focus of discussion in this chapter is for modeling and characterization, more detailed discussion on hysteresis compensation are provided in Chapter 4 and 5.

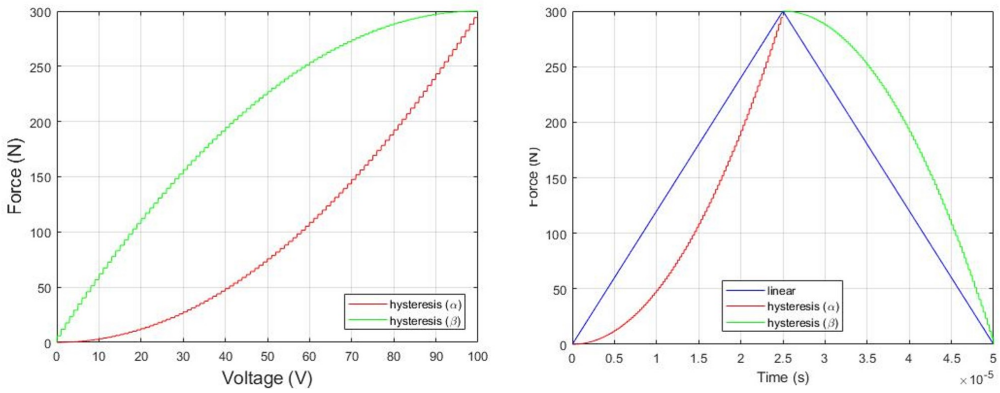

Figure 2-8: Matlab implementation of simulated hysteresis curves for assumed equal Preisach hystron weights across the $\alpha - \beta$ plane with hysteresis loop (left) and deviation from the triangular reference command (right)

Creep Model

The creep nonlinearity is the long term drift of the piezo actuator output with an unchanged input signal. This is a nonlinearity that becomes important in the steady state motion control since the piezoelectric material dipole reorientation process takes significant longer time than the switching of direction. A logarithmic relationship is typically used to model the creep nonlinearity [84] as in Eq.(2.14). The creep rate factor γ is defined as the rate starting at time equal to 0.1 s when the input command signal is set to a constant starting at $t = 0$.

$$\Delta x(t) \approx \Delta x(t = 0.1) \left[1 + \gamma \log_{10} \left(\frac{t}{0.1} \right) \right] \tag{2.14}$$

The creep effect is easy to compensate with feedback control. The long term drift can usually be eliminated with an integral controller. Open loop compensation is also possible with the identified model [85].

Non-linear Capacitance

In the electrical domain, the piezoelectric actuator can be modeled as a non-ideal

capacitor. The electric model can be approximated by an ideal capacitor with a series equivalent resistor. Electrical power can dissipate through the equivalent resistor to cause heat dissipation. Moreover, the capacitance value varies with the applied voltage, temperature and mechanical load. The capacitance affects the current requirement significantly, this nonlinearity needs to be considered for the driving electronics design. As a rule of thumb, adding a safety factor of 70% to the capacitance would be sufficient to account for the capacitance variation [86].

2.3.3 Scanner System Identification Methods

To capture the dynamic performance of the scanner, system identification and signal processing techniques are applied. For linear dynamics, obtaining the frequency response of the scanner is usually sufficient for controller design purpose. The parameter values can be fitted through least square estimation if needed. For the non-linear dynamics, the goal of system identification is to estimate the weights of the discretized model so that it can be inverted to compensate for the positioning inaccuracy. This section illustrates the system identification methods used in this work.

Linear Dynamics Identification

There are primarily two methods commonly used to obtain the frequency response of the scanner. They are the frequency sweep and the stochastic signal system identification.

During a frequency sweep, a sine wave with controlled amplitude and phase is used. It can be applied as the input to a simple input single output (SISO) system. The frequency of the sine wave input is gradually increased either in a linear or a logarithmic scale. For a linear time invariant system, the output of the system in response to a sine wave input is another sine wave at the same frequency but with a different amplitude and a different phase after the initial transition period. The amplitude ratio and the phase difference between the steady state output and the known sine wave input can be measured at each frequency to form the Bode plot. To achieve accurate measurement of the Bode plot, the linearity of the system and the signal to noise ratio are both important. As an example, a simple time delay

nonlinearity in the measurement system can appear as a frequency dependent phase lag in the Bode plot. Significant hysteresis nonlinearity can become problematic.

A dynamic signal analyzer is typically used for an automatic sweep to generate the Bode plot. The algorithm can also be custom implemented on data acquisition systems. The frequency sweep can not only be used for system identification of the scanner but also for the cantilever probe in dynamic mode operation. A custom implementation with National Instruments data acquisition system is used in this work. The applications include identification of the AFM positioning system dynamics and cantilever resonance for dynamic mode operation.

Instead of sweeping through the frequency spectrum one point at a time, a stochastic system identification procedure can be applied to get the response of a range of frequencies simultaneously. To do so, a bandwidth limited white noise signal is used as the input to excite the dynamics of the system.

By definition, the power spectral density is just the Fourier transformation of the auto-correlation function for a signal. An ideal white noise signal is assumed to have a constant power spectral density $S_x = \sigma_w^2$ across all frequencies, which corresponds to an ideal scaled impulse function for the auto-correlation function. This essentially means all the samples in the signal are all independent from each other.

To generate a white noise signal, a series of independent samples with identical statistical distribution are sampled. If each sample follows a Gaussian distribution with zero mean and variance σ, a Gaussian white noise is obtained. In practice, the white noise are always bandwidth limited by the data acquisition system so that the power spectral densities at higher frequencies are attenuated.

During system identification, a band-pass filter is added deliberately to process the signal. This helps to concentrate the energy in the frequency range of interest. The cross power spectral density $S_{xy}(f)$ is related to the power spectral density of the input signal $S_x(f)$ and the system transfer function $H(f)$ as shown in Eq.(2.15). The system transfer function $H(f)$ can be derived after obtaining $S_x(f)$ and $S_{xy}(f)$.

$$S_{xy}(f) = H(f)S_x(f) \Rightarrow H(f) = \frac{S_{xy}(f)}{S_x(f)} \tag{2.15}$$

To determine the linearity of the system, the magnitude-squared coherence $C_{xy}(f)$ can be used. It has a range between 0 to 1 and is defined as in Eq.(2.16). An ideal constant coefficient LTI system without additional noise signals would yield a value of 1 while the presence of system nonlinearities or noise signals will result in a value closer to 0.

$$C_{xy}(f) = \frac{|S_{xy}(f)|^2}{S_x(f)S_y(f)} \tag{2.16}$$

A binary stochastic signal is preferred for piezo actuator system identification. A threshold can be applied at the mean of a stochastic signal to convert the samples into binary values. The resulting binary stochastic signal can be used as the input for system identification without exciting the hysteresis nonlinearity. This is because the system switches between two states without exciting the memory effect of hysteresis. The hystrons that are changing directions fall in a triangle in the $\alpha - \beta$ plan between the two values of the binary signal as the orange area in Fig. 2-9.

The general procedure for applying binary stochastic system identification for AFM scanners is summarized below.

1. Generate a white noise signal
2. Filter the signal to keep frequencies of interest
3. (Optional) threshold the signal at zero value to obtain binary values
4. Record the signal input $x[n]$
5. Record the signal output $y[n]$
6. Compute the cross power spectral density of $x[n]$ and $y[n]$
7. Compute the auto power spectral density of $x[n]$
8. Solve for both the system transfer function and coherence value

Compared to the sine wave sweep method, the binary stochastic system identification method has several benefits. It is faster to obtain the frequency response. It also does not excite the hysteresis nonlinearity in the piezo actuators.

For signal processing software development, a number of built-in Matlab functions are available. To implement the math operations starting from the low level, the "cpsd" function can be used to estimate the cross power spectral density and compute the desired transfer function. On the high level, the "efte" function and "mscohere" function can be used to estimate the transfer function and coherence. More information on the system identification and parameter settings can be found in [87, 88, 89].

Hysteresis Model Identification

In this section, we discuss the identification of hysteresis nonlinearity modeled with the Preisach operator. The parameters of the model can be obtained by least square estimation of experimentally measured data.

A Preisach model with discretization level n_d is used for the range of hystron elements α_{min}, α_{max}, β_{min}, β_{max}. The total number of weights N_h to be fitted is given in Eq.(2.17).

$$N_h = \frac{n_d(n_d+1)}{2} \tag{2.17}$$

In order to identify the N_h weights, a signal that sweeps across the entire range of α and β is applied. A suitable signal should cover the entire range and excite the system sufficiently so that the memory of all hystrons are cleared and the states are activated and deactivated during the process. As shown in Fig 2-9, a sinusoidal waveform with increasing gain and increasing amplitude so that the minimum values are always α_{min} is selected as a suitable input signal for system identification.

Both the input and output signals can be recorded for a total of N_t samples. The activation state of each hystron at discrete time measurement t_j can be computed for each time instant as shown in Eq.(2.18).

$$F(t_j) = \sum_{i=1}^{N_h} w_i F_i(t_j) + \eta_0 \tag{2.18}$$

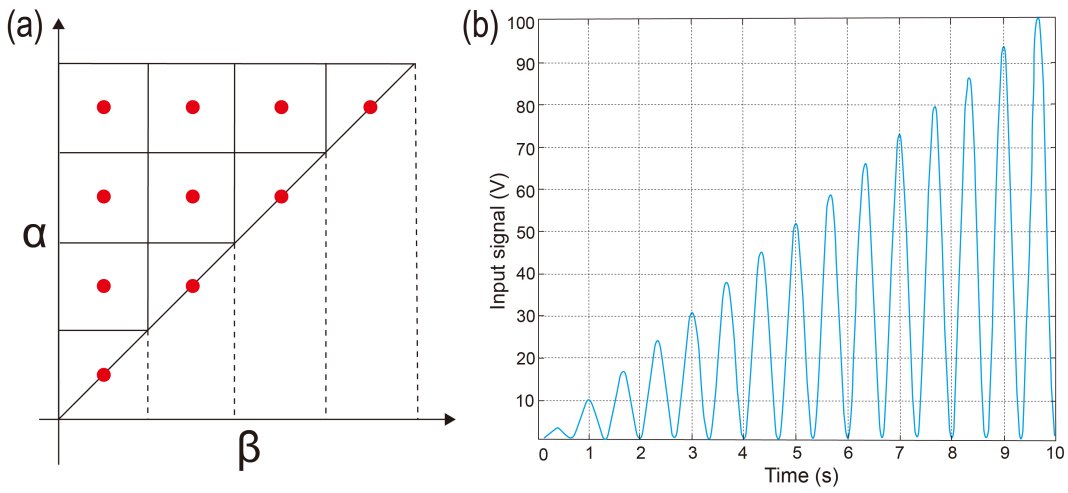

Figure 2-9: Hystron weights identification for Preisach model: (a) discretized $\alpha - \beta$ plane, (b) sinusoidal sweeping signal with increasing amplitude (right)

The actual force output $F(t_j)$ can be measured indirectly through position of the scanner with calibrated flexure stiffness. The weight w_i and offset η_0 are time independent and need to be identified. The estimated force output of each hystron $F_i(t_j)$ are computed with the activation state and corresponding weight to be identified. With a total of $N_t >> N_h$ measurements, an over constrained set of equations can be written in matrix form as in Eq.(2.19).

$$\underbrace{\begin{bmatrix} F(t_1) \\ F(t_2) \\ \vdots \\ F(t_{N_t}) \end{bmatrix}}_{\mathbf{F}:\ N_t \times 1} = \underbrace{\begin{bmatrix} F_1(t_1) & \cdots & F_{N_h}(t_1) & 1 \\ F_1(t_2) & \cdots & F_{N_h}(t_2) & 1 \\ \vdots & \ddots & \vdots & 1 \\ F_1(t_{N_t}) & \cdots & F_{N_h}(t_{N_t}) & 1 \end{bmatrix}}_{\mathbf{A}:\ N_t \times (N_h+1)} \underbrace{\begin{bmatrix} \hat{w}_1 \\ \vdots \\ \hat{w}_{N_h} \\ \hat{\eta}_0 \end{bmatrix}}_{\mathbf{W}:\ (N_h+1) \times 1} \tag{2.19}$$

Without considering the constrains, the solution of this linear regression problem can be written with the pseudo inverse as in Eq.(2.20).

$$\hat{\mathbf{W}} = (A^T A)^{-1} A^T \mathbf{F} \tag{2.20}$$

The FINAL solution can be different if the non-negative Preisach model parameter constraint is considered. Non-negative least squares algorithms such as the active-

set method are used. The "lsqnonneg" function in Matlab software can be used to solve this optimization problem. Weights that are non-significant can be neglected. A number of other identification methods including parametric methods and online identification methods have also been proposed with more details in reference [81].

2.4 AFM Scanner Design Examples

In this work, a number of AFM scanners have been designed for different AFM imaging application scenarios. A review of AFM scanner development is provided first. The implementation and characterization of the three AFM scanners developed in this work are then discussed in detail.

2.4.1 Review of Scanner Development

Piezo tube is the most common used scanner design for commercial AFM systems. As shown in Fig. 2-10, a hollow tube structure with piezoelectric material is split into four quadrants on the outer surface with inner surface as electrical ground. In this design, the piezoelectric tube has outside diameter D, length L, tube wall thickness h and piezoelectric constant d_{31}.

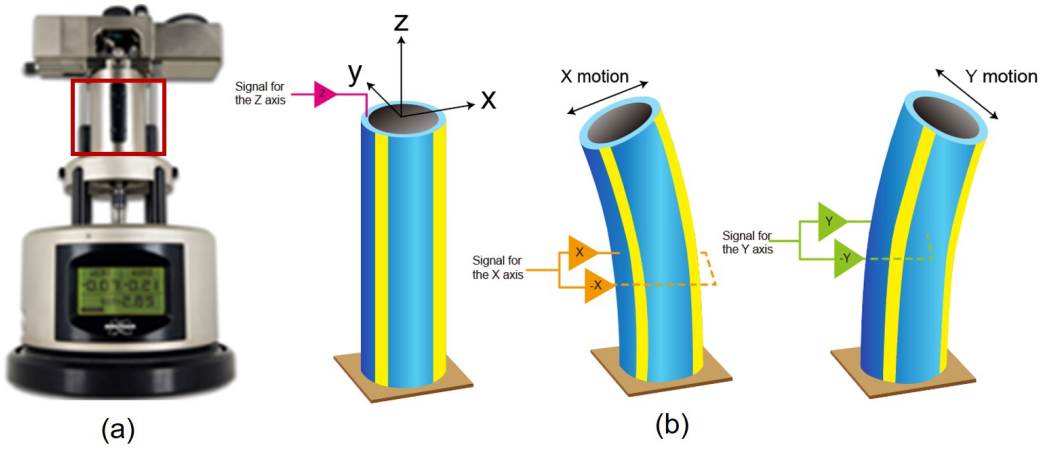

Figure 2-10: Piezo tube scanner: (a) example scanner on a Bruker Multimode 8 AFM in the lab, (b) actuation principle illustration of a four quadrant piezo tube with exaggerated motion

If a common mode voltage is applied to all four quadrants, a vertical motion in the Z-axis is generated. A differential voltage V_x between the $X+$ and $X-$ electrodes will cause a tilting motion of on the top of the tube. The x-axis direction motion Δx is given in Eq.(2.21) with variables defined previously. With the length of piezo tube typically around several centimeters and the motion range Δx on the order of tens of micrometers, the tilting angle is very small and can be neglected in practice. The motion in the Y-axis direction is similar and also shown in Eq.(2.21).

$$\begin{cases} \Delta x = \frac{2\sqrt{2}d_{31}L^2}{\pi Dh}V_x \\ \Delta y = \frac{2\sqrt{2}d_{31}L^2}{\pi Dh}V_y \\ \Delta z = \frac{d_{31}L}{h}V_z \end{cases} \tag{2.21}$$

Compared to scanners with flexure constrained piezo actuators, the piezo tubes are easier to design and fabricate. The scanner can be used in vacuum environments if a suitable material such as lead zirconate titanate (PZT) is used. Although suitable for conventional applications, the bandwidth of the piezo tube scanner is limited to several hundred Hertz, which is insufficient for high-speed applications. It is also desired to remove the slight motion coupling due to the tilting motion especially for large scanning ranges.

To improve the imaging throughput of SPM systems, the bandwidth of the scanner needs to be increased. With a simplified linear second order system model of the scanner with very small damping, the natural frequency $\omega = \sqrt{k/m}$ is approximately given by the square root of stiffness k and mass m. A higher stiffness will increase the resonance but also the actuator force. However, to increase the actuator force, an actuator with larger cross sectional area and therefore larger mass is needed, which reduces the resonance frequency. Therefore, the bandwidth of the scanner is typically limited. Moreover, there is a trade-off between the bandwidth and the range. With the limited $1:1000$ strain ratio of piezo material, a larger actuator or amplifying flexure structures are needed, which would increase the mass and reduce the scanner bandwidth.

A number of scanners have been developed over the years using piezo actuators [90,

91, 92, 93, 94, 95]. A good review of the scanners with various range and bandwidth combination can be found in a review literature [96]. If only a small imaging range is needed, a frame rate over 80 FPS for 128 by 128 pixels with 300 nm by 300 nm range can be achieved [97]. One way to simultaneously achieve large scanning range and high bandwidth is to excite the structure resonance. As an example, a quartz resonator with resonance frequency excited has been used as a scanner to cover a large in-plane square range at hundreds of microns by hundreds of microns with over one thousand lines per second [98]. Researchers have also created MEMS structure based scanners as an alternative approach to improve the bandwidth performance of the scanner [99, 100].

In our group, we have approached the high-speed and large-range AFM scanner design using two strategies. The first strategy is to use multi-actuated scanner that covers large-range overview and high-speed imaging separately, which will be discussed in detail with the multi-actuated music wire scanner design. The second strategy is to properly constrain the piezo actuators with a multi-layer stacked flexure structure to suppress unwanted resonance modes. Multiple generations of scanner designs have been evaluated to improve the performance and resolve undesired effects such as motion coupling.

2.4.2 Multi-actuated Scanner for Overview and Zoom

In this approach, the design philosophy is to treat the bandwidth and range requirements separately with overview and zoom. A large-range static image is taken first to provide an overview of the sample to identify the area of interest. The system then zooms into the target area for high-speed imaging. Using a single scanner to cover these two tasks is challenging and therefore a multi-actuated design is used.

Shear Piezo Multi-actuated Scanner

The first generation of this design concept uses a 5 axis serial kinematic design as shown in Fig. 2-11. A shear piezo actuator is used for positioning of the high-bandwidth X_1 axis. This design was originally implemented and extensively studied by previous lab members with details in [76].

The X_1 and Z_1 axis requires high speed motion. The X_2, Y and Z_2 positioners can cover a large motion range with specifications summarized in Table 2.1. Notice that there is no need for a high-bandwidth Y axis scanner since its require bandwidth is only half of the frame rate at tens of hertz, which is easy to realize even with the large range positioner.

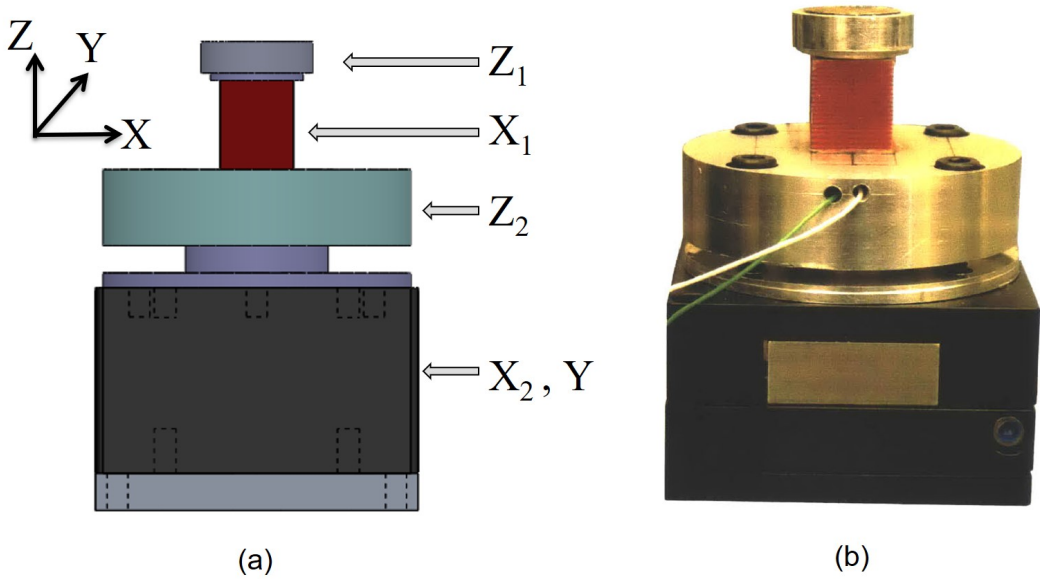

Figure 2-11: Shear piezo multi-actuated scanner design: (a) front view of CAD design with axis labels, (b) picture of the implemented of the scanner in the lab

Axis	Actuator Range (μm)	Scanner Range (μm)	Bandwidth (Hz)
Z_1	2.2	1	100 k
X_1	10	8	5 k
Z_2	6.5	5	5 k
X_2	120	100	180
Y	120	100	165

Table 2.1: Performance summary of the shear piezo multi-actuated scanner design

For implementation, a PL022.31 piezo actuator from PI is used for the Z_1 axis. A P-141.10 shear piezo is used for fast the X_1 axis; a P-885.11 piezo actuator is used for the Z_2 axis. A P-611.XY positioner is used for the X_2 and Z axis. This design has been utilized to perform quasi-video-rate imaging at 8 frames per second [76].

The shear piezo scanner design suffers from several limitations. First, there is a motion coupling between the Z_1 axis and the X_1 axis due to the P-141.10 shear piezo intrinsic material property and thermal expansion. Second, the range of the Z_2 axis can be insufficient for large-range imaging with sample tilt while unnecessarily large for zoomed-in high-speed imaging. The split of actuator efforts to both Z_1 and Z_2 axis also complicates the controller design. Third, the bandwidth of the X_1 axis can be further improved to achieve higher scanning rates.

Music Wire Multi-actuated Scanner

The second generation design following this concept is shown in Fig. 2-12. Instead of using a sheared piezo, two P-885.11 piezo actuators are used to push a center stage constrained by music wire on ball bearings as the X_1 axis. This resolves the motion coupling issue caused by the shear piezo and allows a scanning higher bandwidth.

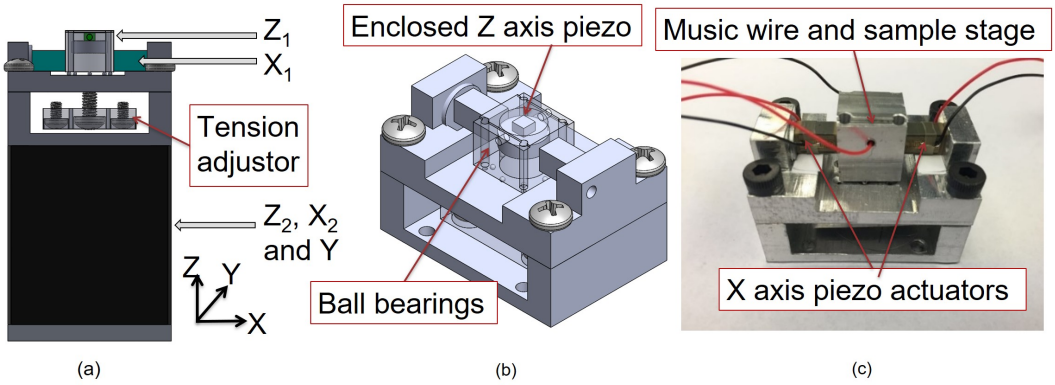

Figure 2-12: Music wire multi-actuated scanner design: (a) front view of CAD design with axis labels, (b) isometric view of the scanner CAD design, (c)picture of the implemented scanner in the lab

The dual-actuated fast X_1 axis structure can be modeled as a second order mass spring damper system. It has two force inputs from the piezo actuators as shown in Fig.2-13. The linear damping arises from the contact between the central stage and ball bearings. The spring constant arises from the stiffness of the piezo actuators that can be computed by dividing the maximum blocking force by the maximum displacement for the piezo when unloaded. The transfer function for the lumped

parameter model is shown in Eq.(2.22).

$$\frac{X_1(s)}{F_1(s) - F_2(s)} = \frac{1}{m_{eff}s^2 + bs + 2k} \tag{2.22}$$

where $X_1(s)$, $F_1(s)$ and $F_2(s)$ are the Laplace transform of the X axis displacement and actuator forces, m_{eff} is the effective mass of the system, b is the damping coefficient and k is the stiffness of a single piezo actuator.

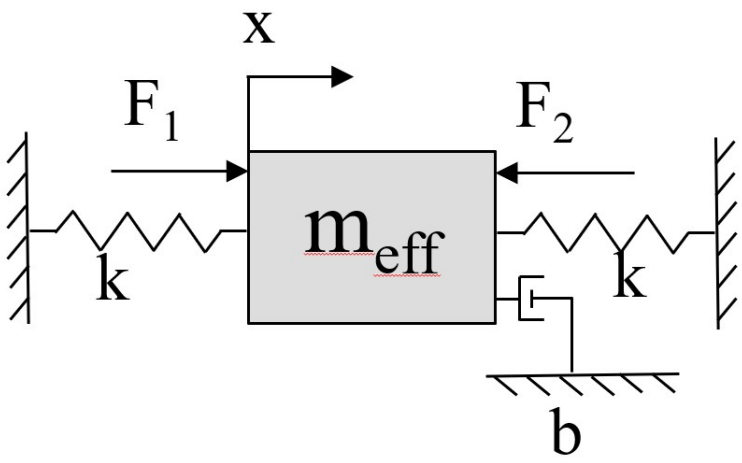

Figure 2-13: Model of the dual actuated X-axis music wire multi-actuated scanner

The X_1 axis is the focus of bandwidth improvement. The Bode plot and magnitude square coherence value obtained from binary stochastic system identification procedure is shown in Fig. 2-14. The empirical transfer function estimate method implemented in Matlab is used to obtain the transfer function in blue. The magnitude square coherence function is shown to verify the integrity of the linear model estimation. A least square fitting is also applied based on the second order model as shown with the green curve in in Fig. 2-14.

To improve the positioning accuracy using feedback controllers, feedback sensors are added. A high bandwidth 6501 active capacitive probe and a 6810 active gauging module from MicroSense are used to measure the scanner X_1 axis motion. More information about this scanner design can be found in reference [101].

For positioning in the Z_2, X_2 and Y axis, large-range scanner is selected. A commercially available P-611.XYZ piezoelectric positioner with parallel kinematics

from PI is used. The music wire scanner is mounted on top of the P-611.XYZ scanner in a serial kinematic configuration. The bandwidth and range performance of the scanner is summarized in Table 2.2.

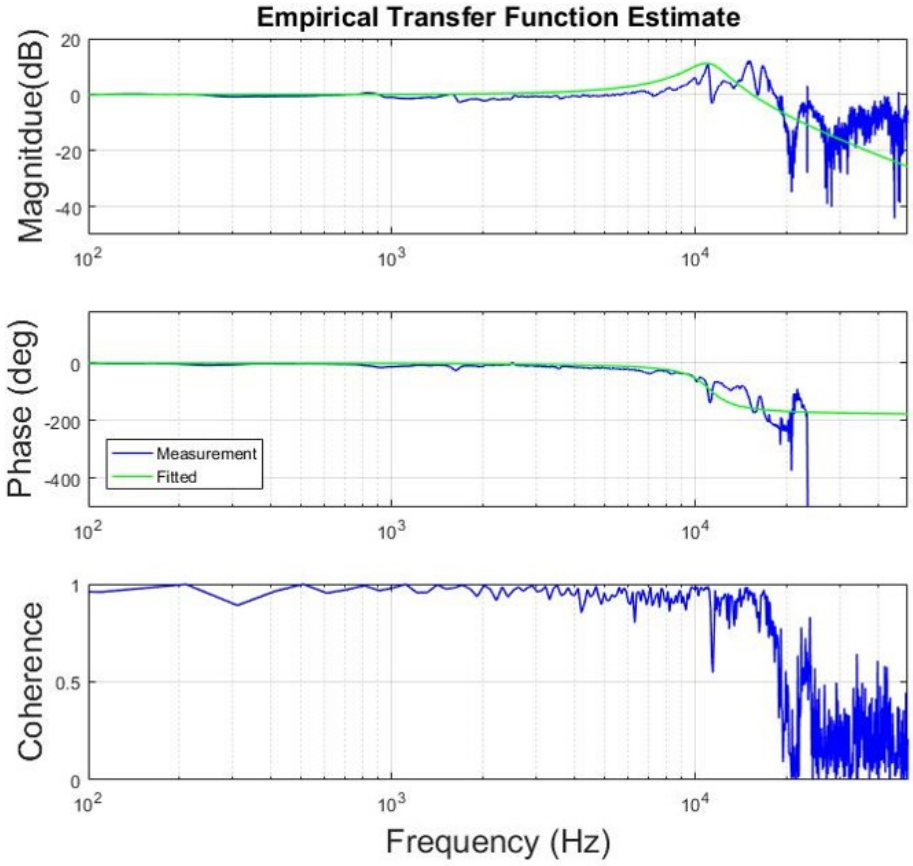

Figure 2-14: System identification results of the music wire multi-actuated scanner fast X_1 axis with Bode plot gain, phase and magnitude squared coherence

Axis	Actuator Range (μm)	Scanner Range (μm)	Bandwidth (Hz)
Z_1	2.2	1	100 k
X_1	6.5	5	10 k
Z_2	120	100	180
X_2	120	100	180
Y	120	100	165

Table 2.2: Performance characteristics of the music wire multi-actuated scanner design

2.4.3 Parallel Kinematic Flexure Scanner

High-bandwidth scanner designs without sacrificing the range of operation are preferred in many applications. As an initial attempt, a parallel kinematic flexure scanner is designed as shown in Fig. 2-15. All three scanner axis are constrained using flexures in this design. Electrical discharge machining techniques are used to fabricate fine features of the scanner flexure in one piece where sharp angles cannot be achieved with conventional machining techniques due to the radius of the end mill.

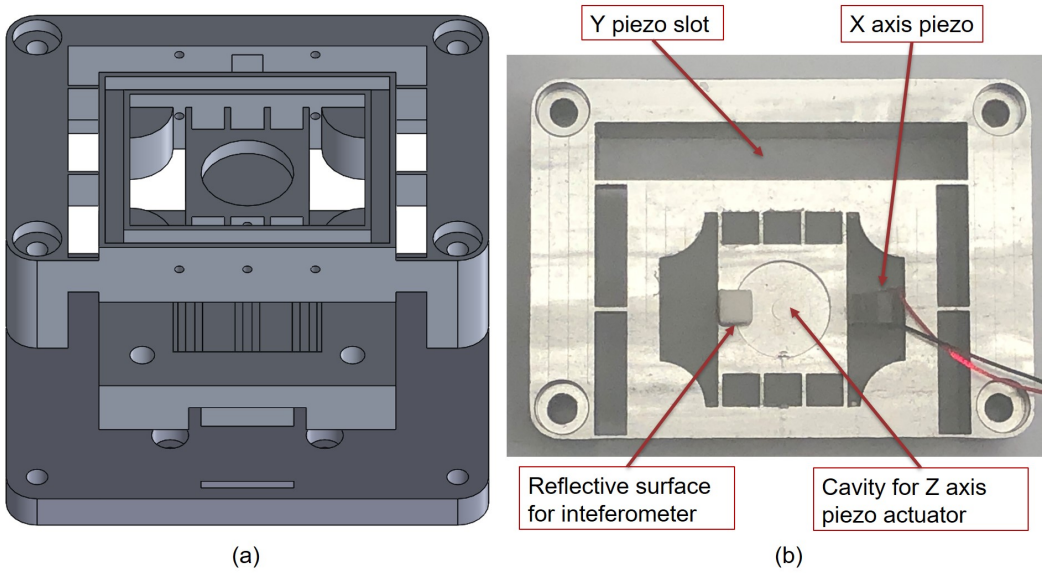

Figure 2-15: Parallel kinematic flexure scanner design: (a) CAD design of the flexure with mounting structure, (b) top view of the fabricated scanner configured for X axis dynamics testing

This design achieves 6 μm motion in the X axis scanning range but has a spurious resonance mode at 5 kHz caused by coupling of flexures in other directions. Moreover, further increasing the actuator length reduces the first resonance frequency. As indicated previously, a longer piezo actuator is needed for a larger traveling range. In this case, the bending mode of the actuator instead of the axial resonance will have the lowest frequency, which can also become significant to generate unwanted low frequency resonance in this scanner design.

2.4.4 Multi-layer Stacked Scanner

The goal of the multi-layer stacked scanner design is to address the challenge of simultaneously achieving high-bandwidth and large-range scanning. The maximal strain of a traditional piezo actuator is on the order of $1:1000$. To achieve a travel range of 20 μm, one would need to either use a longer piezo actuator with length roughly around 20 mm or utilize flexures to amplify small deflection of a shorter piezo actuator. In the first approach, the increased length of a piezo actuator would not only increase the axial length and effective mass of the actuator but also change the lowest resonance mode from axial compression and elongation to bending. The lower frequency bending mode significantly reduces the bandwidth of the scanner. In the second approach, the amplification flexure designs often result in coupling dynamics that affects the dynamic performance in the other axis.

The main idea in this new design is to stack multiple short actuators with flexure constrains between layers. The flexures can suppress unwanted low frequency resonance without significant sacrifice of scanner travel range. This is very difficult to achieve with a single larger piezo actuator for comparable operation range. An illustration of the multi-layer stacked scanner is shown in Fig. 2-16.

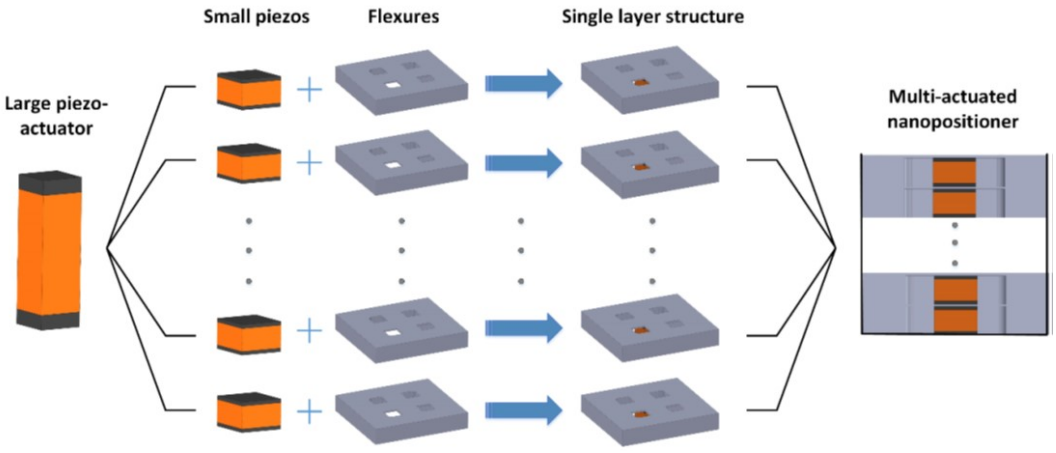

Figure 2-16: Multi-layer stacked scanner design concept illustration

In the initial analysis and implementation of the design, a ten layer design is used. We stacked 10 pieces of PL033.31 piezo actuator together for the X axis. Each

actuator has a square cross sectional area width $w = 3\ mm$ and a $2\ mm$ thickness with $2.2\ \mu m$ unloaded travel range. A flexure with $0.2\ mm$ thickness is used to constrain each layer to suppress the undesired low frequency bending mode. The CAD design and parameter labels are shown in Fig. 2-17. The centrosymmetric flexure design has critical dimensions $w = 3\ mm$ and $d = 2\ mm$ as shown in Fig.2-17 (a). The CAD and finite element analysis (FEA) are both conducted in Solidworks software. As shown in Fig. 2-17 (b), the scanner has its first simulated resonance at 58.685 kHz along the axial direction with first bending mode frequency over 120 kHz.

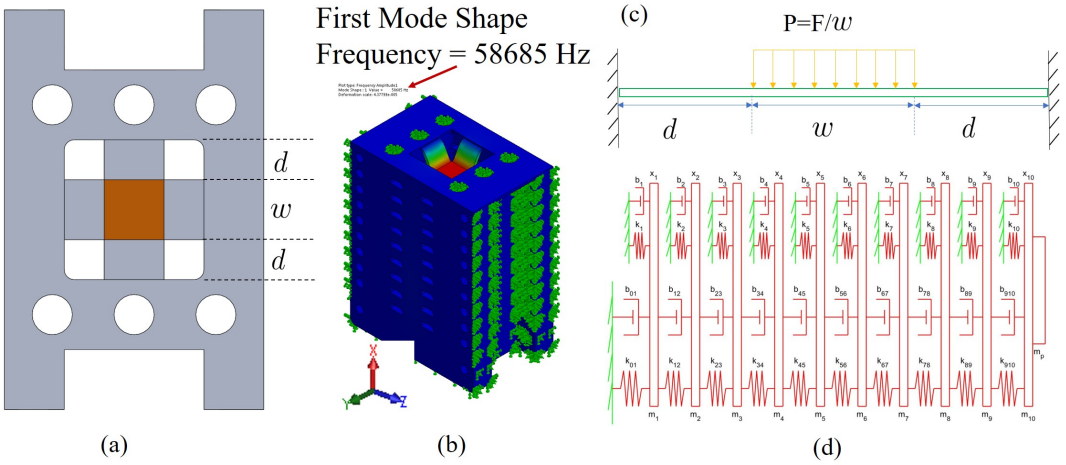

Figure 2-17: Multi-layer stacked scanner design: (a) flexure structure with dimension labels, (b) Solidworks FEA simulation of 10-layer stacked scanner, (c) beam model with fixed boundary conditions and distributed load, (d) lumped parameter dynamic system model of the scanner

To capture the linear scanner dynamics, a multi-input model is created. We denote the flexure surface displacement of each layer with respect to the fixed frame of reference as x_i where i represents the layer count starting from the base to the probe position. We model each layer as a mass block connected to two sets of spring k_{ij} and damper b_{ij} for the piezo actuator as well as another set of spring k_{ii} and damper b_{ii} connected to the ground for the flexure. A 10 layer lumped parameter model of the design is shown in Fig. 2-17 (d). Notice that the subscript i and j corresponds to the connected mass block with mass index m_i or m_j. For simplicity,

we also denote $k_{i^-} := k_{(i-1)i}$, $k_{i^+} = k_{i(i+1)}$ and $k_i := k_{ii} + k_{(i-1)i} + k_{i(i+1)}$ with similar notation for b and for n layer scanner, $m_n^* = m_n + m_p$ where m_p is mass of the probe assembly.

With the notation above, we can create a state space model of the system for an n layer setup as in Eq.(2.23).

$$\begin{aligned} &\dot{X} = AX + BU, \quad Y = CX + DU \\ &X = [x_1, \dot{x}_1, x_2, \dot{x}_2, ...x_i, \dot{x}_i, ...x_n, \dot{x}_n]^T \end{aligned} \tag{2.23}$$

The system matrix A for an n layer scanner is provided in Eq.(2.24) with $2n$ rows and $2n$ columns. Notice that the subscripts i and j are the layer indices.

$$A = \begin{bmatrix} 0 & 1 & 0 & 0 & 0 & 0 & 0 & 0 & \cdots & 0 \\ -\frac{k_1}{m_1} & -\frac{b_1}{m_1} & \frac{k_{12}}{m_1} & \frac{b_{12}}{m_1} & 0 & 0 & 0 & 0 & \cdots & 0 \\ 0 & 0 & 0 & 1 & 0 & 0 & 0 & 0 & \cdots & 0 \\ \frac{k_{12}}{m_2} & \frac{b_{12}}{m_2} & -\frac{k_2}{m_2} & -\frac{b_2}{m_2} & \frac{k_{23}}{m_2} & \frac{b_{23}}{m_2} & 0 & 0 & \cdots & 0 \\ 0 & 0 & 0 & 0 & 0 & 1 & 0 & 0 & \cdots & 0 \\ 0 & 0 & \frac{k_{i^-}}{m_i} & \frac{b_{i^-}}{m_i} & -\frac{k_i}{m_i} & -\frac{b_i}{m_i} & \frac{k_{i^+}}{m_i} & \frac{b_{i^+}}{m_i} & \cdots & 0 \\ \vdots & \vdots & \ddots & \ddots & \ddots & \ddots & \ddots & \ddots & \vdots & \vdots \\ 0 & \cdots & 0 & 0 & 0 & 0 & 0 & 1 & 0 & 0 \\ 0 & \cdots & 0 & 0 & \frac{k_{j^-}}{m_j} & \frac{b_{j^-}}{m_j} & -\frac{k_j}{m_j} & -\frac{b_j}{m_j} & \frac{k_{j^+}}{m_j} & \frac{b_{j^+}}{m_j} \\ 0 & \cdots & 0 & 0 & 0 & 0 & 0 & 0 & 0 & 1 \\ 0 & \cdots & 0 & 0 & 0 & 0 & \frac{k_{n^-}}{m_n^*} & \frac{b_{n^-}}{m_n^*} & -\frac{k_n}{m_n^*} & -\frac{b_n}{m_n^*} \end{bmatrix} \tag{2.24}$$

Assuming the n actuators can be controlled independently, the input matrix B has $2n$ row by n column with zeroes except at the following indices.

$$\begin{aligned} &B(2i, i) = \frac{1}{m_i} \ for \ i = 1, 2, ...n-1, \ and \ B(2n, n) = \frac{1}{m_n^*} \\ &B(2i, i+1) = -\frac{1}{m_i} \ for \ i = 1, 2, ...n-1 \end{aligned}$$

Notice that we need to augment the input matrix B if the 10 piezo actuators cannot be controlled individually due to driving circuit limitations. The output of the system is relatively simple with $C = [0, ...0, 1, 0], \quad D = [0, ..., 0]$

The mass of each layer m_i is the effective piezo mass added to the flexure mass computed from geometry and density. Similar to the case in Eq.(2.10), the effective piezo mass for layer 1 is one third of the piezo mass. Effective mass of the other layers equal to full mass of a single piezo. The top layer also contains additional mass from the probe.

The stiffness of the piezo actuators can be computed easily. This is accomplished by using Eq.(2.25) with the specified blocking force F_{block} and maximum free moving displacement d_{max} from the data sheet.

$$k_{ij} = \frac{F_{block}}{d_{max}} = \frac{300\ N}{2.2\mu m} = 1.3636 \times 10^8\ N/m \tag{2.25}$$

.

The flexure can be approximately modeled as two beams with fixed boundaries. The beams are loaded uniformly at the center as shown in Fig. 2-17 (c). By denoting the total length $L = 2d + w$ and applying the Euler-Bernoulli beam theory, the deflection at the center can be computed by Eq.(2.26) with Young's modulus E, second area moment of inertia of the beam cross sectional area I and temporary constants R_A and M_A. For small deflection $y_{L/2}$, the stiffness value $k = \frac{2F}{y_{L/2}} = 1.8 \times 10^5\ N/m$ can be taken as a linear approximation.

$$\begin{aligned} y_{L/2} &= \frac{R_A L^3 - 6M_A L^2}{48EI} \\ R_A &= \frac{F}{4L^3}(2L^3 + w^3 + 2dw^2 - w^2 L) \\ M_A &= -\frac{F}{24L^2}(6w^2 d + 4w^2 l - 3w^3 - 3L^3) \end{aligned} \tag{2.26}$$

Damping of the system is more complicated to obtain. It is in general very small, not easy to quantitatively evaluate and depends on the structure assembly. The exact

value can be experimentally determined by system identification. For simulation purpose, all damping values are taken as 10 Ns/m to yield a comparable resonance peak to the experiment measurements of frequency response.

The flexures are fabricated with a combination of milling and electrical discharge machining operations. The CAD design of the assembly including all three axis are included in Fig. 2-18 (a). A photo of the implemented 10 layer stacked scanner for testing of X-axis dynamics is shown in Fig. 2-18 (b).

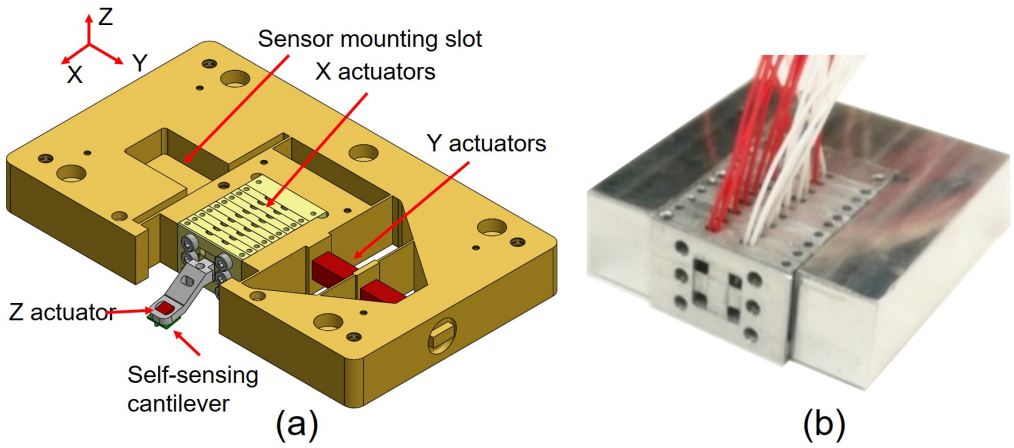

Figure 2-18: Assembly of multi-layer stacked scanner: (a) 10 layer X axis scanner assembly with Y and Z actuators, (b) assembled 10 layer stacked scanner X axis for testing

For assembly, proper preloads need to be applied the piezo actuators to ensure a good dynamic performance. A push nut is used at the fixed end of the X axis to apply the desired preload. In general, Piezo actuators can handle significantly larger compressive loads than tension loads and therefore requires compressive preload for dynamic operation. Piezo actuators used in this scanner (PL033.31 from PI) can withstand a maximum compressive loading of 250 MPa. The recommended preload for the PL033.31 actuator material is around 10 MPa, which corresponds to a 90 N force. A proper preload can be applied by measuring the voltage across the piezo actuator while turning the push nut. This preload has a significant implication on the electrical behavior of the piezo actuator. When externally loaded with compressive

force, the piezo material resistance can reduce significantly from $M\Omega$ to just several Ω when the force exceeds 20% of the maximum mechanical compressive load limit and result in a short circuit. Therefore, it is crucial to ensure proper preload. In addition to the preload, the connection between the layers needs to be carefully bounded with a uniform layer of super glue. This helps to suppress the extra dynamics caused by the backlash from screw moving around the threads.

A scanning range over 20 μm and lowest bandwidth beyond 20 kHz can be achieved with this scanner design. This is significantly higher than previous results as summarized in [90, 96]. To identify the bandwidth of each layer, the frequency sweeps are conducted by individually driving a single actuator at each layer. The measured displacement output of the free end over each actuator input voltage can then be used to produce 10 Bode plots. The amplitude normalized Bode amplitude gain plots for all ten layers are shown in Fig. 2-19.

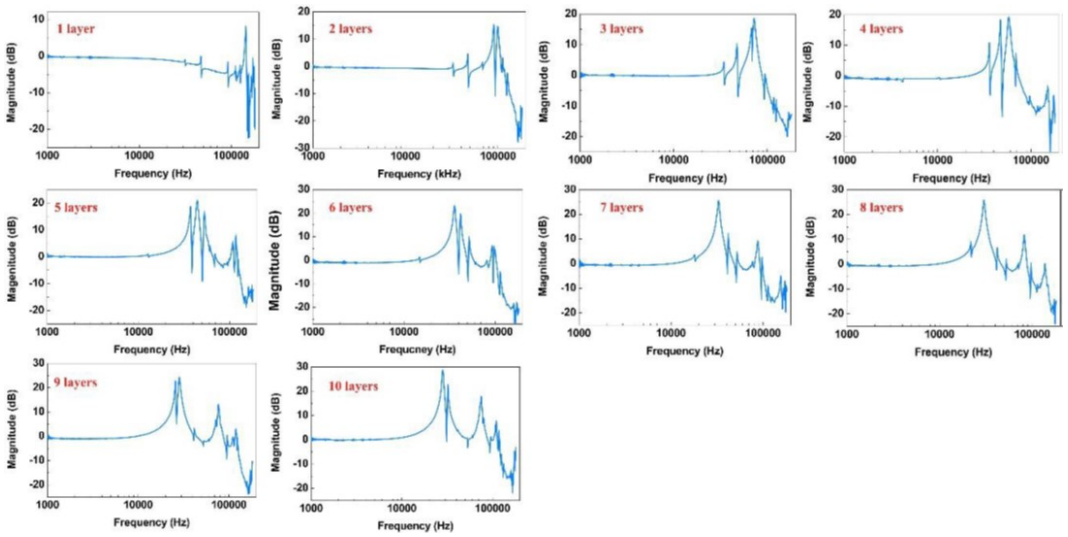

Figure 2-19: Multi-layer stacked scanner Bode amplitude gain plots for free end displacement as output over individually actuated piezo actuator for each of the 10 layers as input demonstrate a higher bandwidth for piezo actuators closer to the output end.

The actuators closer to the free end have higher bandwidths and larger motion ranges. This is reasonable since the top actuator carries the least amount of mass and

is constrained with only one layer of flexure. This phenomenon can be utilized for the design of a bandwidth based repetitive controller as will be discussed in Chapter 4 with more details. The number of layers and actuator size can be changed according to the application needs. More information about this scanner design can be found in reference [102].

2.4.5 Buzzer Actuated Low-cost Scanner

The buzzer actuated low-cost scanner is designed for an educational AFM system. The primary consideration of this design is its safety, affordability and ease of fabrication. Although piezo actuators are widely used as AFM scanners, the high-voltage drives required can be expensive and dangerous for novice users to handle. The flexure structures to constrain the piezo actuator usually requires wire EDM fabrication, which is difficult to access on campus for most universities. Therefore, the piezoelectric buzzer commonly used in the speaker can be used an alternative actuator.

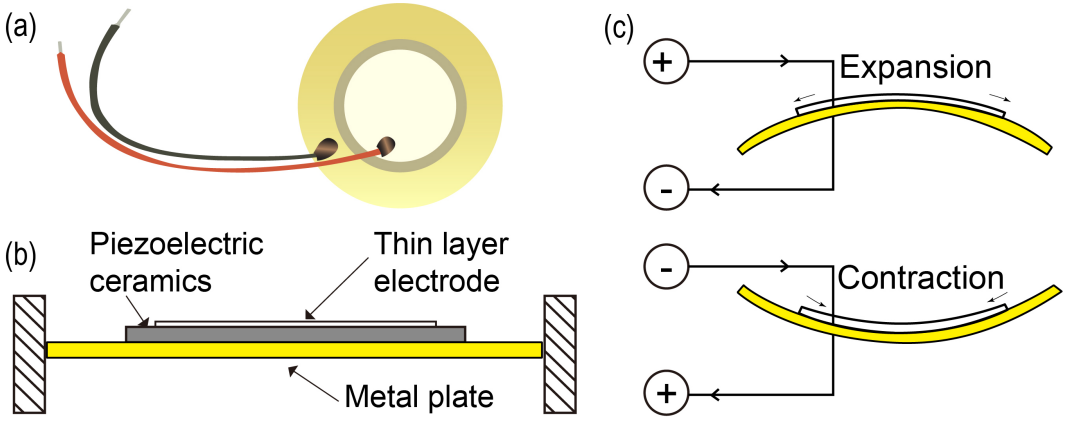

Figure 2-20: Piezoelectric buzzer operation principle: (a) schematic diagram of a piezoelectric buzzer with three layer structure, (b) piezoelectric buzzer deformation with positive or negative voltages applied

Most buzzers have a circular sandwich structure. A buzzer typically includes three layers with a copper disk, a piezoelectric layer and a silver electrode. The voltage-controlled expansion and contraction of the piezoelectric material in the radial direction results in amplified motion perpendicular to the disk. A center deformation

gain of 150 nm/V is typical for most buzzers. A rated voltage of 30 V would result in a motion range up to 4.5 μm.

There are primarily two configurations for piezo buzzer based scanner. In the first configuration, four separate small buzzer actuators are placed evenly around a concentric circle. Four rods are glued to the center of the buzzers and attached to the top stage. The general motion principle is similar to that of the piezo tube scanner with the common mode voltage used for out-of-plane Z direction motion and differential voltages for the in-plane motion in the X and Y directions. Similarly, the tilting angle of the sample is very small and can be safely neglected for imaging purpose. An exaggerated illustration for motion in the X and Z directions is shown in Fig. 2-21 (a).

The second configuration evenly separates the silver electrode of a large buzzer into four quadrants. A single rod is attached to the center of the buzzer with the free end on top of the rod. As shown in Fig. 2-21 (b), the top of the rod moves in the in-plane direction when differential voltages are applied to the X or Y electrodes. Out-of-plane motion can again be generated by common mode voltage to all four electrodes.

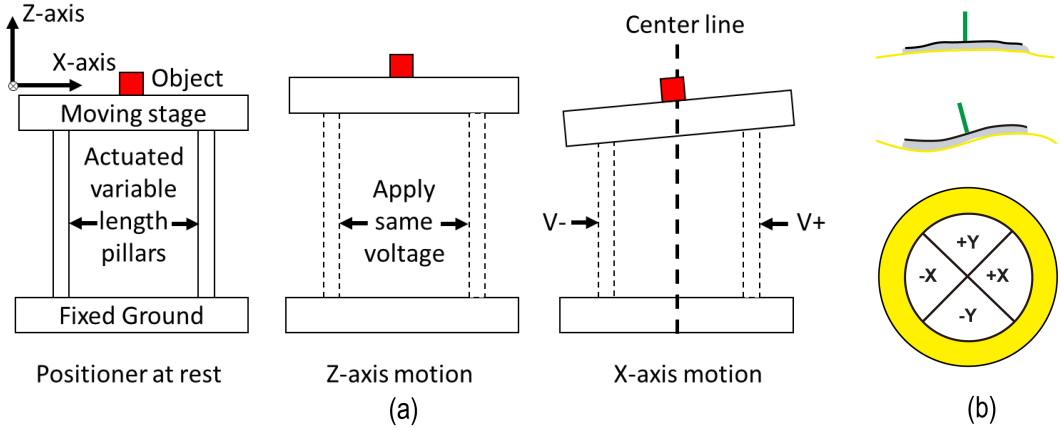

Figure 2-21: Multi-actuated buzzer scanner configuration with variable definitions and motion principle illustration

The first configuration provides a larger in-plane scanning motion. It has a smaller out-of-plane motion compared to the second configuration. Depending on the appli-

cation needs, the scanner configuration can be selected correspondingly.

In this work, the two configurations are stacked to form a multi-actuated scanner design. The geometric configuration of the scanner is shown in Fig. 2-22 with parameter labels. Four 15 mm diameter buzzers are positioned evenly around a circle of radius $r_b = 11.5\ mm$. Aluminum rods of length $l_b = 1.5\ in.$ are used to connect the bottom layer to the middle layer. The dimension labels are shown in Fig. 2-22. For the middle scanner, a large buzzer with 30 mm diameter and four electrode quadrants is used. A magnetic pillar with $l_t = 0.375\ in.$ length connects the center of the buzzer to the sample puck. The spacing between the top of the aluminum rode and the bottom of magnetic pillar is denoted as l_m.

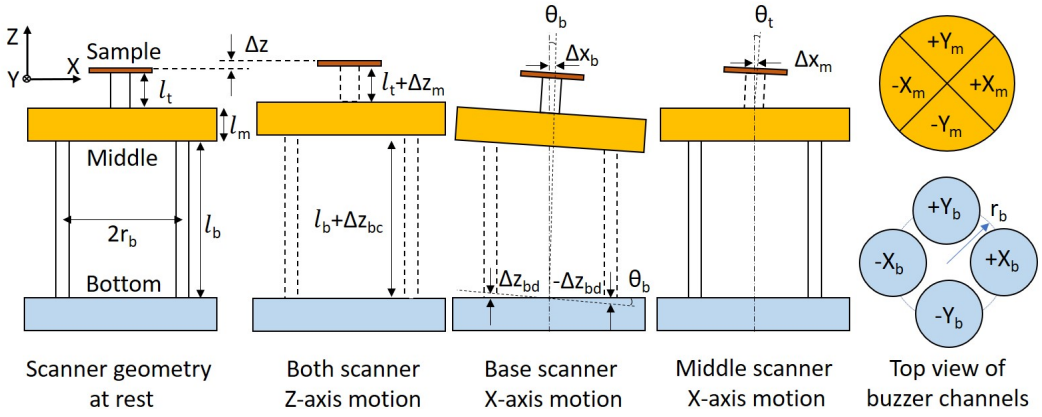

Figure 2-22: Multi-actuated buzzer scanner configuration with variable definitions and motion principle illustrations

The out-of-plane motion is denoted as Δz. It can be obtained from the sum of the bottom buzzer common mode motion Δz_{bc} and the middle buzzer out-of-plane motion Δz_m as $\Delta z = \Delta z_{bc} + \Delta z_m$. The in-plane motion of the sample in the X direction $\Delta x = \Delta x_b + \Delta x_m$ have contributions from both the small buzzers at the bottom x_b and the large buzzer in the center x_m as summarized in Eq.(2.27).

$$\Delta x_b = (l_b + l_m + l_t)\sin\theta_b \approx (l_b + l_m + l_t)\frac{\Delta z_{bd}}{r_b}, \quad \Delta x_m = l_t \sin\theta_m \tag{2.27}$$

In this expression, z_{bd} is the differential drive displacement of the bottom scanner buzzers. Small angle approximation $\sin\theta_b \approx \theta_b$ is applied to relate θ_b to the geometric quantities. The motion equation in the Y direction is similar to the X.

When driven with the rated $\pm 30\ V$ voltage, the scanner operation range can be characterized experimentally with the assembled scanner. The four buzzer configuration can produce 16 μm square in-plane range and 3.75 μm out-of-plane range. The single large buzzer configuration can produce 2.5 μm square in-plane range and 8 μm out-of-plane range. Due to the imperfect alignment, motion coupling between the out-of-plane axis and the in-plane axis are around 1.25% to 1.75%. An in-plane coupling at around 3% between the X and the Y axis is observed. The first resonance frequency is at around 75 kHz, which is sufficient for conventional AFM operation.

The buzzer scanner design has several benefits. It is ease to fabricate, safe to operate and inexpensive to implement. The scanner structure can be 3D printed easily for cost-efficiency. A machined metal structure can better constrain the piezo buzzer for better motion performance. The buzzer scanner design is a suitable choice for an educational AFM system as will be discussed in Chapter 6. The CAD design and photos of the partially assembled buzzer scanner are shown in Fig. 2-23. The custom designed driver for the scanner will be discussed in Chapter 5. Publication for this scanner and the educational AFM system design is submitted under review.

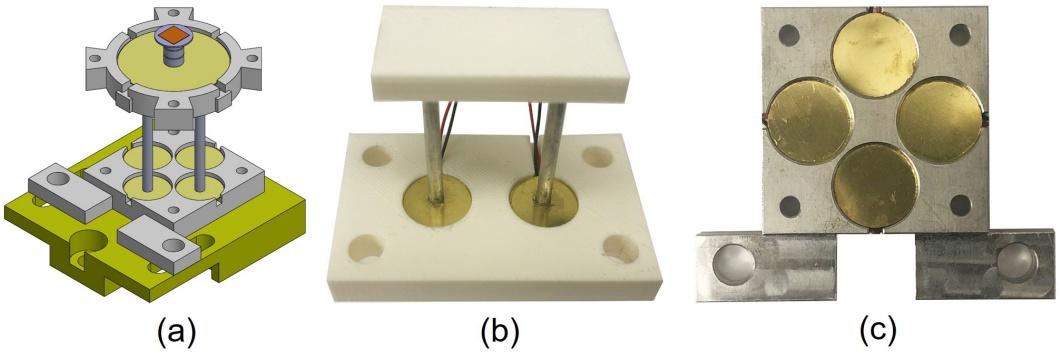

Figure 2-23: Buzzer scanner implementation: (a) 3D CAD mode of the buzzer scanner design, (b) simplified single in-plane axis buzzer scanner for testing, (c) partially assembled scanner with the four-buzzer configuration

2.5 Chapter Summary

In this chapter, the design, model and characterization of nano-positioning systems for AFMs are discussed in detail. The actuators, sensors and mechanical structures commonly used for AFM scanner design are introduced on the principle level. Based on the profound understanding of the scanning requirements and application scenarios, new AFM scanner designs originated from this work are presented. Three of the scanners are selected for AFM integration to be discussed in Chapter 6. First, a dual-actuated scanner with fast X and Z axis combined with a commercial scanner is developed for large-range overview (100 μm in X, Y, Z) and zoomed in (6 μm in X, Y and 1 μm in Z) high-speed scanning (10 kHz line scan bandwidth, 100 kHz out-of-plan bandwidth). Second, a multi-actuated stacked scanner with high-speed (over 20 kHz line scan and 100 kHz out-of-plane) and middle range scanning (20 μm in-plane X, Y and 2 μm out-of-plane Z) is developed for high-speed scanning at a relatively larger range. Third, a buzzer-based low-cost (below \$50) scanner (16 μm in-plane X, Y and 3.75 μm out-of-plane Z) is developed for an educational AFM system. The second main contribution of this work for the high-speed and large-range AFM nano-positioner design is addressed in this chapter.

Chapter 3

AFM Cantilever Probe Design

3.1 Introduction

The cantilever probe is the key component of an AFM system for image generation. The deflection of a passive cantilever probe is often measured by an external optical beam deflection system. In dynamic operation modes, piezo actuators are placed in the probe holder structure for acoustic excitation of the cantilever resonance modes. There are a number of alternative sensing and actuation methods available for AFM cantilever probes. With nano-fabrication technology, sensing and actuation elements can be embedded into the micro-cantilever to form active probes. In this chapter, the cantilever dynamics and general principles suitable for AFM probe sensing and actuation are introduced first. The focus of discussion is placed on an active probe design with piezoresistive sensing and thermomechanical bimorph actuation used in this work. The nano-fabrication and functionalization processes to produce active AFM probes are then discussed. In the end, potential applications of functionalized active probes for AFM imaging are presented.

3.2 Principles for AFM Cantilever Probe Design

A conventional passive AFM cantilever probe typically has three components. These include a sharp tip, a cantilever beam and a base support chip. As discussed in

Chapter 1 and shown in Fig. 1-2, the base support chip has a standard dimension of length 3.4 mm, with 1.6 mm and thickness 0.3 mm. The probe can be handled manually with a tweezer to be mounted in a probe holder. The micro-fabricated cantilever beam typically has length around tens to hundreds of microns depending on the application. The probe tip usually has a pyramid shape with a tip radius as small as one nanometer. For simple applications, the probes are made up of a single material either with silicon or silicon nitride. Multiple cantilevers can be produced on the same base support chip and different probe tip geometry can be fabricated as shown in Fig. 3-1.

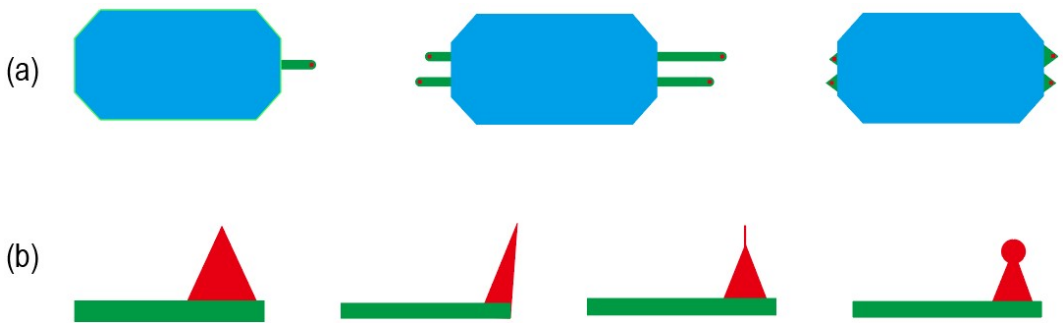

Figure 3-1: Cantilever probe geometry illustration: (a) single rectangular cantilever, four rectangular cantilever on one support chip, and four triangular cantilever on one support chip, (b) pyramid shape probe tip, frontal end tip, sharpened tip, and rounded tip for nano-indentation

The deflection can be measured either directly or indirectly. For direct measurement, the deflection at the back of the probe tip are measured primarily using optical methods. For indirect measurements, the internal stress and strain of the beam structure can be measured to deduce the cantilever tip deflection. During AFM imaging, the vertical deflection of the cantilever probe free-end can go over several hundred nanometers. Subnanometer resolution can be achieved using a variety of methods. If both sensing and actuation elements are embedded into the cantilever using nano-fabrication techniques, the resulting probe is considered an active cantilever probe. Before introducing the potential sensing methods, understanding some key results for the cantilever mechanics can be helpful.

3.2.1 Cantilever Mechanics

Mechanical models can be created to analyze the cantilever deflection. Most AFM cantilevers can be approximately modeled as a uniform beam with a rectangular cross sectional area. The Euler-Bernoulli beam bending theory can be applied to derive analytical closed form solutions for simple geometries. The variable definitions for beam bending analysis is shown in Fig. 3-2.

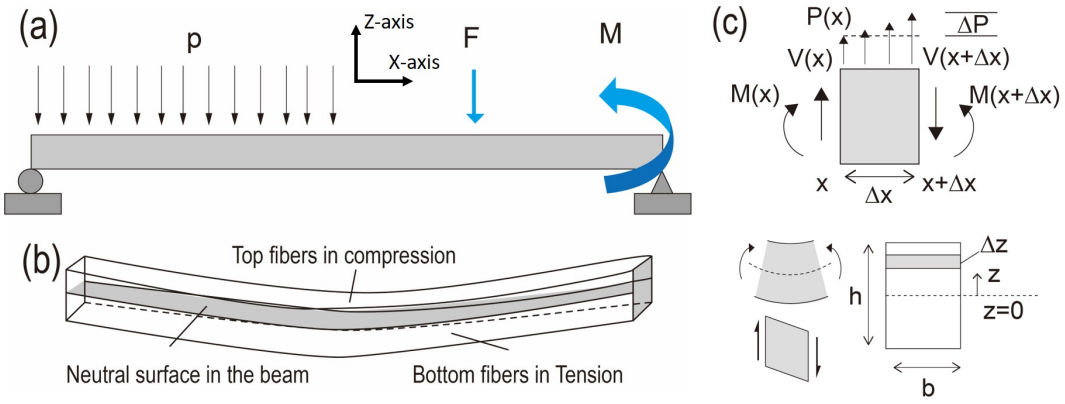

Figure 3-2: Beam loading and deformation: (a) three types of common loads including distributed load p, concentrated force F and concentrated moment M on a beam with simply supported boundary conditions, (b) downward beam deflection with label of neutral axis, fibers in tension, and fibers in compression, (c) beam bending analysis definitions with microscopic element on the beam with variable definitions, deformation illustration of the microscopic element under shear force or moment, and cross sectional view of a beam with rectangular shape

The moment curvature equation describes the beam bending mechanics under small deformation. It can be derived by considering the internal stress σ_{xx} in the beam along the longest x axis direction. The stress σ_{xx} can be expressed in two ways related to its distance z with respect to the neutral plane during bending. Without going into the details of the derivation available in many mechanics textbooks, the stress can be expressed in terms of the external moment $M(x)$, area moment of inertia I of the cross sectional area and distance z. The cantilever overall length is denoted as l. Alternatively, it can also be expressed by the elastic modulus E, bending deformation radius curvature R and distance z. By combining these two relations,

the beam bending moment curvature governing equation is obtained in Eq.(3.1).

$$\sigma_{xx} = -\frac{M(x)z}{I} = -\frac{E}{R}z \Rightarrow M(x) = \frac{EI}{R} = EI\frac{d^2Z}{dx^2} \tag{3.1}$$

Cantilever Statics

The external moment $M(x)$ can be integrated directly from the shear force diagram. For an AFM cantilever beam, $M(x)$ typically arises from the force acting at the probe tip due to its interaction with the sample surface. Assuming only a normal force F acting at the free end, the moment is simply a ramp function as expressed in Eq.(3.2). In most cases during imaging, the AFM cantilever is loaded at the probe tip with its interaction to the sample. The normal force F in the Z axis dominates the bending motion. In-plane direction friction forces can also have relatively smaller effects by generating moments to twist and bend the cantilever.

$$M(x) = Fl - Fx \tag{3.2}$$

For a rectangular cross sectional area of the cantilever, the area moment of inertia can be integrated directly as in Eq.(3.3). Results for other cross sectional geometries can be obtained similarly or looked up from summary tables in most mechanics textbooks.

$$I = \int_A z^2 dA = \int_{-\frac{h}{2}}^{\frac{h}{2}} z^2 b dz = \frac{z^3}{3}\Big|_{-\frac{h}{2}}^{\frac{h}{2}} = \frac{1}{3}\left[\left(\frac{h}{2}\right)^3 - \left(-\frac{h}{2}\right)^3\right] = \frac{bh^3}{12} \tag{3.3}$$

Based on the moment curvature equation, the deflection of and slope at each location of the beam can be obtained by applying definite integral. The two constants in the integral can be determined by applying the boundary conditions $Z(x = 0) = 0$ and slope $dZ(x = 0)/dx = 0$ for the fixed end as shown in Eq.(3.4) and Eq.(3.5).

$$Z(x) = \frac{F}{EI}\left[-\frac{x^3}{6} + \frac{lx^2}{2}\right] \tag{3.4}$$

$$\frac{dZ(x)}{dx} = \frac{F}{EI}\left[-\frac{x^2}{2} + lx\right] \tag{3.5}$$

The maximum beam deflection is at the cantilever free end given by Eq.(3.6).

$$Z(x)|_{x=l} = \frac{Fl^3}{3EI} \tag{3.6}$$

The corresponding angle at the free end can be approximated by the slope for small deflection as in Eq.(3.7). By cancelling out the force term, it is easy to see that the angle $\theta_{x=l}$ is also directly proportional to the deflection $Z(x)_{x=l}$.

$$\theta_{x=l} \approx \left.\frac{dZ(x)}{dx}\right|_{x=l} = \frac{Fl^2}{2EI} \tag{3.7}$$

The effective stiffness k of the cantilever probe can be written as Eq.(3.8).

$$k = \frac{F}{Z(l)} = \frac{3EI}{l^3} \tag{3.8}$$

The location for maximum tensile and compressive stress in the beam need to be identified for sensor placement. The maximum stress locations are observed on the top and bottom beam surfaces at the fixed end with values shown in Eq.(3.9). The strain ε_{xx} can be derived easily by dividing the stress σ_{xx} by the elastic modulus E.

$$\sigma_{xx} = -\frac{M(x)z}{I} = -\frac{Flh/2}{\frac{wh^3}{12}} = -\frac{6Fl}{wh^2} \tag{3.9}$$

These results are helpful for analytical determination of AFM cantilever deflection on a principle level. The true values for the cantilever such as the stiffness can change slightly due to geometric approximation and imperfect nano-fabrication process variations. Calibration methods are often applied to obtain the value specific to each cantilever as will be discussed later in this chapter.

Cantilever Dynamics

In dynamic operation modes, the cantilever resonance is excited. It is important to understand the dynamic behavior of the cantilever. In this section, We provide the analysis results for a cantilever beam without damping. By applying Newton's law to the moment curvature equation on a small element, the partial differential equation for transverse beam vibration can be derived and is shown in Eq.(3.10). The beam is assumed to have a uniform density ρ,a uniform cross sectional area A and subjected to a distributed load $p(x)$.

$$\rho A \frac{\partial Z^2}{\partial t^2} + \frac{\partial^2}{\partial x^2}\left(EI\frac{\partial^2 Z}{\partial x^2}\right) = -p(x) \tag{3.10}$$

This partial differential equation can be solved with the technique for separation of variables. We assume the solution is of the form $Z(x,t) = \phi(x)\eta(t)$. For a cantilever beam without external loads, the distributed load term $p(x)$ becomes 0. The expression can then be rewritten as in Eq.(3.11), where ω is defined that corresponds to the natural frequency.

$$\rho A\phi(x)\frac{\partial^2\eta(t)}{\partial t^2} + EI\eta(t)\frac{\partial^4\phi(x)}{\partial x^4} = 0 \Rightarrow \frac{EI}{\rho A}\frac{1}{\phi(x)}\frac{\partial^4\phi(x)}{\partial x^4} = \frac{1}{\eta(t)}\frac{\partial^2\eta(t)}{\partial t^2} := \omega^2 \tag{3.11}$$

With the method of separation of variables [103], the partial differential equation can be separated into the time domain $\eta(t)$ as in Eq.(3.12) and the space domain $\phi(x)$ as in Eq.(3.13).

$$\frac{\partial^2\eta(t)}{\partial t^2} + \omega^2\eta(t) = 0 \tag{3.12}$$

$$\frac{\partial^4\phi(x)}{\partial x^4} - \frac{\omega^2\rho A}{EI}\phi(x) = 0 \tag{3.13}$$

It is often desirable to know the natural frequency ω of the cantilever. This can be done by solving an eigenvalue problem in the space domain for $\phi(x)$ with prescribed boundary conditions. The second order time domain components can then be solved

relatively easily given initial conditions. For transverse vibration of a cantilever beam, there are a total of four boundary conditions as shown in Eq.(3.14).

$$Z_{x=0} = 0, \quad \left.\frac{dZ(x)}{dx}\right|_{x=0} = 0 \quad M_{x=L} = EI\left.\frac{\partial^2 Z}{\partial x^2}\right|_{x=L} = 0, \quad V_{x=L} = EI\left.\frac{\partial^3 Z}{\partial x^3}\right|_{x=L} = 0 \tag{3.14}$$

A trial solution for $\phi(x)$ can be expressed as shown in Eq.(3.15) with the constant value definition $\lambda^4 = \omega^2 \rho A/EI$.

$$\phi(x) = A\cos(\lambda x) + B\cosh(\lambda x) + C\sin(\lambda x) + D\sinh(\lambda x) \tag{3.15}$$

The four unknown constants can be determined by applying the boundary conditions. With the first two boundary conditions at the fixed end, $Z_{x=0} = 0$ and $\left.\frac{dZ(x)}{dx}\right|_{x=0} = 0$, two governing relations can be obtained as $A + B = 0$ and $C + D = 0$. The equations of the two remaining boundary conditions are summarized in Eq.(3.16).

$$\begin{aligned} & \begin{cases} A\lambda^2(-\cos\lambda l - \cosh\lambda l) + C\lambda^2(-\sin\lambda l - \sinh\lambda l) = 0 \\ A\lambda^3(\sin\lambda l - \sinh\lambda l) + C\lambda^3(-\cos\lambda l - \cosh\lambda l) = 0 \end{cases} \\ \Rightarrow \quad & \begin{bmatrix} \cos\lambda l + \cosh\lambda l & \sin\lambda l + \sinh\lambda l \\ \sin\lambda l - \sinh\lambda l & -\cos\lambda l - \cosh\lambda l \end{bmatrix} \begin{bmatrix} A \\ C \end{bmatrix} = \begin{bmatrix} 0 \\ 0 \end{bmatrix} \end{aligned} \tag{3.16}$$

With zeros on the right hand side of the equations, A and C can only take on the trivial solution value of zeros if the coefficient matrix is invertible. To obtain non-trivial solutions, an eigenvalue problem about λ can be formulated by setting the determinant of the coefficient matrix for A and C to 0 to yield the constrain Eq.(3.17).

$$\begin{aligned} & (\cos\lambda l + \cosh\lambda l)(-\cos\lambda l - \cosh\lambda l) - (\sin\lambda l + \sinh\lambda l)(\sin\lambda l - \sinh\lambda l) = 0 \\ \Rightarrow \quad & \cos\lambda l \cosh\lambda l = -1 \end{aligned} \tag{3.17}$$

There are infinite number of λ_n solutions that can satisfy the constrain in Eq.(3.17).

The first six solutions are provided below.

$$\lambda_1 l = 1.875, \quad \lambda_2 l = 4.694, \quad \lambda_3 l = 7.855, \quad \lambda_4 l = 10.996, \quad \lambda_1 l = 4.137, \quad \lambda_6 l = 17.279$$

The first natural frequency of the cantilever can therefore be expressed in Eq.(3.18).

$$\omega_1 = \lambda_1^2 \sqrt{\frac{EI}{\rho A}} = \frac{1.875^2}{l^2} \sqrt{\frac{EI}{\rho A}} \tag{3.18}$$

This formula can be used to estimate the resonance frequency of a cantilever design. However, the exact value for AFM dynamic mode operation would still need to be measured through the probe calibration process. In many cases, a simplified second order model with mass m, damping b and spring constant k written in the form of natural frequency ω_n and damping ratio ζ is used to capture the time domain cantilever bending resonance oscillation as shown in Eq.(3.19).

$$\frac{d^2 z}{dt^2} + 2\zeta\omega_n \frac{dz}{dt} + \omega_n^2 z = \frac{k}{m} z_\Delta(t), \quad \zeta = \frac{c}{2\sqrt{km}}, \quad \omega_n = \sqrt{\frac{k}{m}} \tag{3.19}$$

The quality factor $Q = \frac{1}{2\zeta}$ is another variable that can be important. It is typically used to describe the damping behavior of the cantilever oscillation. A large Q factor is expected with lower damping such as operation in vacuum environments. The system identification methods for cantilever dynamics are discussed later in this chapter. Notice that the second order dynamic system model is suitable for small cantilever deflections while non-linear Duffing models need to be considered for larger cantilever deformations [104, 105].

3.2.2 Cantilever Deflection Sensing

With understanding of the cantilever mechanics, we now take a closer look at the various methods available for the sensing of cantilever deflection. The measurement can be accomplished directly at the probe tip or indirectly by measuring the internal stress or strain at specific location of the cantilever beam. Sensor located externally for passive cantilever deflection measurement typically use optical based methods

such as the optical beam deflection sensing, interferometry of interdigitated fingers, astigmatic detection with optical pick-up unit and optomechanical method. For active cantilever probes with embedded sensors, the peizoresistive and piezoelectric effects are typically used for indirect measurement of the probe deflection.

Optical Beam Deflection Sensing

The optical beam deflection (OBD) system is the most widely adopted cantilever deflection measurement method. Subnanometer resolution can be achieved with this method in the vertical out-of-plane direction. As shown in Fig. 3-3(a) with a simplified drawing, a monochromatic laser is directed to the back of the cantilever and the laser position is measured by a four quadrant photodiode. With an ideal alignment and small twisting motion of the cantilever, the small angle change of the cantilever probe tip is linearly amplified by the laser beam to become the linear movement of the laser spot on the photodiode.

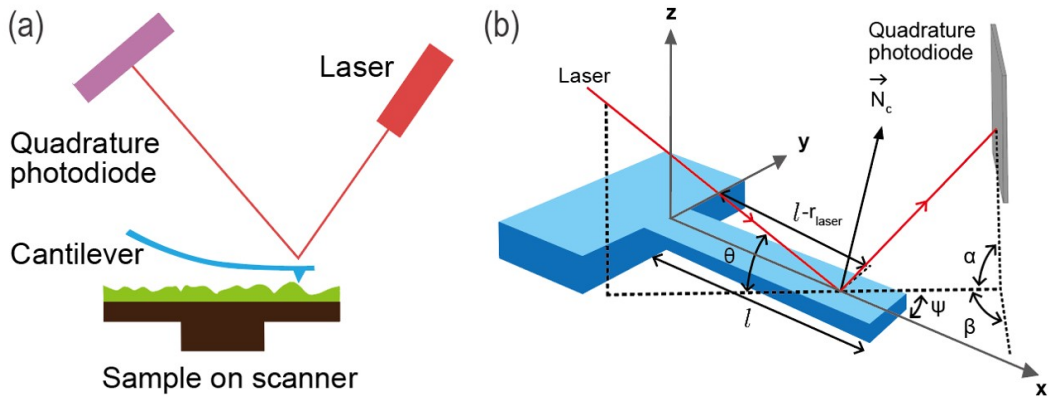

Figure 3-3: Optical beam deflection sensing: (a) 2D illustration of the OBD sensing principle, (b) 3D illustration of multiple angles involved during the alignment process

The small angle change and the actual deflection of the probe tip is linearly related. Assuming the laser beam has a cylindrical shape with radius r_{laser}, an ideal alignment would have the laser spot focused at the free end of the cantilever at $l - r_{laser}$. By cancelling out the force term in Eq.(3.4) and Eq.(3.5), the angle at location $\theta\left(l - \frac{l_b}{2}\right)$

is related to the tip deflection $\Delta z(l)$ by Eq.(3.20).

$$\theta\left(l-\frac{l_b}{2}\right)=\frac{3}{2l}\left[1-\left(\frac{l_b}{2l}\right)^2\right]\Delta z(l) \tag{3.20}$$

The four quadrants of the photodiode can each be viewed as a current source. The output current of each quadrant is proportional to the light intensity of the beam that falls within the quadrant. By using a trans-impedance amplifier for each quadrant, four voltage signals can be obtained. The sum signal $V_{sum} = V_1 + V_2 + V_3 + V_4$ can be used to evaluate the total signal intensity of the reflected laser. The vertical difference signal $V_{ver} = V_1 + V_2 - V_3 - V_4$ is proportional to the cantilever deflection. The horizontal difference signal $V_{hoz} = V_1 - V_2 - V_3 + V_4$ is proportional to the twisting of the cantilever.

The sensitivity of the measurement depends on a number of factors. These can include the reflectivity of the probe surface, the laser power, the photodiode current generation gain, signal conditioning circuit gains, the light attenuation in the environment and the geometric configuration of the alignment. For the cantilever, reflective gold coatings are applied to increase the sensitivity. The laser and photodiode are often selected correspondingly for a suitable current gain at a specific laser wavelength. The gain of the signal conditioning circuits are adjusted based on the range of the analog to digital converter. The sensitivity can be different between each experiment due to the change of imaging environment and the geometric configuration of the alignment. Therefore, a calibration process is often applied when the exact deflection measurement sensitivity is needed for the experiment.

The main aspect for improvement of the OBD system is the alignment of laser and cantilever probe. Both the laser spot diameter and the cantilever width are on around 10 μm, which makes the manual alignment process time consuming especially for liquid environment imaging. Moreover, the alignment is actually completed in the 3D space and not only the position but also the incident angles of the laser can affect the sensitivity of the measurement as shown in Fig. 3-3 (b). A more detailed analysis on this issue is available in reference [106].

Interferometry Sensing

The laser interferometer as discussed in Chapter 2 can also be used to measure cantilever probe deflection. Commercial application is available such as the Cypher AFM system from Asylum Research. The laser beam alignment in this case can be more challenging compared to the optical beam deflection system as it needs to be normal to the cantilever surface. The cost of a laser interferometer can also be relatively high.

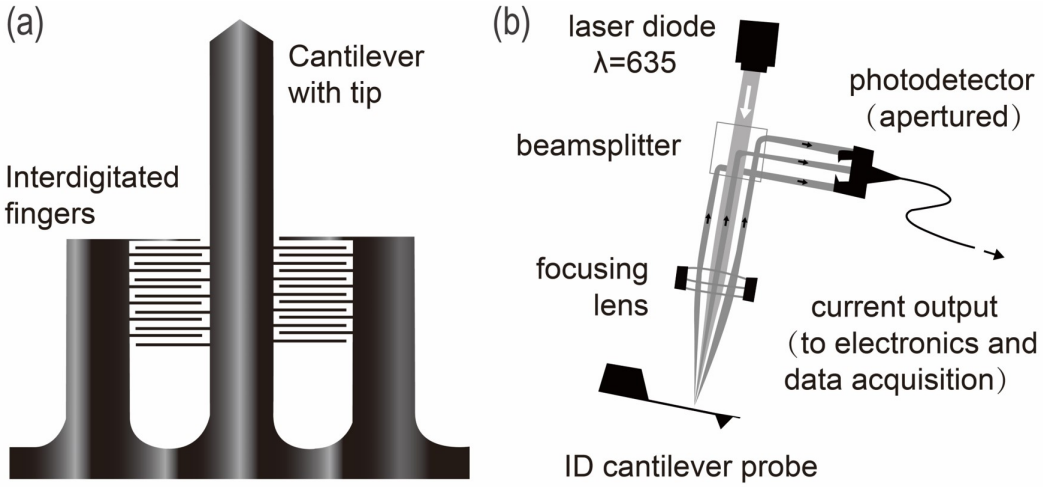

Figure 3-4: Interferometry based probe deflection measurement: (a) interdigitated cantilever probe, (b) optical components for probe deflection measurement

As an alternative design, an interdigitated cantilever probe can be used. As shown in Fig. 3-4, the probe has a specialized geometry with the tip attached to the center cantilever and two fixed cantilevers with multiple fingers. The laser is focused on the intersection area of the fingers instead of the tip of the center cantilever. The reflected laser intensity is gathered by a single quadrant photodiode. A periodic interference pattern is generated due to the light path distance difference between the fingers on the center cantilever and the fingers on the fixed reference cantilever. The center of the interference peak is usually labeled as the 0^{th} peak. The relationships between the current generated in the photodiode and the deflection of the center cantilever δz

for odd peaks I_{odd} and even peaks I_{even} are shown in Eq.(3.21).

$$\begin{cases} I_{odd} \propto \sin^2(\frac{2\pi}{\lambda}\delta z) \\ I_{even} \propto \cos^2(\frac{2\pi}{\lambda}\delta z) \end{cases} \tag{3.21}$$

The expression is non-linear and periodic in general. For maximum sensitivity, it is desirable to adjust the distance between the photodiode and the cantilever such that the sinusoidal curve is at its maximum slope when the cantilever is not loaded. As the center cantilever deflection changes due to the tip interaction with the sample, the interference intensity also changes with the photodiode generated current. With the approximated linear relation, the cantilever deflection can be measured. Notice that the measured deflection is at the fingers and needs to be scaled to obtain the tip deflection. The laser alignment process in this case is easier compared to the optical beam deflection method at the cost of more complex probe fabrication process.

Astigmatic Sensing

Another optical method suitable for AFM cantilever deflection measurement is the astigmatic sensing method. This method is used in most CD/DVD players for detection of pit depth variation that encodes the digital information with optical pick-up units. The error signal S_{FE} from the photodiode is approximately linearly proportional to the defocus distance in a range and can be used measure the analog deflection of the cantilever. With the wide availability of the optical pick-up unit in the CD/DVD players, they have been hacked and used in AFM system to significantly reduce the cost of optical components. One drawback of this technique is that the sensing unit needs to be placed in close proximity to the cantilever probe, limiting its application environments. More details of the astigmatic sensing method can be found in references [107, 108].

Optomechanical Sensing

While most optical methods measure passive cantilever probe deflection externally, an attempt has been made to embed optical sensing into the cantilever. In the optomechanical sensing method, a micro disk with optical wave guides is used. The cantilever is evanescently coupled to the optical micro disk in an optical whispering

gallery mode. External optical fibers are used to guide the laser to the wave guide. The motion of the cantilever causes a frequency modulation of the optical cavity modes, which can be measured by a spectrum analyzer to extract the deflection information. This method can be relatively complicated to implement. However, it is easier to operate as the laser alignment process is replaced by the optical fiber connection. More details of this method can be found in reference [109].

Piezoresistive Sensing

The piezoresistive effect is the change of material resistivity due to mechanical stress. As illustrated in Eq.(2.6) for the gauge factor strain gauges, there is an extra term $d\rho/\rho$ involved in the expression. For metal materials used in most thin foil strain gauges, this change of resistivity is neglected. However, for certain semiconductors, the contribution of this term is significantly higher than the geometric contributions.

The piezoresistive effect are typically described using matrix tensor of piezoresistive coefficients π_i. The coefficients relate the resistivity change $\Delta\rho_i/\rho_0$ to the mechanical stress σ_i in all six directions. For p-doped silicon material, only three primary coefficients need to be considered including the longitudinal coefficient π_L, the transverse coefficient π_T and the shear coefficient π_S as shown in Eq.(3.22).

$$\begin{bmatrix} \Delta\rho_{xx}/\rho_0 \\ \Delta\rho_{yy}/\rho_0 \\ \Delta\rho_{zz}/\rho_0 \\ \Delta\rho_{yz}/\rho_0 \\ \Delta\rho_{xz}/\rho_0 \\ \Delta\rho_{xy}/\rho_0 \end{bmatrix} = \begin{bmatrix} \pi_L & \pi_T & \pi_T & 0 & 0 & 0 \\ \pi_T & \pi_L & \pi_T & 0 & 0 & 0 \\ \pi_T & \pi_T & \pi_L & 0 & 0 & 0 \\ 0 & 0 & 0 & \pi_S & 0 & 0 \\ 0 & 0 & 0 & 0 & \pi_S & 0 \\ 0 & 0 & 0 & 0 & 0 & \pi_S \end{bmatrix} \begin{bmatrix} \sigma_{xx} \\ \sigma_{yy} \\ \sigma_{zz} \\ \tau_{yz} \\ \tau_{xz} \\ \tau_{xy} \end{bmatrix} \tag{3.22}$$

For doped silicon, the piezoresistive effect induced resistance change dominates the geometric contribution. Therefore, the relative resistance change in the longitudinal xx direction for cantilever deflection sensing can be directly computed with the stress as shown in Eq.(3.23). For ideal pure bending without torsion, we have $\sigma_{yy} = \sigma_{zz} = 0$.

$$\frac{\Delta R}{R} = \frac{\Delta\rho_{xx}}{\rho_0} = \pi_L\sigma_{xx} + \pi_T\sigma_{yy} + \pi_T\sigma_{zz} \tag{3.23}$$

Using embedded piezoresistors in a cantilever for deflection measurement was first realized in the 1990s for atomic resolution sensing [110, 111]. The piezoresistor is typically located at the base surface of the cantilever where the internal stress is maximized. Although a single piezoresistor is sufficient to measure the AFM cantilever probe deflection, modern designs use multiple piezoresistive elements for improved sensitivity and reduced thermal drift.

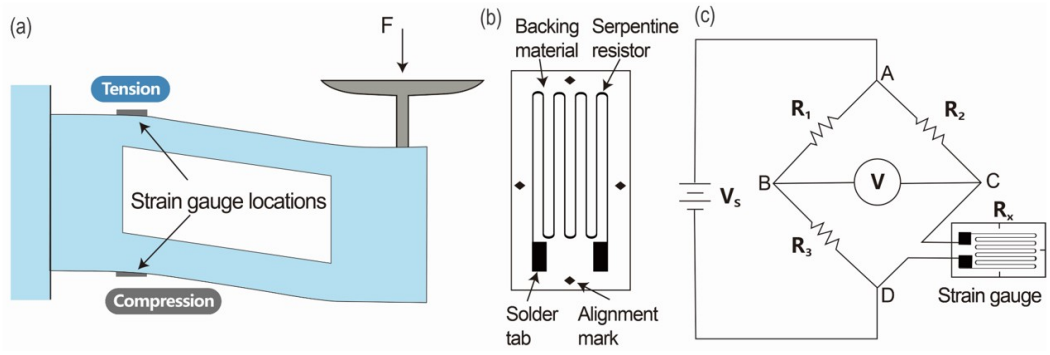

Figure 3-5: (Piezo)resistive strain gauge and Wheatstone bridge circuit: (a) structure with attached strain gauges where resistor value change can come from both geometric change or piezoresistive effect, (b) foil strain gauge structure, (c) quarter Wheatstone bridge configuration for measurement of single resistor value change R_x

To measure small percentage variations in the resistance, a Wheatstone bridge circuit is typically used as shown in Fig. 3-5. For a single resistor R_x, a quarter bridge configuration is used. The subscript x indicates the value of resistor R_x can change instead of being a constant. The bridge is configured to be balanced by choosing the resistors R_1, R_2, R_3 based on the unloaded piezoresistor resistance R_x such that $R_x = R_2R_3/R_1$. By applying Kirchoff's law, the voltage change ΔE_C at node C can be expressed by Eq.(3.24).

$$\Delta E_C = \left(\frac{-R_2 \Delta R_x}{(R_2 + R_x)(R_2 + R_x + \Delta R_x)} \right) V_s \tag{3.24}$$

Since the voltage at node B does not change, the bridge voltage E_{BC} can be obtained as in Eq.(3.25). Notice that the simplified result requires matching of the resistance as $R_x = R_2$ and $\Delta R_x << R_x$ so that the bridge voltage E_{BC} is proportional

to the percentage resistance change $\Delta R_x/R_x$ multiplied by the supplied voltage V_S.

$$E_{BC} = E_B - (E_C + \Delta E_C) = -\Delta E_C = -\left(\frac{-R_2 \Delta R_x}{(R_2 + R_x)(R_2 + R_x)}\right) V_s = \frac{\Delta R_x}{4R_x} V_s \quad (3.25)$$

The half bridge and full bridge can also be used in cases where two or four variable resistors need to be measured. In these configurations, the bridge are again balanced when the cantilever is unloaded.

Piezoelectric Sensing

The piezoelectric effect is the generation of charges in response to externally applied force. As discussed in Chapter 2, the converse piezoelectric effect are used for piezo actuators to generate mechanical force and motion. Similar to the piezoresistive effect, the non-isotropic phenomenon needs to be described with tensor matrices. Variables in the electrical domain include the electrical displacement D (coulomb per meter square), the electric field intensity E (volt per meter), and the absolute dielectric permittivity α (farad per meter) or impermittivity β (meter per farad). Variables in the mechanical domain include the normal stress σ (newton per meter squared), the shear stress τ (newton per meter squared), the strain ε (percentage) and the compliance S (meter squared per newton). Among the four variables defined in Chapter 2 Eq.(2.5), the piezoelectric constant d_{ij} with definition reproduced in Eq.(3.26) is the most important for sensing purpose. It can be physically interpreted as the ratio of the short circuit charge density (electric displacement) developed in the j-axis direction when mechanical stress is applied in the i-axis direction.

$$d_{ij} := \left(\frac{\partial D_i}{\partial \sigma_j}\right)^E \quad (3.26)$$

The overall linear model of the piezoelectric effect can be written in two forms as in Eq.(3.27). The subscript i, j, k and m indicates the directional component of the vector variable. The superscripts E and D indicate that the compliance values are evaluated with the values of E or D fixed. The full expanded matrix description of the piezoelectric effect is relatively complicated and beyond the scope of our discussion

here. More details on piezoelectric effect for transducer applications are available in reference [112].

$$\begin{cases} \varepsilon_i = S_{ij}^E \sigma_j + d_{mi} E_m \\ D_m = d_{mi} \sigma_i + \alpha_{ik}^\sigma E_k \end{cases} \qquad \begin{cases} \varepsilon_i = S_{ij}^D \sigma_j + g_{mi} D_m \\ E_i = g_{mi} \sigma_i + \beta_{ik}^\sigma D_k \end{cases} \tag{3.27}$$

In most applications, only selected directions of the piezoelectric effect are used. Moreover, certain level of nonlinearities also exist in the constitutive relation as modeled in Chapter 2. The piezoelectric effect can be used for embedded sensing of AFM cantilever probe deflection in dynamic operation modes. Measurement of static deflection can be challenging due to leakage current.

3.2.3 Micro/Nano Cantilever Actuation

For dynamic mode operations, the AFM cantilever resonance can be excited using several methods. Depending on the application, piezoacoustic, piezoelectric, thermomechanical, electromagnetic, and electrostatic methods can all be used. Some actuation methods are also capable of static cantilever deflection control, which can be helpful in certain applications. A brief overview of the actuation methods suitable for driving AFM cantilevers is provided in this section.

Piezoacoustic Actuation

Piezoacoustic actuation is the most widely adopted resonance excitation method for passive AFM cantilever probes. As shown in Fig. 3-6, a piezo actuator is embedded into the probe holder and electrically driven with a sine wave at the resonance frequency of the cantilever. The vibration propagates through the probe holder. The oscillation amplitude is amplified by the resonance gain of the cantilever. This method is relatively easy to implement and does not require specialized modification of the cantilever probe.

The effective mass m_{eff} of the cantilever in this case is different from the original mass m of the entire cantilever. This is because motion amplitude at the probe tip is much larger than that of the fixed end. By integrating over the entire cantilever for the kinetic energy, the effective mass can be derived as in Eq.(3.28).

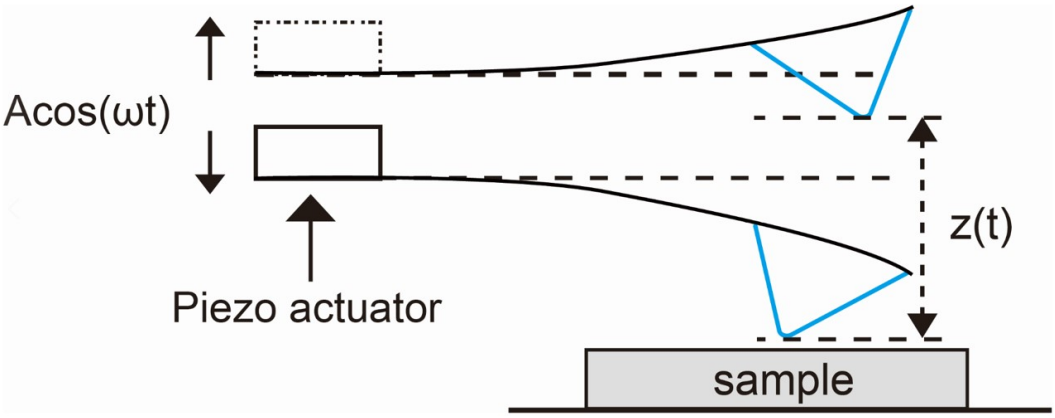

Figure 3-6: Cantilever probe piezoacoustic actuation illustration

$$\begin{aligned} E_k &= \frac{1}{2} m_{eff} \left(\frac{dZ(t,l)}{dt} \right)^2 = \int_0^l \frac{1}{2} \left(\frac{dZ(t,x)}{dt} \right)^2 \frac{m}{l} dx \\ &= \int_0^l \frac{1}{2} \left(\frac{d}{dt} \left[\frac{Z(l,t)}{2} \right] \left[3 \left(\frac{x}{l} \right)^2 - \left(\frac{x}{l} \right)^3 \right] \right)^2 \frac{m}{l} dx = \frac{33}{140} \frac{m}{2} \left(\frac{dZ(t,l)}{dt} \right)^2 \\ \Rightarrow \quad & m_{eff} = \frac{33}{140} m \end{aligned} \tag{3.28}$$

The piezoacoustic driving method has several limitations. First, it cannot control the static deflection of the cantilever. Second, this method can suffer from spurious structure resonance frequencies in the probe holder that might be excited. During the frequency sweep, these resonance can be confused with the cantilever resonance.

Piezoelectric Actuation

The converse piezoelectric effect can also be used to drive the cantilever as an embedded actuation method for active AFM probes. Instead of using an external piezo actuator, piezoelectric materials can be embedded into the cantilever with nano-fabrication. This resolves the spurious resonance issue of the piezo acoustic actuation. However, the fabrication of piezoelectric material together with the sharp tip can be challenging. Due to the presence of leakage current, static deflection control is also difficult to achieve.

Thermomechanical Actuation

The thermomechanical actuation methods make use of the different coefficients of thermal expansion. Specialized cantilever design with multiple layers of materials is needed to realize this actuation scheme. The temperature change can be achieved optically with focused laser beam or electrically with power dissipation in resistive elements. Optical thermal heating requires external optical components while electrical heating can be embedded into the cantilever. On the microscopic length scale, the heating and dissipation into the environment can be achieved at high speed suitable for resonance excitation with cantilever frequency over hundreds of kilohertz. Static deflection control can also be realized when the power input is equal to the heat dissipation. For a bimorph structure with two layers labeled as 1 and 2, the tip deflection $Z(l)$ is related to the coefficients of thermal expansion α, thickness h, elasticity E, cantilever length l, temperature T and original temperature T_0 typically at ambient room condition, as shown in Eq.(3.29). The derivation is based on mechanical stress balance at the boundary layer between the two materials [113, 114].

$$\begin{aligned} Z(l) &= 3 \underbrace{\frac{(\alpha_2-\alpha_1)(h_1+h_2)}{h_2^2\left[3\left((1+\frac{h_1}{h_2}\right)^2+\left(1+\frac{h_1E_1}{h_2E_2}\right)\left(\frac{h_1^2}{h_2^2}+\frac{h_2E_2}{h_1E_1}\right)\right]}}_{:=K}(T-T_0)l^2 \\ &= 3K(T-T_0)l^2 \end{aligned} \tag{3.29}$$

The thermomechanical actuation method does not suffer from the spurious structure resonance problem. It can also control the static deflection of the cantilever. The electrical based heating can be embedded into an active probe with nano-fabrication. However, it is limited in the operation temperature and requires modification of the cantilever structure with multiple materials.

Electromagnetic Actuation

The electromagnetic actuation utilize electromagnetic Lorentz force to drive the cantilever for both resonance excitation and static deflection control. The force can be generated by permanent magnets and coils. The current through the coil is changed to control the force. In one configuration, permanent magnetic material is attached

to the micro-cantilever probe and external coils are used [115]. As an alternative, a current loop is embedded into the probe with magnetic field generated by external permanent magnets [116]. The electromagnetic actuation does not suffer from the limitations of spurious resonance or temperature sensitivity. However, it is relatively complicated to implement with the need to control both current and magnetic fields. External components and modification to the cantilever are both needed to realize this actuation method. The operation with ferromagnetic samples is also limited.

Electrostatic Actuation

The electrostatic force is typically too weak for macroscopic applications. However, it can be useful for driving micro cantilevers [117, 118]. By using a conductive cantilever, the Coulomb force can be generated either through the sample or an extra electrode near the cantilever. A common mode voltage input can generate a repulsive force while differential voltage input can produce an attractive force. The advantages and limitations in this case is similar to the electromagnetic actuation.

AFM Cantilever Sensing/Actuation Summary

Each actuation and sensing method has its corresponding benefits and limitations. They can be mixed and matched for the best performance based on AFM application. Sensing and actuation principles that can be embedded into the cantilever are the enabling foundation for active cantilever probe development. A comprehensive comparison of the principles for their function (sensing or actuation), type of signal (DC or AC), transducer size (external bulk versus embedded), and main limitation are summarized in Table 3.1 for convenience.

3.2.4 Piezoresistive Thermomechanical Active Probe Design

In this thesis, an active cantilever probe design with a piezoresistive sensor and a bimorph thermomechanical actuator with electrical heating is used. As shown in Fig. 3-7, four piezoresistive elements are embedded at the fixed end for deflection sensing. In this design, p-doped silicon material forms the piezoresistive Wheatstone bridge at the base of the cantilever. The transverse and longitudinal piezoresistive coefficients are $71.8 \times 10^{-11}\ Pa^{-1}$ and $-66.3 \times 10^{-11}\ Pa^{-1}$, approximately equal in magnitude.

Physical principle	Function	Signal	Location	Main limitation
Optical beam deflection	Sensing	DC&AC	Bulk	Transparency
Astigmatic detection	Sensing	DC&AC	Bulk	Transparency
Interferometry	Sensing	DC&AC	Bulk	Transparency
Optomechanical	Sensing	DC&AC	Embedded	Transparency
Piezoresistive	Sensing	DC&AC	Embedded	Thermal noise
Piezoelectric	Both	AC only	Embedded	Charge leakage
Piezo-acoustic	Actuation	AC only	Bulk	Structure vibration
Optical thermal	Actuation	DC&AC	Bulk	Thermal sensitivity
Electrical thermal	Actuation	DC&AC	Embedded	Thermal sensitivity
Electromagnetic	Actuation	DC&AC	Bulk	Magnetic sample
Electrostatic	Actuation	DC&AC	Bulk	Sample capacitance

Table 3.1: Cantilever sensing and actuation principle comparison summary

A serpentine shape aluminum heating wire with optimized geometry is used to heat up the bimorph cantilever with silicon and silicon nitride materials for actuation.

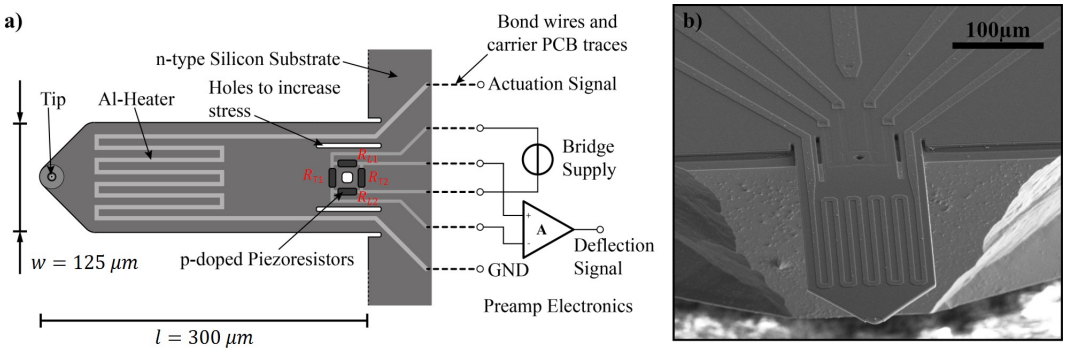

Figure 3-7: Active cantilever probe with piezoresistive sensing and thermomechanical bimorph actuation: (a) probe design with labels for functional groups and piezoresistor definitions in red, (b) SEM image of an assembled active probe

A full Wheatstone bridge configuration is similar to the bridge in Fig. 3-5 with the resistors replaced by the piezoresistors defined in Fig. 3-7. The bridge output voltage U_{out} is related to the supplied voltage U, averaged piezoresistive constant P_R, external force F and active cantilever with length l, width w, and thickness h, as shown in Eq.(3.30). The measurement accuracy is limited primarily by the Johnson noise in the resistor as in Eq.(3.31). In this equation, E is the effective elastic modulus of the cantilever, k_B is the Boltzman constant, R is the nominal resistance of each

piezoresistive element, and B is the measurement bandwidth.

$$U_{out} = -\frac{1}{4}\left(\frac{\Delta R_{L1}}{R_{L1}} - \frac{\Delta R_{T1}}{R_{T1}} + \frac{\Delta R_{L2}}{R_{L2}} - \frac{\Delta R_{T2}}{R_{T2}}\right) U = \frac{6 P_R l U}{w h^2} F \tag{3.30}$$

$$\Delta z_{noise} = \frac{4 l^2 \sqrt{4 k_B T R B}}{3 E P_R h U} \tag{3.31}$$

To excite the cantilever resonance, a sinusoidal waveform is applied to the resistive heating element. In this design, the heating power is proportional to the square of the voltage signal as shown in Eq.(3.32).

$$\begin{aligned} P_{heat} &= \frac{[V_{dc} + V_{ac}\sin(\Omega t)]^2}{R} \\ &= \frac{1}{R}\left[V_{dc}^2 + 2 V_{dc} V_{ac}\sin(\Omega t) + \frac{1}{2} V_{ac}^2 (1 - \cos(2\Omega t))\right] \end{aligned} \tag{3.32}$$

There are three components in the current induced heating power expression. They are the DC component, the original frequency component and the double frequency component. With the large gain amplification of the cantilever probe, the cantilever deflection attenuates the non-resonance frequency inputs significantly so that their presence in the input does not distort the oscillation significantly. In most tapping mode operation, the V_{dc} is set to zero and the frequency Ω is set to half the target cantilever resonance frequency. This avoids the presence of the harmonics at frequency Ω for good noise performance. The DC component can be added if static deflection control is needed. A full signal path diagram with governing equations of physical principles for tapping mode operation is shown in Fig. 3-8. Notice that the derivative of the Lennard-Jones potential is taken with respect to the distance r as a simplified model of tip-sample interaction force.

This particular active AFM probe design has several benefits as summarized below. These advantages have been used for the development of specialized AFM systems for both imaging and nano-fabrication with more details in reference [33].

1. The compact active probe design with embedded sensing and actuation removes

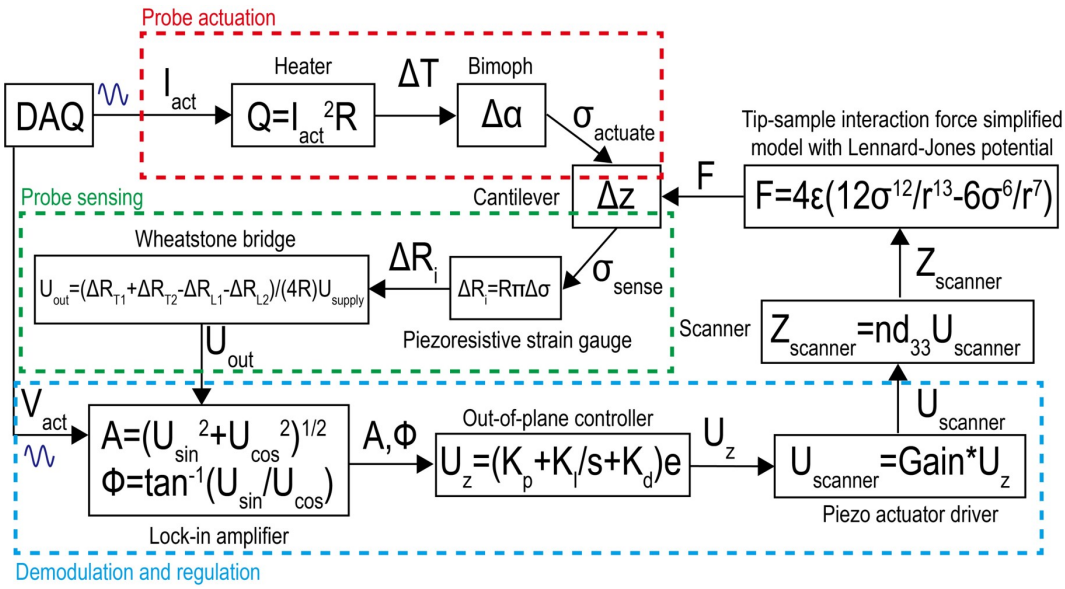

Figure 3-8: Signal path of the active cantilever for tapping mode AFM imaging with governing equations of the physical principles

the need of external bulky optical components. This allows an easier design for probe scan configuration and the AFM systems can be placed into applications with tight space constrains.

2. Without the use of external lasers, the transparent operation environment requirement is removed. The experiment setup overhead is also reduced since the laser-cantilever alignment process is no longer needed.

3. The electrical heating embedded themomechanical actuator avoids spurious structure resonance excitation and offers the ability to control static deflection of the cantilever.

This probe design also have several limitations. The themomechanical actuator is sensitive to temperature variation of the environment, which limits its application in heated or cryogenic environments. The probe fabrication process is also more complicated than passive cantilever probes.

In this work, we also used a semi-active self-sensing cantilever. This design has an embedded piezoresistive sensor and external piezoacoustic actuator. The probe is produced by SCL-Sensor.Tech., as shown in Fig. 3-9. This design has a smaller foot

print suitable for use in the probe scan AFM configuration in contact mode.

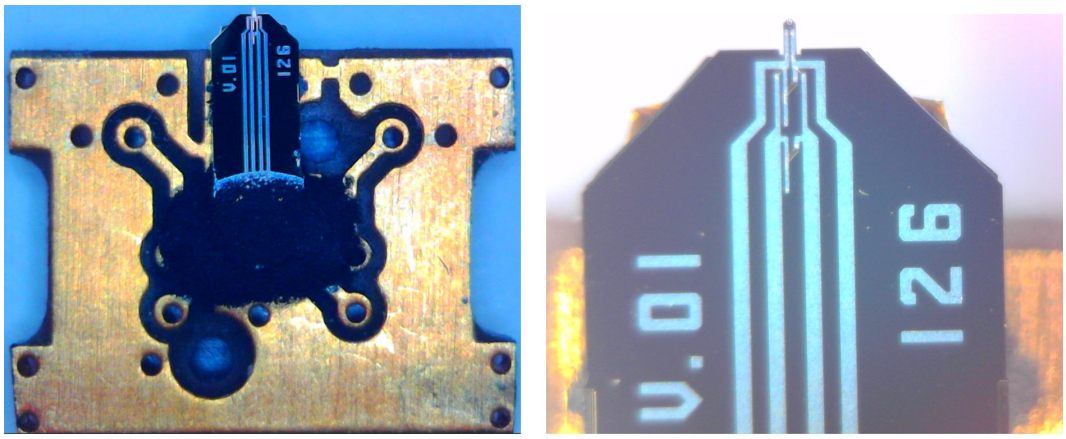

Figure 3-9: Optical microscope images of SCL-Sensor.Tech. piezoresistive self-sensing probe from (a) probe bounded to PCB, (b) zoomed-in view of the cantilever

The combination of piezoresistive sensing and electrical thermomechanical bimorph actuation is only one realization of an active AFM probe. Mix-and-match of the aforementioned principles allows a number of active probes to be realized. As an example, by attaching a sharp tip to a tuning fork with piezoelectric material, a self-sensing and self-actuated cantilever probe can be created for dynamic mode operation [119]. A nano-fabricated probe tip can also be added for larger oscillation amplitude as in the Akiyama probe design [120]. A nano-fabricated piezoelectric cantilever has been demonstrated recently [121, 24]. Moreover, the positioning system can also be embedded into the active cantilever to perform the scanning motion as demonstrated in references [122, 123, 124, 125, 126].

3.3 Active Probe Fabrication

The fabrication of active AFM cantilever probes are realized by a series of nano-fabrication steps for the creation of the micro-electromechanical system (MEMS) device. Since the presentation by Physics Professor Richard Feynman in 1959 titled "There's plenty of room at the bottom", nano-fabrication has developed significantly.

For batch processing, a top down approach is applied to the silicon wafer. A large number of features are produced simultaneously in this approach. The features are formed by repeatedly applying various processes including deposition, etching, patterning, surface modification and many other methods. During the processes, various elements are used including photons, electrons, ions, scanning probes, liquid phase chemicals, etc. As an alternative, the bottom up approach can also be applied by constructing structures from atoms and molecules. For example, the atomic force microscope have been used to manipulate individual atoms to produce structures on the substrate. The AFM probe can also be constructed by assembling or growing tips on the cantilever.

3.3.1 Cantilever Nano-fabrication

The fabrication of a passive AFM probe is relatively simple to achieve. The process plans for both the direct method and the indirect method are illustrated in this section based on references [127, 128].

Direct AFM Probe Fabrication

For silicon material, a direct fabrication is typically applied to achieve a better control of the tip sharpness. The direct fabrication process plan of a passive silicon cantilever probe is shown in Fig. 3-10 with each step listed below.

1. Starting with a silicon wafer (<100> orientation)
2. Thermal oxidation to produce SiO_2 on both sides of the silicon wafer
3. Photoresist spin coating on the bottom side
4. Photolithography UV light exposure via chromium/quartz mask
5. Development of exposed photoresist
6. Photoresist spin coating on top side
7. Photolithography UV light exposure via chromium/quartz mask
8. Development of exposed photoresist

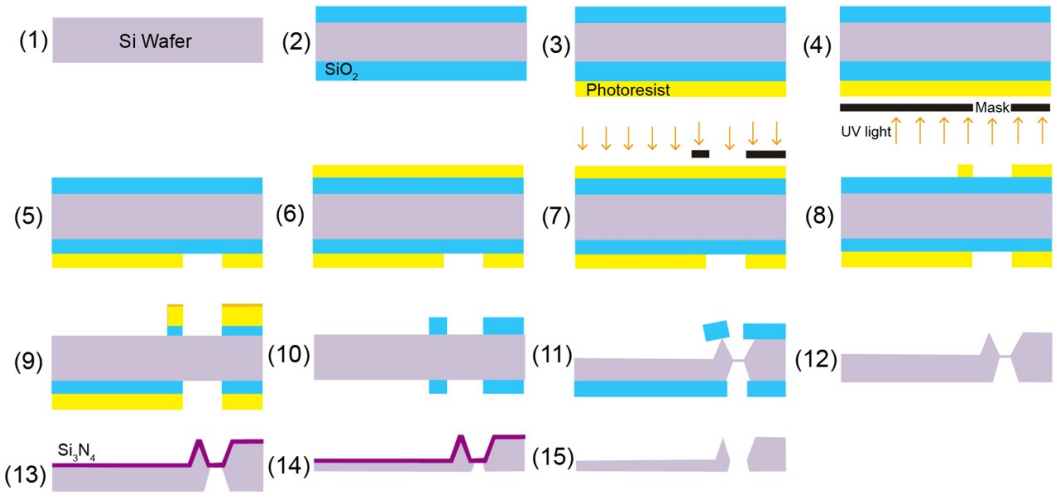

Figure 3-10: Example steps for direct fabrication of a simple passive silicon cantilever probe

9. Isotropic wet etching of SiO_2 with buffered HF
10. Photoresist removal with acetone/isopropanol
11. Anisotropic wet etching of silicon with KOH until tip area SiO_2 falls off
12. Isotropic wet etching of SiO_2 with buffered HF
13. Deposition of silicon nitride on top side for probe tip protection against etching
14. Anisotropic wet etching of silicon KOH with timing control for probe thickness
15. Isotropic wet etching of silicon nitride to release the cantilever

Indirect AFM Probe Fabrication

The indirect method forms a mold for the cantilever first. The desired materials are then deposited into the mold to form the probe. A better flexibility in material is achieved with this method with a less precise control of the tip sharpness. The direct fabrication process plan is shown in Fig. 3-11 with each step listed below.

1. Starting with a silicon wafer (<100> orientation)
2. Thermal oxidation to produce SiO_2 on both sides of silicon wafer
3. Photoresist spin coating on both sides
4. Photolithography UV light exposure via chromium/quartz mask

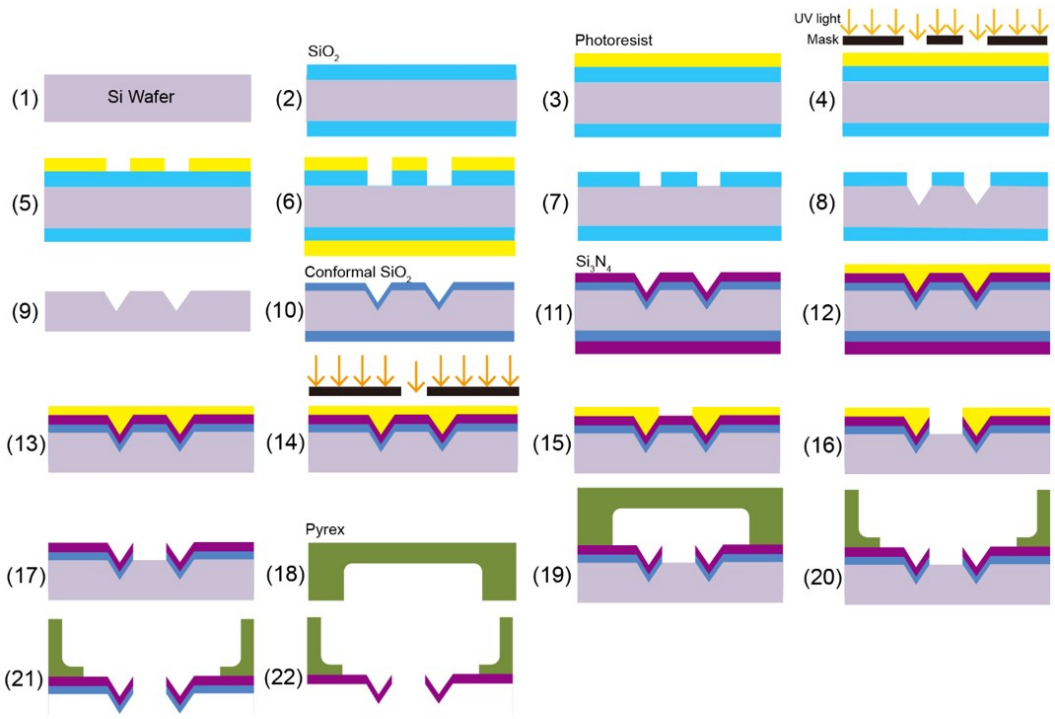

Figure 3-11: Example steps for indirect fabrication of a simple passive silicon cantilever probe

5. Development of exposed photoresist
6. Etching of SiO_2 with buffered HF
7. Photoresist removal with acetone/isopropanol
8. KOH wet directional etch of silicon to form probe tip mold cavity
9. SiO_2 removal by etching with buffered HF
10. Thermal oxidation to produce conformal SiO_2
11. Low-pressure chemical vapor deposition of low-stress silicon nitride
12. Protection photoresist spin coating on the top side
13. Removing both silicon oxide and nitride on the bottom side
14. Photolithography UV light exposure via chromium/quartz mask
15. Development of exposed photoresist
16. Dry etching to remove both silicon nitride and silicon dioxide

17. Photoresist removal with acetone/isopropanol
18. Dicing of Pyrex wafer to be used as a handle
19. Anodic bounding between silicon and a diced Pyrex wafer
20. Dicing for removal of unnecessary Pyrex
21. Silicon etching removal with KOH
22. SiO_2 etching removal with buffered HF

3.3.2 Active Probe Fabrication

The fabrication of the piezoresistive sensing thermomechanical actuation active probe is more complicated. Additional fabrication steps are needed to form the sensing and actuation elements. The process plan is illustrated in Fig. 3-12 and listed below based on references [129, 130].

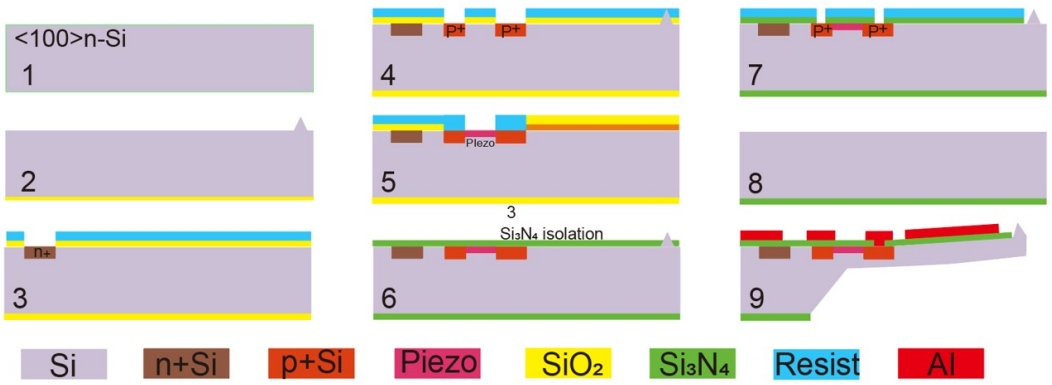

Figure 3-12: Simplified high-level steps for fabrication of active probe with embedded piezoresistive sensor and thermomechanical bimorph actuator

1. Begin with a silicon wafer (<100> orientation)
2. Wafer oxidation and AFM tip formation with anisotropic chemical etching with KOH with oxide mask or anisotropic plasma reactive ion etching with double photoresist silicon dioxide surface protection
3. High-level doping of phosphorous for electrical shielding and contact with wafer oxidation and photoresist coating for tip protection

4. High-level doping of boron for on-chip connections and contact areas
5. Boron implantation for piezoresistive deflection sensor with annealing activation of the implanted elements
6. Wafer passivation by plasma-enhanced chemical vapor deposited (PECVD) layer of SiN_x after photoresist and top layer SiO_2 removal
7. Photolithography and buffered HF etching to form contact to implanted structures with passivation removal around the tip area
8. Vapor deposition of aluminum and photolithography of aluminum structure for the thermal heater and the wiring interconnection
9. After anisotropic etching of silicon with KOH to form the cantilever membrane layer, reactive ion etching is used to form the cantilever beam and the base support chip with a thick layer of photoresist. The photoresist is stripped away using microwave plasma.

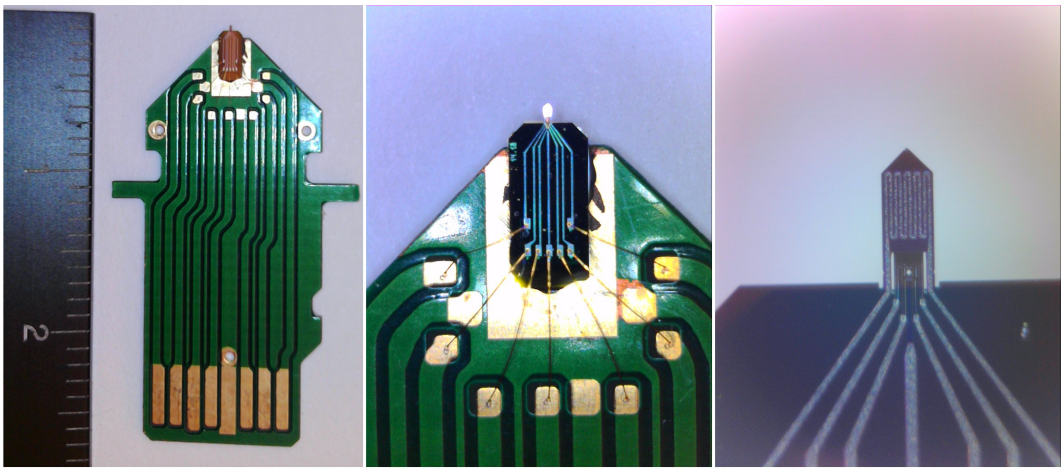

Figure 3-13: Optical microscope image of the fabricated active cantilever probe: (a) SD card shape PCB with ruler reference (label unit: cm), (b) lead wire bounding between the PCB and the PCB, (c) active cantilever with piezoresistive sensor at base, serpentine shape aluminum heater and electrical wiring

After being extracted from the silicon wafer, a bonding process is applied. The cantilever probe is attached to a printed circuit board with SD card shape for easy

manual handling. Electrical connections are also made with lead wire and optional protection epoxy. Multiple active cantilevers can also be produced on the same probe for parallel imaging. An optical microscope image of the fabricated cantilever probe is shown in Fig. 3-13.

The nano-fabrication process steps are primarily completed at Ilmenau University of Technology in Germany together with our collaborator. This process plan is used as the base for the fabrication of specialized active cantilever probes for opaque liquid imaging utilized in this work.

3.3.3 Probe Property Modification

For specialized applications, the AFM cantilever probe can be functionalized in a variety of ways. These primarily include probe tip geometry, tip material and cantilever property modification.

In most imaging applications, a sharper AFM probe tip is desired. The silicon AFM probe tip can be sharpened by repeated oxidation and etching. To image features such as deep trenches, a carbon nanotube can be attached or grown on the original AFM cantilever to obtain a high aspect ratio tip. A number of probe sharpening implementation examples can be found in references [131, 132, 133, 134, 135]. On the other hand, for nano-indentation applications where a round tip with known radius is desired, micro-beads can be attached to the probe tip.

The modification of probe tip material is needed in a number of applications especially for new imaging modalities. For example, a diamond material is desired for sharp AFM tips if repeated high force mechanical interactions between the probe and the sample is expected since diamond is rigid and chemically more stable than silicon [136]. In scattering type near field optical microscopy applications, silver, gold, tungsten or platinum materials are used for the probe tip to enhance the electromagnetic fields around the tip. To measure the electrical property of the sample, conductive material and a lead wire attached to the tip can be fabricated. If operated in liquid, insulation coating for the entire passive cantilever except the probe tip can be done with parylene [137].

A layer of gold coating is usually applied to the back of passive cantilever probes. This helps to increase its reflexibility for optical based deflection measurement. When operating in corrosive environments, protective coatings can be applied to the entire cantilever as will be discussed in more details later in this chapter.

3.4 AFM Probe Operation

The operation of AFM cantilever probes for dynamic mode imaging requires the knowledge of cantilever characteristics. During dynamic mode operation, the AFM cantilever is driven at or near its resonance frequency. The resonance frequencies need to be measured from system identification method. Moreover, the oscillation characteristic such as amplitude and phase need to be demodulated.

3.4.1 AFM Probe Calibration

The AFM cantilever probe needs to be calibrated before imaging in many cases just like the scanner. The deflection gain, frequency response and stiffness are the primary factors to be considered.

Deflection Gain

The deflection sensitivity gain SG characterizes the sensitivity of the cantilever tip motion measurement system. For conventional AFM systems, the alignment of laser and cantilever tip can change from one experiment to another. The voltage variation from the photodiode quadrants need to be calibrated to corresponds to the physical deflection of the cantilever in nanometers. This can be achieved by engaging the probe and a rigid sample and perform a ramp indent to bend the cantilever upwards. As the motion of the scanner is known, by fitting a curve to the voltage signal obtained by the cantilever sensing module, the deflection gain can be obtained. This step is not needed for topography imaging where the cantilever deflection is regulated to a constant but necessary in constant height mode. Knowing the gain can also be helpful to improve the image performance as will be discussed in Chapter 4.

Frequency Response

The frequency response of the cantilever is another important characteristic needed for dynamic modes. The response can be obtained with methods previously introduce in Chapter 2 for scanner system identification. The most common method used is the frequency sweep. Due to the relatively high quality factor Q of the AFM cantilever in air and vacuum, a slight driving frequency shift can result in a big change in the magnitude of the gain. Therefore, a coarse large range sweep is conducted first followed by a finer sweep to accurately locate resonance peak to be used as the driving frequency for tapping mode imaging. The amplitude and phase of the frequency sweep are obtained using oscillation characteristics demodulation techniques, which are discussed in the next section.

Stiffness

The AFM cantilever probe stiffness value k is needed for mechanical property investigation. With the calibrated sensing gain SG, the stiffness can be used to convert the deflection to the tip-sample interaction force. The stiffness can be specified by the vendor, computed from geometry, estimated from resonance frequency, measured using calibration elements or derived from thermal noise input.

The nominal stiffness value of the cantilever is usually provided by the vendor. The value can also be directly computed from cantilever geometry and material as in Eq.(3.8). However, due to dimension inaccuracy and process variation during nanofabrication, the actual stiffness can be significantly different from the specified or computed value. A calibration process can be applied to measure the stiffness value.

Another stiffness estimation method for rectangular AFM cantilevers is based on both measurement and geometric relations as proposed by Sader in [138]. The Sader method uses the measured cantilever resonance frequency in vacuum ω_v, length L, the rectangular cross section width w and thickness h, material density ρ to estimate the stiffness as in Eq.(3.33). The resonance frequency in ambient air can be estimated to be around 2% lower than in vacuum. This method is less sensitive to cantilever thickness inaccuracy and takes experiment measurement of the cantilever

characteristics into consideration for better stiffness estimation.

$$k = 0.2427\rho whL\omega_v^2 \tag{3.33}$$

The calibration can also be done using samples with known stiffness k_{sample} [139]. After deflection sensitivity calibration, the probe is pushed against the sample to record both the probe deflection ΔZ_{probe} and the scanner vertical movement $\Delta Z_{scanner}$. The stiffness of the probe can then be calculated by Eq.(3.34). This method is more accurate but can be more challenging to implement.

$$k = \frac{\Delta Z_{scanner} - \Delta Z_{probe}}{\Delta Z_{probe}} k_{sample} \tag{3.34}$$

The thermal noise based stiffness and damping tuning is the preferred method adopted in many commercial AFM designs. This method is accurate and does not require a calibration grating sample with known properties. To apply this method, several parameters need to be measured. First, the deflection measurement sensitivity gain SG can be obtained from calibration. Second, the thermal noise induced cantilever oscillation voltage power spectral density $S_v(\omega)$ is measured by applying Fourier transformation to the cantilever deflection thermal noise floor. In low frequency ranges, the frequency dependent $1/f$ pink noise from the instrument dominates and should therefore be avoided. Therefore, the spectrum magnitude value $S_{v,avg}$ is taken as the average of the relatively flat region after pink noise diminishes and before reaching the cantilever resonance (typically several kHz). Third, the quality factor Q and first natural frequency ω_n can either be extracted directly from $S_v(\omega)$ or using another frequency sweep. By using statistical mechanics and Parseval's theorem, the stiffness k and damping b can be derived as in Eq.(3.35) with the known Boltzmann constant k_B and temperature T. More details of the derivation can be found in [140].

$$\begin{cases} k = \frac{4k_BT}{Q\omega_n SG^2 S_{v,avg}} \\ b = \frac{4k_BT}{Q^2\omega_n^2 SG^2 S_{v,avg}} \end{cases} \tag{3.35}$$

The aforementioned calibrations assume good sensing linearity. Prior calibration of the rest AFM subsystems is also needed including the scanner, signal conditioning electronics, sensing elements (e.g. strain gauge), etc. For the AFM cantilever probe, there are also other calibration such as the probe tip sharpness. This is usually accomplished with specialized calibration samples.

3.4.2 Oscillation Characteristic Demodulation

Efficient demodulation of oscillation amplitude and phase is important for AFM operation. It is needed for performing the frequency sweep and dynamic mode imaging. In the case of frequency sweep, off-line data processing can be applied on data taken over a relatively long time to get an improved estimation. For dynamic mode operation, a moving window is applied to process the collected data in real time for motion control, which impose a higher requirement on the data acquisition.

Several aspects need to be considered for amplitude and phase demodulation. The bandwidth, latency, computational complexity and disturbance rejection are all important factors [141]. In general, the demodulation methods can be classified into three categories as non-synchronous methods, synchronous methods and closed-loop methods.

Non-synchronous Demodulation

Non-synchronous demodulation can be used for simple amplitude detection tasks. These algorithms assume only one sinusoidal waveform at a single frequency is present in the signal to be detected. To obtain the amplitude A of the time dependent cantilever deflection signal $z(t)$, a peak detection algorithm can be applied to extract the maximum value of the signal at a window close to or significantly larger than the period T of the target sine wave. Average of multiple peaks can be used to obtain a more accurate estimation. If the period T is known exactly, the root mean square of n periods can be used to estimate the amplitude as in Eq.(3.36). For implementation, discrete summation is used instead of continuous integration. The phase information

cannot be detected using these methods.

$$A = \sqrt{\frac{2}{nT}\int_{t}^{t+nT} z^2(t)dt} \tag{3.36}$$

Synchronous Demodulation

The synchronous demodulation methods are used for more complicated situations. They have very good off-frequency noise rejection capability. The algorithm can extract the amplitude A and phase ϕ information at specific frequencies ω even for mixed signals where multiple frequency components are present. The digital lock-in amplification multiplies the input signal $z(t)$ with an in-phase and a quadrature (shifted by $\pi/2$) waveform at the target frequency to get the products $z_{sin,raw}$ and $z_{cos,raw}$ as shown in Eq.(3.37).

$$\begin{cases} z_{sin,raw} = z(t)\sin(\omega t) = \frac{A(t)}{2}\left[\cos(\phi(t)) - \cos(2\omega t + \phi(t))\right] \\ z_{cos,raw} = z(t)\cos(\omega t) = \frac{A(t)}{2}\left[\sin(\phi(t)) + \sin(2\omega t + \phi(t))\right] \end{cases} \tag{3.37}$$

The double frequency 2ω component needs to be removed from the signal. The time dependent amplitude $A(t)$ varies with the sample topography. For AFM tapping mode imaging, the variation frequency is significantly slower than the cantilever natural frequency ω over tens of kHz to ensure good tracking. Therefore, a low pass filter with cutoff frequency between ω and 2ω can be applied to obtain z_{sin} and z_{cos}. A moving average filter can also be applied to cancel out the 2ω component and improve the noise rejection capability. If a moving average filter with length equal to integer multiple of the period corresponding to the 2ω frequency, a shorter integration time can be used for reduced latency. The amplitude and phase can then be extracted using Eq.(3.38).

$$\begin{cases} A(t) = 2\sqrt{z_{cos}^2 + z_{sin}^2} \\ \phi(t) = \arctan\left(\frac{z_{sin}}{z_{cos}}\right) \end{cases} \tag{3.38}$$

In addition to digital multiplication, an analog variable gain amplifier that switches between two gains with equal amplitude but opposite signs can be used. The gain is

switched at the frequency of the target sine wave to reject off-frequency signals. After applying a low pass filtered signal, the z_{sin} and z_{cos} can be obtained. More details of the implementation are available in Chapter 5.

Closed-loop Demodulation

A number of closed-loop demodulation methods are available. These include Kalman filter, Lyapunov filter and direct design closed-loop demodulator. These methods in general have better performance in terms of accuracy at the cost of increased computational overhead. They are often used in specialized applications with more details available in reference [142, 143].

In addition to amplitude and phase demodulation, the small frequency shift in the oscillation can also be used for AFM imaging regulation. In frequency modulated AFM, the slight frequency shift can be detected using a phase lock loop and regulated for imaging. More details on this topic can be found in references [144, 145].

3.5 Coated Active Probe for Harsh Opaque Liquid

The conventional passive probe deflection sensors and actuators have certain limitations. For the optical beam deflection system, the requirement of transparent optical path and need for manual probe-laser alignment. The piezoacoustic actuation can also be problematic during tapping mode for spurious resonance modes. The piezoresistive sensing thermomechanical actuation active probe resolves these issues. With proper coating for protection of the cantilever components, the new capability of harsh opaque liquid imaging can be enabled. This is one of the primary contributions enabled in this work based on the publication [26]. As the development motivations have been introduced in Chapter 1, we discuss the design and implementation of the active cantilever probe in this chapter.

3.5.1 Active Probe Coating

To protect the active cantilever, a specialized coating layer needs to be applied. The coating is used for both electric insulation and resistance to corrosive chemicals. The

coating should satisfy several requirements as discussed below to ensure that it does not compromise the functionality of any subsystem of the active probe.

1. Bond well to the surface material of the cantilever probe (silicon cantilever base, SiO_2 layer, heating metal, etc.)
2. Be thermally conductive with low thermal resistance to allow heat dissipation into the environment for thermomechanical actuation.
3. Form a thin uniform layer of coating without significantly affecting the mechanical properties of the probe (e.g., small additional mass, low residual stress, small increase of overall bending stiffness or damping, etc.).
4. Be chemically inactive for selected environments depending on the application (e.g. crude oil, whole blood, sulfuric acid, etc.).

Dip coating of the active probe is selected as the protective layer fabrication method. Dip coating is suitable to handle the delicate nature of the active cantilever probe and complication in redesigning the manufacturing process. It also allows us to try out different materials for coating easily. Different polymers have been investigated including M-Bond 610, 2K.-Epoxy, M-Bond 43B and photoresist polymers for photolithography. Most of these tested materials except "Positiv 20" suffer from poor bonding, thick coating layers, inability to withstand corrosive chemicals or failure to maintain a usable resonance peak for the probe.

Before coating, we used a viscous two-compound epoxy glue EPO-TEK H70E to protect the lead wires the PCB. The epoxy was cured at 100 °C for 2 hours. The probes were then coated using the photoresist "Positiv 20" manufactured by CRC Industries Europe NV. According to the datasheet, it is able to withstand strong etchants such as hydrofluoric acid (40%), nitric acid (65%) and iron(III) chloride. Furthermore, it has a suitable viscosity to cover a silicon microstructure like an AFM cantilever with a resist layer of only a few $\mu\ m$ thickness. We immersed the cantilever into the photoresist liquid to apply the coating. The coated cantilevers are then placed on a hot plate at 70 °C for 15 min in a dark environment to dry the resist. Next, we exposed the cantilevers to ultraviolet light for five minutes. Finally, we immersed the

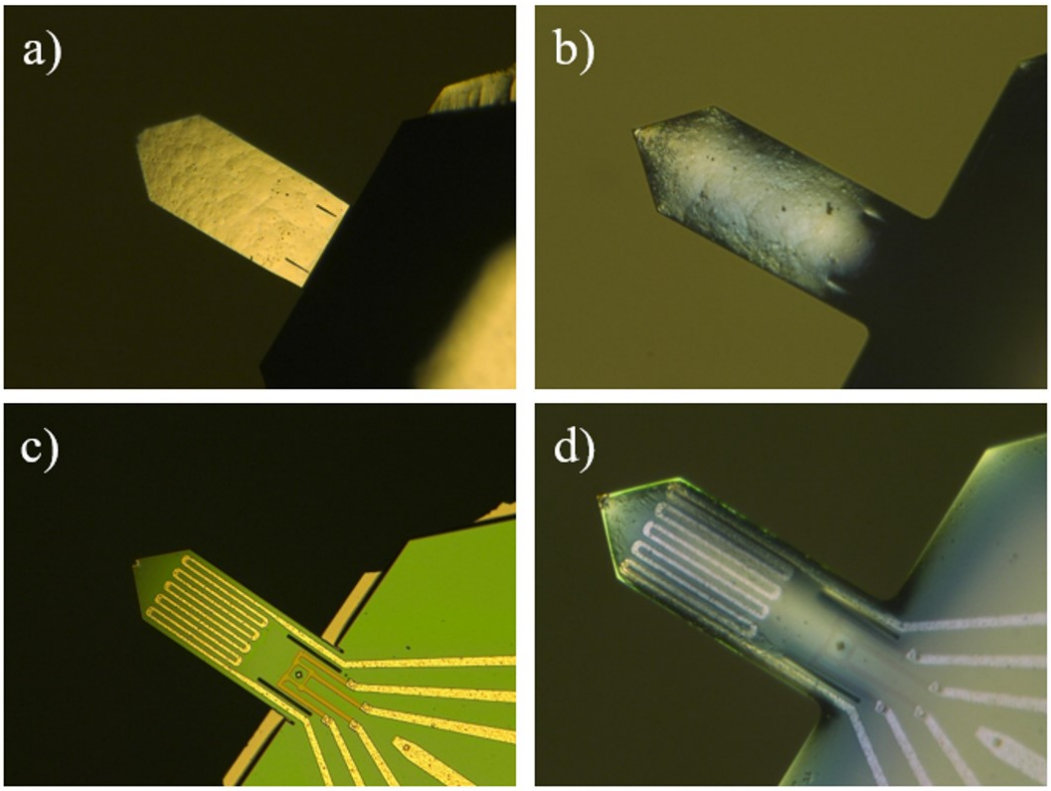

Figure 3-14: Optical microscope imaging of active probe (a) uncoated back surface, (b) coated back surface, (c) uncoated front surface with heating wires, (d) coated front surface with heating wires.

coated cantilevers into a sodium hydroxide solution (7 g/1 L) to develop the resist. Optical microscopy images as shown in Fig. 3-14 are used to preliminarily verify the success of the coating.

3.5.2 Coated Active Probe Characterization

To better understand the effect of coating, frequency response experiments were conducted. The results for the cantilever probes before and after coating are shown in Fig. 3-15.

After applying the coating, the overall mass of the probe increases. This should in principle reduce the resonance frequency of the probe. However, all probes after coating have an increase in their first mode resonance frequency. This indicates the coating increases the stiffness of the cantilever probes, which results in an overall in-

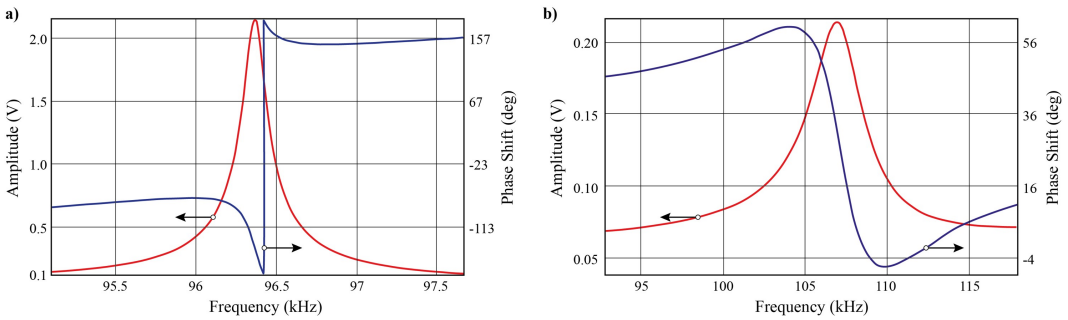

Figure 3-15: Frequency sweep results with amplitude (red), phase (blue) for one cantilever probe (a) before coating with resonance frequency at 96.365 kHz, (b) after coating with resonance frequency at 106.564 kHz. Notice that oscillation amplitudes in unit of volts are recorded instead of gains from the data acquisition system with the same driving signals applied during the sweep for comparison.

crease of resonance frequency. The oscillation amplitude of the probe also decreased to be almost an order of magnitude smaller than the original uncoated probe with identical driving signals. This can partly be attributed to the increase of probe stiffness or damping. Another possible reason is that the coating increases the thermal capacitance and resistance of the probe such that the temperature variation amplitude is decreased. This results in a smaller probe deflection that is measured from the frequency sweep. The decrease of oscillation gain amplitude can partly be compensated by increasing the driving signal but might result in a reduced operation lifetime of the probe due to extensive heating and increased internal stress.

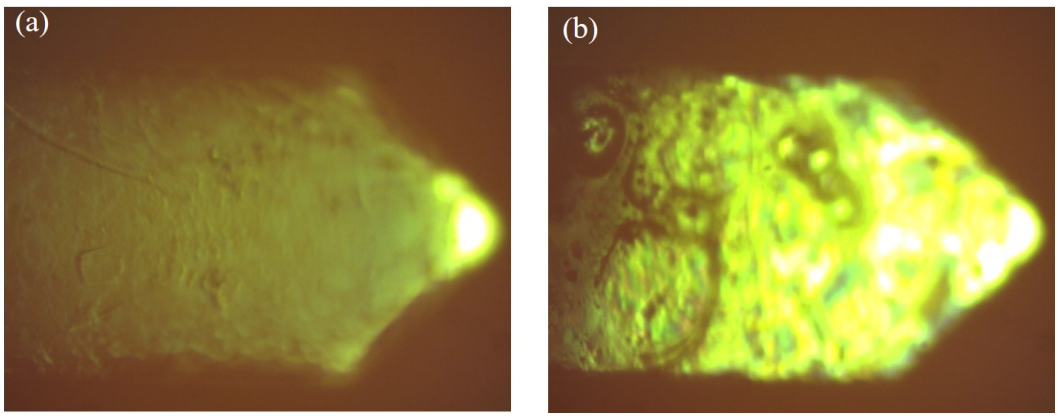

Figure 3-16: Microscope image of active probe: (a) before experiment, (b) after AFM imaging conducted in vinegar

The coating also creates an additional non-linear effect after extended time of

operation. From optical microscope observation of a coated active probe driven in air, visual changes of the coating can be observed as shown in Fig. 3-16. The phenomenon was potentially due to the repeated oscillation and thermal heating of the probe causing the coating to partially detach from the probe surface. Although the coating protection against liquid was still functional, the probe started to behave in a nonlinear manner. The resonance frequency started to depend on the driving amplitude and distortion could be observed in the probe oscillation waveform. This phenomenon is less than ideal as it increases the complexity of the imaging process where probe sweeping needs to be conducted for actuation at different amplitudes. Nevertheless, the imaging capability of the coated probe in harsh opaque liquid environment is enabled with this coating technique. Imaging results using the coated active AFM probe with the custom sample scan AFM system are demonstrated in Chapter 6.

While dip coating is the easiest method for investigating various materials, other techniques can also be applied if equipment are available. Vapor deposition techniques would be a potential coating method because it offers better uniformity, bonding and atomic level thickness control. However, the development of such coating requires augmentation of the nano-fabrication process. This will require significant investment of time and capital for development. Another promising potential method is to apply parylene coating, which allows control of coating thickness below one micron. Parylene coating can also resist harsh chemical environments and be applied after probe fabrication with current design.

3.6 Chapter Summary

In this chapter, the principles, fabrication, applications and operation of active cantilever probes are discussed in detail. Instead of using the conventional optical beam deflection sensing and piezo acoustic actuation, the use of piezoresistie sensing and thermomechanical bimorph actuation allows the development of an active cantilever probe, which helps to reduce the experiment overhead. With a specialized coated ac-

tive probe design, the capability of AFM operation in chemically harsh opaque liquid environments has been enabled. This is helpful to increase the versatility of AFMs. The second main contribution of the thesis work for coated active cantilever probe is addressed in this chapter. Example imaging in harsh opaque liquid operation will be further provided in Chapter 6.

Chapter 4

AFM Control System Design

4.1 Introduction

Control system design is important to ensure the integrity of AFM operation. This is especially true for high-speed imaging as the dynamics of the scanner can cause distortion in the motion commands. The probe or the sample can be damaged in a short time during high-speed scanning if not properly controlled. Moreover, the overall scanner dynamics can be affected by the variation of sample mass. Good controller designs compensate for the disturbance and nonlinearity in the scanner to increase the positioning accuracy. The overall performance of AFM imaging can benefit from smart control algorithms that take the image formation principle into consideration. In this chapter, the control techniques for both nano-positioners and AFM imaging improvement are discussed.

4.2 General Positioning Control Algorithms

Control algorithms can be helpful to improve the positioning accuracy. Both feedforward and feedback control can be applied to compensate for the positioning system nonlinearity. This section illustrates selected conventional methods for improving positioning accuracy in the in-plane direction.

4.2.1 Positioning Challenges

For in-plane motion control, there are several control problems to solve. The positioning inaccuracies primarily arise from the actuator nonlinearity, dynamic resonance, phase lag and system noise floor. As discussed in Chapter 2 for the piezoelectric actuators model, the hysteresis and creep nonlinearity can cause distortion in the scanning trajectory.

For high bandwidth input signals, the frequency dependent phase lag and gain variation can be observed in the Bode plot. This is more significant as the input command signal frequency approaches the first resonance frequency of the scanner. For signals with multiple frequency components such as a triangular wave, the higher harmonic components are heavily attenuated. If not compensated properly, artificial image artifacts will be generated.

The noise floor of the AFM system can be attributed to multiple sources. In the mechanical domain, the external vibration from the environment, motion coupling and thermal deformation are important aspects to consider. In the electrical domain, the noise floor of driver electronics (e.g. Johnson thermal noise), external electromagnetic waves, latency and discretization in the data acquisition system can all contribute to the noise. Significant efforts are placed on hardware design to improve the noise floor with vibration isolation, improved deflection sensor with lower noise [146], etc.

If not compensated, these positioning inaccuracies can result in artifacts in the collected image. For high performance imaging, adding sensors and/or controllers to the positioning system can significantly improve the positioning accuracy.

4.2.2 PID Feedback Control

By installing scanner displacement measurement sensors, feedback controllers can be designed. A straightforward and widely applicable feedback controller is the Proportional-Integral-Derivative (PID) controller. With frequency domain design technique, a PI controller in series with a lead compensator can be used as a varia-

tion of the PID controller to avoid amplification of high frequency noise components. transfer function of the PI controller in series with a lead compensater is given by Eq.(4.1).

$$u(t) = \left(K_p + \frac{K_I}{s}\right)\left(\frac{\alpha\tau_d s + 1}{\tau_d s + 1}\right) \tag{4.1}$$

In this expression, K_p is the proportional gain, K_I is the integral gain, τ_d is the lead compensator time constant to place the frequency and α adjust the amount of phase lead provided by the compensator. System identification techniques can be used to obtain the scanner frequency response as introduced in Chapter 2. Loop shaping design techniques can then be applied to tune the values of these parameters for good tracking performance.

Adding the feedback controller improves the positioning accuracy of the scanner in several aspects. First, the slow varying long term drifts from thermal expansion or creep nonlinearity in the piezo actuators can be completely eliminated by the integral controller. Second, the proportional gain helps to reduce the response time to a new reference input and reject external disturbance. Third, the phase provided by the lead compensator improves the transient response of the system. The feedback controller is sufficient in most cases for generic applications but does not handle non-linear effects such as the hysteresis in piezo actuators.

4.2.3 Feedforward Compensation

For precision mechatronic systems, feedforward control are widely used to improve the performance. An inversion of the system dynamic model obtained through the system identification process can be placed in the feedforward path. This would ideally yield a flat frequency response while in practice the gain and phase will always be limited by the physical system. For example, the digital control systems will have a reduced gain beyond the bandwidth and the delay in for sampling and processing will yield a frequency dependent variable phase lag. In cases where the scanning trajectories are known, a non-causal discrete system can be designed from the inverse of the a

non-minimum phase system.

For piezo hysteresis compensation, the discretized Preisach model can be inverted for feedforward control. An analytical inversion does not exist for the Preisach model. Therefore, numerical approximation methods are utilized such as the closest match algorithm. In this method, the initial state of the model is assumed to be known or manually swept to the minimum or maximum. Since the Preisach model is piecewise monotonic, the optimal input to the system is obtained by by gradually changing the input signal to the simulated model until the output reaches the reference command with minimal difference. With accurate identification of the model, this optimal input signal can be considered as an approximated numerical inversion of the Preisach model. Other inversion methods have also been investigated with more details in references [147, 148, 81].

For high-speed operation, the numerical inversion can be computationally too expensive to implement. Since a large number of weights are needed to accurately capture the model, the computational resources are usually not sufficient for high-bandwidth operation. For example, when scanning with a 10 kHz sine wave with 100 samples per cycle, the computation needs to be finished within 1 μs. The level of discretization of the Preisach model at 100 by 100 discrete levels would result in over $5,000$ weights to ensure good accuracy. After ignoring the insignificant terms, several hundreds of weights are still involved. Evaluating the model output once would require hundreds of summation through the activated hystron elements. With a typical FPGA clock rate at 40 MHz, only 40 addition operations can be completed with a single adder to satisfy the desired sample rate, which is insufficient. Using multiple adders simultaneously to add weights stored in the look-up table can be helpful to meet the time requirement at the cost of more FPGA fabric resources. For numerical model inversion with the closest match algorithm, the model output needs to be evaluated several times to obtain the result, which makes its implementation too complicated to fit on most FPGA systems.

To reduce the computational requirement, an analytical inversion would be preferred but usually does not exist. An analytical inversion does exist for the Prandtl-

Ishlinskii model. However, since this model assume symmetric hysteresis structure, it is not generally applicable with this constrain [149].

4.3 Scanner Control Algorithms

Feedforward numerical inversion compensation of hysteresis can be challenging to implement at high-bandwidth. Therefore, we need different strategies for AFM scanner control. If feedback sensors are available for the fast in-plane scanning axis, feedback control techniques can be applied. Feedback controllers have several advantages. These include model-free design without the need for system identification, good handling of external disturbance and higher robustness to system parameter change (e.g. varying sample mass), etc. Moreover, the periodic nature of the AFM scanning pattern can be utilized to improve tracking performance.

In this section, we discuss three main controllers investigated in this work. They are the iterative learning controller, repetitive controller and bandwidth based repetitive controller implementation for AFM in-plane scanning fast x-axis direction. The iterative learning controller and repetitive controller are generally applicable and used with the fast x axis of the multi-actuated music wire scanner modeled in Chapter 2. The bandwidth based repetitive controller is a specialized design for use with the multi-actuated stacked scanner originated from this work. These controllers all make use of the periodic scanning nature of the reference command. In cases sensors required by feedback controllers are difficult to install, hardware level charge control techniques can be used to handle the piezo hysteresis nonlinearity. More details on charge control are discussed in Chapter 5.

4.3.1 Iterative Learning Control

With periodic scanning commands, a standard iterative learning control technique can be utilized [150]. The error signal in the previous cycle is used to update the reference input to the system in the next cycle for improved tracking performance. The tracking performance is gradually improved after several cycles. The model of

the dual-actuated music wire scanner in-plane dynamics is used to study the iterative learning controller. The controller architecture and convergence of the learning performance is shown in Fig. 4-1. With iterative learning control applied, the tracking error decreases with each trail for the 10 kHz triangular wave tracking.

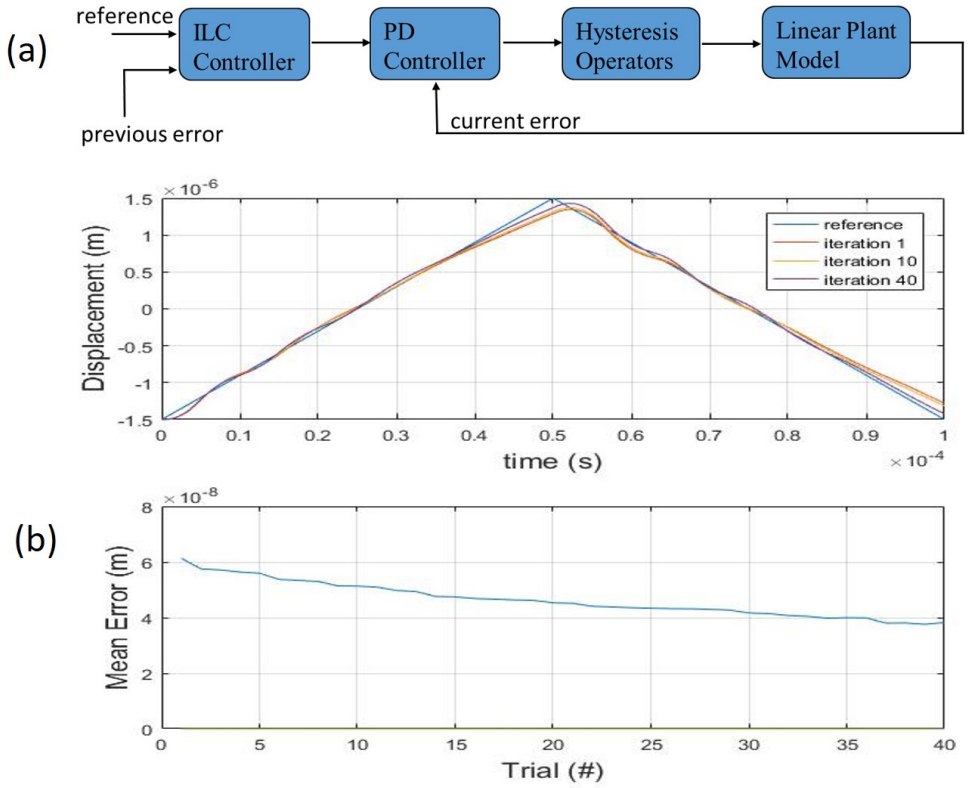

Figure 4-1: Iterative learning controller: (a) simplified architecture of an iterative learning controller with reference command update of the triangular waveform input, (b) convergence of tracking error signal over multiple iterations

Identical initial conditions are required for error convergence. This is the main limitation to apply iterative learning control for scanner control. Although the reference trajectory is usually periodic, the error in displacement and speed results in initial conditions if scanned continuously. This would violate the constrain of identical initial conditions for the iterative learning controller. To resolve this issue, the residual error after each cycle can be eliminated to ensure the requirement is satisfied. The convergence of the iterative learning controller is demonstrated in simulation in

Fig. 4-1. In practice, it is also possible to use another controller that can reset the system initial conditions between adjacent cycles. However, the process to ensure identical initial conditions would require extra loop time and increase the implementation complexity.

4.3.2 Repetitive Control

The repetitive controller is a more suitable algorithm for tracking periodic continuous reference inputs. It does not require the reset step to ensure identical initial conditions as the iterative learning controller. The repetitive controller is designed based on the internal model principle. The internal model principle indicates that a controller can eliminate the tracking error if its internal structure contains the periodic reference trajectory [151]. As an example, the integral controller can eliminate the steady state tracking error for a constant reference because the unilateral Laplace transform of a constant value is identical to that of the scaled integral control term.

A repetitive controller can significantly reduce the tracking error for periodic signals. For effective tracking, the highest frequency component of the periodic reference signal is required to be within the structure bandwidth. In previous research, repetitive controllers have been applied together with inverse model based feedforward for low bandwidth nano-positioning control for 25 Hz triangular waveform [152, 153].

For the dual-actuated scanner design, we use the repetitive controller for the tracking of a 10 kHz sine wave. As shown in Fig. 4-2, the Laplace transform of the cosine function with a gain K_r is placed in parallel with a proportional gain term. The frequency ω of the controller is set to be the same as the reference input sine wave to satisfy the internal model principle. A lead compensator is placed in series in the controller to gain some phase advantage for the system. The controller architecture and Bode plot of the loop transfer function (neglecting hysteresis) are shown in Fig. 4-2.

As discussed in Chapter 2, the sinusoidal raster scan is preferred for high-speed in-plane scanning. The repetitive controller is an ideal technique for sine wave tracking. The simulation tracking performance of the controller with piezo actuator hystere-

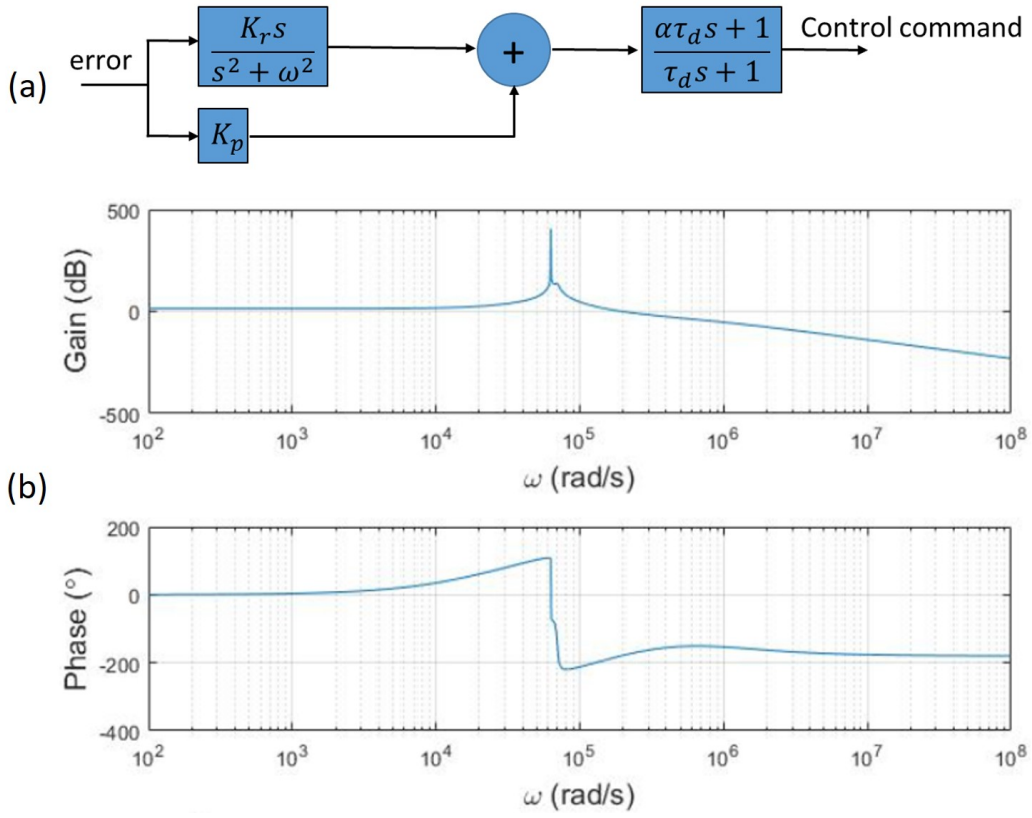

Figure 4-2: Repetitive controller: (a) controller architecture, (b) bode plot of the loop transfer function

sis and error signal are shown in Fig. 4-3(a). The repetitive controller effectively eliminated the tracking error for the cosine reference input at 10 kHz even with the presence of significant piezo actuator hysteresis. The controller can be implemented on high-speed FPGA systems easily when discretized using the bilinear transformation.

The experimental measurement results are shown in Fig. 4-3(b). The open loop gain is set to the value that would achieve 3 μm operation at 100 Hz, which yields a large error at 10 kHz. The repetitive controller compensated the large error of the open loop response. The slight time delay between the reference and measured trajectory is due to the sampling at 500 kHz being only 50 times than the 10 kHz cosine input waveform. The control loop rate is limited by the analog to digital converter sampling frequency and processing time required to compute the controller output. When we account for the sampling delay, the tracking error is less than 10 nm

as predicted in the simulation.

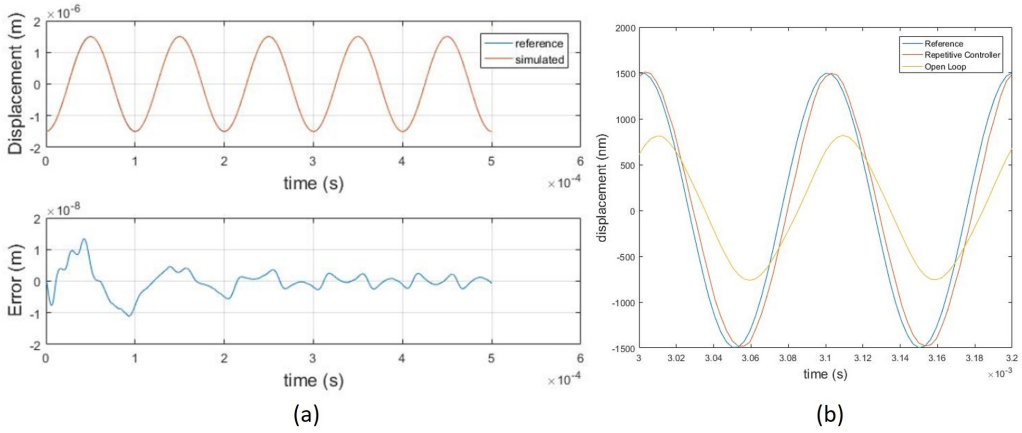

Figure 4-3: Repetitive controller sine wave tracking: (a) simulation of repetitive controller tracking result, (b) reference trajectory, repetitive controller and open loop experimental measurement results

4.3.3 Bandwidth-based Repetitive Control

The bandwidth-based repetitive controller is a specialized design for the the multi-layer stacked scanner. With the modeling and characterization discussed in Chapter 2, the stacked scanner has multiple inputs to control a single output. The system identification of the single output with respect to each individual input actuator demonstrated different bandwidths in the frequency response. For example, the bottom layer has the lowest bandwidth at around 22 kHz and the smallest range. However, the top layer has the largest bandwidth over 100 kHz and has the largest motion range as the mass and total flexure stiffness it carries is the smallest. For a single input scanner with lowest resonance at 22 kHz, it would be very difficult to track a 20 kHz triangular wave with the presence of higher harmonics. However, for the stacked scanner, we can track high frequency harmonics at a smaller range by only applying control inputs to the high-bandwidth actuators.

Considering the characteristic of the scanner, the controller assigns the effort to three groups of actuators differently. The frequency components of the Fourier series expansion below 100 kHz are captured. For triangular wave specifically, the bottom

$1-3$ actuators handle frequencies up to 20 kHz, the middle actuators $4-6$ handle both 20 kHz and 60 kHz input signals where as the top $7-10$ actuators handle all harmonics. With this approach, the dominating 20 kHz harmonics can cover the full range. The higher frequencies harmonics have reduced range but can be realized by actuators with faster dynamics. This is achieved by low-pass filtering the error signal at different frequencies corresponding to the grouped actuators. The processed signals are then passed into the controller for individual actuators correspondingly. As the amplitude of the third 60 kHz and fifth 100 kHz harmonics are 1/9 and 1/25 respectively, the dynamic range of the actuators are sufficient.

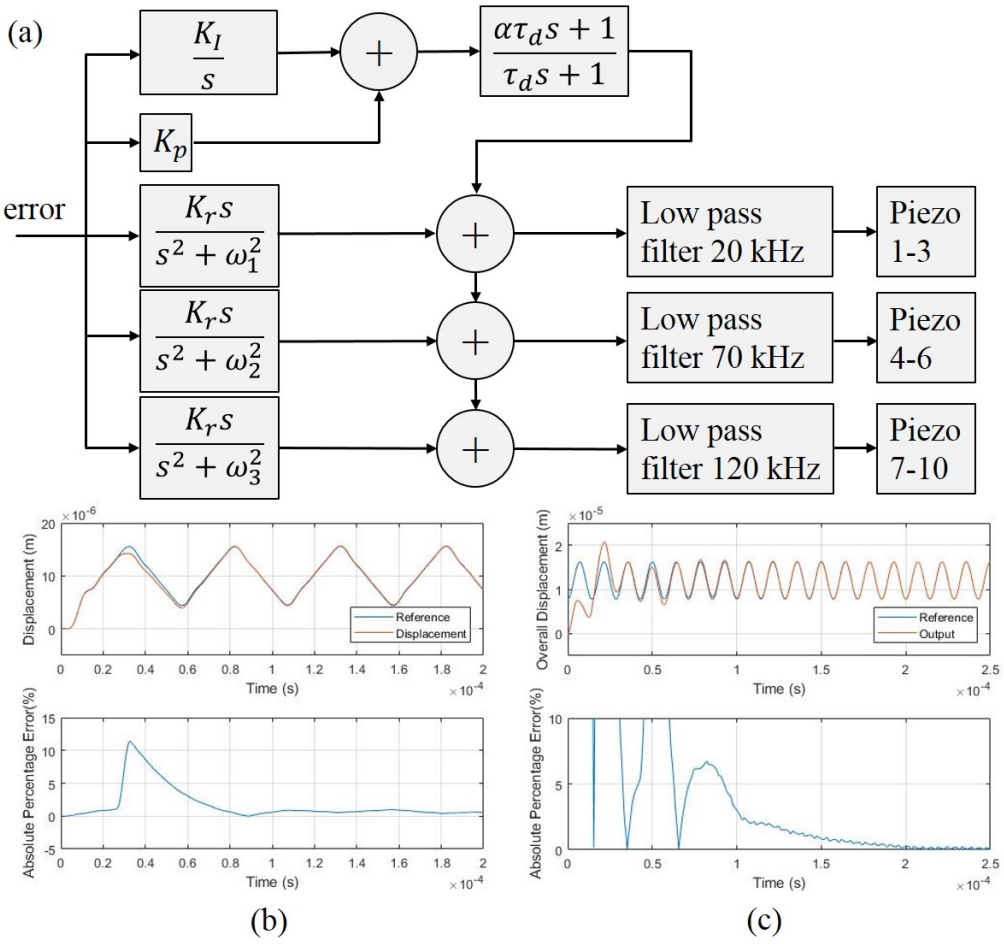

Figure 4-4: (a) Bandwidth based repetitive controller, (b) triangular wave tracking for the new controller, (c) sine wave tracking for the new controller

The bandwidth-based control effort allocation can be combined with the repetitive

controller design. For periodic signals that can be expanded using Fourier series, the harmonics can again be handled by the repetitive controller using the internal model principle. The bandwidth-based repetitive controller design combines the scanner characteristics with multiple repetitive controllers at different frequencies of the reference input.

Arranging the actuators in three groups reduces the implementation complexity. Instead of using 10 filters for all 10 layers in the stacked scanner, only three filters are needed. The architecture of the bandwidth based repetitive controller design for handling triangular wave primary harmonics and sinusoidal signals is shown in Fig. 4-4(a). Tracking performance for the first three harmonics of a 20 kHz triangular wave is shown in Fig. 4-4(b). The average percentage error is below 0.3% at a 12 μm range. The combined method produces very good tracking performance. With adjusted repetitive controller internal model frequencies, good tracking performance is also obtained for a 70 kHz sine wave. This is realized at a reduced scan range of 8.4 μm with steady state tracking error below 0.2%. The bandwidth based repetitive control method realized the full potential of the stacked scanner design for high-speed scanning applications.

We have also investigated other controllers for more generic scanning trajectories. If more generic scanning patterns are used, the disturbance observer controller can be used. In this design, the hysteresis nonlinearity is treated as external disturbance. When operating in the flat region of the bode plot, the plant can be inverted easily as a simple gain. The disturbance can then be observed by passing the measured output to the inverted plant model. The observed disturbance can then be subtracted from the plant to compensate for the nonlinearity. More details of the implementation are available in [102].

We have also investigated the performance of the Linear Quadratic Regulator (LQR) in simulation. Observers are designed to estimate the displacements of all layers of the multi-layer stacked scanner as modeled in Chapter 2. The tracking performance is poor for high bandwidth signals as it is almost impossible for the low bandwidth bottom actuator to track the desired reference. Moreover, the design is

relatively complicated as individual control of each actuator is needed. This would also require 10 channels of piezo actuator drivers. More discussion on the LQR controller and the bandwidth based repetitive controller can be found in reference publication [154].

4.3.4 In-plane Scanning Algorithm Summary

In this section, we summarize the main in-plane scanner control algorithms investigated in this work. The linear dynamics can usually be handled with conventional PID controllers. The creep nonlinearity can be rejected effectively with integral control. The hysteresis nonlinearity can be handled with feedforward methods using inversion of identified model. Model free feedback control can also be used to reject the nonlinearity as disturbance. Hardware level compensation with charge control circuit will be discussed in Chapter 5. For high-speed scanning, we investigated the iterative learning controller and the repetitive controller design. The repetitive controller is more suitable for the periodic signal of an AFM scanner. For the special design of the multi-layer stacked AFM scanner, the LQR and bandwidth-based repetitive controller are investigated with the later having an improved performance.

By applying these controllers to new scanner designs as discussed in Chapter 2, high-speed scanning performance can be improved. The various controller designs can be used as a library and selected for AFM design depending on the applications.

4.4 Overall AFM Imaging Model and Control

The operation of AFM systems requires significant user experience. The main experiment tasks include sample preparation, probe installation, controller tuning, etc. In this section, we discuss our attempt to automate the controller tuning process during AFM imaging. Image level performance improvement algorithms will also be covered.

To regulated the AFM cantilever deflection, a PID controller is usually used to control the out-of-plane positioner. The controller gains are adjusted manually to ensure good tracking performance. For novice AFM users without background knowledge

in control systems, the imaging parameter tuning is mostly a trial and error process. The operators try to minimize the difference between the trace and retrace lines by adjusting the imaging parameters. For more experienced users, empirical tuning rules are summarized and applied.

For low bandwidth scanning at several lines per second, manual controller tuning is possible. The dynamic behavior of the positioning system can be ignored. Even in this simple case, line by line adjustment of the controller gain can be difficult for novice users. Improper tuning of the controller can not only result in distorted images. Moreover, an improper controller gain can increase the risk of sample or probe damage.

Manual tuning can be especially challenging for high-speed scanning. When pushing the scanning speed limit, the scanner dynamics can be excited. More importantly, an improperly tuned controller can damage things in a very short time. As an example, we once conducted high-speed imaging over a calibration grating with 500 nm depth trenches. With a 6 μm by 6 μm scanning area at 500 lines per second in contact mode, we tried to manually adjust the PID controller parameters. In one case where the proportional gain is adjusted to a small value, the topography image disappeared within 3 seconds. After looking into the captured data, we notice that the image disappeared gradually as the cantilever probe tip becomes blunt when scratching through the sample surface.

To resolve these problems, it would be helpful to automate the process to reduce the operation overhead. A comprehensive AFM simulation environment is created in this work to evaluate the controller automation process. We also investigated several new imaging performance improvement algorithms. The model can also be used to train novice AFM users for imaging parameter tuning without the risk of instrument damage.

It is possible to tune the AFM PID controller gain offline. Previous research has demonstrated a semi-automated method for parameter adjustment [155]. If a raster scan pattern is utilized, an iterative learning controller was trained in previous research by scanning over the first line until convergence [156]. These methods are

designed for offline tuning and cannot adapt to sample property variations during imaging.

4.4.1 Simplified Vertical Dynamics Model

The model developed in this thesis aims to capture the essential dynamics for contact mode AFM operation. A simplified lumped parameter model is used to approximate the true dynamics. Since the in-plane scanning models are introduced in Chapter 2, we focus our discussion on the out-of-plane dynamics modeling in this section.

The AFM system out-of-plane Z axis dynamics is mainly composed of three components. The key components to model are the cantilever probe, the sample and the scanner. An illustration of the lumped parameter model is shown in Fig. 4-5(a). In the figure, m_c, b_c and k_c are the cantilever probe mass, damping and stiffness coefficients. Similarly, the subscripts s and p represents the sample and the piezo scanner with (t) indicates time dependency. $F_{cs}(t)$ is the cantilever-sample interaction force, $F_s(t)$ is the disturbance force from sample variation, and $F_p(t)$ is the piezo actuator force input. $z_c(t)$ is the probe deflection. In this model, we assume the probe deflection sensor has good linearity and sufficient bandwidth.

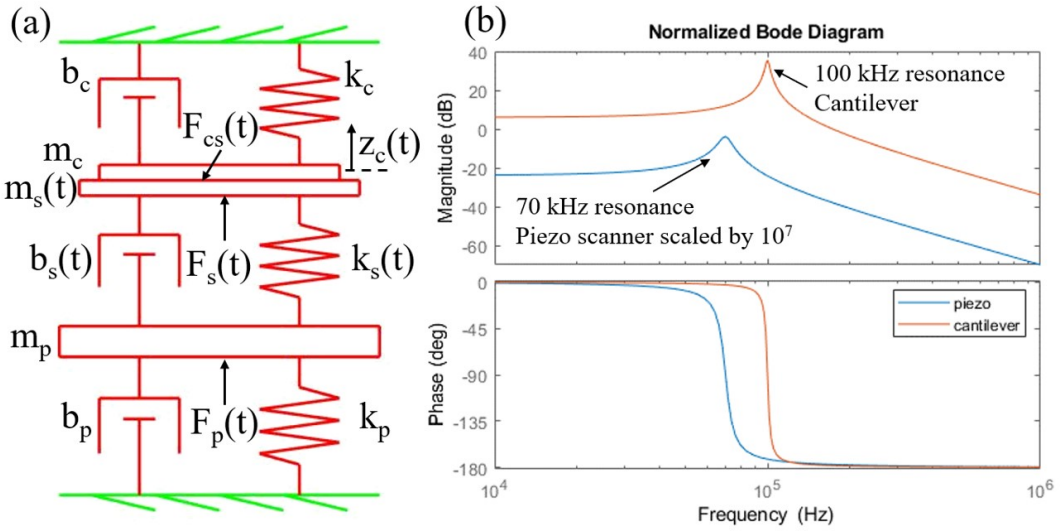

Figure 4-5: (a) Lumped parameter models of the AFM out-of-plane dynamics (b) Simulated displacement output versus force input frequency response of the scanner (scaled by 10^7) and probe model

For the cantilever probe, a second-order mass-spring-damper model is sufficient to capture the first resonance mode. More complex models for higher frequency resonance might be needed for other modes of operation [52, 12]. For the scanner, a mass-spring-damper system with dynamics matching a flexure based scanner using PL033.31 piezo actuator from PI is utilized. The frequency responses of both the cantilever probe and scanner are shown in Fig. 4-5(b). We notice that the cantilever dynamics is faster than the scanner dynamics such that the control loop bandwidth for probe deflection regulation is limited either by the sample or by the scanner. In addition, the piezo hysteresis nonlinearity in the out-of-plane direction is neglected as it can be compensated electrically with charge control based methods [157] with more details in Chapter 5.

The full dynamics of the AFM probe and sample interaction is very complicated. Various microscopic forces and probe tip geometry needs to be considered. The classical model of Lennard-Jones potential can be used as a simplified approximation for attractive and repulsive force modeling. More microscopic forces such as capillary forces, Van der Waals forces, or even covalent bond forces can all be involved in forming the overall force sensed by the AFM cantilever probe.

The tip geometry of the AFM probe also plays an essential role during nano-mechanical property measurements. From the basic Hertzian model to more complicated Johnson-Kendall-Roberts (JKR) and Derjaguin-Müller-Toporov (DMT) models, AFM contact mechanics can be modeled at different levels of complexity. However, even the simplest model has several parameters that are necessary to know but difficult to measure or control.

For efficient simulation of the system dynamics, the sample model is simplified as a mass-spring-damper system. The lumped parameter sample model have proven to be effective in capturing the dominant dynamics as the simulation results match well with the experiment observation for jumping mode AFM in previous research [154]. For contact mode operation with sufficiently large setpoint, the probe and the sample remain in contact and share an added mass.

More complicated models are also available for atomic resolution or tapping mode

simulation. For steady state simulation with atomic resolution, the Hertzian model with estimated parameters and restricted spheres geometry has been utilized for atomic resolution simulation [158]. With superposition, adhesion and repulsive forces from the DMT model have been used for intermittent-contact mode AFM dynamics simulation [159]. On the other hand, for dynamic simulation with lower resolution requirement, approximated models are utilized. For example, in tapping mode operation, asymptotic AFM models [160, 161] have recently been proposed as an approximated model with analytical nonlinear first order derivative of amplitude and phase shift available for simulation.

For the in-plane scanning model, a map with pixel resolution is generated first to represent the true sample topography. Bi-linear interpolation based on the scanner position is utilized. Maps for added sample mass, stiffness, and damping variation of the sample is also created for varying sample material properties. The dynamic model of the dual-actuated scanner as introduced previously is used for the in-plane dynamics together with the repetitive controller.

The overall model is created in Matlab Simulink software. It is used to evaluate the performance of the proposed control algorithms.

4.4.2 Automatic Controller Tuning

The PID controller is conventionally used as a generic control approach for AFM systems. As PID controllers are generically applicable, hundreds of methods have been developed for tuning the parameters for systems with different dynamics. For AFM operation, we propose an automatic tuning procedure for controller parameter and scanning speed adjustment for AFM imaging.

Automatic PID Parameter Tuning Model-free tuning methods that do not rely on system identification are preferred. This is because the probe-sample interaction is very difficult to model exactly. Most AFM models are simplified approximations of the complex true dynamics of the AFM system. Moreover, the properties of the sample can change during imaging. The ZieglerNichols (Z-N) tuning method is a suitable choice for this application with its good disturbance rejection property. The

response to setpoint changes of this method is relatively weak. However, this is not critical with the typically constant deflection setpoint in AFM imaging.

For the controller shown in Eq.(4.2), the Z-N tuning rule of a classic PID controller is shown in Eq.(4.3).

$$u(t) = K_p e(t) + K_i \int_0^t e(\tau)d\tau + K_d \frac{d}{dt} e(t) \tag{4.2}$$

$$K_p = 0.6K_u,\ K_i = 1.2K_u/T_u,\ K_d = 3K_u T_u/40 \tag{4.3}$$

where $u(t)$ is the control effort, $e(t)$ is the error, K_p, K_i and K_d are the proportional, integral and derivative gains respectively, K_u is the ultimate gain when the system becomes marginally unstable and start to oscillate as the proportional gain K_p gradually increases, and T_u is the oscillation period. After determining K_u and T_u, the PID controller parameters can be set based on the rule in Eq.(4.3). If certain aspects of the tracking performances are more important, other empirical parameter setting rules can be used.

To automatically tune the PID controller, the values K_u and T_u need to be determined without risking unstable oscillation. The relay auto-tuning method is selected [162] for this task. Instead of gradually increasing the proportional gain, a relay is used in place of the PID controller as shown in Fig. 4-6(a). The relay switches between two values with equal magnitude d, which limits the controller output to d instead of the scanner ranges. Therefore, regardless of the error signal magnitude, the amplitude is constrained to avoid large amplitude oscillation. As shown in Fig. 4-6(b), with the relay, a sinusoidal steady oscillation $e(t) = A\sin(\omega t + \phi)$ can be observed in the error signal. Based on the describing function analysis, the ultimate gain K_u and period T_u can be calculated as in Eq.(4.4).

$$K_u = \frac{4d}{\pi A}, \quad T_u = \frac{1}{2\pi\omega} \tag{4.4}$$

At this point, automatically determining K_u and T_u can be realized. To do so, we need to obtain the amplitude A and the frequency ω of the sine wave from the error function $e(t)$. The period T_u and corresponding frequency ω can first be estimated

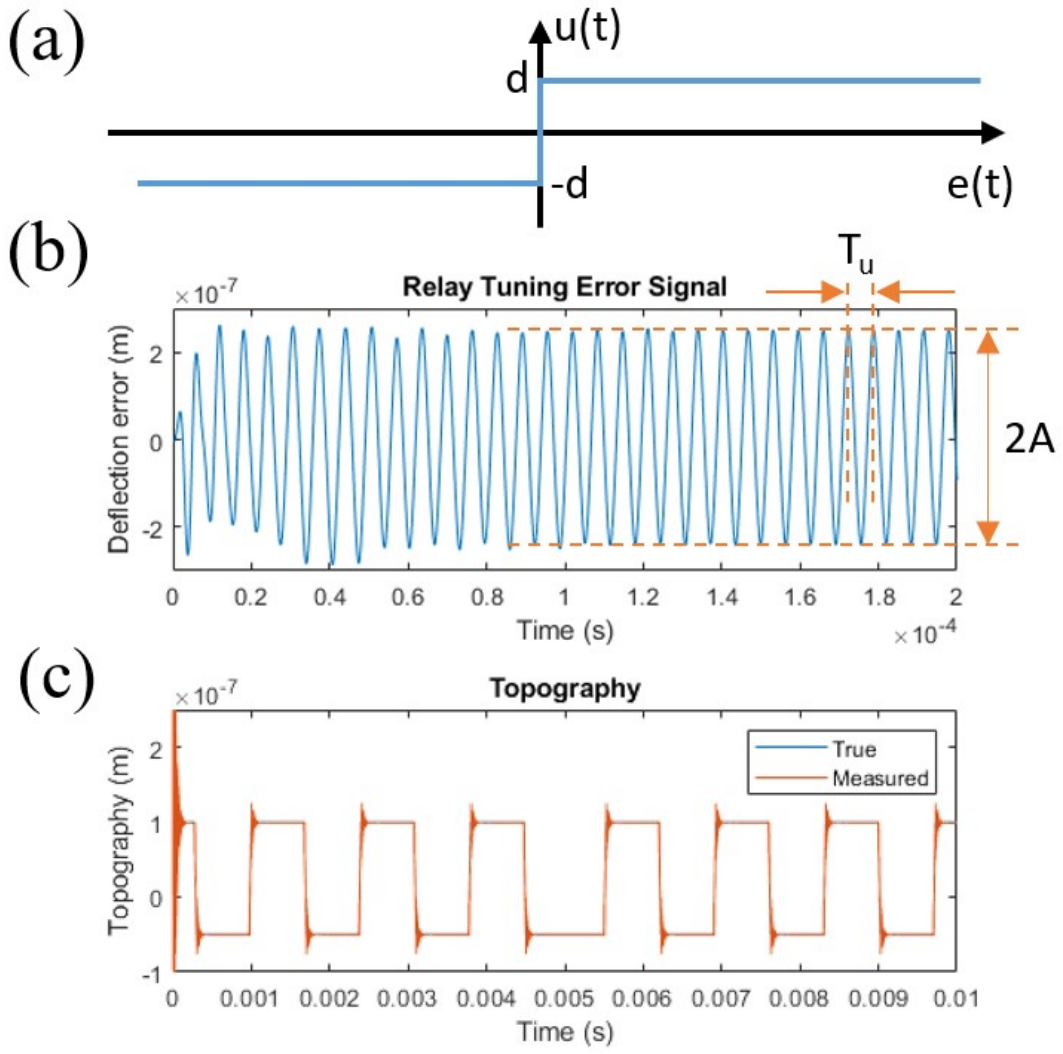

Figure 4-6: (a) Relay with magnitude d (b) Relay tuning error signal with amplitude A and period T_u (c) Simulated tracking of step topography

by extracting the second maximum peak in the auto-correlation function of the error $e(t)$ or the relay control effort $u(t)$. After getting this initial estimate, multiple time difference between local maximum values can be averaged to determine T_u and ω more accurately. Accurately determine the oscillation frequency is important to extract the oscillation amplitude automatically.

To extract the amplitude A, the formula of a digital lock-in amplifier can be used with the known ω as shown in Eq.(4.5). By integrating over multiple periods of

oscillation, the accuracy of the amplitude can also be improved.

$$\begin{cases} A_{sin} = \frac{1}{T}\int_0^T e(\tau)\sin(\omega\tau)d\tau \\ A_{cos} = \frac{1}{T}\int_0^T e(\tau)\cos(\omega\tau)d\tau \\ A = \sqrt{A_{sin}^2 + A_{cos}^2} \end{cases} \tag{4.5}$$

where T is the sampling period, A_{sin} and A_{cos} are the averaged sine and cosine components during the lock-in process to compute the amplitude. The integration can be replaced by summation for discrete sampling. The relay based Z-N rule of automatic PID tuning procedure is summarized below.

1. Engage the AFM probe and disable in-plane scanning.
2. Set relay amplitude d to max allowed probe deflection.
3. Deactivate PID and activate relay unit as the controller.
4. Record $e(t)$ oscillation data over multiple periods.
5. Extract frequency from $e(t)$ with auto-correlation.
6. Extract amplitude with lock-in amplification principle.
7. Compute K_u, T_u and derive K_p, K_i, K_d.

The simulated tracking performance of step topography variation is shown in Fig. 4-6(c). The PID controller is tuned automatically with the aforementioned procedure. The controller provides good tracking with a slight overshoot. Other formula for parameter estimation from K_u and T_u can be used to reduce overshoot with slower response time. Parameter retuning can also be implemented when the line error exceeds user specified threshold.

Automatic Scanning Speed Tuning

A suitable in-plane scanning speed is important to ensure good out-of-plane tracking performance. A slow scanning speed produces good tracking performance but reduces the imaging throughput. A fast scanning speed increases imaging throughput but risk the excitation of the scanner resonance. In this work, we kept the maximum in-plane scanning frequency below the scanner bandwidth. The scanning speed can be automatically adjusted to achieve good topography tracking.

A suitable scanning speed can be initialized after automatically tuning the PID parameters. The root mean square (RMS) roughness $R_q = \sqrt{\frac{1}{n}\sum_{i=0}^{n} z_{topo}^2(i)}$ for the measured topography z_{topo} of the first scan line imaged can be obtained at a relatively low speed first. An initial estimate scanning speed can be obtained empirically based on experience. In the expression, n is the x pixel resolution.

During imaging, the tracking error can be used to adjust the imaging speed. The RMS tracking error signal between the reference and measured cantilever deflection of a scan line is defined as $e_{RMS} = \sqrt{\frac{1}{n}\sum_{i=0}^{n} e^2(i)}$. The scanning speed can be adjusted to be as fast as possible while maintaining e_{RMS} to be smaller than the user defined error threshold. The speed adjustment is updated between each scan line.

Adaptive inline update of the scanning speed is also possible. For samples with partial rough surfaces and partial smooth surfaces, the scanning speed can be allocated more effectively by adjusting the speed in-line (scan slower for larger R_q and faster for smaller R_q). This can be achieved by applying a moving average window to the RMS value for the error and the roughness signals using a smaller window [163].

4.4.3 Image Level Improvement

In this section, we discuss three methods to improve AFM topography tracking and image generation. These methods can be used in conjunction with the automatic PID tuning procedure for AFM imaging performance improvement.

Location Based Sampling

Sinusoidal waveform is preferred for high bandwidth scanning to avoid excitation of scanner dynamics. In a conventional AFM, the data acquisition system uses a constant sampling rate for control and the recorded values are down-sampled to form the images. For trajectories with varying scanning speed magnitude, this would cause the sampled points to spread unevenly in the image as shown in Fig. 4-7. Therefore, a equal space sampling method is needed. Instead of a fixed decimation rate of the collected data, the image pixel points are sampled when the in-plane scanner reference reached each sample location in the look up table. To enable location based sampling, an in-plane scanner location tracking module is designed with a lookup table.

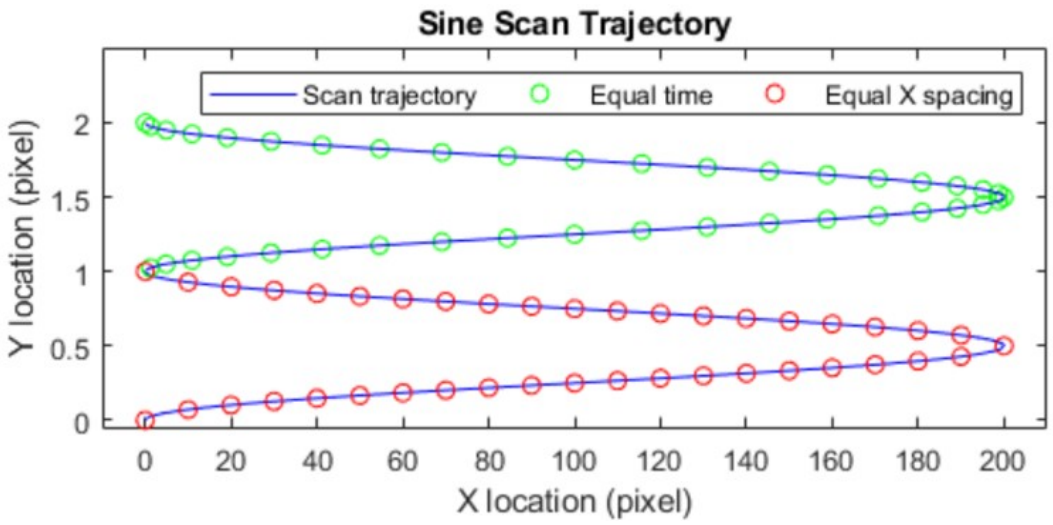

Figure 4-7: Scan trajectory uses sine wave in fast scanning X direction and constant speed in Y. Equal X spacing sampling yields more uniformly distributed pixels than equal time (Y spacing) sampling.

Topography Feedforward

With raster scanning patterns, the topography variation between adjacent lines is usually small. To reduce the tracking error, it is helpful to use the collected data points from the previous line as a feedforward signal. When scanning from different directions, the controller response can be different. Therefore, the trace and retrace lines should be used separately for feedforward. With discrete sampling of topography pixels, the bi-linear interpolation method is used again with the estimated upcoming topography extrapolated. The topography from the previous line scan serves as an anticipated disturbance similar to that from disturbance observer controller. The feedforward method also does not require a reverse plant model, which is difficult to obtain for AFM systems. The tracking performance improvement are evaluated in simulation as shown in Fig. 4-8. The sample has a sinusoidal topography variation with constant material property. The tracking error decreases significantly after the feedforward controller is turned on from the third line scan. The initial transient error peak diminishes after several line scans. Compared to iterative learning controllers [164], this method is significantly easier to implement and does not require system identification for controller design.

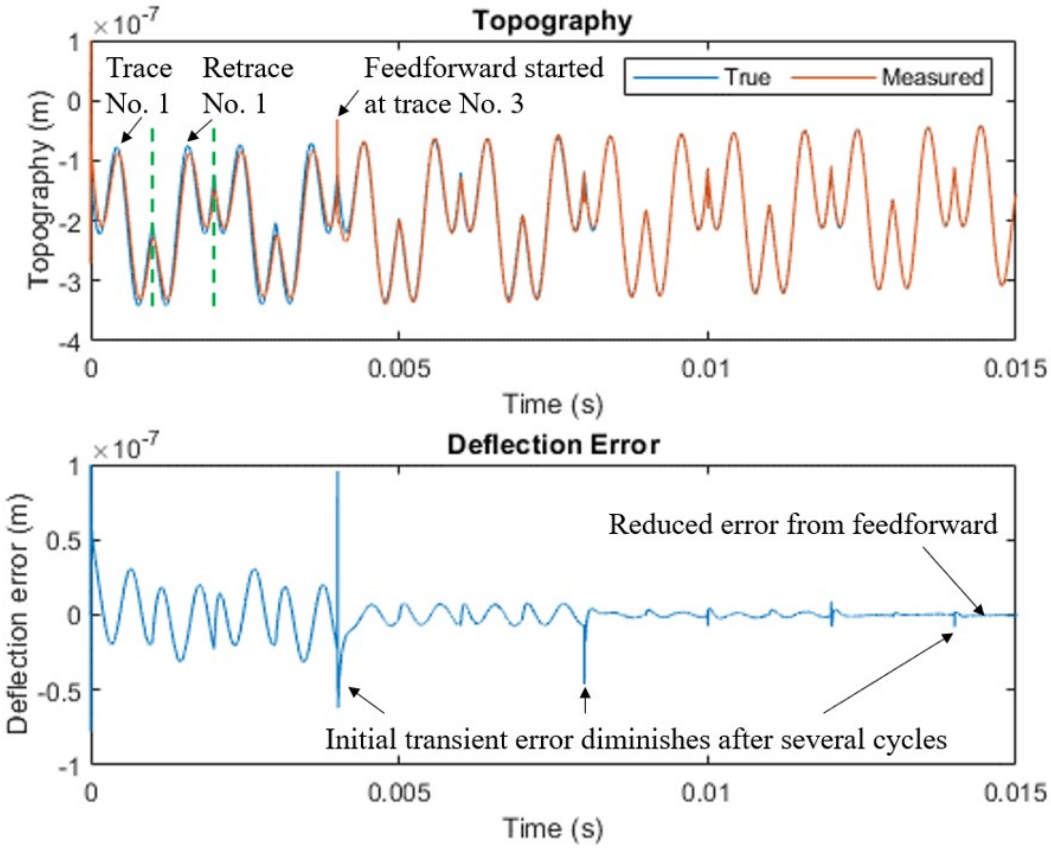

Figure 4-8: Topography feedforward starting at line 3 reduces the tracking error significantly for sample with sinusoidal pattern of $Z = (Ysin(X/500) - Xcos(Y/500))/25$ with X, Y, Z units in nm.

Error-corrected AFM Image Generation

In the early years, AFM systems operating in constant height mode does not regulate tip-sample interaction forces. The topography is measured directly from probe deflection. For modern AFMs with controller regulation of the probe deflection, the scanner command input is recorded as the topography variation. If the proportional sensitivity constant between the probe deflection signal and the physical height is obtained from calibration, the deflection error signal and the scanner command can be added to generate more accurate topography images.

To evaluate the algorithm, the simulated result is shown in Fig. 4-9. Even the tracking performance of the PID controller is poor, the corrected scan line still matches well with the simulated true topography. The small error in the corrected tracking line originates from the deformation of the sample itself. This method has

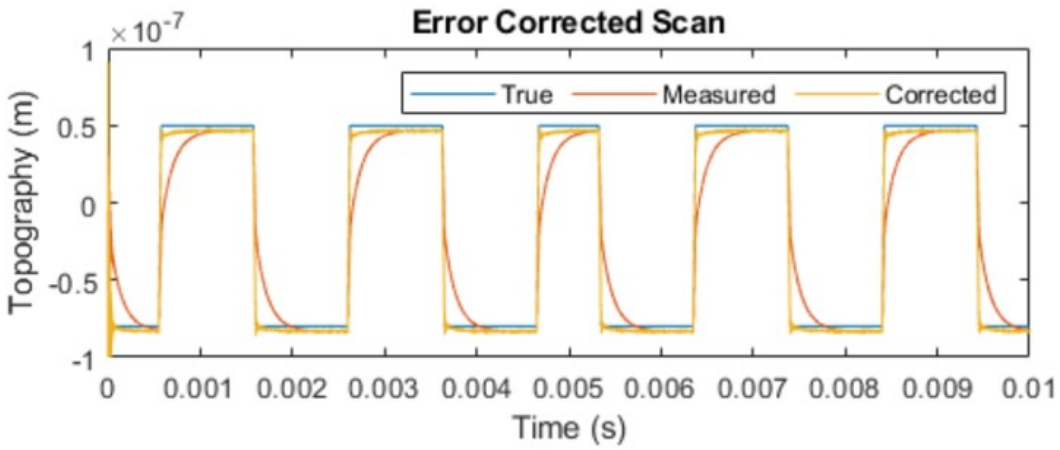

Figure 4-9: Error-corrected image generation method demonstrates good image generation even with non-ideal tracking due to poorly tuned controller

also proven to be helpful in actual AFM imaging experiments as demonstrated in the literature [165].

4.4.4 Adaptive Learning Algorithm

The automatic PID controller tuning algorithm can handle most of the samples. However, it is still difficult to handle samples with significant material property variations. In this section, a data-driven control algorithm is presented to further improve the controller to handle challenging sample automatically.

Limitation of PID and Potential Alternatives

The proposed automatic PID controller tuning method is conducted at a single location on the sample. If the material properties of the sample change significantly, the controller performance can greatly degrade. As shown in Fig. 4-10, the tuned controller can track part of the topography well but becomes unstable at other parts when the sample stiffness changes in a step pattern by 20%. With unknown sample properties, it would be difficult to anticipate the variation and retune the PID controller. Therefore, an adaptive data-driven algorithm would be helpful to handle this situation.

There are many control algorithms available to handle model parameter uncertainties and changing system properties. Robust control, adaptive control, and fuzzy

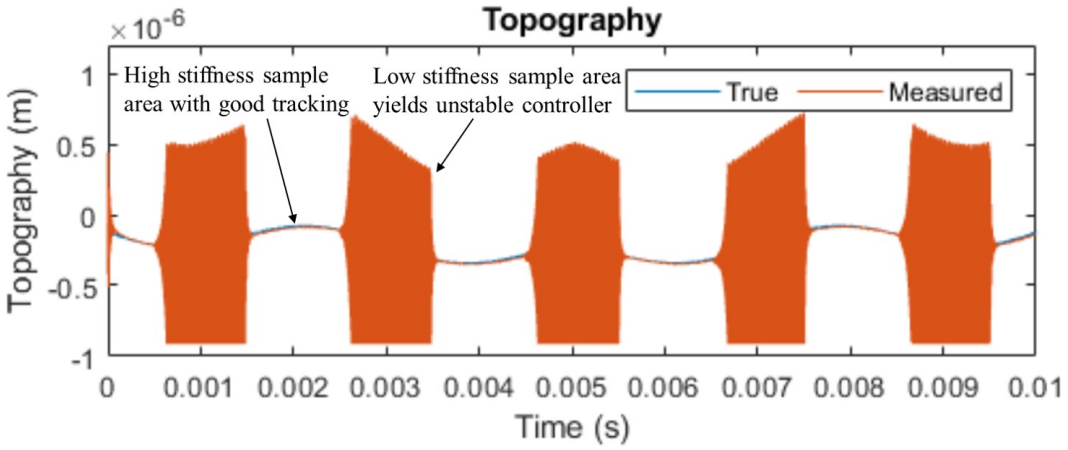

Figure 4-10: Imaging the sample with identical topography as shown in Fig. 4-7 but with step varying stiffness presents challenge as properly tuned PID controller can track high stiffness area well but becomes unstable at low stiffness area.

logic control techniques are common examples in this case. Most of these methods require good dynamic models that are estimated from the AFM system. The process of model identification can be challenging for AFM users without control system backgrounds. As an alternative, data-driven methods such as deep reinforcement learning have demonstrated their capability in handling complex model-free control problems. However, implementation of deep neural networks can be computationally too expensive for high-bandwidth systems. In this work, we propose a Single Neuron PID (SNPID) controller to adapt to challenging samples. This algorithm has a good tradeoff between the computational complexity and the adaptive performance.

Adaptive Single Neuron PID

The SNPID algorithm is based on the Hebb learning rule. It is computationally inexpensive due to its simple structure [166]. The discrete-time implementation of the SNPID controller is discussed in this section. The SNPID controller architecture is shown in Fig. 4-11(a). The formula for the neuron inputs $x_P(n)$, $x_I(n)$ and $x_D(n)$ are given in Eq.(4.6) with $e(n)$ as the error signal of the cantilever deflection.

$$\begin{cases} x_P(n) = e(n) - e(n-1) \\ x_I(n) = e(n) \\ x_D(n) = e(n) - 2e(n-1) + e(n-2) \end{cases} \tag{4.6}$$

The neuron output $u(n)$ is updated at each cycle with increment Δu in Eq.(4.7).

$$\begin{cases} \Delta u(n) = \frac{K(w_P(n)x_P(n)+w_I(n)x_I(n)+w_D(n)x_D(n))}{w_P(n)+w_I(n)+w_D(n)} \\ u(n) = u(n-1) + \Delta u(n) \Rightarrow u(n+1) = u(n) + \Delta u(n+1) \end{cases} \tag{4.7}$$

where K is a constant gain, $w_P(n)$, $w_I(n)$, $w_D(n)$ are updated by Eq.(4.8).

$$\begin{cases} w_P(n+1) = w_P(n) + \eta_P e(n)u(n)x_P(n) \\ w_I(n+1) = w_I(n) + \eta_I e(n)u(n)x_I(n) \\ w_D(n+1) = w_D(n) + \eta_D e(n)u(n)x_D(n) \end{cases} \tag{4.8}$$

where η_P, η_I, η_D are user specified non-negative constant learning rates.

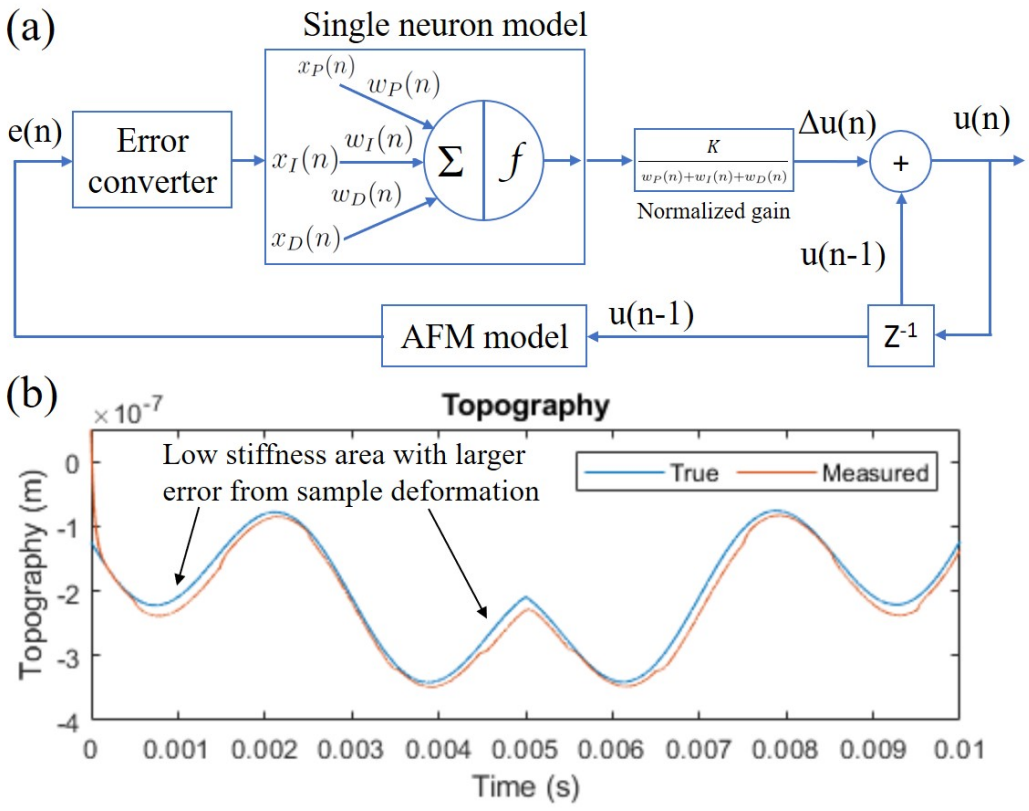

Figure 4-11: Single neuron PID controller: (a) architecture with real-time updated weights, (b) good tracking for sinusoidal topography with step varying stiffness.

It can be proven by stochastic approximation theory that the formula has a form

similar to that of the classic gradient descent method. With sufficiently small learning rates, the weights of the neurons converges to a steady state value [166].

The SNPID controller weights are adjusted as new data are sampled. This is in principle similar to the neuron weight updates in artificial neural networks during the training process. A total of seven constants need to be initialized by the operator. For convergence, the gain K is set to a small value of 0.1. The learning rates η_P, η_I, η_D are set all to 1 and initial values of $w_P(0)$, $w_I(0)$, $w_D(0)$ all set to 0.1.

The simulation results of the sample with stiffness variation using the SNPID controller are shown in Fig. 4-11. The SNPID controller remains stable regardless of the varying material property. The variation of material properties are adapted successfully by the weight updates in the SNPID controller. In this design, AFM imaging of samples with significant property variation can be conducted without operator intervention. One minor drawback of this method is that the learning rates need to be tuned to ensure good convergence of the weights.

4.4.5 AFM Controller Framework

To summarize the automatic PID parameter tuning method, three AFM image level improvement methods and the SNPID controller, a unified framework is created as shown in Fig. 4-12.

All three image level improvement methods can be activated during imaging. They can be especially helpful for imaging performance improvement in high-speed scanning. After user initialization, the system performs the automatic PID tuning and line speed parameter adjustment to start the imaging process.

The controller can switch into adaptive mode to handle samples with large material property variations. The relative error $e_{relative} = e_{RMS}/R_q$ is computed online with a moving window of data. If a large tracking error e_{RMS} is observed for sample area with small topography variation R_q, there is a high chance that the material property variations of the sample can play an important role. Therefore, if the variance of the relative error signal exceeds a threshold, the PID controller switches into the SNPID controller with adaptive online parameter updates as shown in Fig. 4-13.

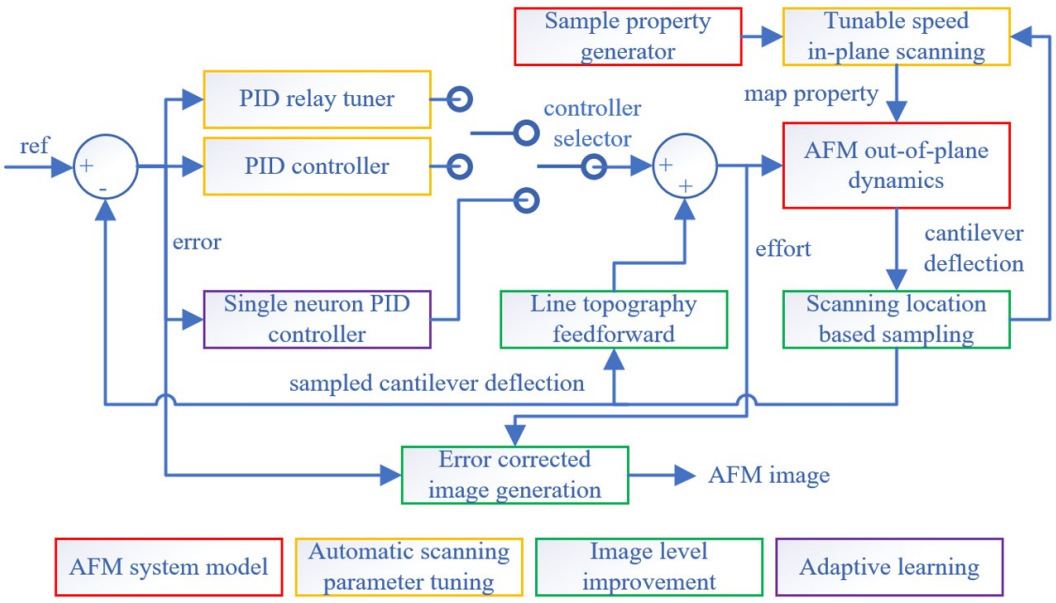

Figure 4-12: Diagram of the unified framework of AFM overall control algorithms in this work

More details on the overall imaging framework can be found in reference [167].

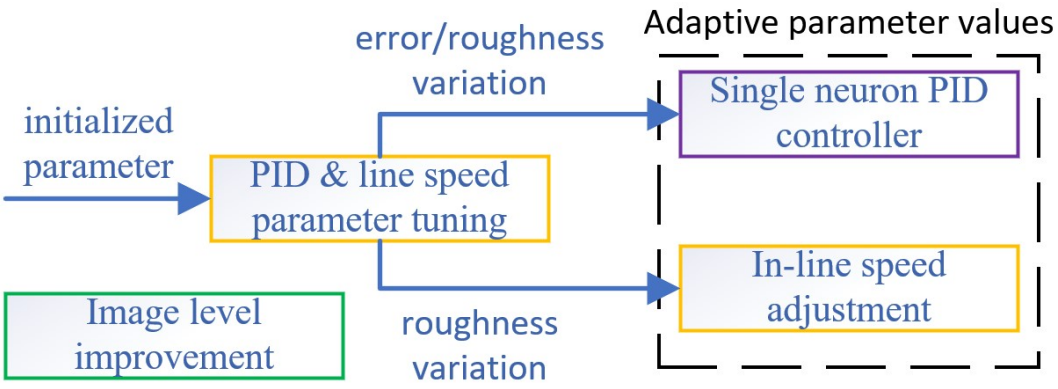

Figure 4-13: Automated roughness and relative error based algorithm switching

4.4.6 Controller Design for Other Imaging Modes

The aforementioned image level improvement algorithms are primarily designed for high-bandwidth contact mode imaging. Some of the image level improvement techniques are also applicable to dynamic modes and jumping modes such as the error-corrected image generation, equal space sampling, etc. For jumping mode operation, it is crucial to regulate the peak probe deflection each time when the probe is brought

into contact with the sample. The jumping mode control has been significantly investigated in my master work with the proposed induced vibration contact detection method [52].

For dynamic mode operation, the oscillation of the cantilever probe is more complicated than in contact mode. The oscillation characteristic can change significantly depending on the imaging environment. For example, when engaged from air into liquid, the quality factor of the cantilever significantly decreases, resulting in a smaller oscillation amplitude even with the same driving signal. Even in ambient operation, the meniscus layer of water on the sample surface can affect the oscillation characteristics. Automated controller tuning in dynamic mode operation is possible but difficult due to these reasons. Moreover, dynamic mode operation is used more often for imaging of delicate soft samples at lower speed and attentive operator monitoring during the imaging process is preferred. Therefore, instead of focusing on controller automation, research efforts have been focused on actively controlling the quality factor during imaging [168, 169, 170] or using multiple resonance modes for material property mapping with improved contrast [171, 172].

4.5 Chapter Summary

In this chapter, the controller design for both scanner motion control and AFM imaging are discussed. For in-plane scanning, iterative learning control, repetitive control, disturbance observer control and linear quadratic regulator control techniques have been investigated. The bandwidth based repetitive controller is an innovative design in this work. It make use of the periodic in-plane scanning motion and the specialized multi-layer stacked scanner. For imaging purpose, a model for the AFM overall dynamics and an intelligent controller framework are developed. the framework include an automatic PID controller tuning method with scan speed adjustment and a single neuron PID controller for sample property variation handling. Image level improvement algorithms including topography feedforward, equal space sampling and error corrected image generation are investigated. Discussion in this chapter corresponds to

the third main contribution of this thesis: algorithms for scanner control, automatic tuning and imaging.

Chapter 5

AFM Sub-system Implementation

5.1 Introduction

A number of additional sub-systems are involved in AFMs to enable or extend their capabilities. In this work, these subsystems primarily include high-bandwidth driving and signal conditioning electronics, the optical system for cantilever probe interface with vision based automation and the software implementation for high-speed big data processing. This chapter discusses the development of these subsystems.

5.2 Scanner Driving Electronics

Piezo actuators are driven by electrical power amplifiers with signals taken from data acquisition (DAQ) systems. We begin by introducing the design of a driver for the piezo buzzer scanner as discussed in Chapter 2. The design works at relatively low voltage and current. It also includes the signal conditioning circuits for interfacing to the DAQ system. Next, we discuss the high power amplifiers used to drive stacked piezo actuators working at high voltages. In the end, we discuss the charge controller implemented within the driving electronics to handle the piezo actuator nonlinearity on a hardware level.

5.2.1 Piezo Buzzer Scanner Driver

The buzzer scanner driver circuit drives the buzzer-actuated scanner as discussed in Chapter 2. The driving requirements of this scanner is relatively low since the scanner design operates at a low voltage and a low bandwidth. The circuit takes in the signals from the National Instrument myRIO 1900 DAQ system. According to the data sheet, the myRIO system contains the following resources for analog output channels as shown on page 10 of the datasheet:

1. DAC on 2 MXP Connector: Total of 4 analog output, 12-bit resolution with range 0V to 5V
2. DAC on 1 MSP Connector: Total of 2 analog output, 12-bit resolution with range $-10\ V$ to $+10\ V$.
3. Audio and accelerometer analog signal ports are not used for this application.

The driving electronic circuit design for a four quadrant buzzer scanner uses differential voltages for in-plane scanning. Common mode voltage is used for driving the out-of-plane motion. A full functioning driver should have 6 inputs from myRIO-1900 and 8 outputs to the buzzer elements. Two digital to analog converters (DAC) with $0-5\ V$ range on the myRIO MXP connector are used to control the in-plane motions for both the bottom buzzers and middle buzzer. Two myRIO MSP connector $\pm 10\ V$ DAC are used for the out-of-plane motion.

To drive the scanner, the $2.5\ V$ offset of the in-plane voltage command $0-5\ V$ is removed and amplified to $\pm 10\ V$ range. The signal is duplicated with an inverter to produce differential drive signals to the two opposing buzzers for in-plane scanning. The $\pm 10\ V$ voltage signal for the Z axis command is then added to both signals from the differential drive stage and amplified by a gain of 3 to drive the buzzers. As an example, we take a detailed look at the four functional groups for the differential in-plane motion drive in Fig. 5-1. Notice that a final addition stage for the common mode out-of-plane signal would be needed to drive the actual buzzer scanner.

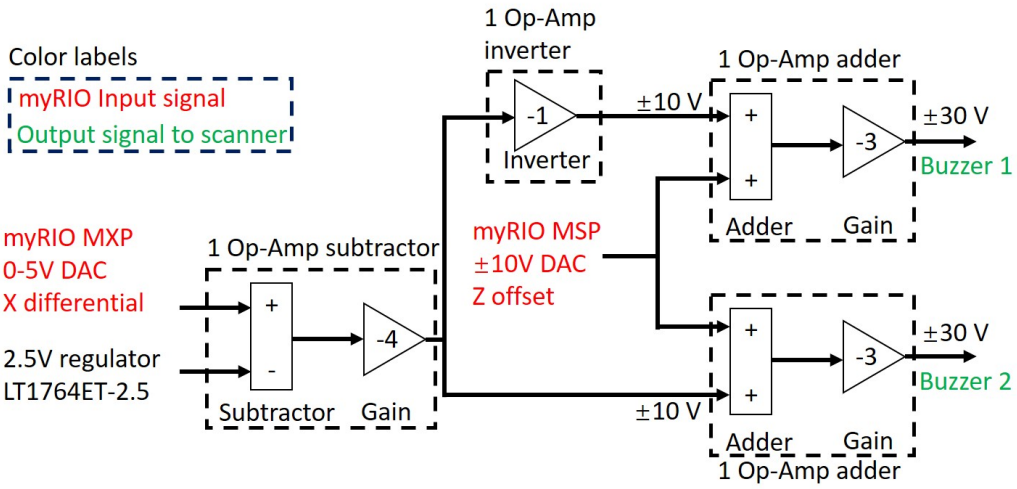

Figure 5-1: Schematic diagram of the functional groups for driving one axis of the in-plane motion for the buzzer-based scanner in both configurations

In the first functional group, a scaled subtractor with gain -4 and a 2.5 V voltage regulator is used to convert the the myRIO MXP $0-5$ V signal to ± 10 V range. The second operational group uses an inverting amplifier with gain of -1 to produce an additional inverted signal. The third and fourth subgroups are identical in configuration as they add the differential signal with a common mode ± 10 V range signal from myRIO MSP connector. Gains for both the third and fourth stages are set to -3 from the summing amplifier so that a ± 30 V output range to the buzzer is achieved. Multiple high-voltage (± 45 V) OPA445 operational amplifiers are used to implement the functional groups.

The overall diagram of the circuit for all 8 quadrants is shown in Fig. 5-2(a). As a specific implementation in this work, the in-plane scanning X and Y for the middle and bottom is not simultaneously used during operation. Therefore, we can merge channels for the in-plane scanning differential drive and add switches to choose which in-plane scanning is activated. This would reduce the number of the operational amplifiers and thereby reduce the overall cost of the design. A total of 4 inputs would be needed 4 inputs (X,Y, small Z and large Z) and 8 outputs. The implemented driver circuit is shown in Fig. 5-2(b).

A range and resolution tradeoff exists in this scanner design. It is evident from the

driving principle that the maximum range of the in-plane motion and the out-of plane motion for the same set of buzzer cannot be realized simultaneously due to the voltage limitation. With a fixed DAC resolution, a smaller scanning range produces a higher positioning accuracy. The multi-actuated scanner design provides more flexibility in operation for scanning at different range and resolution. The bottom four buzzers offer a larger in-plane range but a smaller out-of-plane range compared to the middle buzzer with four quadrants.

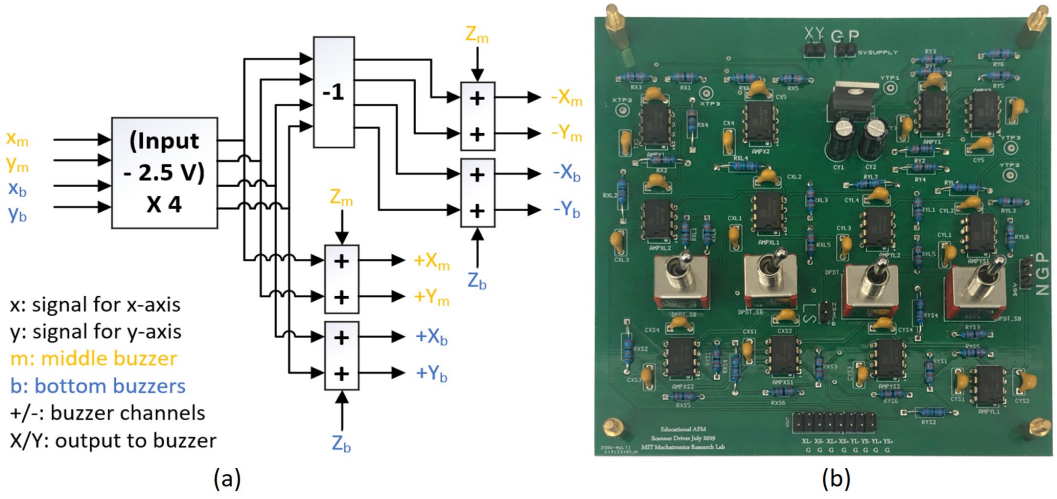

Figure 5-2: Buzzer scanner driver design: (a) overall functional schematic of the driver circuit for interface between myRIO micro-controller and the scanner, (b) implemented driver circuit with three signal inputs and eight actuator outputs for the buzzer scanner with switches for selection of activated channels

5.2.2 Power Amplifier

The current supplying capability of the power amplifier is important for high-bandwidth operation. Since piezo actuators are capacitive loads, changing its voltage would require rapid charge and discharge of the capacitor. The current requirement depends on the frequency of the driving signal. This is not a big problem for the buzzer scanner driver as they operate at relatively low frequencies.

We take a P885.51 piezo actuator used in the dual-actuated scanner as an example. According to the datasheet, it has a 700 nF nominal capacitance. Up to 200 nF

increase in the capacitance can be expected due to nonlinearity for high voltage operation. The driving signal U is a sine wave with 10 kHz frequency and 50 V amplitude for the full range swing. The peak current required for the piezo actuator driver is calculated in Eq.(5.1).

$$\begin{aligned} U &= A\sin(\omega t) \Rightarrow I = K \cdot C\frac{dU}{dt} = K \cdot C \cdot A\omega\cos(\omega t) \Rightarrow I_{peak} = K \cdot C \cdot A \cdot \omega \\ \Rightarrow I_{peak} &= 1.8 \times 500 \times 10^{-9}\ Farad \times 50\ V \times 2\pi \times 10 \times 10^{3}\ rad/s \\ &= 2.827\ A \end{aligned} \tag{5.1}$$

Typical piezo actuators can operate up to 300 V depending on the application. The capacitance values of the piezo actuators depend on their physical size with small ones below 100 nF and large ones over several μF. Piezo actuators used in this work have typical voltage range for $0-100\ V$ or $0-150\ V$.

High-bandwidth driving of piezo actuators in the kilohertz range are not commonly used. Most commercially available piezo actuator drivers do not meet our application needs. For high bandwidth operation, a piezo driver is custom designed to interface between the national instrument data acquisition system and the piezo actuator. Power amplifier integrated circuit such as the PA93 and PAD129 have both been investigated for the implementation of the driver. The PAD129 amplifier has a higher current supplying capability, which makes it more suitable for driving the piezo actuator at a high bandwidth. More cost efficient amplifiers such as the PA85 can also be used for lower bandwidth applications.

The implementation of the main circuits primarily followed the design guidelines provided in the data sheet of the amplifiers. Additional signal conditioning functional groups using AD8021 operational amplifiers are added to match the DAC range for either $\pm 1\ V$ or $\pm 10\ V$ inputs. The output of the circuits can be switched between $0-100\ V$ and $0-150\ V$ to drive different piezo actuators. Cooling fans and heat sinks are added to the power amplifier for heat dissipation during high current operation.The implemented printed circuit boards are shown in Fig. 5-3.

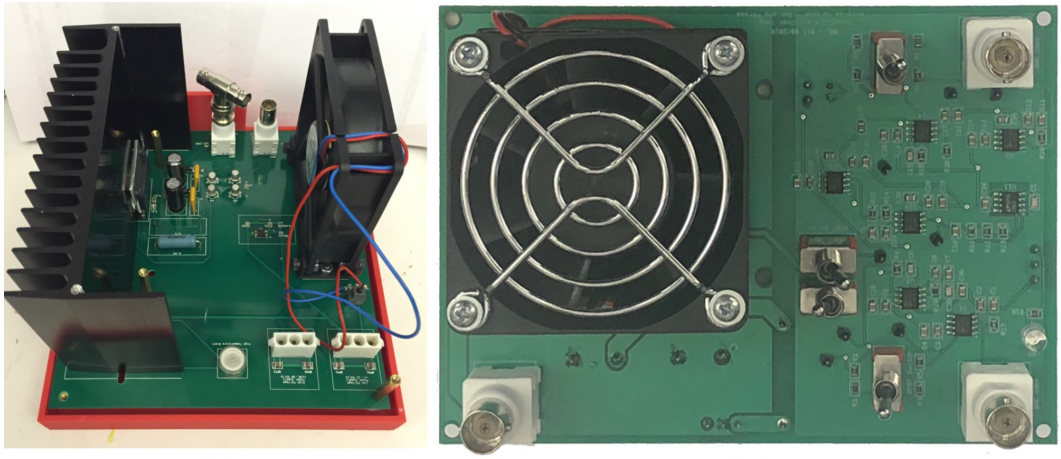

Figure 5-3: High-bandwidth custom designed piezo actuator driver: (a) PA93 based circuit design, (b) PAD129 based circuit design

5.2.3 Analog Charge Control Circuit

The analog charge controller is an alternative method to compensate for the hysteresis nonlinearity. As discussed in Chapter 4, the feedforward compensation methods require accurate system identification of the hysteresis model. Moreover, the computational resources required by the inverted hysteresis model can be too complicated for implementation digitally on FPGAs. The feedback control techniques have proven their effectiveness in handling the hysteresis with sensor measurements. However, in certain applications, adding a sensor to measure the scanner position can be expensive and might not be feasible. For example, adding a sensor for measurement of the AFM out-of-plane motion can sometimes be challenging due to the space constrain. In this case, the analog charge control circuit is an ideal solution since its a sensorless approach.

In charge control, the physical property of the piezoelectric materials is utilized to account for the hysteresis nonlinearity. In principle, the hysteresis effect can be eliminated if the free charge of the piezo actuator is kept as a linear function of the reference input signal. This can be proven by using the piezoelectric constitutive equations and the Gauss's law [173].

The concept diagram of a basic charge controller is shown in Fig. 5-4. By simple circuit analysis, the charge across the piezo actuator Q_p is equal to the product of the reference voltage input V_{in} and the capacitance of the sensing capacitor C_1 as $Q_p = CV_{in}$. In practice, this simple configuration has a number of problems. This design has a floating load, which is unsuitable for many piezo actuators. Other performance problems of the design include high-sensitivity to the input bias current, limited quasi-static performance, loss of stroke, difficulties in matching DC and AC voltage gains, etc. A number of different charge controllers have been designed before to address some of the issues [174, 175, 176]. However, these limitations have not been fully resolved.

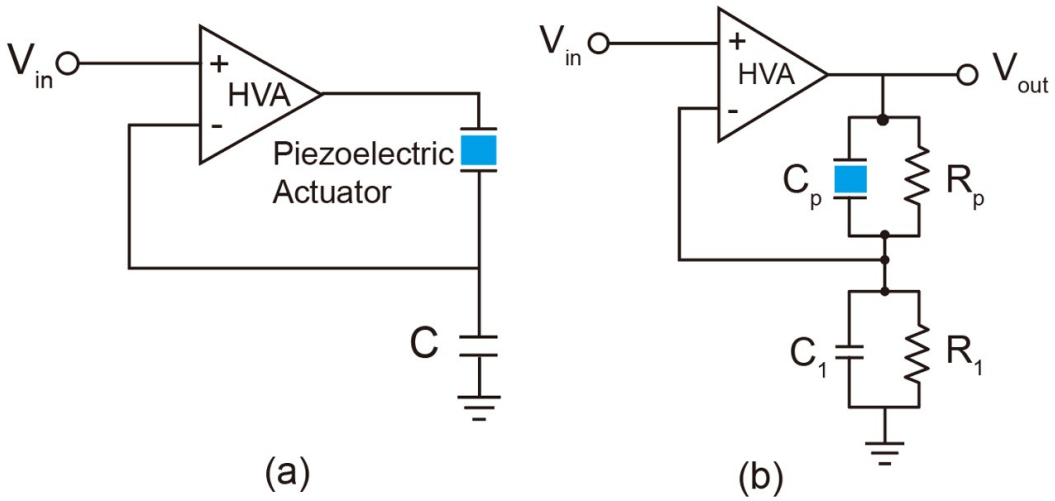

Figure 5-4: Charge controller concept: (a) fundamental concept of charge controller, (b) floating-load charge controller with resistive path for leakage current steady state drift compensation

In this design, a steady state drift exists for DC input signals that drives the amplifier to saturation. This is caused by the current drift and finite input impedance of the operational amplifier. A passive resistive feedback path is usually added to address this issue as shown in Fig. 5-4. The leakage current can be effectively compensated with the additional resistive path. To maintain a constant gain across the spectrum for both DC and AC signals, the resistors and capacitors are chosen to

satisfy the relation in Eq.(5.2).

$$\frac{R_1}{R_p} = \frac{C_1}{C_p} \tag{5.2}$$

Careful matching of the resistors to satisfy this relation can be difficult. The nonlinear behavior of the piezo actuator capacitance model results in changes of its value during operation. The extra dynamics added by the feedback resistor also yields a cutoff frequency f_c as shown in Eq.(5.3).

$$f_c = \frac{1}{2\pi R_p C_p} \tag{5.3}$$

Below the cutoff frequency, the charge controller essentially becomes a normal voltage drive due to the resistive path. To address this issue, a decoupled scheme is proposed as in Fig. 5-5

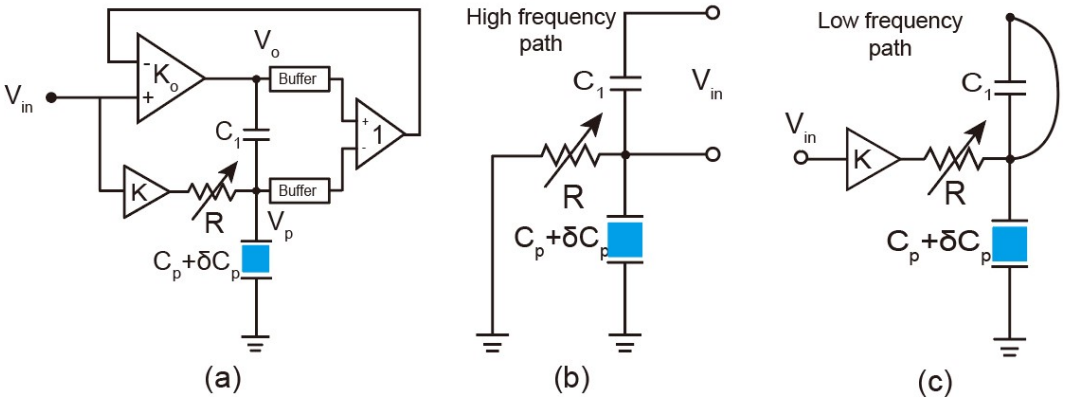

Figure 5-5: Charge controller with decoupled high frequency and low frequency path for handling input signal component at different frequency ranges: (a) circuit design, (b) high frequency path, (c) low frequency path

The proposed charge controller circuit has a grounded-load manner to overcome the reduced stroke issue. It allows general application to various types of piezo actuators. Moreover, the high frequency and low frequency paths are decoupled. The voltage across the sensing capacitor C_1 can be viewed as a voltage source to drive the variable resistor R and the load capacitor C_p with a variable nonlinearity term δC_p.

The resistive branch R can be viewed as an open circuit since the impedance of the capacitor is much smaller than that of the resistor at high frequencies. In the low frequency path, the sensing capacitor can be viewed as a short circuit. The amplified input voltage V_{in} drives the load capacitor with large impedance at low frequency directly, which helps to produce a DC offset.

The block diagram representation of the overall circuit design is shown in Fig. 5-6 with the decoupled section of the circuit enclosed in the dashed box.

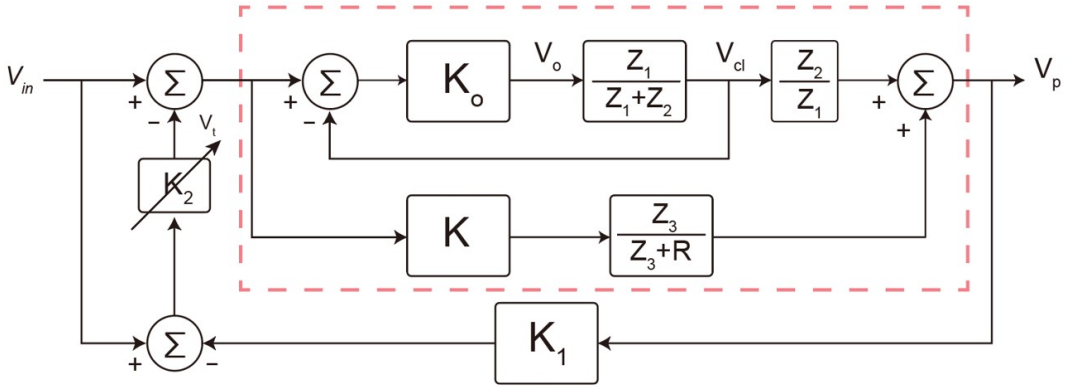

Figure 5-6: Overall block diagram model of the charge controller design with dashed box label of decoupled inner circuit path

The definitions of the impedance terms in the block diagram are shown in Eq.(5.4).

$$\begin{cases} Z_1(s) = \frac{1}{C_1 s} \\ Z_2(s) = \frac{R}{R(C_p+\delta C_p)s+1} \\ Z_3(s) = \frac{1}{(C_p+\delta C_p)s} \end{cases} \tag{5.4}$$

The overall transfer function $G(s)$ of the block diagram can be derived as shown in Eq.(5.5).

$$G_(s) = \frac{V_p(s)}{V_{in}(s)} = \frac{C_1}{C_p+\delta C_p} \frac{s+\frac{1}{RC_p}}{s+\frac{1}{R(C_p+\delta C_p)}} \tag{5.5}$$

The frequency dependent magnitudes can be computed using Eq.(5.6), which

agrees with our previous analysis for the DC and AC path.

$$|G_(s)|_{s=j\omega} = \left|\frac{V_p(s)}{V_{in}(s)}\right| = \frac{C_1}{C_p}\sqrt{\frac{1+\omega^2 C_p^2 R^2}{1+\omega^2(C_p+\delta C_p)^2 R^2}} = \begin{cases} \frac{C_1}{C_p} & \omega \to 0 \\ \frac{C_1}{C_p+\delta C_p} & \omega \to \infty \end{cases} \tag{5.6}$$

We notice that the capacitance change term δC_p in this expression can still be problematic. To address this issue, a compensating scheme is used by adding a feedback path around the decoupled charge controller. This is done by subtracting the scaled piezo actuator voltage from the reference signal to obtain the error signal from the nonlinearity. By amplifying the error signal with a tunable gain and adding to the V_{in} signal, the non-linear capacitance effect can be compensated. The circuit diagram and physical implementation of the self-compensating charge controller is shown in Fig. 5-7.

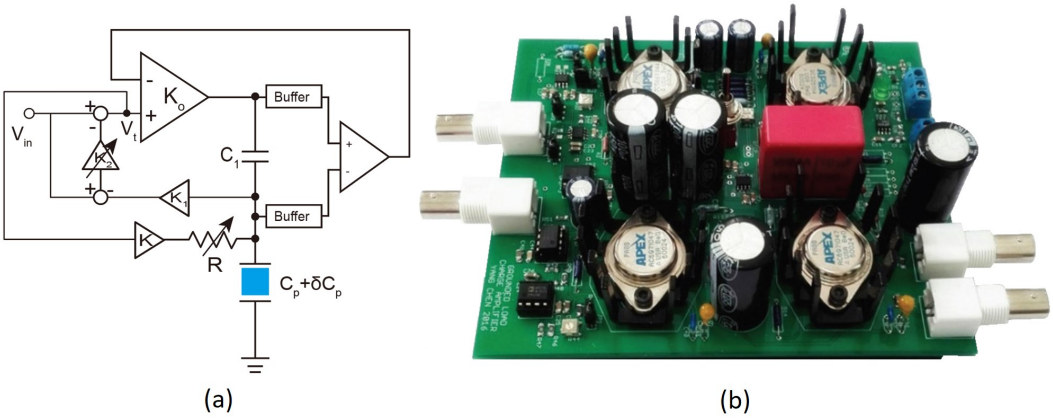

Figure 5-7: Charge controller with decoupled and self-compensating configuration for piezo hysteresis compensation in a wide bandwidth: (a) circuit design, (b) physical implementation

The collaborative work of charge controller development in our lab is primarily led by Dr. Chen Yang. More details for the topic on charge controller design and performance analysis can be found in references [157, 177]. The charge controller has effectively improved the performance of the piezoactuator positioning control especially in cases where feedback sensors are not easy to add. This design can be

very helpful for the piezo actuator driven scanners widely used in AFMs.

5.3 Cantilever Probe Interface

External subsystems are needed to interface with the cantilever probe. In this section, the cantilever probe holder design for both passive probes with piezo acoustic actuation and active probes will be introduced first. Next, we discuss the optical beam deflection system and its signal conditioning circuit for the quadrature photodiode. In the end, we discuss a low cost signal generation and demodulation circuit for AFM tapping mode operation. While the functionality of this circuit can be implemented using digital DAQ system, the analog circuit significantly reduced the cost. The design is used for an educational AFM design with more details in Chapter 6.

5.3.1 Cantilever Probe Holder Design

The AFM probe holder is a fixture that maintains the position of the cantilever probe during imaging. A piezo actuator can be embedded into the probe holder for piezoacoustic actuation of passive cantilevers. The holder CAD design for both passive and active probes are shown in Fig. 5-8.

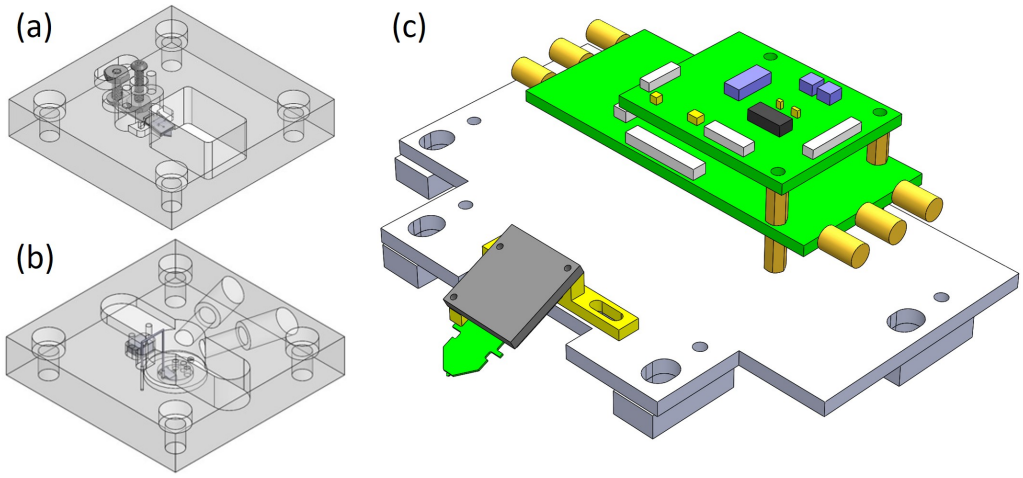

Figure 5-8: Probe holder CAD designs in isometric view: (a) passive probe air operation, (b) passive probe liquid operation, (c) active probe including electronics

For operation in ambient air, the piezo actuator can be placed directly beneath the machined slot. A flexible clip is used to secure the standard passive cantilever probes.

For operation in liquid, the piezo actuator is embedded into the holder structure. The cantilever probe is completely immersed into the liquid. Vibration generated by the piezo actuator propagates through the holder and get amplified by the cantilever at resonance frequency. A double layer acrylic structure with an enclosed piezo actuator and a spring loaded clipping wire is used in our design. The acrylic material provides a transparent path for the laser to through while enclosing the liquid. Channels for accessing the center of the sample chamber is also available to allow liquid circulation.

The holder for the piezoresistive sensing thermomechanical actuation active cantilever probes are relatively simple. Since the probe is bounded to an SD card shaped PCB that is plugged into the first stage amplifier, a machined mechanical structure to hold the first stage amplifier would be sufficient. The assembled probe holders are shown in Fig. 5-9.

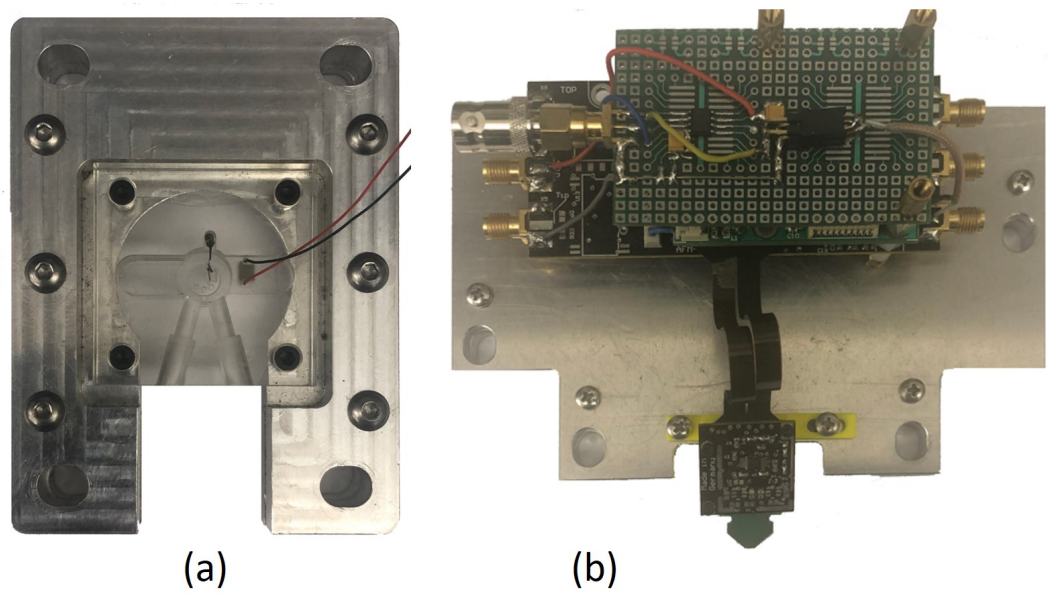

Figure 5-9: Images of assembled probe holder: (a) passive probe liquid operation holder in aluminum bracket, (b) active probe holder with driver electronics

Both probe holders are used in the versatile sample scan AFM design to be introduced in Chapter 6. The probe holder design for the other AFM systems are similar in principle.

5.3.2 Focused Laser Optics for Small Probes

The optical system for a passive probe AFM combines an optical view with a focused laser for deflection measurement. Based on the principle of optical beam deflection as introduced in Chapter 3, a modified system is designed in this work.

For high-speed imaging, small cantilevers (e.g. 10 μm by 20μm) are typically used. These probes have higher bandwidths without increasing stiffness considerably. For external measurement of its deflection, a specialized optical detection system is needed to focus the laser spot [69]. The design of the optical system is shown in Fig. 5-10 with component functionalities listed below:

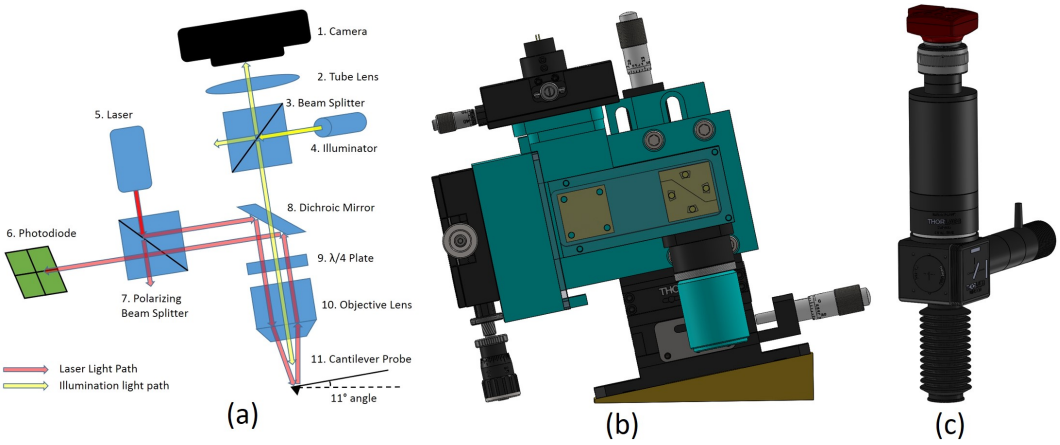

Figure 5-10: Optical beam deflection system: (a) optical components functional diagram, (b) CAD design for the housing and positioner for optical beam deflection system, (c) CAD design of camera, tube lens and illumination system with variable length fixtures for precise image plane positioning

1. A camera (DCC1645C, Thorlabs) is used for capturing optical images. Spacers are used to ensure the focal distance of 200 mm between the camera image plane and the tube lens.

2. A collimation tube lens (TTL200, Thorlabs) used to work with the infinite-

corrected objective lens to allow a longer variable light path distance between camera and the objective lens to place the extra components.

3. A $50:50$ beam splitter (BSW10R, Thorlabs) with housing (DFM1, Thorlabs) is used to direct the illumination light without obstructing the optical view.
4. An illumination kit (WFA1010 Thorlabs) with driver (LEDD1B Thorlabs) is used as a light source to illuminate the sample and cantilever during alignment.
5. A laser source with 635 nm wavelength (a 670 nm wave length (VPSL-0670-005-X-5-B, BlueSky Research) with RF-modulation to reduce laser optical feedback noise as discussed in reference [178] is utilized in the first iteration of this design. A 670 nm wavelength ultra low-Noise laser diode modules (Coherent) with better noise performance is used in the final design.
6. A quadrature SI PIN photodiode (S4349, Hamamatsu) with driving circuit is used to convert laser intensity to voltage signal.
7. A polarizing beam-splitter with a wavelength range of $420-680$ nm (48-999, Edmund) is used to generate polarized laser.
8. A dichroic short-pass mirror with a reflection band wavelength range of $625-795$ nm (69-192 Edmund) is used to guide the laser path by reflecting the laser beam while allowing illumination light for the camera to go through.
9. A $\lambda/4$ plate for wavelength $610-850$ nm wavelength light (63-935 Edmund) is used to change the polarization of the polarized laser reflected from the polarizing beam splitter. Passing the same light twice through a $\lambda/4$ plate would transform it to another linearly polarized light that is perpendicular to the original polarization. Compared to a non-polarizing beam splitter that reduces the laser intensity to 25% after passing the laser twice through the splitter, the polarized beam-splitter setup with the $\lambda/4$ plate only reduces the laser intensity to 50% when used together with the $\lambda/4$ plate.
10. A high-NA infinite-corrected objective lens (Nikon SLWD L-Plan 20X) is used to focus the laser to a 3.5 μm diameter spot size compatible with small cantilevers.

A low-NA objective lens (Olympus Plan N 4X) can also be used for off-axis detection configuration.

The optical components are mounted on a three-axis positioner (MT3, Thorlabs) that can be adjusted both manually and programmatically with piezo inertia actuators (PIA13, Thorlabs) and drivers (TIM101 or KIM101, Thorlabs). Single axis positioners (ST1XY-S, Thorlabs) are used for adjusting the laser and photodiode during alignment. A 11° wedge is added to the system for ease of laser alignment.

A signal conditioning circuit is custom designed to amplify and process the current signal from the four quadrant photodiode. The cantilever vertical deflection is obtained as $V_{out} = (V_1 + V_2) - (V_3 + V_4)$. The summation signal of all four quadrants are also processed to ensure good signal quality. The design of the circuit involves the calculation of trans-impedance amplifier gain based on the laser power and selection of appropriate operational amplifiers to reduce the noise. The assembled PCB components without the photodiode is shown in Fig. 5-11. More details of the design can be found in my master work [52].

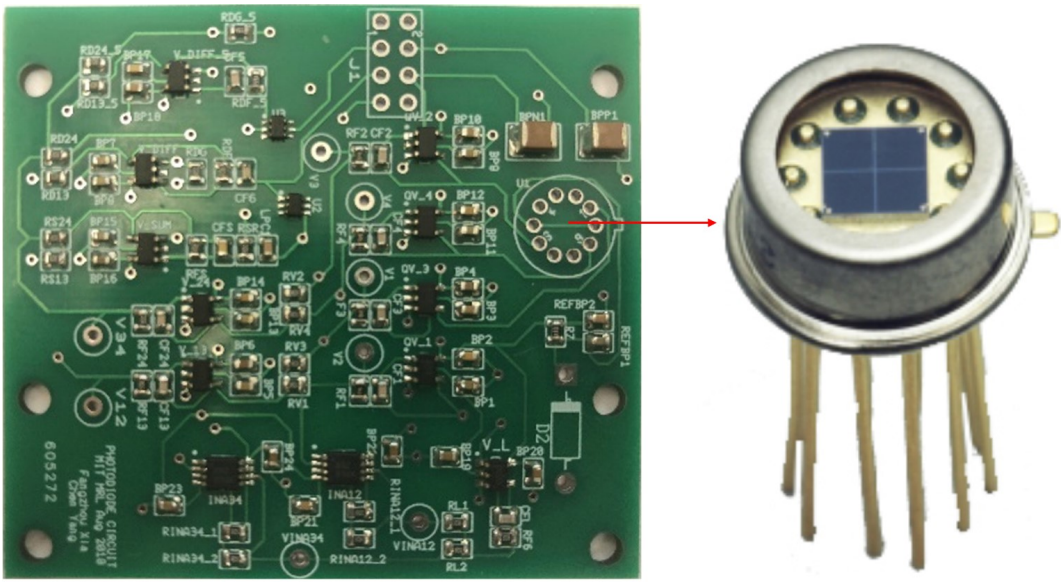

Figure 5-11: Quadrature photodiode signal condition circuit assembly (left) and Hamamatsu S4349 photodiode (right)

5.3.3 Signal Generation and Demodulation

For tapping mode operation, high frequency actuation sine wave signal and demodulation for amplitude and phase are needed. The piezoresistive sensing thermomechanical actuation active cantilever probes used in this work have typical first mode resonance frequencies between 20 kHz to 100 kHz. For the educational AFM design to be introduced in Chapter 6, the budget constrain limits the selection of data acquisition system to be the NI myRIO microcontroller with limited capability. The Digital to Analog Converter (DAC) sampling frequency of myRIO is at 345 kHz and the Analog to Digital (ADC) sampling rate is 500 khZ. This is insufficient to handle the signal generation and demodulation task for the active cantilever probe. Therefore, a custom designed analog circuit is proposed to resolve this issue.

Sine Wave Generation

For resonance excitation, the AD9833 integrated circuit (IC) is used to generate the sine wave with direct digital synthesis. It has a Serial Peripheral Interface (SPI) for digital communication to configure the output frequency and phase. Triangle waves and square waves can also be configured as outputs. The frequency reference clock of the circuit can be generated by an external crystal as a standard clock. In this design, the practical aspect of clock mismatch is taken into consideration. If a slight frequency difference exists between the external crystal for excitation signal generation and in the myRIO reference clock for the demodulation signal, a phase difference will quickly accumulate. This would result in a demodulation error. In this design, the myRIO digital output line is used to provide a 20 MHz reference clock to the AD9833. This design helps to resolve the clock mismatch issue. The sine wave produced by the AD9833 chip has a fixed maximum voltage at $0.65V$ and a minimum voltage at $0.038\,V$. The generated signal is passed through several Op-Amp functional groups to remove the offset and increase the gain to drive the cantilever heater. A half resonance frequency driving scheme is typically used for the thermomechanical excitation as discussed in Chapter 3.

A total of four functional groups are needed to implement the cantilever probe

driving signal generation PCB. The first functional group uses the AD9833 IC for direct digital synthesis of the waveform. The second functional group is an AC-coupled gain amplifier for removing the offset. The third functional group is a variable gain amplifier for adjusting the amplitude of the sine wave. The optional fourth functional group adds an offset to the signal so that the entire circuit can operate as a function generator.

Demodulation

The analog demodulation circuit is based on two AD630 balanced modulator/demodulator IC chips from Analog Devices. The AD630 is configured as a lock-in amplifier for synchronous demodulation. In principle, the AD630 is a variable gain amplifier with either $\pm$ 1 or $\pm$ 2 gains depending on the connection. The gain is controlled by the output of a voltage comparator to determine the sign of the gain. A synchronous demodulation can be realized if a square wave at the desired frequency is generated at the comparator output to generate a phase sensitive demodulated signal. If the square wave of the comparator is in phase with the input sine wave, a full-bridge rectified sign signal is produced. By applying an RC low-pass filter to the output signal, the RMS value of the sine wave can be obtained as shown in 5-12. If a 90° offset in phase exists between the sine wave and the square wave, the filtered signal output will have an average of 0. For 180° and 270° phase offsets, a negative RMS value and another zero value will be observed. The output is essentially a phase sensitive demodulator with output $V = \frac{\sqrt{2}}{2} A \cos(\Delta\phi)$ where A is the amplitude of the input sine wave and $\Delta\phi$ is the phase difference between the sine wave and the square wave at the same frequency.

As discussed in Chapter 3, if two channels of the demodulators with square wave inputs offset by 90° are used, both the amplitude and phase can be obtained from the demodulator signals z_{cos} and z_{sin} using the lock-in formula as shown in Eq.(5.7).

$$A(t) = 2\sqrt{z_{cos}^2 + z_{sin}^2}, \quad \phi(t) = \arctan\left(\frac{z_{sin}}{z_{cos}}\right) \tag{5.7}$$

A block diagram is provide in Fig. 5-13 to summarize the signal generation and

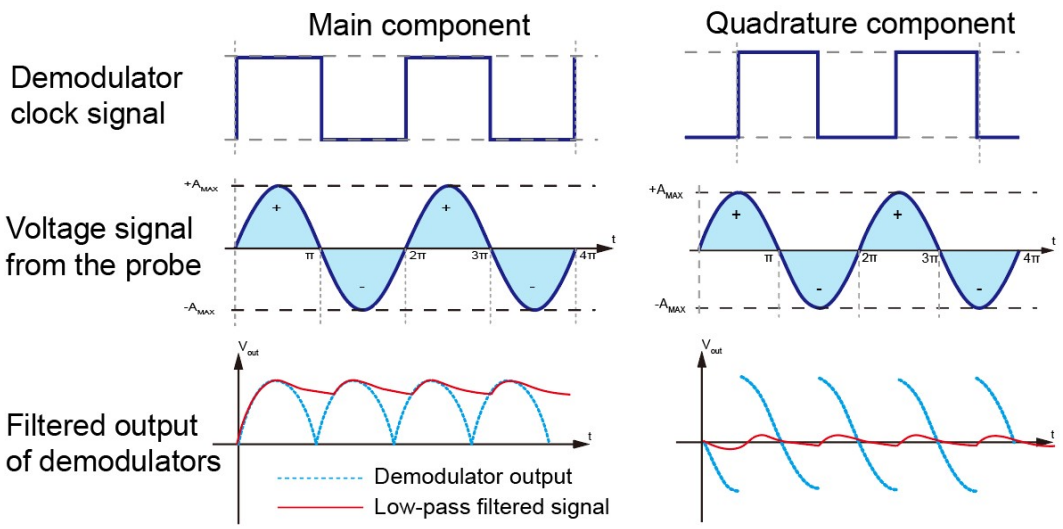

Figure 5-12: Signals processed by the demodulator and low-pass filter with main components and quadrature components shifted by 90°

demodulation signal flow.

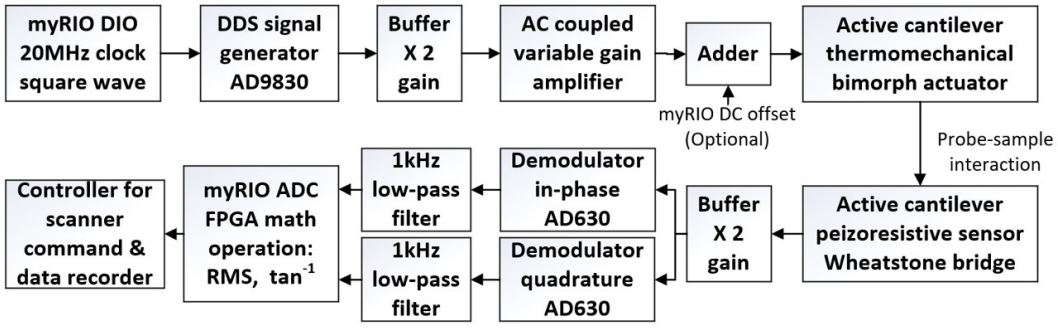

Figure 5-13: Signal processing circuit functional diagram with variable gain function generator and amplitude/phase demodulator

For circuit implementation, a total of four analog functional groups are used for demodulation. The first functional group is a non-inverting amplifier that buffers the input signal with a gain of 2. The second functional group is to interface with the myRIO system with the comparator. The GPIO lines for digital outputs on the myRIO are used for generating the square wave at a 40 MHz sample rate of the FPGA clock that switches between 0 V and 3.3 V. A voltage regulator with 1.5 V output is connected to the negative input of the comparator. The target frequency of the demodulator can be controlled accurately with the high-bandwidth digital

output. The third functional group is the AD630 demodulator AC configured with gain of ± 2. The fourth functional group is an active RC low-pass filter with 1 kHz cut-off frequency. The output of two channels of this design are fed into the myRIO ADC with ± 10 V range. A moving average of 50 samples is applied to each channel. The amplitude and the phase are digitally extracted by taking the root mean square and the inverse tangent of the ratios.

For circuit board layout, the schematic diagram design of the signal generation and the sine wave demodulation can be integrated on a single PCB. The physically implemented PCB for probe driving and demodulation is shown in Fig. 5-14.

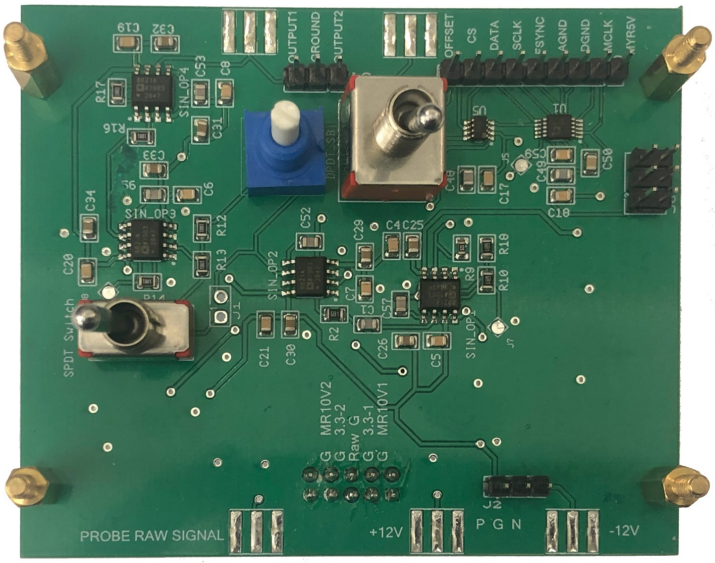

Figure 5-14: Assembled PCB of the circuit with variable function generator and amplitude/phase demodulator

5.4 AFM Software Design

Various algorithms need to be implemented with programming languages to drive the AFM system. In this work, the software development primarily includes the LabVIEW FPGA high-bandwidth controller implementation, LabVIEW real-time user interface, vision based probe search with Python, and Python SPM image processing with Gwyddion. Notice that the Matlab software is also used for dynamic system

simulation and evaluation of controller as discussed in Chapter 4. However, Matlab software is not needed for operation of the AFM instrument.

The software used during AFM imaging is primarily deployed on National Instruments data acquisitions systems. The system includes a PXIe-1085 chassis with a PXIe-8135 embedded controller, two FPGAs (PXIe-7975R and PXIe-7066R, National Instrument) and a high-bandwidth analog dual-input, dual-output transceiver adapter module (NI 5782). The graphical programming interface and automatic translation to hardware description language allows fast development of the cycle with reduced debugging time. A down-scaled version of the code is implemented on the myRIO-1900 system with limited resources to significantly reduce the cost. The overall AFM software architecture diagram is shown in Fig. 5-15. Although similar in overall architecture, software implementation variations exist between hardware platforms on ADC/DAC assignments and system parameters.

The Python, Matlab and Gwyddion software used for probe-laser alignment and post processing of AFM images can be run on regular Windows computers after installation of required packages.

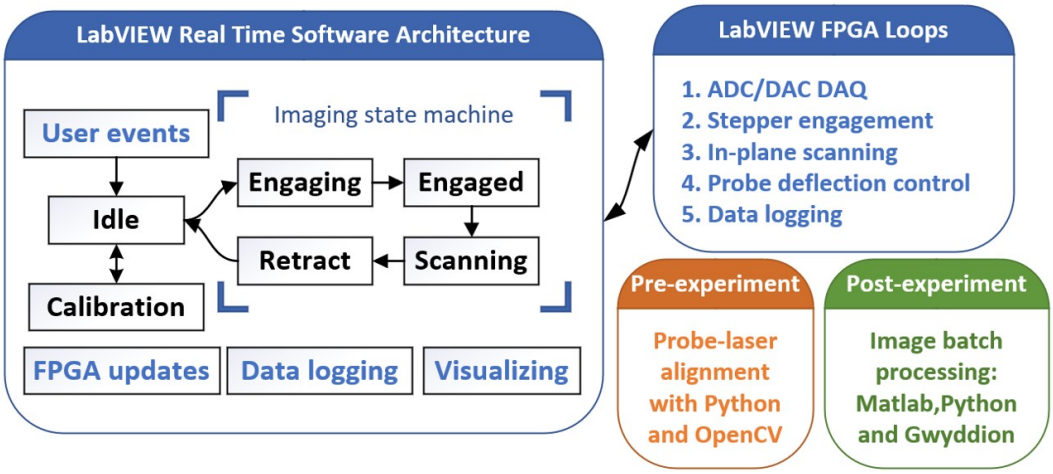

Figure 5-15: Overall software architecture for the AFM systems developed in this work using LabVIEW for imaging as well as Python, Gwyddion and Matlab for pre/post-experiment tasks

5.4.1 FPGA Controller Implementation

The low level algorithm on the FPGA handles instrument level control and signal processing tasks. They have relatively fast loop rates and high bandwidth ADC/DAC in the MHz range. As most of the controller design techniques use continuous design techniques, the bilinear transformation is used to distretize the controllers for FPGA implementation.

For all three AFM systems implemented in this work, similar low-level control architectures are utilized with parallel loops running at multiple rates to interface with different hardware systems. A total of five parallel loops are typically used in the design. The first loop is the data acquisition loop for input and output of the ADC/DAC. The second loop handles the stepper motor for engagement. The third loop controls the in-plane scanning. Feedback control for handling of piezo hysteresis nonlinearity is included in this loop to improve precision. The fourth loop regulates the cantilever deflection or oscillation characteristics by generating the scanner out-of-plane direction command. Demodulation for tapping mode and imaging improvement algorithms can be included into this loop. The fifth loop logs the data into a First In First Out (FIFO) pipeline to transfer to the real-time system. The status and operation of the loops are controlled by commands from the high-level real-time system.

During the implementation process, a number of lessons have been learned from debugging the LabVIEW code. The main tricks for high-bandwidth FPGA controller design include loop rate management, clock synchronization, quantization error mitigation, data transferring, and saving FPGA resources.

On the FPGA level, a loop can be completed within a single clock cycle or in multiple clock cycles. For more complicated operations, multiple clock cycles are usually needed to complete the operation. This limits the data throughput rate. However, a pipeline can be used to decompose one complicated operation into multiple steps that can be completed within a simple clock cycle. This would increase the overall throughput at the cost of more FPGA resources and potential increase in the

latency. Another way to increase the throughput is to use derived clock with a higher frequency than the basic FPGA clock (typically 40 MHz for NI systems). However, due to the physical placement of signal lines during routing, the timing constrains due to the electronic transition dynamics can be violated that causes the compilation to fail. Therefore, some trial and error and trade-offs are needed to increase the loop throughput desired by high-speed operation.

The clock synchronization problem is important in many cases. As mentioned in the demodulation section, the clock generation crystal for different sources usually have small differences due to the physical properties. If multiple clock sources are involved in the FPGA or the sampling module, a clock synchronization process is needed. An easy solution is to designate one clock source as the master clock across the all devices.

For FPGA implementation, fixed point arithmetic is utilized for math operations. To represent decimal numbers, an increasing number of bits can improve the accuracy but in most cases will have a remainder error, as shown in Fig. 5-16. If this number is used as an input to the accumulator, the error can build up in the long run that causes inaccuracy. One way to resolve this issue is to use whole numbers instead of decimal numbers when possible for the accumulator and scale the output.

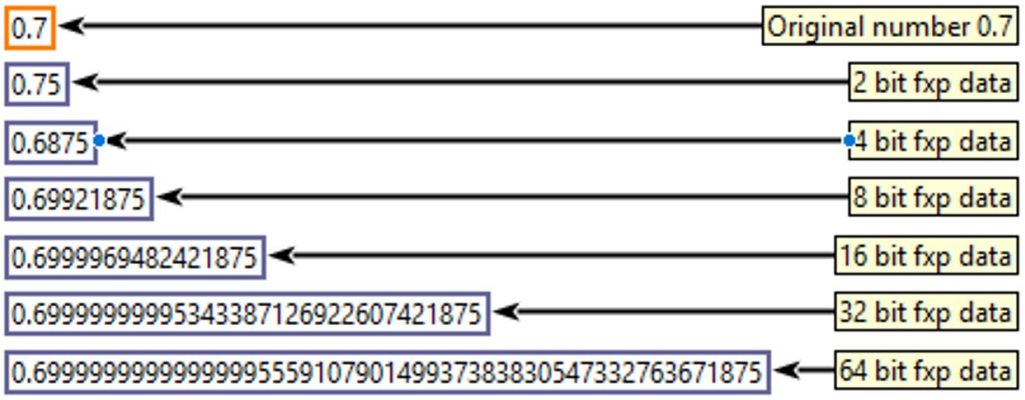

Figure 5-16: Residual error illustration of fixed point representation of decimal number 0.7 on the FPGA with fixed point number rounding enforced in LabVIEW

Many methods are available in LabVIEW for data transfer between parallel loops.

Selected methods include register items, local or global variables, memory items implemented with block memory, block memory FIFOs and handshake items. The FIFOs and handshake methods are non-lossy but need to ensure that the data are handled sufficiently fast to avoid filling up the pipeline. More details available in reference [179].

Saving FPGA resources is a big concern with resource limited system such as the myRIO. It is helpful to specify the resolution of the fixed point mathematical operations at a minimum level without affecting functionalities to reduce resource consumption. Moreover, manual configuration of the DSP48E block on myRIO can be helpful to reduce FPGA resource consumption due to routing.

The aforementioned techniques are a small subset of tricks for LabVIEW programming. They can are important for AFM system software algorithm implementation. More design recommendations on LabVIEW software architectures and implementation can be found in reference [180].

5.4.2 User Interface Implementation

The high level software handles user interface and visualization of the collected data. The loop rate of these functionalities are typically around several kilohertz. An event driven state machine architecture is used to streamline the design process. Event driven structures react to the user input such as clicking of buttons, parameter update, etc. As shown in Fig. 5-15, the AFM imaging operation can in general be divided into five stages including idle, engaging, engaged, scanning, and retract. An extra calibration state for probe or scanner is included for tuning the instrument. A state machine is easy to implement and helpful to prevent unwanted actions. In addition to the state machine, several other subroutines are involved in the code including FPGA communication updates, data logging and visualization.

The LabVIEW front panel user interface design include multiple tabs. The tabs organize user adjustable parameters based on their functional groups. As shown in Fig. 5-17, the scanner command and error signals, 2D and 3D topography maps of the scanned surface and error map are visualized in real time. An optical microscope

view using the Thorlabs camera software is also shown on the top left of the screen to visualize the sample and the cantilever.

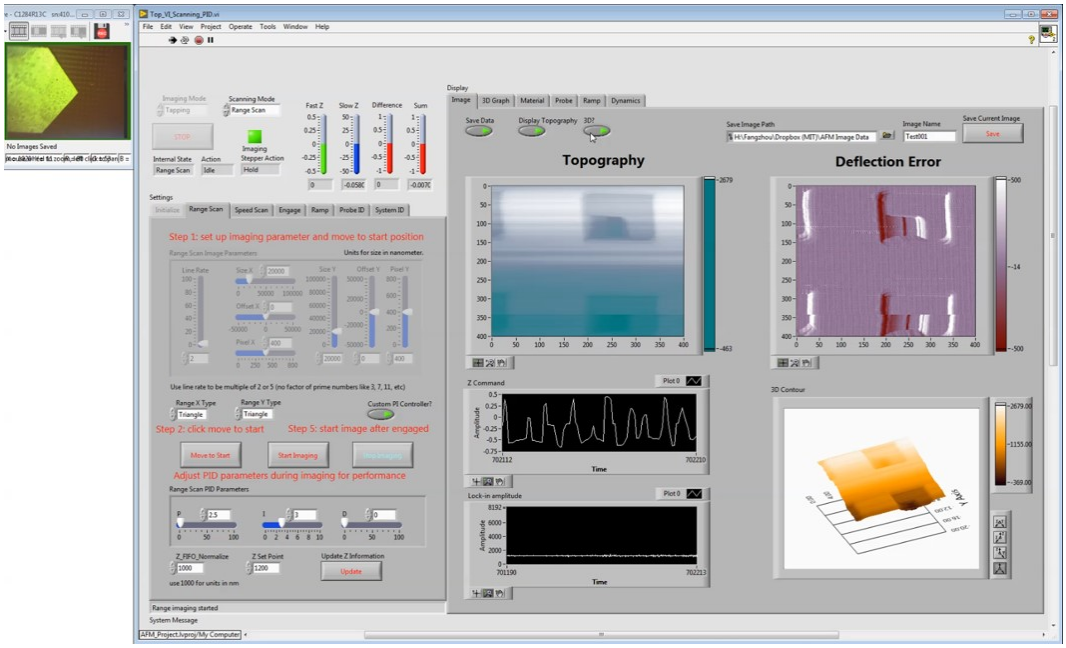

Figure 5-17: AFM LabVIEW front panel graphical user interface

5.4.3 Automatic Probe-laser Alignment

The alignment of laser spot with the passive probe is a task usually completed manually. With the custom designed optical system for laser focusing introduced earlier in this chapter, the field of view is reduced. An automatic probe-laser alignment system is developed in Python using computer vision algorithms to search for the probe by scanning the piezo inertia actuators and identify the probe in the field view using the optical microscope. An illustration of the overall goal for probe laser alignment is shown in Fig. 5-18.

The localization of the red laser spot on the sample surface is relatively easy with a simple color threshold. Finding the cantilever probe of unknown geometry is relatively more difficult. Fortunately, there are not many different geometric shape of the passive cantilever design. If an optical image of the cantilever is available, a template matching algorithm can identify find the probe relatively easily.

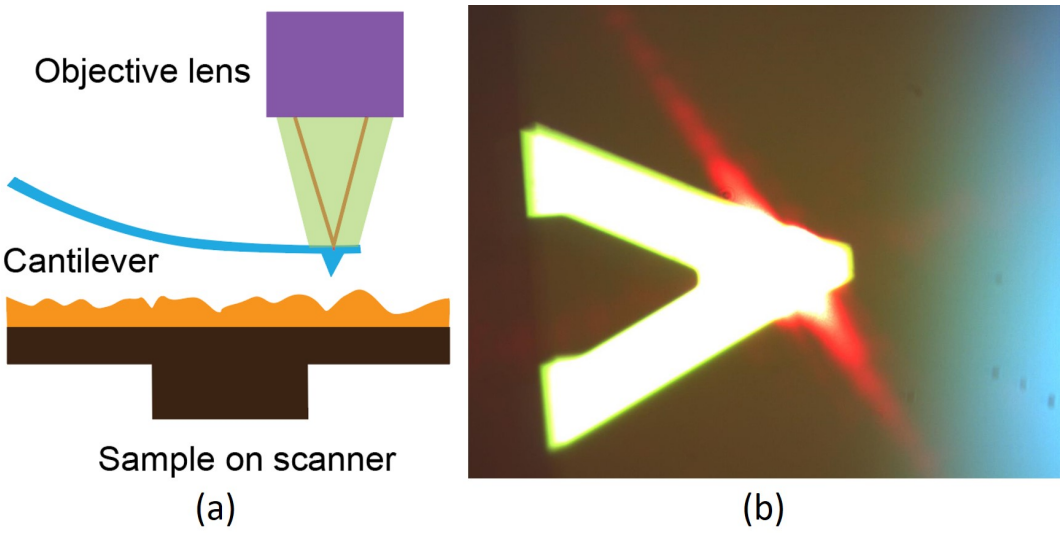

Figure 5-18: Cantilever probe laser alignment: (a) conceptual illustration of the overall goal, (b) optical microscope image of aligned cantilever probe (away from the sample) and laser

The main challenge of finding the cantilever tip is the 3D space search over a relatively large area. Very few guiding features are available when the optical view is not focused onto the sample or the cantilever probe. This task becomes more challenging with the limited field of view and depth of focus of the objective lens with high numerical aperture used for laser focus. Instead of searching for the cantilever directly, we decided to search for the edge of the probe base support chip, which has a larger dimension and relatively easy to identify.

The automatic alignment process has primarily three steps. The steps are: (1) sample surface focus, (2) probe edge search and (3) cantilever search.

Sample Surface Focus

The first step in the alignment process is to identify the sample surface as a reference point. This is done by a search along the out-of-plane direction. We assumed the objective lens is far away from the sample and the filed of view is beyond the far end of the cantilever. This allows proper focus on the sample surface without being obstructed by the cantilever probe holder. To determine whether the sample surface is in focus or not, the Laplacian of the 2D image is used as a contrast measure as

we try to maximize the sharpness of the image. This process is relatively simple as various sharpness evaluation methods and auto focus algorithm in the literature can be applied [181, 182].

After the camera is focused on the sample surface, the laser is turned on. A threshold in the red color channel is applied to the optical microscope image. The center location of the laser can be determined by fitting a circle around the laser spot or using a weighted average. Since the laser optics is moving together with the optical system, its relative position is fixed in the frame. We turn off the laser after getting its location in the optical view during the search for the cantilever to avoid optical confusion. The laser is turned on again after the alignment process is completed.

Probe Edge Search

The next step is to search in 3D for the probe base support chip edge. Before probe sample engagement, the cantilever tip is typically several millimeters above the sample surface. With a small depth of focus of the objective lens used in this design, the sample surface will be out of focus during the search of the cantilever. We start the search by gradually move up the objective lens 50 μm at a time. To reduce the search space, we start from the far end to the cantilever base support chip and move until an edge is found. If no edge is found, we raise the objective lens to search in the next focal plane.

The algorithm uses two separate methods of edge detection. The first algorithm is the binary brightness threshold with use of Otsu's method to account for possible differences in microscope brightness settings. This method can easily detect the probe edge, even when it is slightly out of focus, but it also tends to give false positives. Even a gradual change in brightness will create a threshold. The second method is the Canny edge detection. By taking local contrast into consideration, Canny edge detection does not create false positives on gradual gradients. However, the contrast between the dark probe body and the dark background is difficult to detect. Lowering the threshold for Canny edge detection tends to introduce artifacts from small light intensity variation due to the sample.

Straight lines are extracted from the detected edges. The proposed algorithm

applies the probabilistic Hough line transformation to the output images created by both methods, specifically filtering for long lines indicative of a long, straight edge. By combining results from both methods, we can correct for the different kinds of false positives detected by each method to produce a better result.

Cantilever Search

The last step is to find the cantilever tip and align it to the laser location obtained in the first step. This is completed by tracing along the support chip edge and applying template matching to find the cantilever. To follow the base support chip edge, we use the lines generated from the Hough line transformation. The template matching algorithm is applied to determine if the cantilever is within the field of view or not. The line tracing continues if the cantilever cannot be detected in the field of view.

The cantilever itself can be an issue for line tracing. Since the cantilever is much brighter than the background due to the reflective coating, the edge will disappear if the probe tip comes into view using Otsu's method for threshold. To resolve this issue, we ignore all pixels above a certain brightness while following the edge. The brightness threshold also helps the identification of the cantilever itself. We locate the probe tip by taking the far end away from the probe base chip edge as the cantilever tip to be aligned with the laser spot.

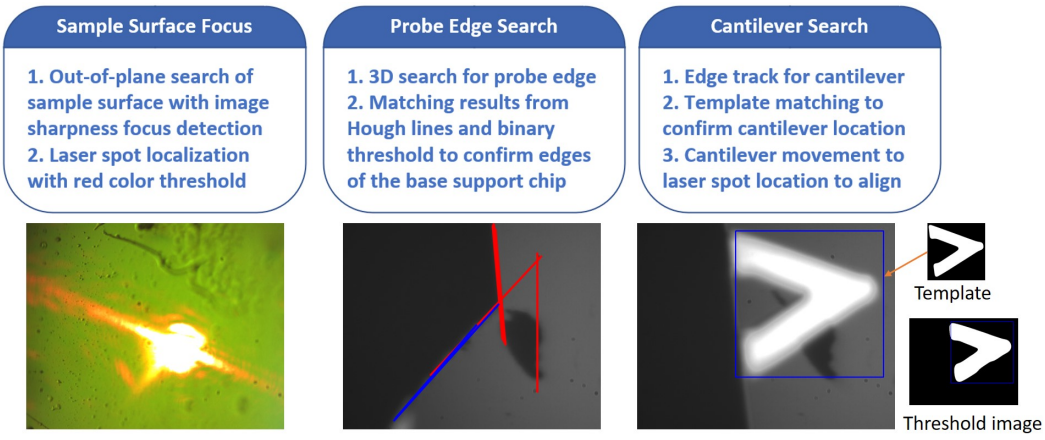

Figure 5-19: Algorithm illustration and imaging processing steps for the automatic probe-laser alignment process

A visual illustration of the proposed algorithm is shown in Fig. 5-19. The proposed method is effective in locating the cantilever but can be time consuming primarily due to relatively slow motion speed of the piezo inertia actuator.

A better focus of optical microscope on the cantilever is needed in some cases. A finer search across the depth with smaller incremental steps can be used after finding the cantilever to improve the focus. The sharpness measure for focus detection used in step one can potentially be applied again around an dilated area of the identified cantilever.

5.4.4 AFM Data Processing

The data collected by the AFM instrument usually require post processing. Image processing algorithms are applied to visualize, correct and analyze the data to extract feature information. Depending on the purpose of the experiment, image processing techniques can be applied to count the number of blobs in the image, measure the volume of residual above certain thresholds, compensate for sample tilt during the experiment, etc. The open source Gwyddion software includes a number of verified algorithm implementation suitable for SPM data analysis. Gwyddion also offers interfaces to the Python programming language for the batch processing of multiple AFM images. Dedicated software by AFM vendors such as Bruker NanoScope Analysis.

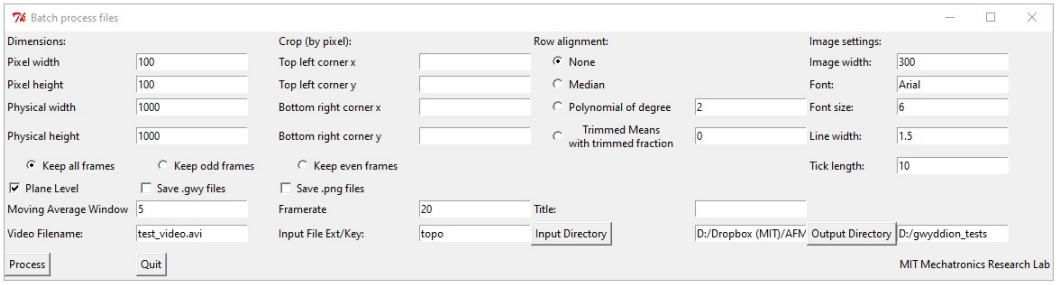

Figure 5-20: PyGwyddion software graphical user interface for batch processing AFM images stored in a folder with identical settings as a predefined macro

In this work, the processing of a series of AFM images are needed with data taken by the high-speed system. To do so, a Python to Gwyddion interface as shown in Fig.

5-20 has been developed. The software interface allows programmatic batch processing of multiple images by repetitively applying the processing steps like a recorded macro. After selecting the desired input data files generated from LabVIEW, each image is processed with prescribed steps such as tilt correction, line matching, etc. The Python-Gwyddion interface partially automates the post-processing procedure to save manual labor from conducting repetitive tasks.

Depending on the modes of operation, modern AFM systems can collect large amounts of data in a short time. The data can then be analyzed with big data techniques [183]. Each spatial location can have multi-dimensional data associated like a spectrum, which makes the image a map of hyper-pixels. A basic version for handling topography data is implemented in this work for video generation. Matlab offers better flexibility to add custom processing code while Gwyddion provides more built-in functionalities to safe development time.

Collecting large amounts of data in a short time demands high-throughput DAQ systems. The required data collection rate D can be computed based on Eq.(5.8) with the frame rate FPS, the discrete frequency bins F, the pixel resolutions X, Y, the number of modality channels (parameters) n, and the data bit resolution B. A visual representation of the contributing factors is also provided in Fig. 5-21.

$$D = FPS \cdot F \cdot (X \cdot Y) \cdot F \cdot N \tag{5.8}$$

For example, if we consider an AFM imaging data with resolution $B = 16$ bit resolution and high in-plane pixel resolution $X = 1024$ and $Y = 1024$. For a common AFM image, the sweeping frequency would just be a single point $F = 1$. There will be the topography and the error signals so that $N = 2$. Assuming a high frame rate of $FPS = 25$ is used. This would result in a data rate approximately at 800 $Mbps$. Even in this simple case, this is already a significant data transfer rate. If additional modalities need to be captured at each pixel, the requirement of data transfer rate can be even more significant.

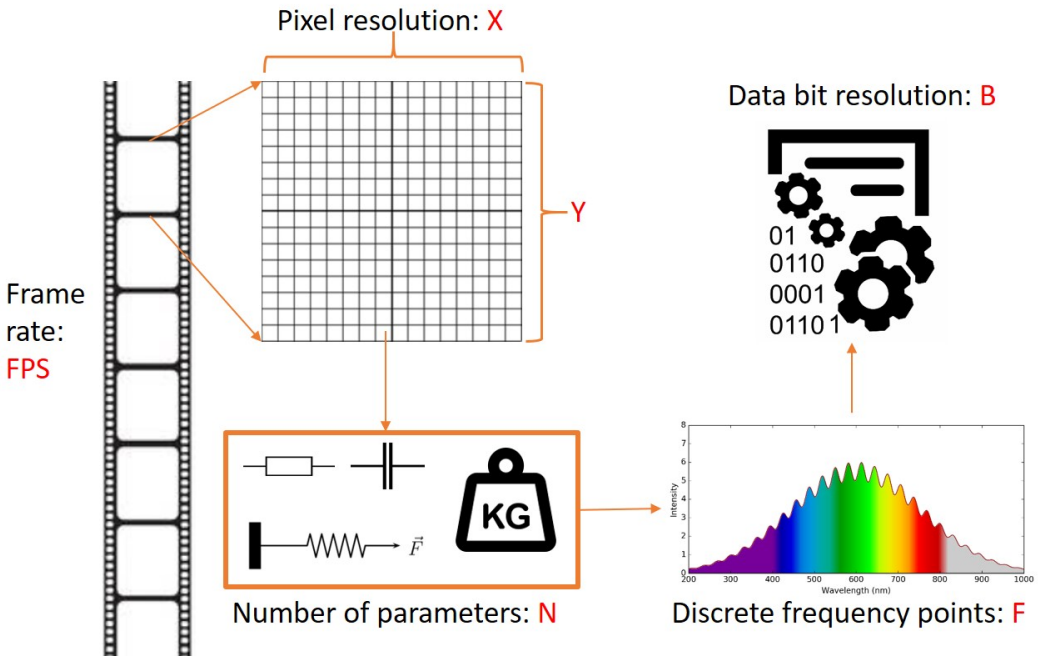

Figure 5-21: Multidimensional SPM data collection resulting in a quick growth of image size and storage space requirement

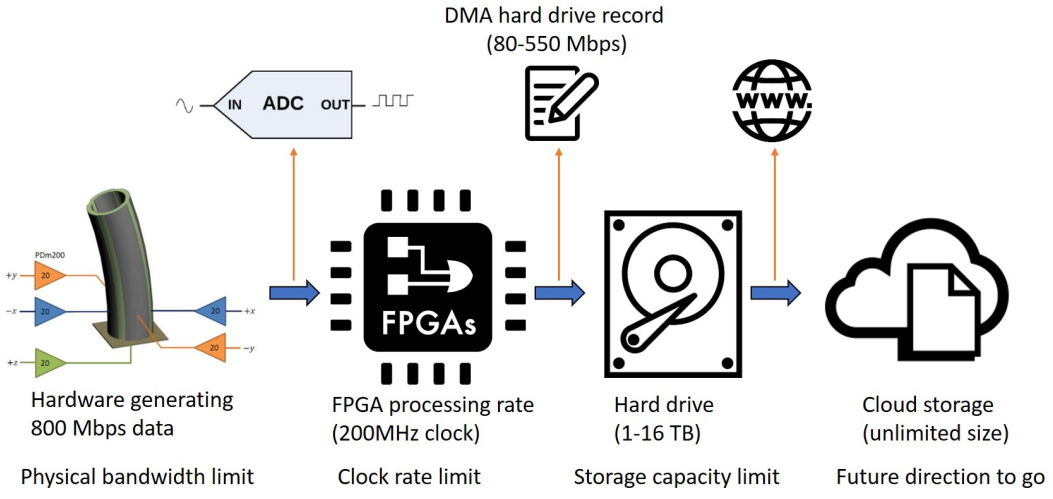

Figure 5-22: SPM data collection pipeline and typical capabilities and limitations of existing systems for proessing speed and data storage size

In addition to the DAQ system bandwidth, the data processing capability of various systems can become a bottle neck. As illustrated in Fig. 5-22, the collection

of AFM data goes through multiple stages of processing that are limited in bandwidth. With recent development of data acquisition systems with higher bandwidth, large amount of data can accumulate quickly at the rate of mega samples per second.

The concept of deep data is also suitable for describing AFM imaging. Multiple processing steps are involved to collect and analyze AFM data as shown in Fig. 5-23. Starting from the force interaction, the measured data has been processed by the cantilever transducer, deflection readout sensor, data acquisition system, demodulation and control algorithm, SPM image formation and image processing algorithm. The AFM data analysis could benefit from identification and optimization to reduce source of error. Meaningful insights may also be extracted by applying data driven learning techniques for analysis.

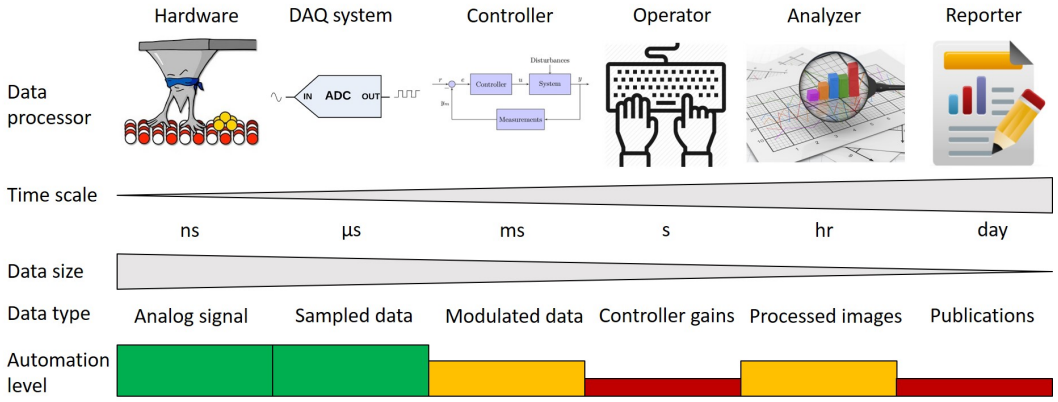

Figure 5-23: AFM experiment data generation and processing pipeline illustrating a multi-step process with increasing feedback timescale and reducing data size to extract meaningful insights

5.5 Additional Components

In addition to the aforementioned components, a number of additional components are involved. These include optical tables for vibration noise isolation, voltage range mapping electronics for DAQ to controller interface, power sources for electronics, various mechanical fixtures, etc. For development of AFMs with additional modalities, more accessories are added to realize the functionality such as optical components for

scanning near-field optical microscopy.

5.6 Chapter Summary

In this chapter, the supporting AFM subsystems centered around the cantilever probe and the scanner are discussed. First, the design of high-bandwidth driving electronics and charge control circuit for piezo hysteresis compensation are discussed. Next, the cantilever interface components such as mechanical holder, optical system and electronics for tapping mode signal processing are covered. In the end, the software implementation of control algorithms, probe-laser alignment and AFM post-processing are illustrated. These systems work with the cantilever probe and the scanner to form complete AFMs for various applications. The development in this chapter corresponds to the fourth to sixth main contributions for electronic drivers, optical system with vision-based automation, and software implementation.

Chapter 6

System Integration and Imaging

6.1 Introduction

Throughout my years of research at MIT, three AFM systems have been developed in our lab. Based on their application scenarios, they are described as the versatile sample scan system, the multi-layer stacked scanner AFM and the low-cost educational AFM. The AFM designs are based on mix and match of the subsystems introduced previously in this thesis. In this chapter, we focus on the overall system integration design of these AFMs and provide imaging results for various applications.

6.2 Versatile Sample Scan AFM

The versatile sample scan AFM is the first system constructed in this work. The overall goal of this design is to develop a versatile AFM that can visualize dynamic processes with overview and zoom. The system utilizes a sample scan configuration that can handle samples with diameter up to 10 mm. The design can work with small passive cantilever probes for high-speed imaging in both ambient air liquid. As an upgrade based on the design previously developed in this lab [76, 184], the AFM can now work with coated piezoresistive sensing thermomechanical actuation active cantilever probe for harsh opaque liquid imaging.

The imaging requirements for AFM operation can cover a vast range. This can be

better understood via an analogy. Let us consider scanning over an area of 100 μm by 100 μm as creating a topography map for the entire mainland of the United States. With similar ratio in terms of area, scanning over an area of 500 nm by 500 nm would approximately be equivalent to topography mapping of the Boston city. An airplane with a camera system and a distance sensor would be sufficient to cover the topography mapping of the Boston area. On the other hand, a satellite would be more appropriate for mapping of the entire U.S. due to the size.

The versatile sample scan AFM system takes an overview and zoom approach for handling imaging at different scan ranges and bandwidths. A large-range scan at a relatively low line rate is performed first to obtain a static overview of the sample. After identifying the area of interest, a high-speed local scan is performed to obtain video with high temporal resolution. The system is capable of scanning a 100 μ by 100 μ large in-plane range at a rate of 4 lines per second. For the large area overview, a 100 μm out-of-plane tracking range is available to cover the topography variation. For high-speed local imaging, a nominal 3 μm by 3 μm in-plane range with $10,000$ line per second can be realized for contact mode scanning. A maximum range of 6 μm by 6 μm is possible at a reduced line rate. An out-of-plane range of 1 μm is available for topography tracking. The actual scanning speed used for image generation also depends on the sample properties to ensure good tracking.

6.2.1 System Integration

The overall design of the versatile sample scan AFM is shown in Fig. 6-1. The primary components include the positioning system, the optical system, the cantilever probe and interface, electronics and data acquisition system.

Positioning System

For coarse positioning, a DS40-XYZ positioner from Newport is driven by a PK523HPA-H50S stepper motor from Oriental motors coupled with a flexible bearing. The out-of-plane engagement has 12.7 nm per step resolution as computed in Chapter 2.

For scanning, the multi-actuated music wire fast scanner stacked on P-611.XYZ

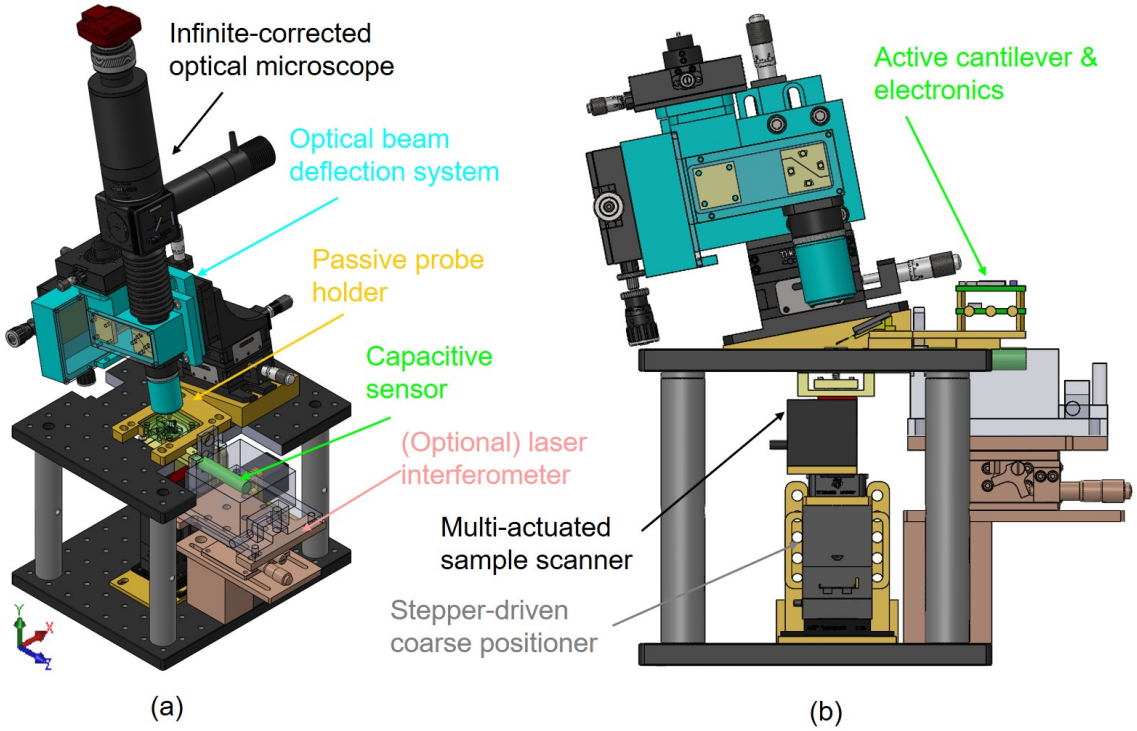

Figure 6-1: Versatile sample scan AFM design: (a) isometric view of the system configured for passive probe imaging, (b) front view of the system configured for passive cantilever probe

positioner from PI is used as shown in Fig. 2-12 in Chapter 2. A capacitive sensor (Microsense 6800) is added to provide feedback signal to the controller. A Teflon sheet is added to protect the scanner from potential liquid spill during experiments.

Cantilever Probe and Holder

Both passive and active cantilever probes can be used in this AFM system design. For passive cantilever probes, commercially available standard cantilevers can be mounted onto the custom designed holders. A piezo actuator is embedded into the cantilever holder for piezoacoustic actuation as introduced in Chapter 5. For high-speed imaging, smaller probes with higher resonance frequencies such as USC-F0.3-k0.3 and USC-F1.2-k0.15 from NanoWorld can be used.

For active probes, the piezoresistive sensing thermomechanical actuation cantilever is used. The first and second stage of amplification electronics are installed on a plate holder together to directly replace the passive probe holder.

Optical System

The optical system design as introduced in Chapter 5 is used for deflection measurement of small passive cantilever probes. The objective lens can be exchanged to work with cantilever probes of different sizes. The automatic alignment system is also implemented on this AFM for handling of passive probes. The optical system is bolted on a machined optical breadboard assembled using mechanical components from Thorlabs. Visualizations of the mechanical components for the implemented sample scan AFM system are shown in Fig. 6-2.

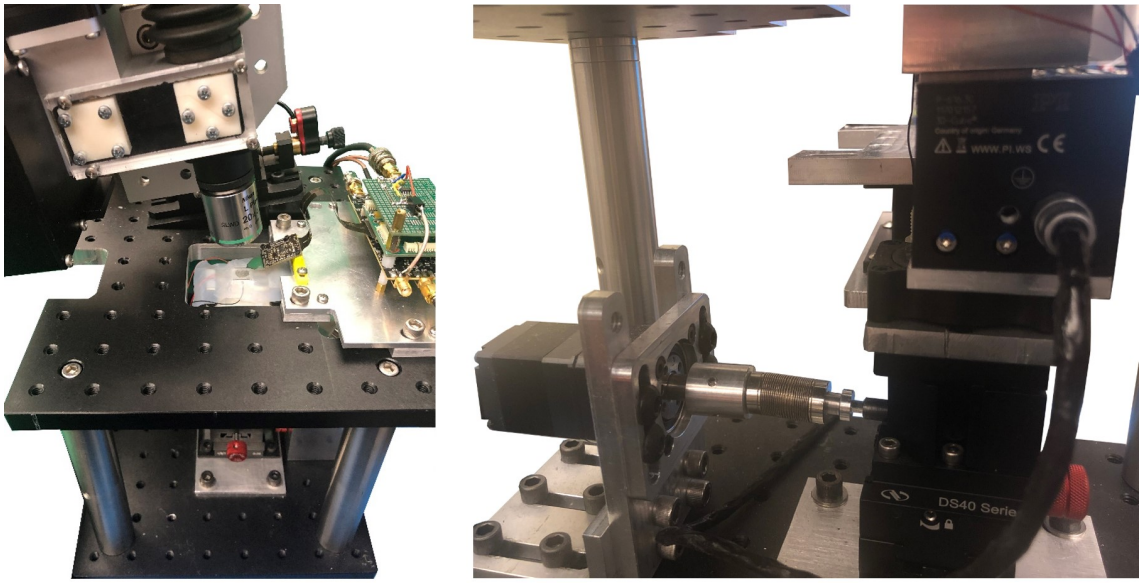

(a) (b)

Figure 6-2: Versatile sample scan AFM implementation: (a) top front view image of the implemented AFM system with active cantilever probe configuration, (b) zoomed in view of the stepper motor, coarse positioiner and multi-actuated scanner

Electronics and Data Acquisition

To drive the piezo actuator, power amplifiers from various vendors are used. These include PI, PiezoDrive, Techproject, nano analytik GmbH and custom designed drivers as introduced in Chapter 5. For signal processing, the photodiode circuit is used for the optical deflection system. Wheatstone bridge circuits with amplifiers are used to obtain the deflection signal. In this design, the (de)modulation, scanning and controller design are all implemented digitally on two FPGA systems. A Na-

tional Instruments PXIe-1085 chassis with a PXIe-8135 embedded controller are used as the host computer for the two FPGAs PXIe-7975R and PXIe-7066R. The PXIe-7975R handles the high-speed (de)modulation, motion control in the out-of-plane Z direction and data logging. Two output signals to the probe and the hgih-speed Z positioner and one input from the probe deflection measurement are sampled with a high-bandwidth analog dual-input and dual-output transceiver adapter module (NI 5782) interfacing with the PXIe-7975R FPGA. The PXIe-7066R FPGA handles the in-plane fast scanning, coarse scanning and engagement of the AFM. The LabVIEW software for overall control and Python software for automatic probe laser alignment as discussed in Chapter 5 are both running on the PXIe-8135 controller.

6.2.2 Large-range Imaging

The large-range scanning capability of the probe scan AFM system is used to overview the sample at relatively slow scan rate. To verify its capability, an 100 μm by 100 μm overview AFM image of calibration grating is taken as shown in Fig. 6-3.

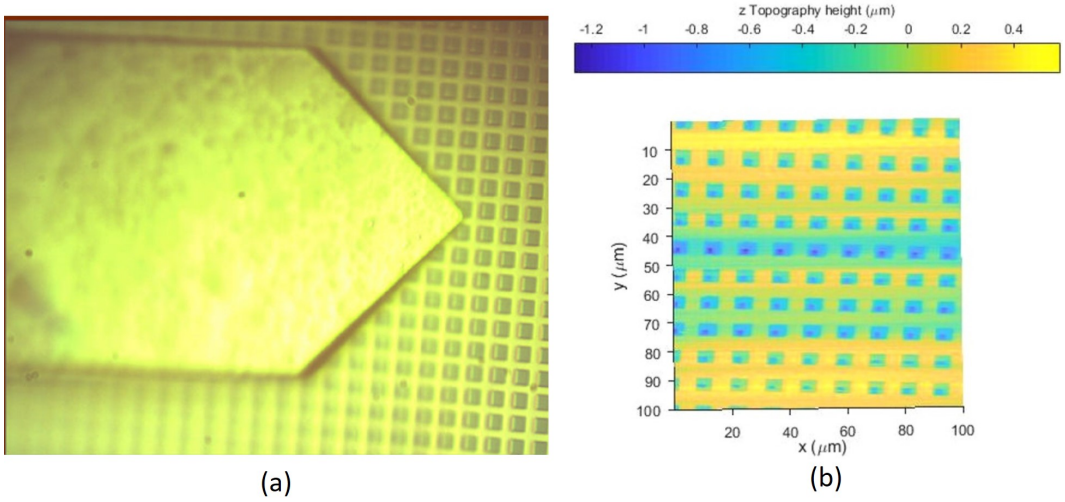

Figure 6-3: Large range overview of a calibration grating with 10 μm pitch period and 500 nm depth with active cantilever: (a) optical microscope image of the calibration grating and active probe, (b) AFM tapping mode image taken at 100 μm by 100 μm maximum scanning range and 2000 by 2000 high pixel resolution

The large-range scanner from PI is used for both in-plane scanning and out-of-

plane tracking. The image was taken using the active cantilever probe in tapping mode operation at a 2000 by 2000 pixel resolution with a speed of 4 lines per second.

6.2.3 High-speed Imaging

The versatile sample scan AFM system is capable of high-speed imaging at a small area. To verify the capability, images of calcite etching in sulfuric acid is taken in contact mode. The video is taken at 20 frames per second with an in-plane scan range of 3 μm by 3 μm corresponding to 200 by 200 pixels. Ten frames of the video spanning over 5 seconds are shown in Fig. 6-4.

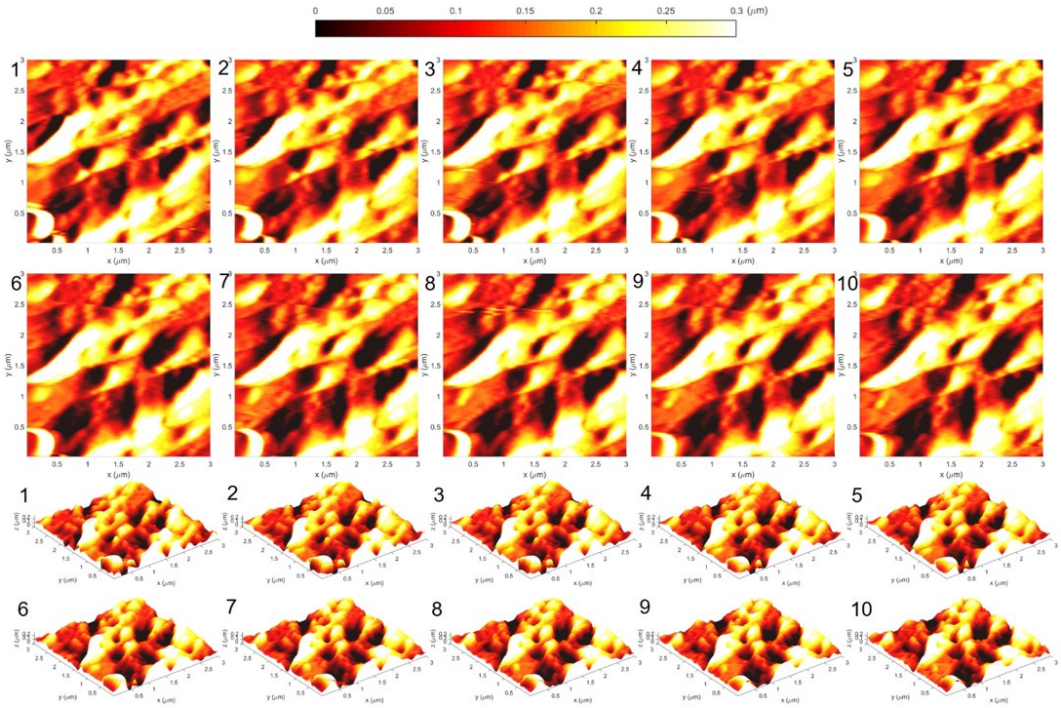

Figure 6-4: High-speed imaging of calcite etching in sulfuric acid recorded at 200 by 200 pixel resolution for 3 μm by 3 μm range at 20 frames per second. Ten frames of the data spanning of 5 seconds are visualized for both top view and isometric view. The topography changes gradually with the etching progresses.

The high-speed local imaging capability allows visualization of dynamic processes to observe the topography variation. This capability is helpful for fundamental research study of nanoscale surface phenomenon dynamics.

6.2.4 Active Probe Harsh Opaque Liquid Imaging

The versatile sample scan AFM design enabled imaging in harsh opaque liquid using coated active probes. With protective coating, the sharpness of the active cantilever probe tip is reduced. In this case, amplitude regulation tapping mode is more suitable than contact mode for better imaging resolution. We first evaluated the imaging performance of coated active probe comparatively with uncoated active probe in air. The capability of the coated active probe is then investigated in various chemical and biological environments. With tapping mode operation and considering feature size of the sample, we utilized the large range scanner to cover areas of 6 μm by 6 μm for oil imaging and 12 μm by 12 μm for acid imaging respectively.

Comparative Imaging with Crude Oil Environment

A comparative study is conducted to evaluate the capability of the coated cantilever probe imaging performance. The same sample was imaged with uncoated active probe in air, coated active probe in air and coated active probe in crude oil. The results are shown in Fig. 6-5 for comparison. In this case, a TGZ-100 calibration grating sample from Ted Pella Inc with trenches at 110 ± 2 nm step height and 3 ± 0.01 μm pitch period was imaged. We used a crude oil sample obtained from South Dakota, USA for the opaque liquid environment.

As can be seen in Fig. 6-5, the height sensitivity of the coated active cantilever probe is comparable to the uncoated probe. With tapping mode imaging of step trenches, a "parachuting effect" occurs when a sudden height reduction is scanned in the topography. The cantilever needs time to reach a larger oscillation amplitude that in turn drives the controller as it tracks the topography. Slower scanning speed, high resonance frequency and smaller oscillation amplitude setpoint helps reduce this effect but at the cost of longer imaging time and lower sensitivity. From the images (a) and (b) in Fig. 6-5, the coated probe actually demonstrated less parachuting effect, evidenced in the more evenly spread pattern in Fig. 6-5(b). This can be attributed to the smaller oscillation amplitude and setpoint for the coated active probe since other imaging parameters and imaging environment are identical. On the

other hand, the topography edge noise of the coated probe operating in oil is higher than uncoated probe in air at 4 lines per second scanning rate as can be compared between Fig. 6-5(a) and (c). By lowering the scanning rate, the noise can be reduced as shown in Fig. 6-5(d). Hence, the opaque liquid imaging capability of the coated active probe is demonstrated in tapping mode.

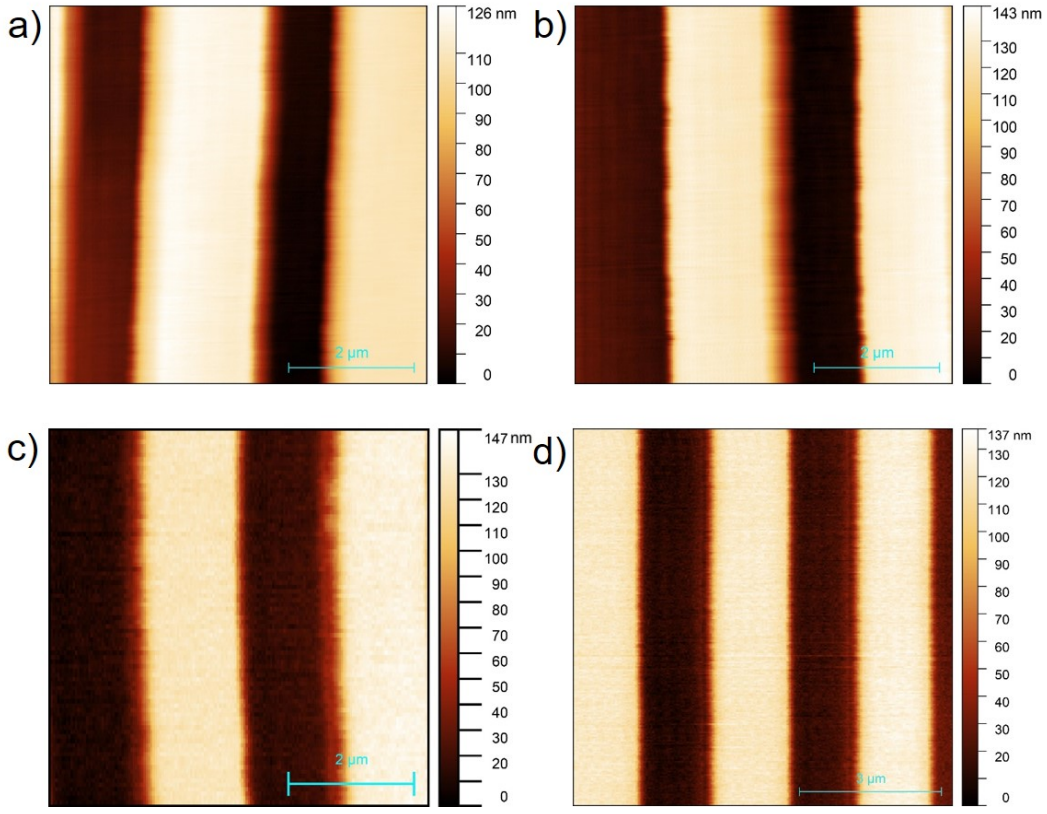

Figure 6-5: Imaging of TGZ-100 calibration sample with 6 μm by 6 μm size (a to c) for at 400 by 400 pixel resolution in tapping mode at 4 lines per second: (a) uncoated regular active probe in air, (b) coated probe in air, (c) coated probe in crude oil environment, (d) coated probe in crude oil with 8 μm by 8 μm size and 600 by 600 pixel resolution image at lower speed 0.5 line per second for better edge resolution.

Chemical Inertness Verification in Corrosive Environment

To investigate the capability of the coated probes to resist corrosive environments, acid environment imaging was conducted. A sample with larger height variation is selected and vinegar with black color and pH value around 3 was used. Sample setup

of a TGZ-500 calibration grating and tapping mode AFM imaging result are shown in Fig. 6-6.

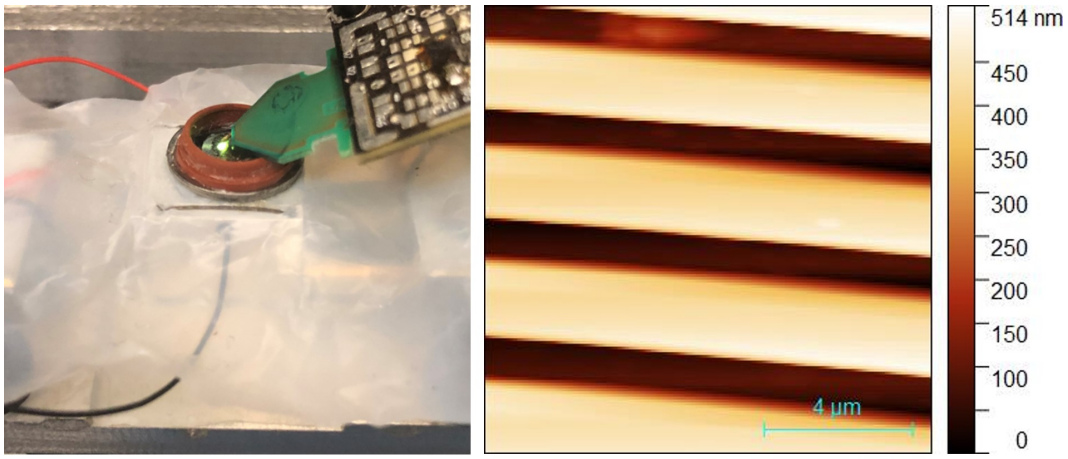

Figure 6-6: Acid imaging: (a) sample in vinegar on the Teflon sheet protected scanner, (b) tapping mode imaging of calibration grating with $Z = 520 \pm 3$ nm step height and 3 ± 0.01 μm pitch period from Ted Pella Inc with 12 μm by 12 μm range at 2 lines per second

The coated active probe performs well compared to the uncoated probe. This indicates that the coating effectively insulate the probe from electrical and chemical agents in the harsh opaque liquid environment.

Biological Sample Immersion Test

We also conducted immersion test for whole blood sample with Ethylenediaminetetraacetic acid (EDTA) anti-coagulation treatment from AllCells LLC. The coated probe worked well at the beginning of the immersion in terms of resonance identification. However, due to the difference in densities of its components, the blood sample formed a deposition of multiple layers. In addition, the presence of heterogeneous floating cells affected the resonance frequency of the probe. These complications made the probe engagement with the sample surface a time consuming task. Furthermore, even with anti-coagulation treatment, the blood sample solidified within approximately 30 min of exposure to ambient air by forming an outer shell at the air-

blood interface. This phenomenon significantly affects the resonance of the probe and can even break the active probe. Hence, the coated probe is functional in the whole blood sample but effective imaging will require specialized treatment with chemical agents or dedicated environmental control to prevent blood sample solidification.

Coated Active Probe Operation

A number of issues can arise when operating in liquid environments. The first issue is that upon moving the probe from a gas (air) into a liquid environment, its resonance frequency often shifts due to added mass of the liquid. This shift can be confused for engagement with the sample for reduced oscillation amplitude. Several other resonance frequency shifts occur at the end of the engagement upon approaching the solid surface. Hence, several cantilever frequency sweeps need to be conducted to ensure the actual surface of the sample is reached. Second, depending on the density and viscosity of the liquid, the first resonance frequency can become significantly lower such that the amplitude demodulation speed is too slow. In this case, second mode of the resonance frequency can be utilized for imaging. Finally, due to the surface tension and wetting effects of liquids, residuals of the liquid remain on the polymer coating of the probe after experiment. After drying in air, the residual particles can change the mechanical properties of the probe or react with liquid in the next experiment. Therefore, it is necessary to clean the probe in chemical solution to dissolve residual particles. The probe needs to be rinsed in deionized water and then dried in a clean environment to avoid dust attachment.

Based on our experience with the coated active cantilever probe, several potential improvements can be made. First, the thickness of the coating should be reduced for a smaller added mass. Second, the overall probe stiffness increase caused by the coating should be minimized to maintain original probe oscillation amplitude for imaging sensitivity considerations. Third, bonding strength of the coating with the probe should be improved to sustain long time operation without added nonlinearity. Last but not least, increasing the overall coated area to cover the entire electronics area to allow deeper immersion into the liquid environment would be helpful for experiment purpose. Vapor deposition techniques would be an ideal future method of adding the

coating because it offers good bonding and atomic level thickness control. However, the development of such coating requires augmentation of the nano-fabrication process. This will require significant investment of time and capital for development. Another promising potential method is to apply parylene coating, which allows control of coating thickness below one micron. Parylene coating can also resist harsh chemical environments and be applied after probe fabrication with current design. More information on the coated active probe AFM can be found in [26].

In summary, the sample scan AFM system has addressed multiple challenges as introduced in Chapter 1. First, the imaging speed issue is addressed with an overview-and-zoom approach. Second, the AFM versatility problem has been tackled by using coated active cantilever probe for harsh opaque liquid imaging. Moreover, the interchangeable holders allow working with both active and passive cantilever probes to further improve the versatility. Third, the experimental setup overhead for probe laser alignment is removed by the use of active cantilevers. For passive cantilevers, the automatic probe-laser alignment algorithms as discussed in Chapter 5 are implemented on this system.

6.3 Multi-layer Stacked Scanner AFM

The stacked scanner AFM is the second AFM system developed in this work. Due to the bandwidth and range trade-off as discussed in Chapter 2, scanning a large area at high frame rate can be challenging. The previous overview-and-zoom approach avoids directly handling this problem while this design attempts to have a balanced trade-off. With the specialized design of the multi-layer stacked scanner, high-bandwidth scanning at a relatively larger range can be achieved. The system can use a probe scan configuration to handle samples with larger physical dimension. In cases when the sample dimension is smaller than the cantilever probe, a sample scan configuration is preferred for high bandwidth operation. The overall multi-layer stacked AFM system CAD design is show in Fig. 6-7.

The stacked scanner AFM system integration is to a large extent similar to the

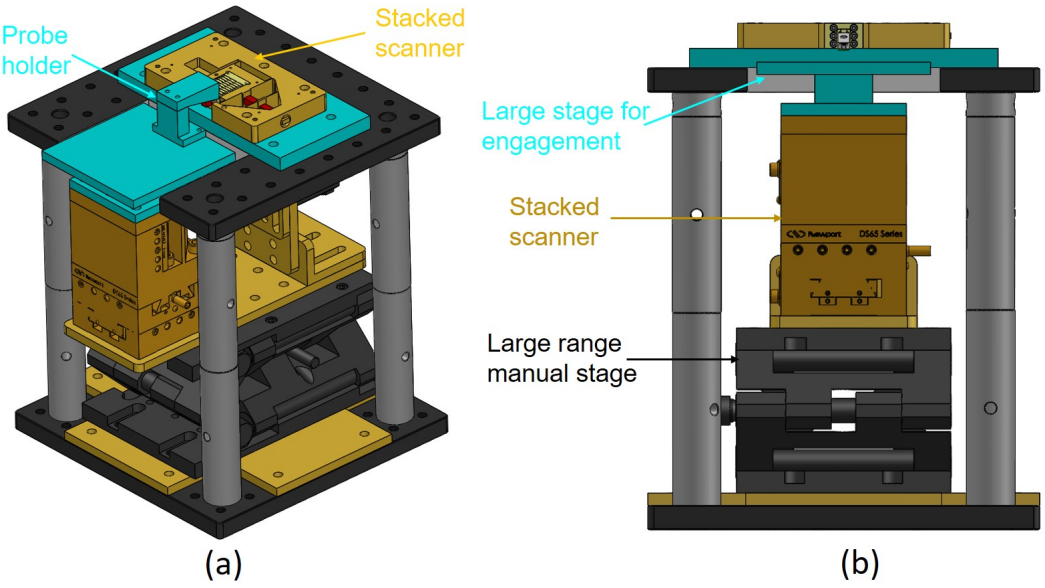

Figure 6-7: Multi-layer stacked scanner AFM CAD design: (a) isometric view of for sample scan configuration, (b) front view for probe scan configuration

sample scan AFM with several exceptions. First, the sample scanner is replaced by the multi-actuated stacked scanner. Notice that five flexure layers are used with two stacked piezo actuators within each layer to simplify the assembly without sacrificing the performance. A DS60-XYZ positioner from Newport and PK223PB-SG36 stepper motor from Oriental Motors are used for automatic probe-sample engagement. Second, a piezoresistive sensing cantilever from SCL is attached directly to Z axis positioner for out-of-plane positioning. This cantilever has a smaller packaging geometry compared to the piezoresistive sensing thermomechanical actuation active probe, which is ideal for high bandwidth scanning. As the system only uses cantilevers with embedded sensing, there is no need for the external optical components. Third, charge control driving electronics and signal conditioning circuits to process the piezoresistive cantilever measurement are used. Due to the geometric constrain of the scanner, it is not convenient to add feedback sensors for piezo hysteresis compensation so that hardware level compensation with charge controllers are utilized. Other than these differences, the data acquisition and mechanical components integration are similar to that of the sample scan AFM discussed previously.

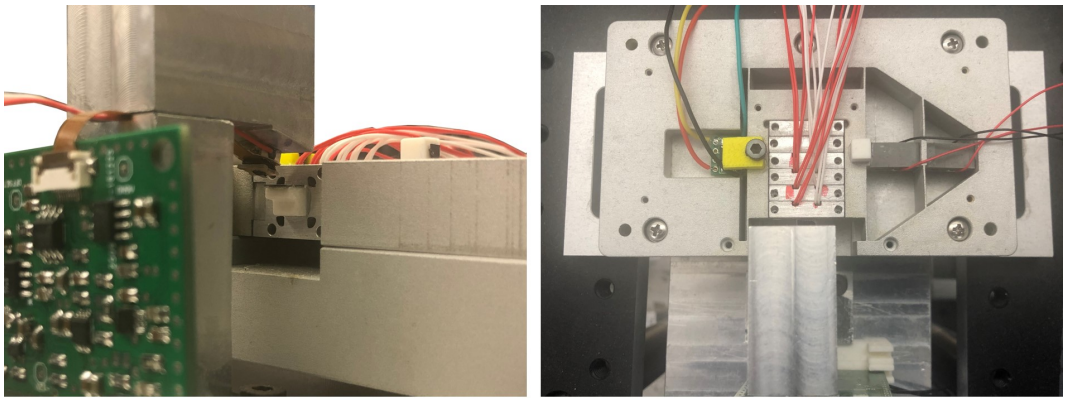

Figure 6-8: Multi-layer stacked scanner AFM implementation: (a) top view of the system in sample scan configuration, (b) closed-up view of the sample, scanner and probe assembly

6.3.1 Imaging Experiments

To demonstrate the functionality of the stacked scanner AFM design, high-speed videos on calibration gratings are taken as shown in Fig. 6-9 and Fig. 6-10.

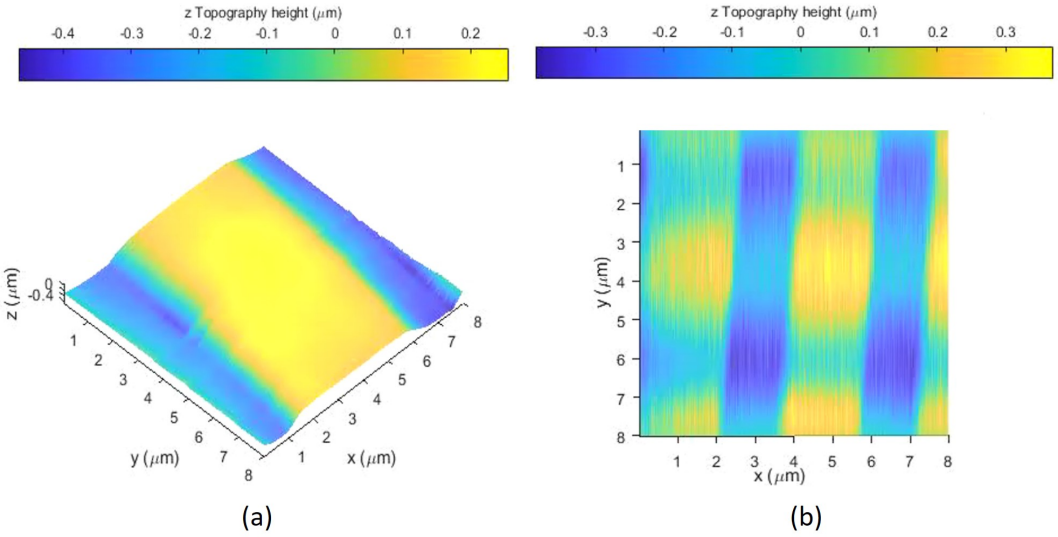

Figure 6-9: Multi-layer stacked scanner AFM image with 8 μm by 8 μm range and 400 by 400 pixels: (a) isometric view of 10 μm pitch period image taken at 20 lines per second, (b) top view of 3 μm pitch period taken at 1 frame per second (400 lines per second)

The 3D isometric view of the calibration grating area with a 5 μm wide (10 μm

pitch period) and 500 nm height step is shown in Fig. 6-9(a). Triangular wave raster scan at 20 lines per second is used to generate the static image. In Fig. 6-9(b), a 400 lines per second triangular wave raster scan is performed to push the frame rate up to 1 FPS. The sample is a calibration grating with 3 μm pitch period trenches.

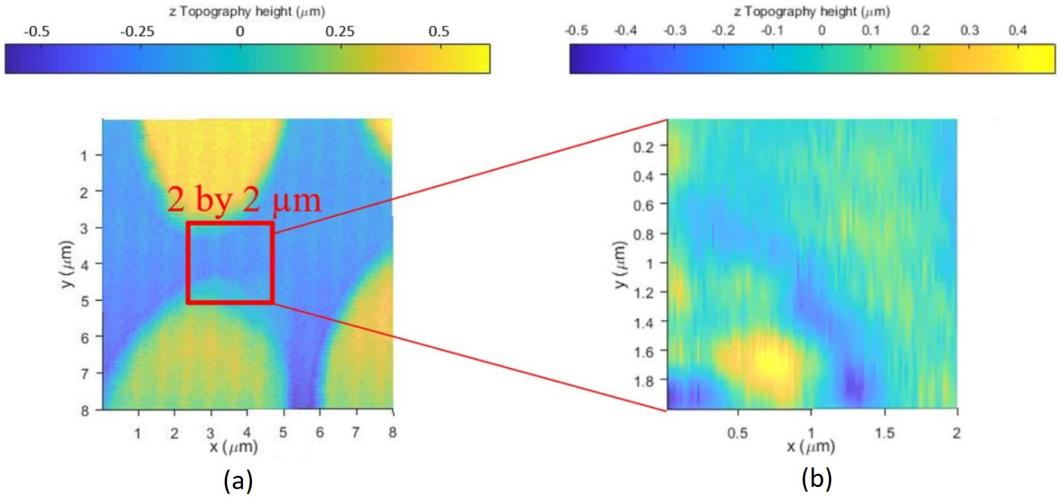

Figure 6-10: Multi-layer stacked scanner AFM image of calibration grating with 5 μm size circular pillars with 500 nm depth: (a) 400 by 400 pixel overview for 8 μm by 8 μm range at slow scan rate (4 lines per second), (b) zoomed-in high-speed imaging at 2000 line per second with 2 μm by 2 μm range

An overview-and-zoom scheme is applied again in Fig. 6-10. A static image of circular pillars is taken with a relatively large 8 μm by 8 μm area at low speed (4 LPS). A zoomed-in high-speed image is taken using the high-bandwidth capability of the multi-layer stacked scanner at 2 kHz. The multi-layer stacked scanner is capable of covering a larger range than the dual-actuated music wire scanner. Therefore it can be used for imaging of samples with larger feature sizes. When handling samples with larger geometric size, the probe scan configuration can also be used. In terms of drawbacks, the multi-layer stacked scanner AFM cannot be used for liquid environment operation due to the lack of protective coating for the commercially bought piezoresistive sensing cantilever. The driving needs of the scanner is also more complicated due to the increased number of actuators involved.

With the development of the versatile sample scan AFM and the multi-layer stacked scanner AFM, the first three limitations discussed in Chapter 1 have been

addressed. The designs increased AFM imaging throughput, extended AFM operation versatility and reduced AFM experimental overhead using various strategies. The images taken by the two integrated AFM systems have also demonstrated the functionalities of the subsystems introduced in the previous chapters.

6.4 Low-cost Educational AFM

The third AFM developed in this work is the low-cost educational AFM. We introduced the development of this AFM starting from the design intent.

Most AFM users are nanotechnology researchers working in the fields of material science, chemistry and biology. However, the modification of AFM systems requires knowledge in the fields of mechatronics and instrumentation typically beyond the expertise of nanotechnology researchers. As discussed in Chapter 1, there is a lack of education for hands-on AFM design and implementation, which is mainly due to the lack of modular affordable AFM platforms. Therefore, we propose a low-cost educational AFM system design in this work. We start by analyzing the contemporary AFM education and establishing the educational AFM platform design principles. Existing educational AFM systems are analyzed based on the educational needs and design principles. We then optimized the AFM subsystems to work with limited resources for cost reduction such as the buzzer scanner, hardware (de)modulation circuit and myRIO software implementation as discussed in previous chapters. The system integration and imaging capability verification results are covered in later part of this section. In the end, the educational curriculum development centered around this AFM platform is discussed to emphasize the broader impact on the community.

6.4.1 Contemporary AFM Education

The most common type of AFM education focuses on the operation of the equipment for imaging purposes. The target audience are typically students conducting nanotechnology research. Starting from basic contact mode topography imaging, students are gradually exposed to more complicated applications such as non-contact

(tapping) mode operation, liquid environment imaging, nano-mechanical property mapping, etc. For example, the characterization facility at the University of Minnesota offers a series of 2 hour training sessions for novice users. AFM textbooks for equipment operation such as reference [185] can be used as principle introduction to combine with the hands-on training. To produce high quality images for research papers, expensive high-end AFM systems and a significant time commitment from the trainer are invested for a small number of advanced users. Full scale AFM systems are usually needed in this situation.

The second type of AFM education aims to provide a general overview of AFM imaging. In this case, a relatively low cost and sometimes portable AFM system is utilized for demonstration. The students are introduced to the general operation of AFM systems in one or two lectures followed by a hands-on demonstration. The 2.675 Micro and Nano Engineering Laboratory class at the Massachusetts Institute of Technology (MIT) is a good example for this level of education where AFM is introduced as one of the nano-scale imaging tools. Affordable or portable AFM designs are ideal for such demonstration [186, 187, 188].

The third type of AFM education focuses on theoretical understanding of the operational principles of the AFM system while hands-on operation of the system might not be necessary. Due to the complexity of the AFM instrument, a semester long class named Fundamentals of Atomic Force Microscopy was developed at Purdue University to introduce the detailed physical models for AFM operation [189]. There is no need for an actual AFM system with the focus on physical principles. Modeling tools such as Matlab or Mathematica can be helpful [190].

With different education purposes, the AFM system suitable for each scenario varies to a great extent. This work intends to extend the educational capabilities of AFM systems to include the advanced mechatronics and precision instrumentation curriculum. Hence, the system design principle will be significantly different from existing systems due to the difference in educational purposes.

6.4.2 Educational AFM Design Principles

First, the system needs to be affordable. The cost of the overall platform should be comparable to the budget typically available for a lab-based university class. In addition to initial fixed cost investment, the consumable components for each semester should also be kept low. In an AFM training class, the primary consumables are the samples and the probes. However, for a class focused on instrument development, the consumable components may also include custom designed scanners, driving electronics and mechanical mountings. The manufacturing cost for materials and tools should also be considered.

Second, the system design should be modular. In the field of mechatronics, it is important to obtain hands-on experience by implementing the system. However, due to the complex nature of the AFM system, there is a high chance of failure. In order to ensure a rewarding learning experience for the student, a modular design is ideal to ensure a functional assembly as broken subsystems can be replaced. More importantly, subsystems can be upgraded easily to allow more advanced research applications.

Third, the system operation should resemble a conventional AFM system but be more user friendly. The proper alignment of the laser spot and probe tip plays an important role for successful AFM imaging. This is often a time-consuming task that demands significant experience with the instrument. The handling of small size passive probes can also be intimidating to novice users especially with the delicate and expensive nature of the probes. For an educational environment, it would be ideal to reduce experiment overhead and avoid equipment damage due to operational mistakes on a fundamental design level. Therefore, the system design should be more user friendly to reduce experiment overhead. High power electronics should also be avoided to ensure safety of novice users.

Fourth, the AFM should be designed with a number of experiments that can be run on the individual subsystems. During the learning process, it is important to make connections between the theoretical models and the experimental results. As

an AFM platform designed for educational purpose, corresponding lab experiments designed with each subsystem can help the students to further their understanding of the instrument.

Benchmark Systems

Before diving into the design of the proposed system, an overview of the existing low-cost AFM systems for educational is provided as benchmarks. The expensive high-end research grade AFM systems are not included into this analysis due to the budget limitation for university classes.

The first type of commercialized educational AFM system focuses on the development of a portable device. The designs maintain the original functionality and operation of AFM system as much as possible. Two good examples of this category include the NaioAFM [186] developed by the company Nanosurf Inc. and the ezAFM [187] developed by the company NanoMagnetics Instruments. Both of these two instruments have a compact size that can fit into a suitcase for easy storage and transportation. This allows in-class demonstration of the AFM imaging process. The cost of these instruments is on the order of $\$ 20K$.

The second category of commercialized educational AFM systems focuses on cost reduction instead of portability. With a larger AFM footprint, the systems feature modular design and allow user customization of subsystems for specialized applications. Good examples of this type of AFMs include the B-AFM [191] from AFM-Workshops and the Educational AFM system from Thorlabs. The price for base level AFM systems of this category is around $\$ 10-20K$, which is lower than the portable systems.

The third type of commercialized educational AFM system is the nGauge AFM from ICSPI based on active probe technology [188]. At a $\$ 7K$ price tag, a portable AFM with on-chip integrated scanner can be used for imaging demonstration in ambient air environment. By using the active probe technology, this system has great portability and ease of operation. However, the integration of the MEMS scanner into the cantilever chip makes it difficult to be used for instrumentation education where custom design and modification of the scanner are desired.

The fourth type of commercialized educational AFM system utilizes optical pick-up unit hacking for significant cost reduction. This type of AFM system originated from research and development for STEM education. It is commercialized by Strømlinet Nano with the name Strømlingo Neseembly AFM [192]. Instead of using a conventional optical beam deflection system, an optical pick-up unit for compact disk reading and writing is utilized for probe deflection estimation. In addition, an AFM control system based on open source Arduino platform has been developed for this design. This allows significant reduction of cost to have a Do-it-yourself (DIY) system with a price around $\$\ 5-6K$.

A comparison table of the aforementioned systems with the proposed design in this work based on the four design principles is provided in Table 6.1. The proposed design has the lowest cost with modular design suitable for instrumentation education. By using an active AFM cantilever probe with embedded sensing and actuation, it is also easy to operate for imaging experiments.

AFM System	Cost ($)	Modularity	Operation	Experiment
Nanosurf Naio	27,900	Packaged	OBD	Imaging
Nanomagnetics ezAFM	22,000	Packaged	OBD	Imaging
AFM Workshop B-AFM	19,495	Modular	OBD	Instrumentation
Thorlabs Educational	13,145	Modular	OBD	Instrumentation
ICSPI nGauge	7,000	Packaged	Active	Imaging
Stromlingo Nssembly	5,000	Unconventional	OPU	DIY
Design in this work	4,000	Modular	Active	Instrumentation

Table 6.1: Comparison of commercialized AFM systems and the proposed design

In addition to commercialized AFM systems, various open source educational SPM systems are also available. Examples include the Teaching AFM developed at MIT Media Lab and the home-built STM by Dan Berard. The MIT teaching AFM is used in nano-engineering lab classes [193] for demonstration purpose. This system features custom designed interdigitated cantilever probes with a photodiode for laser interference-based probe deflection detection. Based on the bill of materials in 2007, a cost of around $\$\ 7k$ is needed to construct this system.

Macroscopic AFMs have also been designed to illustrate the principles of AFM for

education. Examples include the LEGO2NAO project, the optical beam deflection based macroscopic AFM [194] and the voice coil actuated self-sensing cantilever based macroscopic AFM [195]. The voice coil actuated macroscopic AFM design has been used in a MIT graduate level class 2.737 Mechatronics as a teaching tool.

6.4.3 System Integration

The educational AFM developed in this work addresses the challenge by following the design principles. The overall CAD design is shown in Fig. 6-11. For the key subsystems, the buzzer based scanner introduced in Chapter 2 is used as a low-cost positioner for imaging. The active cantilever probe with piezoresistive sensing and thermomechanical actuation introduced in Chapter 3 is used again as the transducer. Custom designed driving electronics as introduced in Chapter 5 are used for signal processing. The myRIO micro-controller from National Instruments is used for data acquisition and software integration of a scaled down version of software architecture as introduced in Chapter 5.

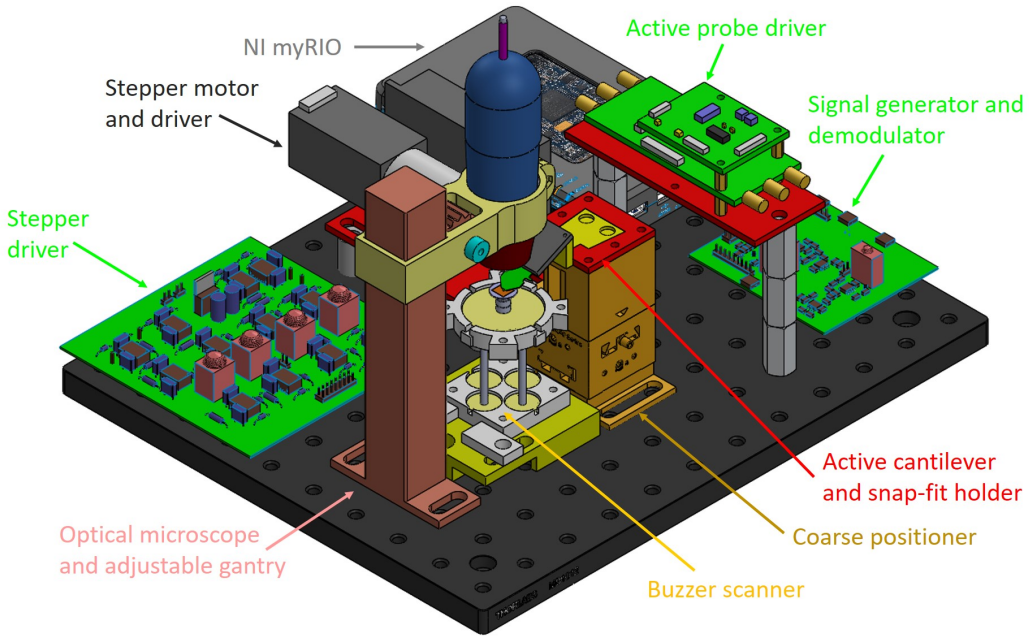

Figure 6-11: Modular low-cost educational AFM CAD design with color coded labels of subsystems

In addition to the primary subsystems introduced before, several additional com-

ponents are involved. For coarse positioning, a DS40-XYZ dovetail linear stage with 0.55 *in* square in-plane range and 0.25 *in* out-of-plane range. The in-plane directions are adjusted manually for coarse positioning. The out-of-plane direction is driven by a Nema 11 stepper motor with 100 gear reduction from StepperOnline together with a DM320T stepper driver. For the optical view, an Opti-Tekscope digital microscope with $200x$ zoom and 1600 by 1200 pixel resolution is used.

The new AFM design significantly reduced the total cost to less than \$ $4,000$. Most of the materials (around \$ $3,000$) can be reused and considered as fixed cost. For the custom designed PCBs and scanners, a \$ $1,000$ per system variable cost would be sufficient for recurring class offering. The bill of material of the system is provided below.

1. Engagement system
    - Nema 11 Stepper Motor with 100 gear reduction (\$ 41.75)
    - Bracket mount for the stepper motor (\$5.66)
    - DS40-XYZ positioning stage (\$ 435)
    - Shaft coupler (\$ 3)
2. Buzzer scanner
    - Buzzers for trial for different designs (< \$ 20)
    - 3D printing structure materials (< \$ 30)
3. Electronic Components
    - Custom designed buzzer scanner driver PCB (< \$ 100)
    - Custom demodulation and signal generation PCB (< \$ 120)
    - AC to DC power converter (< \$ 150)
    - Driver circuit for active cantilever probe (\$ 400)
4. System integration

- Optical Breadboard ($ 134.64)
- Mechanical fixtures for nuts, bolts, spacers, etc. (<$ 50)

5. NI myRIO 1900 ($ 567) (shared cost with other courses)
6. Active cantilever probe: ($ 130piece)
7. Optical microscope: ($ 69.95)

6.4.4 Imaging Experiments

To verify the imaging capability of the low-cost educational AFM system, imaging experiments are conducted. A TG-XYZ03 calibration sample with 500 nm feature depth in the 5 μm pitch area with pits is selected for imaging. The bottom buzzers are used for in-plane scanning across a 15 μm square range and the middle buzzer is used for out-of-plane topography tracking. The imaging result is shown in Fig. 6-12. With the tilting angle of 15° of the active cantilever probe, the bottom of the pits is a bit distorted. This is potentially due to the the probe oscillation being affected by the edge of the pits rather than reaching the bottom and the "parachuting effect" of the controller when encountering a sudden step-down in the topography. Nevertheless, the imaging capability of the system is demonstrated.

6.4.5 Educational Impacts

The low-cost educational AFM and corresponding graduate-level full-semester curriculum designs provide a unified framework for multidisciplinary education with in-depth hands-on learning. The course can be offered to students interested in research at the interface of mechanical, electrical and computer engineering for applications in material science, physics, chemistry and biology. The class reviews mechatronic system development with focus on micro/nano scale measurement and actuation. Data-driven design techniques will be applied with both numerical simulation and experimental system identification for performance improvement in practice. Students obtain significant hands-on experience in weekly lab sessions. Modeling and

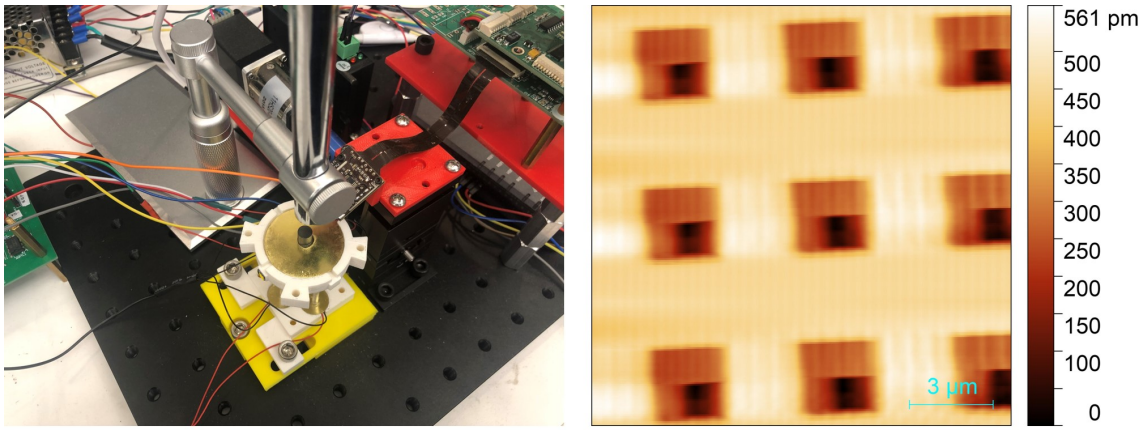

Figure 6-12: System integration and experiment results: (a) image of the assembled AFM system with electronics and an optical microscope, (b) 15 μm by 15 μm image of a TGXYZ03 calibration grating pits area with 5 μm pitch

post-processing techniques will be covered for interpretation of the collected SPM data using computer vision algorithms. The final project allows students to design and fabricate an AFM to obtain topography images of proposed samples. The educational AFM design with the proposed curriculum provides multiple potential benefits as listed below.

1. A unified framework for multidisciplinary precision instrument design
2. Practical data-driven design optimization for precision mechatronic systems
3. Great addition to existing curriculum with in-depth hands-on project
4. Potential of further research of imaging instrument and micro/nano robotics
5. Formation of on-campus SPM user and developer community

The class is organized around five modules that address various aspects of micro/-nano instrumentation as shown below.

1. Tools for mechatronics and instrumentation
2. Systems, signals and control
3. SPM principles, operation and instrumentation
4. Physical understanding and Advanced Applications

5. Advances on SPM related fields

The first two modules review general knowledge of mechatronic systems that are building blocks for construction of the AFM system. Generic introduction of the field is provided first, with the scope gradually narrowed down to fields relevant to construction of the AFM system during final project. Students practice through guided lab sessions for deeper understanding of concepts in the lecture. The last three modules provide knowledge more specific to the operation and design of the SPM system with AFM as an example. The proposed custom educational AFM design has a number of corresponding experiments for hands-on practice using the subsystems with selected ideas listed below.

1. AFM Cantilever: deflection sensitivity calibration, frequency response identification, stiffness measurement, thermomechanical actuation model verification
2. Positioning Systems: LabVIEW stepper motor control, scanner design with piezoelectric buzzer actuator, scanner characterization with interferometer
3. Electronics Design: signal generation, demodulation, piezoelectric buzzer driver
4. Imaging: AFM imaging of selected samples, image processing with Gwyddion
5. Investigation: LabVIEW control/simulation exercises, feedforward AFM imaging algorithm implementation, cantilever nano-fabrication, micro/nano sensor instrumentation, precision motion control algorithms

A test run of the first five lectures have been offered during the 2020 winter independent activity period at MIT. More details about the course are beyond the scope of this thesis but will be available in the future on the class website.

6.5 Chapter Summary

In this chapter, the design integration of three AFM systems developed in this work are discussed. The versatile sample scan AFM and the muti-layer stacked scanner AFM address the primary limitations of high-speed and large-range imaging, operation environment versatility and experimental overhead reduction as presented in

Chapter 1. The educational AFM development addresses the challenge for lack of affordable platform for precision mechatronics and instrumentation education needed for AFM modification in research. This chapter corresponds to the seventh main contribution: AFM system integration for visualization.

Chapter 7

Conclusions and Recommendations for Future Work

7.1 Conclusion

In this thesis, the design, control and instrumentation of multiple AFMs and corresponding subsystems are discussed in detail. The work primarily addressed four limitations of AFM systems including low imaging throughput and temporal resolution, inability to operate in harsh opaque environments, high experiment overhead and lack of an affordable platform for AFM instrumentation education needed to enable new functionalities for research. This is accomplished by the design and improvement of key subsystems to develop three AFM systems that address these limitations.

1. **AFM nano-positioners with high-speed, large range or low-cost characteristics:** With multiple design iterations for improvement, three scanner designs are selected for AFM imaging system. The first dual-actuated music-wire scanner allows large-range overview and zoomed-in high-speed scanning. The second multi-actuated stacked scanner allows high-speed scanning at a relatively larger range. The third buzzer-based scanner is a low-cost and safe-to-operate design.
2. **Coated active cantilever probes for harsh opaque liquid operation:**

An active cantilever probe with embedded piezoresistive sensor and thermomechanical actuator is protected with coating. The active probe removes the need for laser-probe alignment and enabled imaging in harsh opaque liquid.

3. **Algorithms for scanner control, automatic tuning and AFM imaging:** To improve the scanner performance and handle piezo hysteresis nonlinearity, multiple controllers including PID, iterative learning, and repetitive controllers are evaluated. The bandwidth-based repetitive controller is proposed for use with the multi-actuated stacked scanner. A complete AFM model for both in-plane scanning and out-of-plane tracking is developed for simulation study of imaging level improvement algorithms. The algorithms investigated include equal space sampling, topography feedforward, error corrected image generation, adaptive scanning speed, relay PID auto-tuning and single neuron PID controller. The algorithms help to improve imaging performance and reduces operational overhead in controller tuning.

4. **High-bandwidth driver and signal processing electronics:** To drive high-bandwidth piezo scanners and four quadrant photodiode for deflection measurement, high-bandwidth electronics are custom designed. A charge controller for sensorless hysteresis compensation of piezo actuators has also been developed with significant contribution from other researchers in the group. The instrumentation development helps to realize the functionality of the scanner and the cantilever transducer.

5. **Optical system for small probes with vision-based automation:** An optical beam deflection system with focused laser beam and optical view is designed to interface with smaller passive cantilevers. An automated probe and laser alignment system is designed using computer vision based algorithm. This development helps to improve the cantilever transducer bandwidth and reduce the experimental setup overhead.

6. **Software development for high-speed big data processing:** To realize the control algorithms at high-bandwidth, the code are implemented on FPGAs

in National Instruments data acquisition systems. A number of techniques for timing management, data transfer and FPGA resource management are identified during the process. An event-driven state machine architecture is designed for ease of user interface control. Development of batch processing software for the collected data offers convenience in visualization of the imaging results.

7. **AFM system integration for visualization:** A total of three AFM systems are developed in this work by integrating the aforementioned subsystems for imaging. The first sample scan AFM system uses overview and zoom strategy for large-range and high-speed imaging. The system is versatile to work with both passive probe with automatic alignment and coated active probes for opaque liquid imaging. The second stacked scan AFM system works with a self-sensing cantilever for simultaneous high-speed and large-range imaging. The third low-cost AFM system is modular and easy to operate, which makes it ideal for precision instrumentation education.

The research development in this work has produced a total of 9 published papers as referenced across the thesis. These include 2 papers on scanner design [101, 102, 154], 3 papers on controller designs for scanner and imaging [12, 167], 2 papers on charge control electronics design [157, 177], and 2 papers on cantilever probe development and imaging [33, 26]. Three patents have also been filed for both US and Patent Cooperation Treaty (PCT) international patent based on the work presented in these papers for charge control, scanner design and coated active cantilever probe. Several more publications have been submitted for review including 2 papers, 2 invention disclosures and 1 textbook. A number of conference presentation and invited seminar talks have been delivered based on the content in these publications as well as the unpublished contributions of this work.

The developments have also attracted attentions of researchers from various disciplines across the global. By the time of the thesis submission, 2 international collaborations to further extend the AFM capability have been established. Moreover,

3 project proposals have been submitted to various funding sources that expressed their interest in further AFM research for capability extension. These new projects will build upon the technical expertise and knowledge obtained in the work presented in this thesis. The research on AFM based techniques will continue in the future for both fundamental research and industrial applications.

7.2 Broader Impact of the Research

The research presented in this thesis extends the capabilities of AFM systems and various subsystems. The development has several practical implications in the broader areas of science, technology and education. First, the extended AFM capabilities allow new discoveries in science studies. With high imaging throughput, visualization of dynamic processes with high temporal resolution can be realized, which would be helpful for verification of model simulations to improve the fundamental understanding. The capability of harsh opaque liquid imaging allows observation of samples in their native environment. These AFM capabilities can help nanotechnology researchers for fundamental science studies. Science and technology fields that require real-time visualization of nano-scale phenomena or high-speed manipulation/indentation can also benefit from the results of this work.

Second, the subsystems developed in this work have broader range of applications in precision instrumentation and mechatronic system technologies. For example, the high-speed and large-range nano-positioner design can be used in applications where precision positioning is needed. The development of nano-fabrication techniques for the active cantilever probe can be applied to the manufacturing of MEMS sensors. The control algorithms developed in this work can be applied in similar application scenarios where periodic reference trajectories are applied. These technologies are widely used in the industries for fabrication of optical components, semiconductor, etc.

Third, the development of the educational system and technical knowledge acquired during this work can be helpful for the AFM community. In many situations,

custom modification of commercial AFM systems are needed for specialized imaging applications. The curriculum design centered around the low-cost AFM system allows researchers previously not familiar with AFM design to gain practical knowledge about the system. The knowledge can help the community to implement novel application ideas based on AFM systems.

In summary, it is not too far fetched to claim that research outcomes in this work will have impact directly or indirectly on many aspects of physics, chemistry, material science, biology, medicine, mechatronics, precision instrumentation and system engineering. For more information related this thesis including videos, supporting documents, class materials and future developments, please visit the MIT Mechatronics Research lab website https://mechatronics.mit.edu/.

7.3 Recommendations for Future Work

Based on the development presented in this work, further improvements of the AFM system can be made with selected ideas presented below from on-going proposals.

7.3.1 Operational Modes Extension

The AFM design in this work for high-speed imaging primarily operates in contact mode on rigid sample surfaces. However, for more delicate soft samples in many biological applications, tapping mode operation would be preferred to reduce the interaction forces. An interesting potential direction to pursue is to extend the high-speed imaging capability from contact mode to other modes including tapping and mechanical property measurement modes. Previous research for mechanical property mapping have demonstrated its usefulness while primarily at a low imaging speed [196, 197]. Improving the temporal resolution of this technique would be beneficial. For example, AFM-based Single Molecule Force Spectroscopy (SMFS) is a powerful tool to understand the delicate interactions between cell membranes for biological research [198]. Mechanical property information can be mapped in this mode by jumping from one pixel location to another by analyzing the force-distance curve. It

would be ideal to have high-speed mapping of mechanical properties for understanding of cell response to external stimulus. In conventional AFMs, the positioning command for the force-distance curve is limited by the relatively low resonance frequency of the Z-scanner, resulting in a low temporal resolution of defining adhesion events. With our work on customized video-rate AFM design, it is promising to further extend the imaging modes to realize the desired imaging capabilities and help to obtain better results from fundamental studies.

7.3.2 New Imaging Capabilities

In addition to mechanical properties, new imaging modalities can be developed. Combination of electrical and optical modalities with the current development can be helpful to reveal new information from the sample. For example, spectroscopy methods can be used to excite the material with electromagnetic radiation and measure the waveform emitted by the material. These methods are primarily limited in spatial resolution due to the wavelength. By combining the spectroscopy methods with SPM systems, an evanescent field is generated between the tip and the sample. If the cantilever probe tip and sample separation distance is modulated, the evanescent wave can be extracted at the corresponding frequency to isolate it from the background scattered light. This significantly increases the spatial resolution to be comparable to the tip radius (down to several nanometers). External optical components are needed in addition to the AFM system for implementation. Tip-enhanced SNOM is a family of methods that includes multiple imaging modes such as Nanoscale Fourier Transformation Infrared (nano-FTIR) spectroscopy, photo-thermal induced resonance microscopy, photo-conductive force microscopy, photo-induced force microscopy, etc. Based on the development of multiple AFM systems in this work, it is interesting to custom design AFM systems with new imaging modalities and ideally maintain the high throughput for dynamic process visualization. The capabilities of nano-fabrication such as scanning probe lithography may also be added in addition to imaging. The established collaborations discussed in the last section largely fall into this category to extend AFM imaging capabilities for different applications in

various environments. Innovative subsystem level development will again be needed to realize the new target capabilities.

7.3.3 Educational AFM Curriculum Design

The design of the curriculum centered around the educational AFM system require additional content development effort. For example, packaging the Matlab simulation code developed in this work with graphical user interface would be helpful. This development would allow students to get familiar with AFMs without the risk of damaging the equipment and explore control algorithms beyond lab sessions. Moreover, preparation of lecture presentation materials and manuals for lab experiments to formalize the class implementation is needed to provide a reference package for instructors. The feedback comments obtained from offering of the first module of the class is be very helpful for the improvement of the curriculum design. We plan to update the curriculum design and offer the full semester class once ready.

Bibliography

[1] H. Zhang, J. Huang, Y. Wang, R. Liu, X. Huai, J. Jiang, and C. Anfuso, "Atomic force microscopy for two-dimensional materials: A tutorial review," *Optics Communications*, vol. 406, pp. 3 – 17, 2018. Optoelectronics and Photonics Based on Two-dimensional Materials.

[2] A. Cricenti, S. Colonna, M. Girasole, P. Gori, F. Ronci, G. Longo, S. Dinarelli, M. Luce, M. Rinaldi, and M. Ortenzi, "Scanning probe microscopy in material science and biology," *Journal of Physics D: Applied Physics*, vol. 44, p. 464008, nov 2011.

[3] M. Firtel and T. Beveridge, "Scanning probe microscopy in microbiology," *Micron*, vol. 26, no. 4, pp. 347 – 362, 1995.

[4] A. F. Raigoza, J. W. Dugger, and L. J. Webb, "Review: Recent advances and current challenges in scanning probe microscopy of biomolecular surfaces and interfaces," *ACS Applied Materials & Interfaces*, vol. 5, no. 19, pp. 9249–9261, 2013. PMID: 23848270.

[5] G. Binnig, C. F. Quate, C. Gerber, and etc, "Atomic force microscope," *Phys. Rev. Lett.*, vol. 56, pp. 930–933, Mar 1986.

[6] S. P. Jarvis and J. G. Hardy, "Resolving intra- and inter-molecular structure with non-contact atomic force microscopy," in *International journal of molecular sciences*, 2015.

[7] O. Custance, R. Perez, and S. Morita, "Atomic force microscopy as a tool for atom manipulation," *Nature nanotechnology*, vol. 4, no. 12, p. 803, 2009.

[8] T. Michels and I. W. Rangelow, "Review of scanning probe micromachining and its applications within nanoscience," *Microelectronic Engineering*, vol. 126, pp. 191 – 203, 2014.

[9] V. Ishchuk, E. Guliyev, C. Aydogan, I. Buliev, M. Kaestner, T. Ivanov, A. Ahmad, A. Reum, S. Lenk, C. Lenk, *et al.*, "Scanning probe-based high-accuracy overlay alignment concept for lithography applications," *Applied Physics A*, vol. 123, no. 1, p. 89, 2017.

[10] J. Shi, Y. Hu, S. Hu, J. Ma, and C. Su, "Method and apparatus of using peak force tapping mode to measure physical properties of a sample," Feb. 11 2014. US Patent 8,650,660.

[11] G. Smolyakov, S. Pruvost, L. Cardoso, B. Alonso, E. Belamie, and J. Duchet-Rumeau, "{AFM} peakforce {QNM} mode: Evidencing nanometer-scale mechanical properties of chitin-silica hybrid nanocomposites," *Carbohydrate Polymers*, vol. 151, pp. 373 – 380, 2016.

[12] F. Xia, I. S. Bozchalooi, and K. Youcef-Toumi, "Induced vibration contact detection for minimizing cantilever tip-sample interaction forces in jumping mode atomic force microscopy," in *2017 American Control Conference (ACC)*, pp. 4141–4146, IEEE, 2017.

[13] P. Biczysko, A. Dzierka, G. Jówiak, M. Rudek, T. Gotszalk, P. Janus, P. Grabiec, and I. Rangelow, "Contact atomic force microscopy using piezoresistive cantilevers in load force modulation mode," *Ultramicroscopy*, vol. 184, 09 2017.

[14] A. Rosa-Zeiser, E. Weilandt, S. Hild, and O. Marti, "The simultaneous measurement of elastic, electrostatic and adhesive properties by scanning force microscopy: pulsed-force mode operation," *Measurement Science and Technology*, vol. 8, no. 11, p. 1333, 1997.

[15] C. T. Gibson, G. S. Watson, and S. Myhra, "Lateral force microscopya quantitative approach," *Wear*, vol. 213, no. 1-2, pp. 72–79, 1997.

[16] I. E. Dzyaloshinskii, E. M. Lifshitz, and L. P. Pitaevskii, "The general theory of van der waals forces," *Advances in Physics*, vol. 10, no. 38, pp. 165–209, 1961.

[17] P. C. Braga and D. Ricci, *Atomic force microscopy in biomedical research: methods and protocols*. Springer, 2011.

[18] N. Kristi, A. Gafur, L. Kong, X. Ma, Z. Ye, and G. Wang, "Atomic force microscopy in mechanoimmunology analysis: A new perspective for cancer immunotherapy," *Biotechnology Journal*, p. 1900559, 2020.

[19] G. Horlick, "Introduction to fourier transform spectroscopy," *Applied Spectroscopy*, vol. 22, no. 6, pp. 617–626, 1968.

[20] L. Benavente, C. Coetsier, A. Venault, Y. Chang, C. Causserand, P. Bacchin, and P. Aimar, "Ftir mapping as a simple and powerful approach to study membrane coating and fouling," *Journal of Membrane Science*, vol. 520, pp. 477 – 489, 2016.

[21] S. Li, J. Ihli, W. J. Marchant, M. Zeng, L. Chen, K. Wehbe, G. Cinque, O. Cespedes, N. Kapur, and F. C. Meldrum, "Synchrotron ftir mapping of mineralization in a microfluidic device," *Lab Chip*, vol. 17, pp. 1616–1624, 2017.

[22] Y. Sarov, T. Ivanov, A. Frank, J.-P. Zöllner, N. Nikolov, and I. W. Rangelow, "Realization of cantilever arrays for parallel proximity imaging," *Journal of Physics: Conference Series*, vol. 253, p. 012050, nov 2010.

[23] T. Angelov, A. Ahmad, E. Guliyev, A. Reum, I. Atanasov, T. Ivanov, V. Ishchuk, M. Kaestner, Y. Krivoshapkina, S. Lenk, C. Lenk, I. W. Rangelow, M. Holz, and N. Nikolov, "Six-axis afm in sem with self-sensing and self-transduced cantilever for high speed analysis and nanolithography," *Journal of Vacuum Science & Technology B*, vol. 34, no. 6, p. 06KB01, 2016.

[24] M. G. Ruppert, S. I. Moore, M. Zawierta, A. J. Fleming, G. Putrino, and Y. K. Yong, "Multimodal atomic force microscopy with optimized higher eigenmode sensitivity using on-chip piezoelectric actuation and sensing," *Nanotechnology*, vol. 30, p. 085503, jan 2019.

[25] K. Edinger, T. Gotszalk, and I. W. Rangelow, "Novel high resolution scanning thermal probe," *Journal of Vacuum Science & Technology B: Microelectronics and Nanometer Structures Processing, Measurement, and Phenomena*, vol. 19, no. 6, pp. 2856–2860, 2001.

[26] F. Xia, C. Yang, Y. Wang, K. Youcef-Toumi, C. Reuter, T. Ivanov, M. Holz, and I. W. Rangelow, "Lights out! nano-scale topography imaging of sample surface in opaque liquid environments with coated active cantilever probes," *Nanomaterials*, vol. 9, no. 7, p. 1013, 2019.

[27] D. Filenko, T. Gotszalk, Z. Kazantseva, O. Rabinovych, I. Koshets, Y. Shirshov, V. Kalchenko, and I. Rangelow, "Chemical gas sensors based on calixarene-coated discontinuous gold films," *Sensors and Actuators B: Chemical*, vol. 111, pp. 264–270, 11 2005.

[28] L. A. Pinnaduwage, A. Wig, D. L. Hedden, A. Gehl, D. Yi, T. Thundat, and R. T. Lareau, "Detection of trinitrotoluene via deflagration on a microcantilever," *Journal of Applied Physics*, vol. 95, no. 10, pp. 5871–5875, 2004.

[29] C. Riesch, E. Reichel, F. Keplinger, and B. Jakoby, "Characterizing vibrating cantilevers for liquid viscosity and density sensing," *Journal of Sensors*, vol. 2008, 08 2008.

[30] N. Abedinov, P. Grabiec, T. Gotszalk, T. Ivanov, J. Voigt, and I. W. Rangelow, "Micromachined piezoresistive cantilever array with integrated resistive microheater for calorimetry and mass detection," *Journal of Vacuum Science & Technology A*, vol. 19, no. 6, pp. 2884–2888, 2001.

[31] M. Ilg, C. D. Weis, J. Schwartz, A. Persaud, Q. Ji, C. Chi Lo, J. Bokor, A. Hegyi, E. Guliyev, I. W. Rangelow, *et al.*, "Improved single ion implantation with scanning probe alignment," *Journal of Vacuum Science & Technology B, Nanotechnology and Microelectronics: Materials, Processing, Measurement, and Phenomena*, vol. 30, no. 6, p. 06FD04, 2012.

[32] J. Voigt, F. Shi, K. Edinger, P. Güthner, and I. Rangelow, "Nanofabrication with scanning nanonozzle nanojet," *Microelectronic Engineering*, vol. 57-58, pp. 1035 – 1042, 2001. Micro- and Nano-Engineering 2000.

[33] I. W. Rangelow, T. Ivanov, A. Ahmad, M. Kaestner, C. Lenk, I. S. Bozchalooi, F. Xia, K. Youcef-Toumi, M. Holz, and A. Reum, "Active scanning probes: A versatile toolkit for fast imaging and emerging nanofabrication," *Journal of Vacuum Science & Technology B, Nanotechnology and Microelectronics: Materials, Processing, Measurement, and Phenomena*, vol. 35, no. 6, p. 06G101, 2017.

[34] T. Ando, "High-speed {AFM} imaging," *Current Opinion in Structural Biology*, vol. 28, pp. 63 – 68, 2014.

[35] T. Ando, "Molecular machines directly observed by high-speed atomic force microscopy," *{FEBS} Letters*, vol. 587, no. 8, pp. 997 – 1007, 2013. The many faces of proteins.

[36] T. Ando, "Filming dynamic processes of proteins by high-speed afm," *Biophysical Journal*, vol. 104, no. 2, Supplement 1, pp. 386a –, 2013.

[37] I. Casuso, N. Kodera, C. L. Grimellec, T. Ando, and S. Scheuring, "Contact-mode high-resolution high-speed atomic force microscopy movies of the purple membrane," *Biophysical Journal*, vol. 97, no. 5, pp. 1354 – 1361, 2009.

[38] M. Rangl, L. Rima, J. Klement, A. Miyagi, S. Keller, and S. Scheuring, "Real-time visualization of phospholipid degradation by outer membrane phospholipase a using high-speed atomic force microscopy," *Journal of Molecular Biology*, vol. 429, no. 7, pp. 977 – 986, 2017.

[39] F. Eghiaian, F. Rico, A. Colom, I. Casuso, and S. Scheuring, "High-speed atomic force microscopy: Imaging and force spectroscopy," *{FEBS} Letters*, vol. 588, no. 19, pp. 3631 – 3638, 2014. SI: Single molecule techniques - Applications in biology.

[40] T. Ando, T. Uchihashi, and T. Fukuma, "High-speed atomic force microscopy for nano-visualization of dynamic biomolecular processes," *Progress in Surface Science*, vol. 83, no. 7, pp. 337 – 437, 2008.

[41] E. Ruiz-Agudo, C. Putnis, C. Jimenez-Lopez, and C. Rodriguez-Navarro, "An atomic force microscopy study of calcite dissolution in saline solutions: The role of magnesium ions," *Geochimica et Cosmochimica Acta*, vol. 73, pp. 3201–3217, 06 2009.

[42] J. Therrien, A. Dindar, and D. Smith, "Afm studies of nanoparticle deposition via electrospray ionization," *Microscopy Research and Technique*, vol. 70, no. 6, pp. 530–533, 2007.

[43] R. Pearce and G. J. Vancso, "Imaging of melting and crystallization of poly(ethylene oxide) in real-time by hot-stage atomic force microscopy," *Macromolecules*, vol. 30, no. 19, pp. 5843–5848, 1997.

[44] M. H. Nielsen, S. Aloni, and J. J. De Yoreo, "In situ tem imaging of caco3 nucleation reveals coexistence of direct and indirect pathways," *Science*, vol. 345, no. 6201, pp. 1158–1162, 2014.

[45] B. Crist and J. Schultz, *Atomic Force Microscopy Studies of Polymer Crystals: Nucleation, Growth, Annealing, and Melting*, pp. 1–25. 01 2013.

[46] S. J. Rowan, "Polymer self-assembly: Micelles make a living.," *Nature materials*, vol. 8 2, pp. 89–91, 2009.

[47] S. V. Kalinin and D. A. Bonnell, "Effect of phase transition on the surface potential of the batio3 (100) surface by variable temperature scanning surface potential microscopy," *Journal of Applied Physics*, vol. 87, no. 8, pp. 3950–3957, 2000.

[48] A. Miyagi, T. Ando, and Y. L. Lyubchenko, "Dynamics of nucleosomes assessed with time-lapse high-speed atomic force microscopy," *Biochemistry*, vol. 50, no. 37, pp. 7901–7908, 2011. PMID: 21846149.

[49] T. Ando, N. Kodera, E. Takai, D. Maruyama, K. Saito, and A. Toda, "A high-speed atomic force microscope for studying biological macromolecules," *Proceedings of the National Academy of Sciences*, vol. 98, no. 22, pp. 12468–12472, 2001.

[50] D. C. Coffey and D. S. Ginger, "Patterning phase separation in polymer films with dip-pen nanolithography," *Journal of the American Chemical Society*, vol. 127, no. 13, pp. 4564–4565, 2005. PMID: 15796508.

[51] H. T. Nia, I. S. Bozchalooi, Y. Li, L. Han, H. tsun Hung, E. H. Frank, K. Youcef-Toumi, C. C. Ortiz, and A. J. Grodzinsky, "High-bandwidth afm-based rheology reveals that cartilage is most sensitive to high loading rates at early stages of impairment.," *Biophysical journal*, vol. 104 7, pp. 1529–37, 2013.

[52] F. Xia, *Design and control optimization for high-speed jumping mode Atomic Force Microscope*. PhD thesis, Massachusetts Institute of Technology, 2017.

[53] D. Lord and J. Buckley, "An afm study of the morphological features that affect wetting at crude oil-water-mica interfaces," *Colloids and Surfaces A: Physicochemical and Engineering Aspects*, vol. 206, 07 2002.

[54] K. Kumar, E. Dao, and K. Mohanty, "Afm study of mineral wettability with reservoir oils," *Journal of Colloid and Interface Science*, vol. 289, no. 1, pp. 206 – 217, 2005.

[55] D.-M. Kaimaki, B. E. Smith, and C. Durkan, "On the use of nanomechanical atomic force microscopy to characterise oil-exposed surfaces," *RSC Adv.*, vol. 8, pp. 6680–6689, 2018.

[56] P. Lavalle, J. F. Stoltz, B. Senger, J. C. Voegel, and P. Schaaf, "Red blood cell adhesion on a solid/liquid interface," *Proc Natl Acad Sci U S A*, vol. 93, pp. 15136–15140, Dec 1996. 8986776[pmid].

[57] A. Dujardin, P. De Wolf, F. Lafont, and V. Dupres, "Automated multi-sample acquisition and analysis using atomic force microscopy for biomedical applications," *PloS one*, vol. 14, no. 3, 2019.

[58] L. Ju, Z. Shi, N. Nair, Y. Lv, C. Jin, J. Velasco Jr, C. Ojeda-Aristizabal, H. A. Bechtel, M. C. Martin, A. Zettl, J. Analytis, and F. Wang, "Topological valley transport at bilayer graphene domain walls," *Nature*, vol. 520, pp. 650 EP –, Apr 2015.

[59] L. Jiang, Z. Shi, B. Zeng, S. Wang, J.-H. Kang, T. Joshi, C. Jin, L. Ju, J. Kim, T. Lyu, Y.-R. Shen, M. Crommie, H.-J. Gao, and F. Wang, "Soliton-dependent plasmon reflection at bilayer graphene domain walls," *Nature Materials*, vol. 15, pp. 840 EP –, May 2016.

[60] M. Holz, C. Reuter, A. Ahmad, A. Reum, M. Hofmann, T. Ivanov, and I. W. Rangelow, "Correlative microscopy and nanofabrication with afm integrated with sem," *Microscopy Today*, vol. 27, no. 6, pp. 24–30, 2019.

[61] K. El Rifai, O. El Rifai, and K. Youcef-Toumi, "On dual actuation in atomic force microscopes," in *Proceedings of the 2004 American Control Conference*, vol. 4, pp. 3128–3133 vol.4, June 2004.

[62] A. J. Fleming, B. J. Kenton, and K. K. Leang, "Ultra-fast dual-stage vertical positioning for high performance spms," in *Proceedings of the 2010 American Control Conference*, pp. 4975–4980, June 2010.

[63] A. J. Fleming, "Dual-stage vertical feedback for high-speed scanning probe microscopy," *IEEE Transactions on Control Systems Technology*, vol. 19, pp. 156–165, Jan 2011.

[64] A. J. Fleming, "High-speed vertical positioning for contact-mode atomic force microscopy," *2009 IEEE/ASME International Conference on Advanced Intelligent Mechatronics*, pp. 522–527, 2009.

[65] D. Bullen and C. A. M. and, "Design, fabrication, and characterization of thermally actuated probe arrays for dip pen nanolithography," *Journal of Microelectromechanical Systems*, vol. 13, pp. 594–602, Aug 2004.

[66] G. Fantner, D. Burns, A. M. Belcher, I. Rangelow, and K. Youcef-Toumi, "Dmcmn: In depth characterization and control of afm cantilevers with integrated

sensing and actuation," *Journal of Dynamic Systems, Measurement and Control, Transactions of the ASME*, vol. 131, 11 2009.

[67] D. Y. Abramovitch, S. B. Andersson, L. Y. Pao, and G. Schitter, "A tutorial on the mechanisms, dynamics, and control of atomic force microscopes," in *2007 American Control Conference*, pp. 3488–3502, July 2007.

[68] A. Daniele, S. Salapaka, M. V. Salapaka, and M. Dahleh, "Piezoelectric scanners for atomic force microscopes: design of lateral sensors, identification and control," in *Proceedings of the 1999 American Control Conference (Cat. No. 99CH36251)*, vol. 1, pp. 253–257 vol.1, June 1999.

[69] C. Braunsmann and T. E. Schäffer, "High-speed atomic force microscopy for large scan sizes using small cantilevers," *Nanotechnology*, vol. 21, p. 225705, may 2010.

[70] T. Jukic and N. Peric, "Model based backlash compensation," in *Proceedings of the 2001 American Control Conference.(Cat. No. 01CH37148)*, vol. 2, pp. 775–780, IEEE, 2001.

[71] Y. Tarng, J. Kao, and Y. Lin, "Identification of and compensation for backlash on the contouring accuracy of cnc machining centres," *The International Journal of Advanced Manufacturing Technology*, vol. 13, no. 2, pp. 77–85, 1997.

[72] Y. Kiryu, "Harmonic gear apparatus," Oct. 28 1986. US Patent 4,619,156.

[73] T. Kwok, *Design and implementation of a high precision profilometer*. PhD thesis, Massachusetts Institute of Technology, 1995.

[74] T. Ando, "Molecular machines directly observed by high-speed atomic force microscopy," *{FEBS} Letters*, vol. 587, no. 8, pp. 997 – 1007, 2013. The many faces of proteins.

[75] Y. R. Teo, Y. K. Yong, and A. J. Fleming, "A comparison of scanning methods and the vertical control implications for scanning probe microscopy," *Asian Journal of Control*, vol. 30, no. 4, pp. 1–15, 2018.

[76] I. S. Bozchalooi, *Design and Control of High-Speed and Large-Range Atomic Force Microscope*. PhD thesis, Massachusetts Institute of Technology, 2015.

[77] P. USA, "Piezoelectric actuators, piezo transducers: Piezo stacks, flexures, tubes, benders, shear actuators," June 2020.

[78] J. B. Hopkins and M. L. Culpepper, "Synthesis of multi-degree of freedom, parallel flexure system concepts via freedom and constraint topology (fact)–part i: Principles," *Precision Engineering*, vol. 34, no. 2, pp. 259–270, 2010.

[79] J. B. Hopkins and M. L. Culpepper, "Synthesis of multi-degree of freedom, parallel flexure system concepts via freedom and constraint topology (fact). part ii: Practice," *Precision Engineering*, vol. 34, no. 2, pp. 271–278, 2010.

[80] D. Hall, "Review nonlinearity in piezoelectric ceramics," *Journal of materials science*, vol. 36, no. 19, pp. 4575–4601, 2001.

[81] J. Å. Stakvik, "Identification, inversion and implementaion of the preisach hysteresis model in nanopositioning," Master's thesis, Institutt for teknisk kybernetikk, 2014.

[82] T. G. Zsurzsan, M. A. E. Andersen, Z. Zhang, and N. A. Andersen, "Preisach model of hysteresis for the piezoelectric actuator drive," IECON'15, pp. 002788–002793, Nov 2015.

[83] R. V. Iyer, X. Tan, and P. Krishnaprasad, "Approximate inversion of the preisach hysteresis operator with application to control of smart actuators," *IEEE Transactions on Automatic Control*, vol. 50, no. 6, pp. 798–810, 2005.

[84] H. Jung and D.-G. Gweon, "Creep characteristics of piezoelectric actuators," *Review of scientific Instruments*, vol. 71, no. 4, pp. 1896–1900, 2000.

[85] R. Changhai and S. Lining, "Hysteresis and creep compensation for piezoelectric actuator in open-loop operation," *Sensors and Actuators A: Physical*, vol. 122, no. 1, pp. 124–130, 2005.

[86] P. Instrumente, "Electrical operation of piezo actuators," 2020.

[87] L. Ljung, *System Identification*, pp. 1–19. American Cancer Society, 2017.

[88] P. Welch, "The use of fast fourier transform for the estimation of power spectra: a method based on time averaging over short, modified periodograms," *IEEE Transactions on audio and electroacoustics*, vol. 15, no. 2, pp. 70–73, 1967.

[89] P. K. Rahi and R. Mehra, "Analysis of power spectrum estimation using welch method for various window techniques," *International Journal of Emerging Technologies and Engineering*, vol. 2, no. 6, pp. 106–109, 2014.

[90] B. J. Kenton, *Design, characterization, and control of a high-bandwidth serial-kinematic nanopositioning stage for scanning probe microscopy applications*. PhD thesis, 2010.

[91] G. Schitter, K. J. Astrom, B. E. DeMartini, P. J. Thurner, K. L. Turner, and P. K. Hansma, "Design and modeling of a high-speed afm-scanner," *IEEE Transactions on Control Systems Technology*, vol. 15, pp. 906–915, Sep. 2007.

[92] S. P. Wadikhaye, Y. K. Yong, and S. O. Reza Moheimani, "A serial-kinematic nanopositioner for high-speed atomic force microscopy," *Review of Scientific Instruments*, vol. 85, no. 10, p. 105104, 2014.

[93] I. S. Bozchalooi, A. C. Houck, J. AlGhamdi, and K. Youcef-Toumi, "Design and control of multi-actuated atomic force microscope for large-range and high-speed imaging," *Ultramicroscopy*, vol. 160, pp. 213 – 224, 2016.

[94] B. J. Kenton and K. K. Leang, "Design and control of a three-axis serial-kinematic high-bandwidth nanopositioner," *IEEE/ASME Transactions on Mechatronics*, vol. 17, no. 2, pp. 356–369, 2011.

[95] K. K. Leang and A. J. Fleming, "High-speed serial-kinematic spm scanner: Design and drive considerations," *Asian journal of control*, vol. 11, no. 2, pp. 144–153, 2009.

[96] Y. K. Yong, S. O. R. Moheimani, B. J. Kenton, and K. K. Leang, "Invited review article: High-speed flexure-guided nanopositioning: Mechanical design and control issues," *Review of Scientific Instruments*, vol. 83, no. 12, p. 121101, 2012.

[97] M. J. Rost, L. Crama, P. Schakel, E. van Tol, G. B. E. M. van Velzen-Williams, C. F. Overgauw, H. ter Horst, H. Dekker, B. Okhuijsen, M. Seynen, A. Vijftigschild, P. Han, A. J. Katan, K. Schoots, R. Schumm, W. van Loo, T. H. Oosterkamp, and J. W. M. Frenken, "Scanning probe microscopes go video rate and beyond," *Review of Scientific Instruments*, vol. 76, no. 5, p. 053710, 2005.

[98] J.-Y. Wang, N. Mullin, and J. K. Hobbs, "High-speed large area atomic force microscopy using a quartz resonator," *Nanotechnology*, vol. 29, p. 335502, jun 2018.

[99] E. C. M. Disseldorp, F. C. Tabak, A. J. Katan, M. B. S. Hesselberth, T. H. Oosterkamp, J. W. M. Frenken, and W. M. van Spengen, "Mems-based high speed scanning probe microscopy," *Review of Scientific Instruments*, vol. 81, no. 4, p. 043702, 2010.

[100] E. Guliyev, T. Michels, B. Volland, T. Ivanov, M. Hofer, and I. Rangelow, "High speed quasi-monolithic silicon/piezostack spm scanning stage," *Microelectronic engineering*, vol. 98, pp. 520–523, 2012.

[101] F. Xia, S. Truncale, Y. Wang, and K. Youcef-Toumi, "Design and control of a multi-actuated high-bandwidth and large-range scanner for atomic force microscopy," in *2018 Annual American Control Conference (ACC)*, pp. 4330–4335, June 2018.

[102] C. Yang, F. Xia, Y. Wang, S. Truncale, and K. Youcef-Toumi, "Design and control of a multi-actuated nanopositioning stage with stacked structure," *2019 American Control Conference (ACC)*, pp. 3782–3788, 2019.

[103] W. A. Strauss, *Partial differential equations: An introduction*. John Wiley & Sons, 2007.

[104] G. Duffing, *Forced vibrations with "a variable natural frequency and their technical meaning*. No. 41-42, F. Vieweg son, 1918.

[105] I. Kovacic and M. J. Brennan, *The Duffing equation: nonlinear oscillators and their behaviour*. John Wiley & Sons, 2011.

[106] L. Beaulieu, M. Godin, O. Laroche, V. Tabard-Cossa, and P. Grütter, "A complete analysis of the laser beam deflection systems used in cantilever-based systems," *Ultramicroscopy*, vol. 107, no. 4-5, pp. 422–430, 2007.

[107] E. E.-T. Hwu and A. Boisen, "Hacking cd/dvd/blu-ray for biosensing," *ACS sensors*, vol. 3, no. 7, pp. 1222–1232, 2018.

[108] E.-T. Hwu, S.-K. Hung, C.-W. Yang, I.-S. Hwang, and K.-Y. Huang, "Simultaneous detection of translational and angular displacements of micromachined elements," *Applied Physics Letters*, vol. 91, no. 22, p. 221908, 2007.

[109] T. Michels, I. W. Rangelow, and V. Aksyuk, "Cantilever array with optomechanical read-out and integrated actuation for simultaneous high sensitivity force detection," in *2016 International Conference on Optical MEMS and Nanophotonics (OMN)*, pp. 1–2, 2016.

[110] M. Tortonese, R. Barrett, and C. Quate, "Atomic resolution with an atomic force microscope using piezoresistive detection," *Applied physics letters*, vol. 62, no. 8, pp. 834–836, 1993.

[111] M. Tortonese, H. Yamada, R. Barrett, and C. Quate, "Atomic force microscopy using a piezoresistive cantilever," in *TRANSDUCERS'91: 1991 International Conference on Solid-State Sensors and Actuators. Digest of Technical Papers*, pp. 448–451, IEEE, 1991.

[112] S. R. Moheimani and A. J. Fleming, *Piezoelectric transducers for vibration control and damping*. Springer Science & Business Media, 2006.

[113] S. Timoshenko, "Analysis of bi-metal thermostats," *Josa*, vol. 11, no. 3, pp. 233–255, 1925.

[114] N. V. Lavrik, M. J. Sepaniak, and P. G. Datskos, "Cantilever transducers as a platform for chemical and biological sensors," *Review of scientific instruments*, vol. 75, no. 7, pp. 2229–2253, 2004.

[115] H. Bhaskaran, M. Li, D. Garcia-Sanchez, P. Zhao, I. Takeuchi, and H. X. Tang, "Active microcantilevers based on piezoresistive ferromagnetic thin films," *Applied Physics Letters*, vol. 98, no. 1, p. 013502, 2011.

[116] D. Kopiec, P. Pałetko, W. Majstrzyk, P. Kunicki, A. Sierakowski, and T. Gotszalk, "Electromagnetically actuated microcantilever for chemical and biochemical sensing in static mode," *Procedia Engineering*, vol. 87, pp. 955–958, 2014.

[117] C. J. Long and R. J. Cannara, "Modular apparatus for electrostatic actuation of common atomic force microscope cantilevers," *Review of Scientific Instruments*, vol. 86, no. 7, p. 073703, 2015.

[118] B. X. Desbiolles, G. Furlan, A. M. Schwartzberg, P. D. Ashby, and D. Ziegler, "Electrostatically actuated encased cantilevers," *Beilstein Journal of Nanotechnology*, vol. 9, no. 1, pp. 1381–1389, 2018.

[119] F. J. Giessibl, "The qplus sensor, a powerful core for the atomic force microscope," *Review of Scientific Instruments*, vol. 90, no. 1, p. 011101, 2019.

[120] T. Akiyama, N. F. de Rooij, U. Staufer, M. Detterbeck, D. Braendlin, S. Waldmeier, and M. Scheidiger, "Implementation and characterization of a quartz tuning fork based probe consisted of discrete resonators for dynamic mode atomic force microscopy," *Review of Scientific Instruments*, vol. 81, no. 6, p. 063706, 2010.

[121] A.-H. Lin, J.-Y. Lee, J. Yan, and A. Seshia, "Methods for enhanced electrical transduction and characterization of micromechanical resonators," *Sensors and Actuators A: Physical*, vol. 158, no. 2, pp. 263–272, 2010.

[122] M. G. Ruppert, A. G. Fowler, M. Maroufi, and S. O. R. Moheimani, "On-chip dynamic mode atomic force microscopy: A silicon-on-insulator mems approach," *Journal of Microelectromechanical Systems*, vol. 26, pp. 215–225, Feb 2017.

[123] A. Fowler, A. Laskovski, A. Hammond, and S. Moheimani, "A 2-dof electrostatically actuated mems nanopositioner for on-chip afm," *Journal of Microelectromechanical Systems*, vol. 21, no. 4, pp. 771–773, 2012.

[124] A. Mohammadi, A. G. Fowler, Y. K. Yong, and S. R. Moheimani, "A feedback controlled mems nanopositioner for on-chip high-speed afm," *Journal of Microelectromechanical Systems*, vol. 23, no. 3, pp. 610–619, 2013.

[125] N. Sarkar, R. R. Mansour, O. Patange, and K. Trainor, "Cmos-mems atomic force microscope," in *2011 16th International Solid-State Sensors, Actuators and Microsystems Conference*, pp. 2610–2613, 2011.

[126] N. Sarkar, G. Lee, and R. R. Mansour, "Cmos-mems dynamic fm atomic force microscope," in *2013 Transducers Eurosensors XXVII: The 17th International Conference on Solid-State Sensors, Actuators and Microsystems (TRANSDUCERS EUROSENSORS XXVII)*, pp. 916–919, 2013.

[127] O. Krause, "Afm probe manufacturing," 2016.

[128] S. Zheng, "Nanofabrication of direct positioning atomic force microscope (afm) probes and a novel method to attain controllable lift-off," Master's thesis, University of Waterloo, 2017.

[129] T. Gotszalk, J. Radojewski, P. Grabiec, P. Dumania, F. Shi, P. Hudek, and I. Rangelow, "Fabrication of multipurpose piezoresistive wheatstone bridge cantilevers with conductive microtips for electrostatic and scanning capacitance

microscopy," *Journal of Vacuum Science & Technology B: Microelectronics and Nanometer Structures Processing, Measurement, and Phenomena*, vol. 16, no. 6, pp. 3948–3953, 1998.

[130] Y. Sarov, T. Ivanov, A. Frank, J.-P. Zöllner, N. Nikolov, and I. W. Rangelow, "Realization of cantilever arrays for parallel proximity imaging," *Journal of Physics: Conference Series*, vol. 253, p. 012050, nov 2010.

[131] J.-d. Li, J. Xie, W. Xue, and D.-m. Wu, "Fabrication of cantilever with self-sharpening nano-silicon-tip for afm applications," *Microsystem technologies*, vol. 19, no. 2, pp. 285–290, 2013.

[132] B. Tang, K. Sato, H. Tanaka, and M. Gosalvez, "Fabrication of sharp tips with high aspect ratio by surfactant-modified wet etching for the afm probe," in *2011 IEEE 24th International Conference on Micro Electro Mechanical Systems*, pp. 328–331, IEEE, 2011.

[133] N. Hosseini, M. Neuenschwander, O. Peric, S. H. Andany, J. D. Adams, and G. E. Fantner, "Integration of sharp silicon nitride tips into high-speed su8 cantilevers in a batch fabrication process," *Beilstein Journal of Nanotechnology*, vol. 10, no. 1, pp. 2357–2363, 2019.

[134] N. R. Wilson and J. V. Macpherson, "Carbon nanotube tips for atomic force microscopy," *Nature nanotechnology*, vol. 4, no. 8, p. 483, 2009.

[135] J. Li, A. M. Cassell, and H. Dai, "Carbon nanotubes as afm tips: measuring dna molecules at the liquid/solid interface," *Surface and Interface Analysis: An International Journal devoted to the development and application of techniques for the analysis of surfaces, interfaces and thin films*, vol. 28, no. 1, pp. 8–11, 1999.

[136] H. J. Kim, N. Moldovan, J. R. Felts, S. Somnath, Z. Dai, T. D. Jacobs, R. W. Carpick, J. A. Carlisle, and W. P. King, "Ultrananocrystalline diamond tip integrated onto a heated atomic force microscope cantilever," *Nanotechnology*, vol. 23, no. 49, p. 495302, 2012.

[137] M. A. Derylo, K. C. Morton, and L. A. Baker, "Parylene insulated probes for scanning electrochemical-atomic force microscopy," *Langmuir*, vol. 27, no. 22, pp. 13925–13930, 2011.

[138] J. E. Sader, J. W. M. Chon, and P. Mulvaney, "Calibration of rectangular atomic force microscope cantilevers," *Review of Scientific Instruments*, vol. 70, no. 10, pp. 3967–3969, 1999.

[139] G. Jówiak, D. Kopiec, P. Zawierucha, T. Gotszalk, P. Janus, P. Grabiec, and I. Rangelow, "The spring constant calibration of the piezoresistive cantilever based biosensor," *Sensors and Actuators B: Chemical*, vol. 170, pp. 201 – 206, 2012. Eurosensors XXIV, 2010.

[140] M. Shusteff, T. P. Burg, and S. R. Manalis, "Measuring boltzmanns constant with a low-cost atomic force microscope: An undergraduate experiment," *American Journal of Physics*, vol. 74, no. 10, pp. 873–879, 2006.

[141] M. G. Ruppert, D. M. Harcombe, M. R. Ragazzon, S. R. Moheimani, and A. J. Fleming, "A review of demodulation techniques for amplitude-modulation atomic force microscopy," *Beilstein journal of nanotechnology*, vol. 8, no. 1, pp. 1407–1426, 2017.

[142] D. M. Harcombe, M. G. Ruppert, and A. J. Fleming, "A review of demodulation techniques for multifrequency atomic force microscopy," *Beilstein Journal of Nanotechnology*, vol. 11, no. 1, pp. 76–91, 2020.

[143] D. M. Harcombe, M. G. Ruppert, M. R. Ragazzon, and A. J. Fleming, "Lyapunov estimation for high-speed demodulation in multifrequency atomic force microscopy," *Beilstein Journal of Nanotechnology*, vol. 9, no. 1, pp. 490–498, 2018.

[144] R. E. Best, *Phase locked loops: design, simulation, and applications*. McGraw-Hill Professional, 2007.

[145] Átila Madureira Bueno, J. M. Balthazar, and J. R. C. Piqueira, "Phase-locked loop design applied to frequency-modulated atomic force microscope," *Communications in Nonlinear Science and Numerical Simulation*, vol. 16, no. 9, pp. 3835 – 3843, 2011.

[146] T. Fukuma, M. Kimura, K. Kobayashi, K. Matsushige, and H. Yamada, "Development of low noise cantilever deflection sensor for multienvironment frequency-modulation atomic force microscopy," *Review of Scientific Instruments*, vol. 76, no. 5, p. 053704, 2005.

[147] R. V. Iyer and X. Tan, "Control of hysteretic systems through inverse compensation," *IEEE Control Systems Magazine*, vol. 29, no. 1, pp. 83–99, 2009.

[148] J. Stakvik, M. Ragazzon, A. Eielsen, and J. Gravdahl, "On implementation of the preisach model identification and inversion for hysteresis compensation," vol. 36, pp. 133–142, 07 2015.

[149] S. Bashash and N. Jalili, "Robust multiple frequency trajectory tracking control of piezoelectrically driven micro/nanopositioning systems," *IEEE Transactions on Control Systems Technology*, vol. 15, no. 5, pp. 867–878, 2007.

[150] L. Liu, K. K. Tan, A. S. Putra, and T. H. Lee, "Compensation of hysteresis in piezoelectric actuator with iterative learning control," in *ICAIM'09*, pp. 1300–1305, July 2009.

[151] B. A. Francis and W. M. Wonham, "The internal model principle of control theory," *Automatica*, vol. 12, pp. 457–465, Sept. 1976.

[152] U. Aridogan, Y. Shan, and K. Leang, "Design and analysis of discrete-time repetitive control for scanning probe microscopes," *J. Dyn. Syst. Meas. Control*, vol. 131, pp. 1–12, 11 2009.

[153] Y. Shan and K. K. Leang, "Repetitive control with prandtl-ishlinskii hysteresis inverse for piezo-based nanopositioning," ACC'09, pp. 301–306.

[154] F. Xia, C. Yang, Y. Wang, and K. Youcef-Toumi, "Bandwidth based repetitive controller design for a modular multi-actuated afm scanner," in *2019 American Control Conference (ACC)*, pp. 3776–3781, July 2019.

[155] D. Y. Abramovitch, S. Hoen, and R. Workman, "Semi-automatic tuning of pid gains for atomic force microscopes," in *ACC'08*, pp. 2684–2689, June 2008.

[156] "Intelligent tuning method of pid parameters based on iterative learning control for atomic force microscopy," *Micron*, vol. 104, pp. 26 – 36, 2018.

[157] C. Yang, C. Li, F. Xia, Y. Zhu, J. Zhao, and K. Youcef-Toumi, "Charge controller with decoupled and self-compensating configurations for linear operation of piezoelectric actuators in a wide bandwidth," *IEEE Transactions on Industrial Electronics*, vol. 66, no. 7, pp. 5392–5402, 2018.

[158] S. Belikov and S. Magonov, "Simulation of atomic force microscopy of molecular structures and interplay with experiment," in *Proceedings of the 2010 American Control Conference*, pp. 5745–5750, June 2010.

[159] A. Varol, I. Gunev, B. Orun, and C. Basdogan, "Numerical simulation of nano scanning in intermittent-contact mode AFM underQcontrol," *Nanotechnology*, vol. 19, p. 075503, jan 2008.

[160] S. Belikov and S. Magonov, "Tip-sample interaction force modeling for afm simulation, control design, and material property measurement," in *ACC'11*, pp. 2867–2872.

[161] S. Belikov and S. Magonov, "Simulation of asymptotic amplitude-phase dynamics for afm resonant modes*," in *ACC'19*, pp. 2477–2482.

[162] K. Ástr "Automatic tuning of simple regulators with specifications on phase and amplitude margins," *Automatica*, vol. 20, no. 5, pp. 645 – 651, 1984.

[163] Y. Zhang, Y. Fang, J. Yu, and X. Dong, "Note: A novel atomic force microscope fast imaging approach: Variable-speed scanning," *Review of Scientific Instruments*, vol. 82, no. 5, p. 056103, 2011.

[164] Y. Wu, Q. Zou, and C. Su, "A current cycle feedback iterative learning control approach for afm imaging," *IEEE Transactions on Nanotechnology*, vol. 8, pp. 515–527, 2009.

[165] J. L. Bosse and B. D. Huey, "Error-corrected AFM: a simple and broadly applicable approach for substantially improving AFM image accuracy," *Nanotechnology*, vol. 25, p. 155704, mar 2014.

[166] L. Li, Q. Chen, G. Tan, and H. Zhu, "High precision position control of voice coil motor based on single neuron pid," *ISPEMI*, vol. 8759, 2013.

[167] F. Xia, C. Yang, Y. Wang, and K. Youcef-Toumi, "Model and controller design for high-speed atomic force microscope imaging and autotuning," in *Proceedings of the ASPE Spring Topical Meeting on Design and Control of Precision Mechatronic Systems*, American Society for Precision Engineering, 2020.

[168] T. R. Rodrıguez and R. Garcıa, "Theory of q control in atomic force microscopy," *Applied Physics Letters*, vol. 82, no. 26, pp. 4821–4823, 2003.

[169] T. Sulchek, R. Hsieh, J. Adams, G. Yaralioglu, S. Minne, C. Quate, J. Cleveland, A. Atalar, and D. Adderton, "High-speed tapping mode imaging with active q control for atomic force microscopy," *Applied Physics Letters*, vol. 76, no. 11, pp. 1473–1475, 2000.

[170] M. B. Coskun, H. Alemansour, A. G. Fowler, M. Maroufi, and S. O. R. Moheimani, "q control of an active afm cantilever with differential sensing configuration," *IEEE Transactions on Control Systems Technology*, vol. 27, pp. 2271–2278, Sep. 2019.

[171] A. Schuh, I. S. Bozchalooi, I. W. Rangelow, and K. Youcef-Toumi, "Multi-eigenmode control for high material contrast in bimodal and higher harmonic atomic force microscopy," *Nanotechnology*, vol. 26, p. 235706, may 2015.

[172] A. Schuh, I. S. Bozchalooi, I. W. Rangelow, and K. Youcef-Toumi, "Estimator based multi-eigenmode control of cantilevers in multifrequency atomic force microscopy," in *2015 American Control Conference (ACC)*, pp. 1905–1910, July 2015.

[173] J. A. Main, E. Garcia, and D. V. Newton, "Precision position control of piezoelectric actuators using charge feedback," *Journal of Guidance, control, and dynamics*, vol. 18, no. 5, pp. 1068–1073, 1995.

[174] K. A. Yi and R. J. Veillette, "A charge controller for linear operation of a piezoelectric stack actuator," *IEEE transactions on control systems technology*, vol. 13, no. 4, pp. 517–526, 2005.

[175] A. J. Fleming and S. R. Moheimani, "A grounded-load charge amplifier for reducing hysteresis in piezoelectric tube scanners," *Review of Scientific Instruments*, vol. 76, no. 7, p. 073707, 2005.

[176] A. J. Fleming, "Charge drive with active dc stabilization for linearization of piezoelectric hysteresis," *IEEE transactions on ultrasonics, ferroelectrics, and frequency control*, vol. 60, no. 8, pp. 1630–1637, 2013.

[177] C. Yang, N. Verbeek, F. Xia, Y. Wang, and K. Youcef-Toumi, "Modeling and control of piezoelectric hysteresis: A polynomial-based fractional order disturbance compensation approach," *IEEE Transactions on Industrial Electronics*, 2020.

[178] T. Fukuma and S. P. Jarvis, "Development of liquid-environment frequency modulation atomic force microscope with low noise deflection sensor for cantilevers of various dimensions," *Review of Scientific Instruments*, vol. 77, no. 4, p. 043701, 2006.

[179] N. Instruments, "Implementing multiple clock domains (fpga module)," 2016.

[180] T. Bress, *Effective LabVIEW Programming*. Nts Press, 2013.

[181] X. Xu, Y. Wang, J. Tang, X. Zhang, and X. Liu, "Robust automatic focus algorithm for low contrast images using a new contrast measure," *Sensors*, vol. 11, no. 9, pp. 8281–8294, 2011.

[182] L. Shih, "Autofocus survey: a comparison of algorithms," in *Digital Photography III*, vol. 6502, p. 65020B, International Society for Optics and Photonics, 2007.

[183] S. V. Kalinin, E. Strelcov, A. Belianinov, S. Somnath, R. K. Vasudevan, E. J. Lingerfelt, R. K. Archibald, C. Chen, R. Proksch, N. Laanait, *et al.*, "Big, deep, and smart data in scanning probe microscopy," 2016.

[184] I. S. Bozchalooi, A. C. Houck, J. AlGhamdi, and K. Youcef-Toumi, "Design and control of multi-actuated atomic force microscope for large-range and high-speed imaging," *Ultramicroscopy*, vol. 160, pp. 213 – 224, 2016.

[185] G. Haugstad, *Atomic force microscopy: understanding basic modes and advanced applications*. John Wiley & Sons, 2012.

[186] N. Inc., "Naioafm: The leading afm for nanoeducation," 2017.

[187] N. Instruments, "Atomic force microscope - ezafm," 2017.

[188] I. Corp, "Nanoscale images anywhere with the ngauge afm," 2020.

[189] R. Reifenberger and A. Raman, "Me 597/phys 570: Fundamentals of atomic force microscopy (fall 2010)," Sep 2010.

[190] D. Sarid, *Exploring scanning probe microscopy with Mathematica*. John Wiley & Sons, 2007.

[191] A. Corp., "Basic atomic force microscope for routine scanning and education," 2020.

[192] S. mlinet Nano Inc., "Strømlingo nssembly afm," 2017.

[193] M. Shusteff and S. Manalis, "An atomic force microscope (afm) for the instructional laboratory," 2006.

[194] H. Liao, K. Huang, C. Chang, and C. Lin, "Magnifying the nanoworld: An educational atomic force microscope," in *The ASME Asia-Pacific Engineering Education Congress*, 2009.

[195] D. Amin-Shahidi and D. Trumper, "Macro-scale atomic force microscope: An experimental platform for teaching precision mechatronics," *Mechatronics*, vol. 31, pp. 234 – 242, 2015.

[196] M. Chyasnavichyus, S. L. Young, R. Geryak, and V. V. Tsukruk, "Probing elastic properties of soft materials with afm: Data analysis for different tip geometries," *Polymer*, vol. 102, pp. 317 – 325, 2016. Polymers at Interfaces: Probing Mechanics and Interactions by Atomic Force Microscopy.

[197] E. Thormann, T. Pettersson, J. Kettle, and P. M. Claesson, "Probing material properties of polymeric surface layers with tapping mode afm: Which cantilever spring constant, tapping amplitude and amplitude set point gives good image contrast and minimal surface damage?," *Ultramicroscopy*, vol. 110, no. 4, pp. 313 – 319, 2010.

[198] R. Newton, M. Delguste, M. Koehler, A. C. Dumitru, P. R. Laskowski, D. J. Müller, and D. Alsteens, "Combining confocal and atomic force microscopy to quantify single-virus binding to mammalian cell surfaces," *nature protocols*, vol. 12, no. 11, p. 2275, 2017.